ULTRA-HIGH TEMPERATURE DISTRIBUTED WIRELESS SENSORS

FINAL TECHNICAL REPORT

Reporting Period Start Date: October 1, 2009
Reporting Period End Date: March 31, 2013

Report Issue Date: June 2013

DOE Award Number: DE-FE0001249

Principal Authors: Russell May, Prime Photonics LC
Raymond Rumpf, Prime Photonics LC
John Coggin, Prime Photonics LC
William Davis, Virginia Tech
Taeyoung Yang, Virginia Tech
Alan O'Donnell, Virginia Tech
Peter Bresnahan, Virginia Tech

Submitting Organization: Prime Photonics, LC
1116 South Main Street
Blacksburg, VA 24060

Subcontractor: Virginia Tech
300 Turner Street, Suite 4200
Blacksburg, VA 24041-0170

Abstract

Research was conducted towards the development of a passive wireless sensor for measurement of temperature in coal gasifiers and coal-fired boiler plants. Approaches investigated included metamaterial sensors based on guided mode resonance filters, and temperature-sensitive antennas that modulate the frequency of incident radio waves as they are re-radiated by the antenna.

In the guided mode resonant filter metamaterial approach, temperature is encoded as changes in the sharpness of the filter response, which changes with temperature because the dielectric loss of the guided mode resonance filter is temperature-dependent.

In the mechanically modulated antenna approach, the resonant frequency of a vibrating cantilever beam attached to the antenna changes with temperature. The vibration of the beam perturbs the electrical impedance of the antenna, so that incident radio waves are phase modulated at a frequency equal to the resonant frequency of the vibrating beam. Since the beam resonant frequency depends on temperature, a Doppler radar can be used to remotely measure the temperature of the antenna.

Laboratory testing of the guided mode resonance filter failed to produce the spectral response predicted by simulations. It was concluded that the spectral response was dominated by spectral reflections of radio waves incident on the filter.

Laboratory testing of the mechanically modulated antenna demonstrated that the device frequency shifted incident radio waves, and that the frequency of the re-radiated waves varied linearly with temperature.

Radio wave propagation tests in the convection pass of a small research boiler plant identified a spectral window between 10 and 13 GHz for low loss propagation of radio waves in the interior of the boiler.

Table of Contents

Table of Tables

Table of Figures

1 EXECUTIVE SUMMARY

This report documents the progress and results of a research program to develop a passive wireless sensor for measurement of temperature in coal-fired power plants and coal gasifier plants. Two technical approaches were investigated in the course of the program. In the first, a metamaterial sensor employing guided mode resonance (GMR) was studied. Changes in the temperature of the metamaterial sensor produce changes in the electromagnetic response of the metamaterial, which can be detected remotely by a microwave radar. In the second, a mechanically modulated antenna was studied. The antenna contained a mechanically vibrating element which phase modulates microwaves re-radiated by the antenna. A Doppler radar system is used to interrogate the antenna, and as the antennas temperature changes, the mechanical resonance frequency of the vibrating element shifts, changing the frequency of the phase modulation.

In the GMR approach, a microwave diffraction grating is attached to the slab waveguide. For a narrow range of frequencies, incident microwaves will be diffracted by the grating and coupled into guided electromagnetic modes in the slab waveguide. Since the waveguide is a reciprocal device, the guided modes are leaked into radiating modes. These radiating modes combine with the incident microwaves to form the electromagnetic response of the metamaterial guided mode resonance filter (GMRF). The GMRF metamaterial can be designed to either pass a narrower range of frequencies and reflect the rest, forming a bandpass filter, or reflect a narrow range and pass the rest, forming a band stop filter. If the slab waveguide is made from a dielectric material that has conductivity that changes with temperature, then the width and sharpness of the filter spectral response (the Q or quality factor) will change with temperature, providing a mechanism for measuring temperature.

In this program, computational electromagnetics numerical modeling was used to design a GMRF filter with a passband centered in the microwave X-band. Various materials for forming the slab waveguide were considered, and silicon carbide (SiC) was identified as a suitable material. Laboratory measurements of the dielectric properties of a sample of high-conductivity chemical vapor deposition (CVD) synthesized SiC showed that its conductivity varied quadratically with temperature.

Laboratory testing of a prototype GMRF sensor with a silicon carbide waveguide did not exhibit the predicted electromagnetic spectral response. However, testing of a two-dimensional dipole array did exhibit a resonance in the spectral response as predicted, ruling out experimental error in the GMRF test. Analysis of test results lead to the conclusion that the GMRF metamaterial sensor's response was dominated by background reflections, that a large number of grating periods (and hence a large sensor) is required for a strong spectral response, and that the spectral response depend strongly on the angle of incidence of interrogating microwaves. For this reason, research was initiated into the development of a mechanically modulated antenna as an alternative passive wireless temperature sensor.

The mechanically modulated antenna (MMA) design consisted of a folded slot antenna on a copper ground plane, with a vibrating copper cantilever beam fixed on one end and free on the other. The free end of the cantilever beam was positioned in close proximity to a copper stub that was attached to the ground plane. The fixed end of the cantilever beam was attached to a copper post also mounted on the ground plane. To operate the sensor, the cantilever beam is stimulated to vibrate resonantly either by insonifying the beam with acoustic waves at a frequency equal to the beam's natural frequency, or by mechanically vibrating the antenna mechanically at the beam's resonant natural frequency. As the

cantilever beam vibrates, the spacing between the free end of the beam and the ground plane varies harmonically, changing the capacitive load across the antenna slot sinusoidally at the beam natural frequency. The resulting harmonically varying antenna impedance imparts a phase modulation to incident microwaves as they re-radiate, which can be detected by a Doppler radar. Changes in the temperature of the antenna produce changes in the stiffness and dimensions of the vibrating beam, shifting its resonant frequency. The charge in resonant frequency can be related to the change in temperature by calibration.

Finite element electromagnetic numerical models were used to design a prototype MMA sensor, and a prototype was fabricated and evaluated at room temperature. Excitation of resonant vibration of a cantilever beam was achieved by insonification using a loudspeaker, and in a separate test by heating with an intensity modulated laser. An X-band Doppler radar successfully detected the modulation of incident microwaves.

More extensive computational electromagnetics modeling of mechanically modulated slot antennas and mechanically modulated dipole antennas was performed and determined that MMA response is primarily due to phase modulation of the incident microwaves and not amplitude modulation. Additional modeling was used to predict the effect of changing the antenna slot size and the ground plane size. Results indicated that phase response of the MMA is increased for smaller ground planes.

A fiber optic interferometer and a stroboscope were used to analyze the vibrational motion of the cantilever on an MMA prototype excited by a vibration shaker table. The results revealed the presence of several torsional vibration modes in the cantilever motion, and prompted a mechanical redesign of the MMA to widen the beam to suppress the torsional modes.

Testing was conducted at Babcock & Wilcox's Small Boiler Simulator (SBS) in Barberton, OH to investigate the attenuation of microwaves by the gases and particulates exhausted by a burner in a boiler plant. Two antennas were designed and built to fit in viewports in the SBS, and a vector network analyzer was used to measure scattering parameters as microwaves transited the interior convection pass of the SBS, from which the attenuation could be calculated. Testing was conducted under conditions of natural gas firing, of biomass firing, and pulverized coal firing. A window of low attenuation of less than 2 dB/m was found in the band from 10 to 13 GHz.

Prototype MMA sensors for high temperature testing were fabricated using polycrystalline alumina and platinum. An additional prototype was assembled using alumina and copper. Testing of the MMA response was conducted in a box furnace, and the cantilever beam resonant frequency was observed to change approximately linearly with increasing temperature. The signal amplitude, as output by the Doppler radar interrogator, decreased as the temperature was increased until the sensor could no longer be resolved below the noise floor of the interrogator. This reduction in signal strength limited operation of the alumina and copper MMA sensor to 800° C, and the alumina and platinum sensor to 270° C. Further testing was conducted to rule out experimental setup is being responsible for the reduction in signal strength at high temperature, which suggested a fundamental limitation in the sensor design or fabrication.

2 METAMATERIAL SENSOR DEVELOPMENT

The first technical approach investigated in this program to develop wireless sensors involved metamaterial technology. Metamaterials can be defined as engineered composites that exhibit superior properties not found in nature and not observed in the constituent materials.[1,2] They provide a powerful means to dramatically enhance and control the interaction between a device and applied electromagnetic energy. Electromagnetic metamaterials are composed of periodic subwavelength features that exhibit new and useful properties such as a negative index of refraction, tailorable dielectric and magnetic polarizability, strong dispersion, and frequency selective transmission, reflection and absorption. Metamaterials can be broadly separated into two categories, *electromagnetic band gap (EBG) materials* and *effective media*. EBG materials exploit scattering and resonance in periodic structures to control propagation of electromagnetic energy.[3,4] They are able to manipulate radio frequencies in ways analogous to the manipulation of electrons in computer chips. EBG materials can even exhibit complete band gaps where energy is forbidden to propagate at any angle within some spectral band. They can also provide strong and anomalous dispersion properties such as negative refraction, negative dispersion, slow propagation, superprism effects, and more. The EBG provides a powerful means to engineer the dispersion and reflectivity of a material.

The principle of operation of the metamaterial wireless sensor system investigated in this program is illustrated in Figure 1. A broadband RF source illuminates an array of passive sensors which filter and reflect some of the incident energy. The reflected signals travel back to the source where they are detected and processed by the receiver. The sensors are designed so that temperature modifies the spectral response in a manner that can be used to distinguish the sensors and make accurate measurements

In the metamaterial approach investigated here, temperature is encoded as changes in the quality factor (Q) of a resonator. The Q of a resonance can be defined as the center frequency divided by its full width at half maximum (FWHM).

$$Q = \frac{f_c}{\text{FWHM}} \tag{1}$$

A simple LC circuit will produce a resonance from which an initial Q can be defined. When resistance is incorporated into the circuit, the resonance is weakened and broadened which lowers the Q. A property like temperature can be measured through changes in the Q if the resistive element changes with temperature. In the approach investigated here, resonance would be produced using subwavelength metamaterials to interact with the radio waves and produce an analogous resonance. Resistive high temperature materials like YSZ or SiC will be incorporated to dampen the resonance in response to temperature.

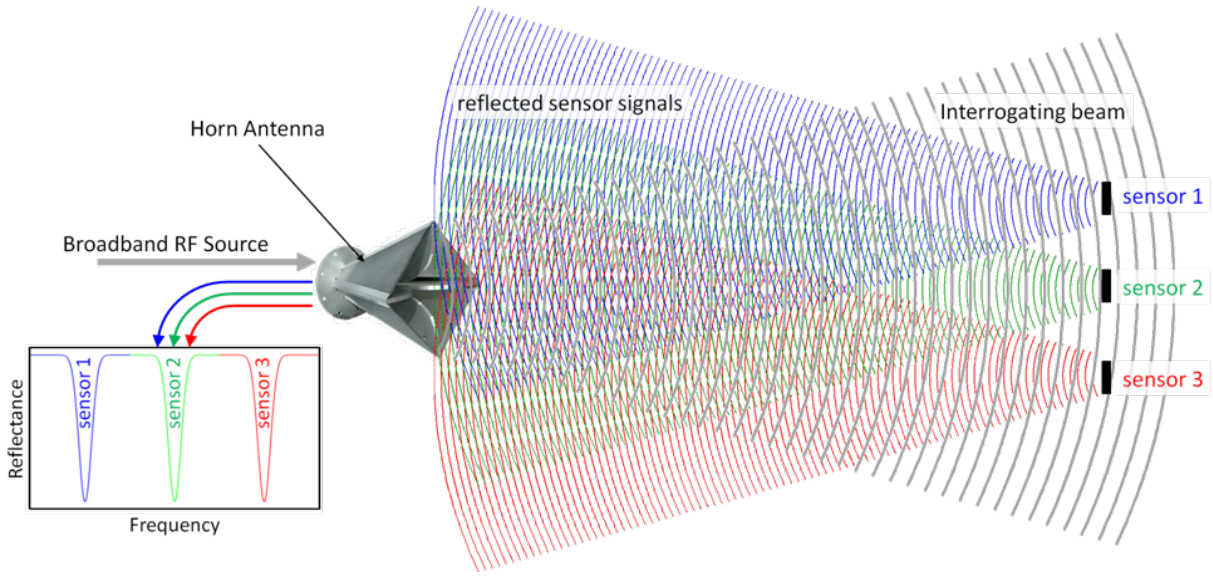

Figure 1. Concept diagram of wireless sensor system

The Q approach for sensing is attractive because it provides a degree of immunity to mechanical deformations and channel attenuation which can distort the measurements. In addition, sensor arrays can be multiplexed for distributed sensing by operating them at distinct frequencies. As thermal expansion causes the dimensions of a sensor to fluctuate, the center frequency and FWHM will scale by the same factor making the Q independent of scale and immune to this effect. The Q is also unaffected by uniform channel attenuation because its value is independent of the amplitude of the resonance.

2.1 Material Selection

The initial design of the metamaterial high-temperature wireless sensor approach was a laminate comprising a frequency selective metamaterial sandwiched between two conductive ceramic layers. This structure is resonant due to the capacitance and inductance of the metamaterial. When excited by an external radio frequency wave, the metamaterial resonates at its characteristic frequency. Frequencies away from resonance either pass through the device or are reflected by it with little loss. At resonance, the energy is confined and concentrated in the conductive ceramic layers, which dampens the resonance. As a result of this, the response of the sensor may be characterized by the quality factor *Q* of the resonance, as illustrated in Figure 2. This is approximately equal to the center frequency divided by the width of the resonance. Typically, the full width at half maximum (FWHM) is used as the measure of resonance width.

$$Q \cong \frac{f_c}{\text{FWHM}} \tag{2}$$

The structure becomes a temperature sensor when it incorporates conductive ceramic layers with conductivity that depends on temperature.

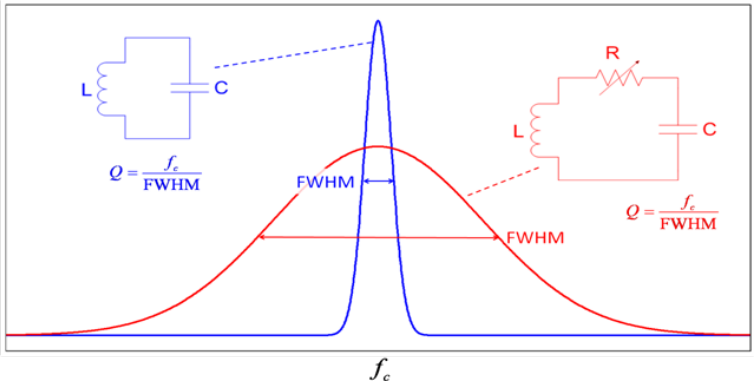

Figure 2. Dependence of resonant circuit *Q* on resistive losses.

At low frequencies, the resistive loss of conductive ceramics results from the electrical conductivity. To achieve high conductivity, the ceramic must have a high concentration of charge carriers in addition to high mobility of those carriers. The carriers may be charged ions, electrons, or electron holes. Accordingly, the total electrical conductivity at low frequencies is a combination of ionic conductivity and electronic conductivity. For high ionic conductivity, diffusing ions must have sufficient thermal energy to exceed the energy barrier represented by the intermediate position between lattice sites in the crystal structure.

When an appreciable concentration of electrons populates the conduction band of the ceramic, electronic conductivity results. In most materials, electrons have much higher mobility than ions. Some transition metal oxides, including ReO_3, CrO_2, and TiO, exhibit high levels of electronic conductivity, approaching that of metal conductors. In other ceramics, the concentrations of the electrons and electron holes can be increased by adding appropriate solutes to generate nonstoichiometric compounds.

At high frequencies, electrical loss in the ceramic can be characterized by its dielectric conductivity σ or its loss tangent, $\tan\delta$. The dielectric conductivity is related to the imaginary part of the permittivity ε'' through

$$\sigma = \omega\varepsilon'' \tag{3}$$

where is É is the radian frequency of the electromagnetic wave. The complex permittivity is

$$\varepsilon = \varepsilon' + j\varepsilon'' \tag{4}$$

The loss tangent is the ratio of the imaginary component of the complex permittivity to the real component.

$$\tan\delta = \frac{\varepsilon''}{\varepsilon'} \tag{5}$$

For the metamaterials sensor application, we require materials with a high dielectric conductivity (or loss tangent) at high temperatures and high frequencies. There are three mechanisms that contribute to electromagnetic loss in dielectric materials:

- ion migration losses (includes DC conductivity losses, ion jump losses, and dipole relaxation losses),
- ion vibration and deformation losses
- electron polarization losses.

Electronic polarization losses are significant at frequencies corresponding to the visible light spectrum. At the frequencies of interest to this program (10^{10} – 10^{11} Hz), only ion vibration and deformation effects have relaxation times comparable to the periods of the high-frequency electromagnetic waves, as shown in Figure 3.[5]

A review of the technical literature suggests that the dielectric conductivity and other loss mechanisms have not been well characterized simultaneously at the very high frequencies (> 10^{10} Hz) and very high temperatures (> 1000 °C) required for this project. A 2006 paper by Kang et al[6] investigating high-temperature conductivity of nanocrystalline barium titanate ceramics examined conductivity at 1 MHz at temperatures up to 800 °C. Their results showed that conductivity decreased as temperature increased, which the authors attributed to accumulation of charges at grain boundaries.

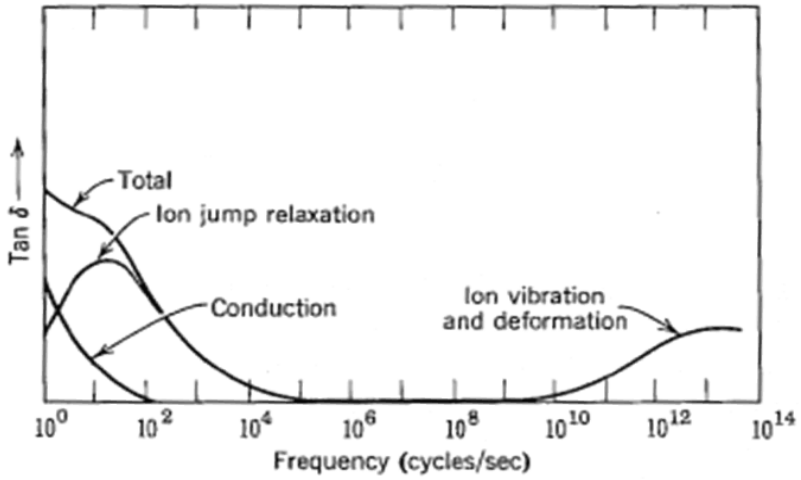

Figure 3. Frequency dependence of mechanisms contributing to dielectric loss at room temperature.[5]

Silicon carbide (SiC) appears to be a promising material for use as the conductive layers in sensor assembly. In a 2002 report, Baeraky characterized the dielectric properties of pure SiC at temperatures up to 1800 °C and at frequencies to 3.8 GHz.[7] For temperatures greater than 1000 °C, the dielectric conductivity was found to increase exponentially with increasing temperature. Figure 4 shows some typical results, which also indicate that conductivity decreases with increasing frequency. While SiC is subject to corrosion and oxidation at temperatures exceeding 1200 °C under conditions of 10 atm (150 psi) of steam,[8] in the proposed sensor package, the conductive ceramic layers and metamaterial will be hermetically encapsulated from the gasifier or boiler environment.

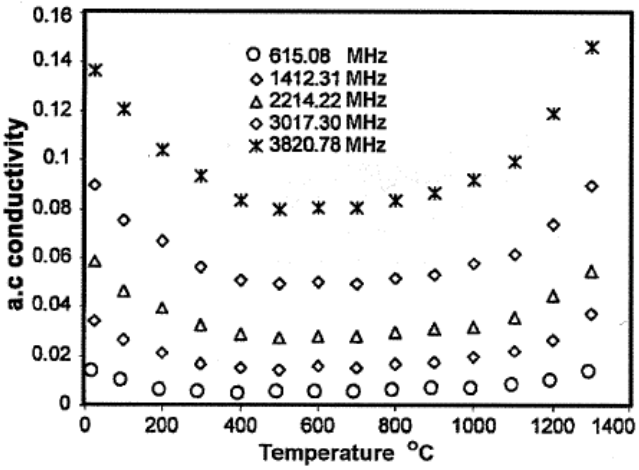

Figure 4. Dielectric conductivity of SiC as a function of frequency and temperature.[7]

2.1.1 Characterization of Silicon Carbide Conductivity

Tests were performed to characterize the change in dielectric properties of silicon carbide as a function of temperature. Electromagnetic parameters were extracted from transmission and reflection measurements of material slabs placed in a high temperature furnace.

In order to verify the measurement technique and setup for dielectric characterization of silicon carbide material, four different methods were evaluated and used to test a well-known material (FR4, a glass reinforced epoxy laminate sheet) with well-characterized dielectric properties ($\varepsilon_r = 4.5$ and $\tan\delta = 0.025$). A network analyzer was used to obtain the complex reflection and transmission coefficients from which the dielectric constant and conductivity will be calculated. Note that FR4 is cheap, popular material for RF circuit boards. However, the electrical property of the FR4 varies from batch to batch, and is slightly anisotropic. Despite these limitations, it was felt that FR4 afforded an inexpensive, straightforward path to evaluate set-ups for characterization of dielectric properties.

First, a TRL (Through-Reflection-Line) full 2-port calibration approach (Figure 5a) was considered to eliminate the transition effects from the SMA connectors. After the TRL calibration, the complex propagation constant can be obtained from the transmission coefficient of the line standard. The material property of the substrate can be estimated from the known closed-form expression of microstrip line structures.[9] The through and line standards of the TRL calibration can be used to extract the complex propagation constant. Because SMA connectors become good radiators above approximately 12 GHz, the estimation frequency range of these approaches is limited.

The second approach was to use a coaxial air line (Figure 5b). In this case, a material under test (DUT) in an annular ring shape is inserted into the air line. Using the reflection/transmission approach,[10] the complex dielectric constant of the DUT can be estimated. Because a coaxial structure does not have a cut-off frequency, the coaxial line

approach provides a very wideband measurement range, though the low-frequency limit of the approach is limited by thickness of the test material.

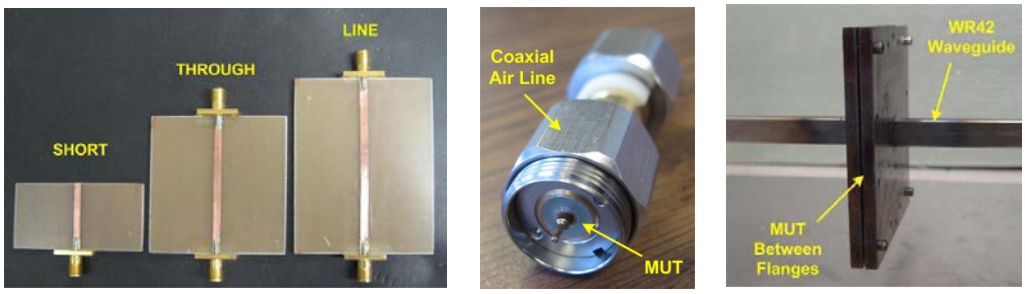

(a) (b) (c)

Figure 5. Picture of various measurement components – (a) Microstrip line standards, (b) 50 mm Coaxial air line loaded with material under test (MUT), and (c) MUT slab between flanges of WR-42 waveguide.

Unfortunately, none of the above approaches can be used in a high temperature environment. Instead, a test rig using stainless steel WR-42 waveguides (f_c = 14.05 GHz) was prepared with large flanges, as shown in Figure 5c and Figure 6. A test material sample was then inserted between the flanges. If the test material is highly lossy, no significant fringing fields occur between the flanges, and the setup can be modeled as a test material inside a rectangular waveguide.

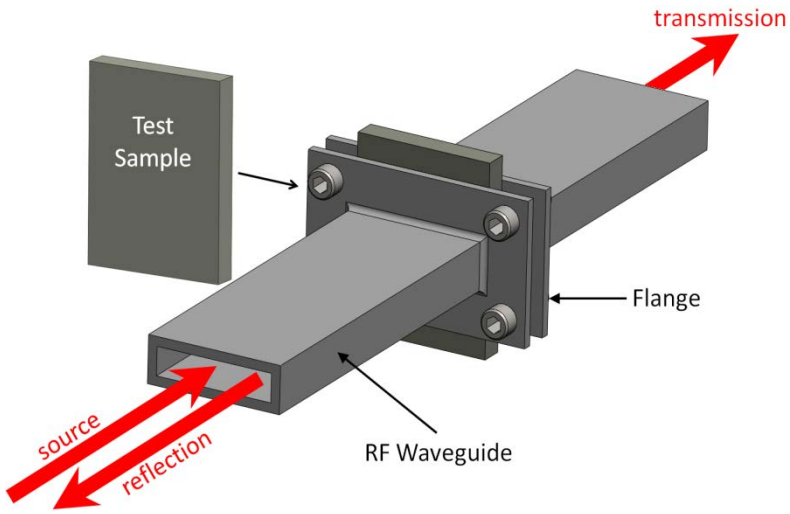

Figure 6. Experimental setup for charactering RF properties at high temperature

In Table 1, the estimated dielectric constant and loss tangent for FR4 are compared for different measurement approaches. There are minor differences in the estimated values from different approaches due to different sources of errors, i.e. different measurement fixtures and standards. As noted previously, FR4 substrate material varies with production batches. One

reason for the choice of FR4 material was that the loss property of FR4 varies significantly over frequency, as shown in Table 1. The comparison of the above approaches shows that the measurement setup for the high temperature environment will predict the material properties with a reasonable accuracy. Since our ultimate goal was observe a relative change of material property for temperature variation, the proposed measurement setup shown in Figure 5c was appropriate for the high temperature environment.

The conductivity (σ) at a given angular frequency (ω) can be found from following relationship:

$$\sigma = \omega \varepsilon_0 \varepsilon_r \tan\delta \tag{6}$$

where ε_0 is the permittivity in free space (= 8.854e-12 F/m).

Table 1. Comparison of measured dielectric constant and loss tangent of FR4 for various measurement setups.

Measurement Approach	Dielectric Constant (ε_r)	Loss Tangent (tanδ)
TRL	5.25 @ 5 GHz	0.019 @ 5 GHz
Two-Transmission-Line	4.48 @ 5 GHz	0.018 @ 5 GHz
Coaxial Air Line	4.05 @ 5 GHz 4.50 @ 20 GHz	0.020 @ 5 GHz 0.357 @ 20 GHz
WR-42 Waveguide	4.10 @ 20 GHz	0.370 @ 20 GHz

Figure 7 shows the overall setup for the dielectric property estimation with temperature variation. The test material (silicon carbide) is loaded in between the flanges of the WR-42 waveguides. The flanges and test sample are then placed in a custom-made clamshell. The temperature inside the flanges was monitored and controlled using an Omega temperature controller with thermocouple. The reflected signal from the test material and transmitted signal through the test material were measured by using a HP 8510C vector network analyzer at sampled temperatures between 25° C and 800° C. The experiments were repeated several times with two different HP 8510C network analyzers. The measured data from the multiple experiments were consistent.

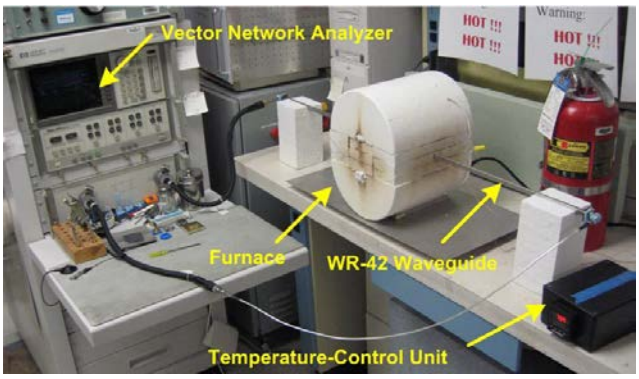

(a)

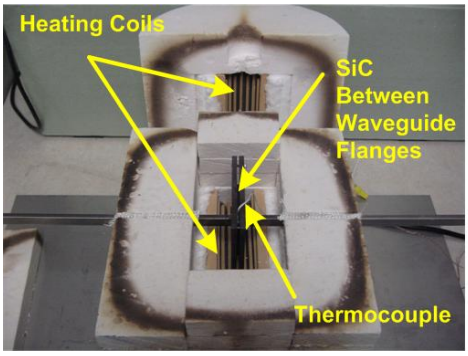

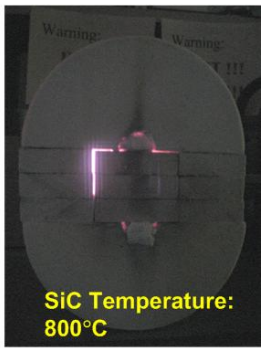

(b) (c)

Figure 7. Pictures of measurement setup for material characterization with temperature variation: (a) Overall setup, (b) Inside furnace, and (c) Furnace in operation.

Electrical properties of materials are typically characterized in terms of relative-permittivity (ε_r) and permeability (μ_r) relative to free-space permittivity ($\varepsilon_0 \approx 0.85418781761 * 10^{-12}$ [F/m]) and permeability ($\mu_0 \approx 4\pi * 10^{-7}$ [H/m]). The permittivity (ε) and permeability (μ) are defined as

$$\varepsilon = \varepsilon_0(\varepsilon_r' - j\varepsilon_r'') = \varepsilon_0\varepsilon_r'(1 - j\tan\delta_\varepsilon) \tag{7}$$

or

$$\varepsilon = \varepsilon_0\varepsilon_r' - j\frac{\sigma_e}{\omega}, \tag{8}$$

and

$$\mu = \mu_0(\mu_r' - j\mu_r'') = \mu_0\mu_r'(1 - j\tan\delta_\mu) \tag{9}$$

where ε_r is the relative permittivity, μ_r is the relative permeability, $\tan\delta_\varepsilon$ and $\tan\delta_\mu$ are electric and magnetic loss tangents respectively, σ_e is electric conductivity, and ω is angular

frequency ($2\pi *$ frequency), and where the single prime denotes the real component and the double prime denotes the imaginary component. Typically, the loss is represented with either the loss tangent or the conductivity. Both loss tangent and conductivity are figures of merit representing the imaginary term (loss term) of the permittivity. For the case of materials with diamagnetic properties (μ_r H1), the conductivity (σ) of silicon carbide can be written in terms of the relative permittivity and loss tangent as

$$\sigma = \omega\varepsilon_0\varepsilon_r' \tan\delta_e = \omega\varepsilon_0\varepsilon_r'' \tag{10}$$

In reality, the conductivity and the permittivity loss represent two different mechanisms of loss, one due to free charge motion and the other due to bound charge. However, the distinction is not important in this work and they are equated.

Two assumptions were made for the material characterization and post-processing of the measured data due to the limited situation to obtain a specific sample size and thickness:

Assumption #1: Silicon carbides do not have a strong magnetic property, i.e. they are diamagnetic and μ_r H1.

Assumption #2: The variation of the imaginary component $\varepsilon_0\varepsilon_r''$ of permittivity is the dominant factor in the variation of permittivity ε with temperature.

The estimation of relative permeability μ_r of the test material is strongly influenced by the reflection coefficient, while the relative permittivity ε_r is influenced by the transmission coefficient extracted from the composite reflected (s_{11}) and transmitted signal (s_{21}). Both these *S*-parameters include multiple reflections and transmissions with phase variations at the boundary between the air and test material. Because the sample could not be inserted completely inside the waveguide structure, some minor fringing fields are expected. These fringing fields may make the estimated reflection coefficient less accurate than the transmission coefficient, meaning that the estimated relative permittivity μ_r may be less accurate. In addition, the estimation of the relative permittivity ε_r depends on the relative permeability μ_r estimation. Assumption #1 allows us to obtain a more accurate relative permittivity ε_r estimation from the transmission data directly. At least one reference[11] reported that the susceptibility ($\chi = \mu_r' - 1$) for silicon carbide (6H) is 10.6×10^{-6} g-mol at 1300 °C, which suggests that the silicon carbide is not strongly magnetic.

The measured scattering parameters (s_{11} and s_{21}) using the vector network analyzers are in a phasor format, providing both magnitude and phase versus frequency. Therefore, the phase information of the scattering parameters is the minimum relative phase ignoring a variation of $n2\pi$ (n = 0, 1, 2, …). However, the absolute phase information is critical to estimate the material property, which leads us to a phase-unwrapping issue. For thin test materials, the phase-unwrapping process is not an issue. However, a strong loss, even for thin test materials, makes the material look electrically long, which is the case if our test sample is heated. In this case, the loss property (ε_r'') change is dominant over the dielectric constant (ε_r') change (the assumption #2), giving similar real and imaginary values of the complex propagation constant inside the test

material.[i] Based on this observation, we can resolve the phase unwrapping issue. In addition, the influence of the fringing fields becomes minor for the high loss case, unless air gaps are created in the heating process.

Figure 8 and Figure 9 show the measured reflected-signal power level ($|s_{11}|^2$) from the test material and transmitted-signal power level ($|s_{21}|^2$) though the test material for test sample #1 and #2 respectively. The estimated dynamic range of the vector network analyzer for the measurement setup is around 85 dB. The transmitted-signal power level ($|s_{21}|^2$) at high temperatures seems to be at very low level, but it is still within the 85 dB dynamic range. The variation of both $|s_{11}|^2$ and $|s_{21}|^2$ for the sample #1 and #2 are similar, though there is a minor amplitude difference.

For loss-free samples, the sum of $|s_{11}|^2$ and $|s_{21}|^2$ should be unity, i.e. $|s_{11}|^2 + |s_{21}|^2 = 1$. Obviously, the reflected-signal power level ($|s_{11}|^2$) over temperature variation shows less change than the transmitted-signal power level ($|s_{21}|^2$), which suggests that there is a strong loss process inside the test material. On the other hand, the estimated dielectric constant (ε_r') over the temperature variation is relatively flat, compared to the loss variation (ε_r'') in Figure 10, which indicates that Assumption #2 is justified.

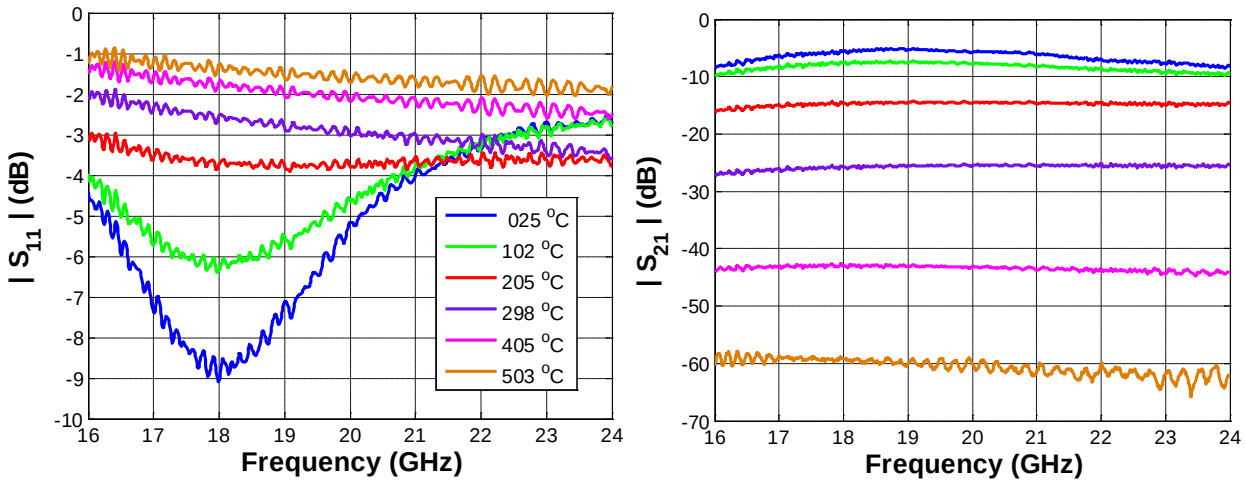

(a) (b)

Figure 8. Measured reflected ($|s_{11}|^2$) and transmitted ($|s_{21}|^2$) signal power level through the silicon carbide sample #1 for various temperatures.

[i] The real part of the complex propagation constant (γ) represents an attenuation variation, while the imaginary part represents a phase variation. The complex propagation constant is directly related to estimate of the transmission coefficient.

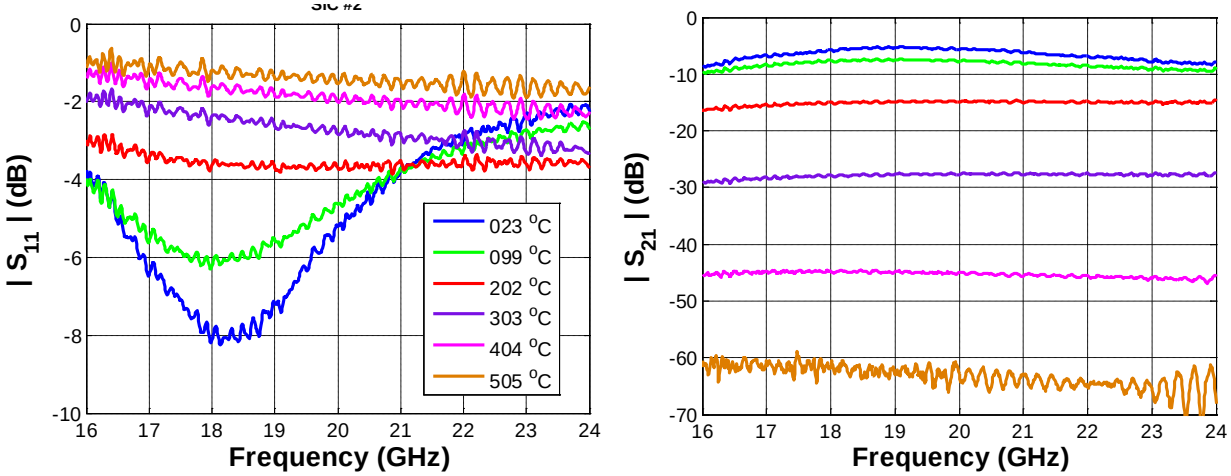

(a) (b)

Figure 9. Measured reflected (s_{11}) and transmitted (s_{21}) signal power level through the silicon carbide sample #2 for various temperatures.

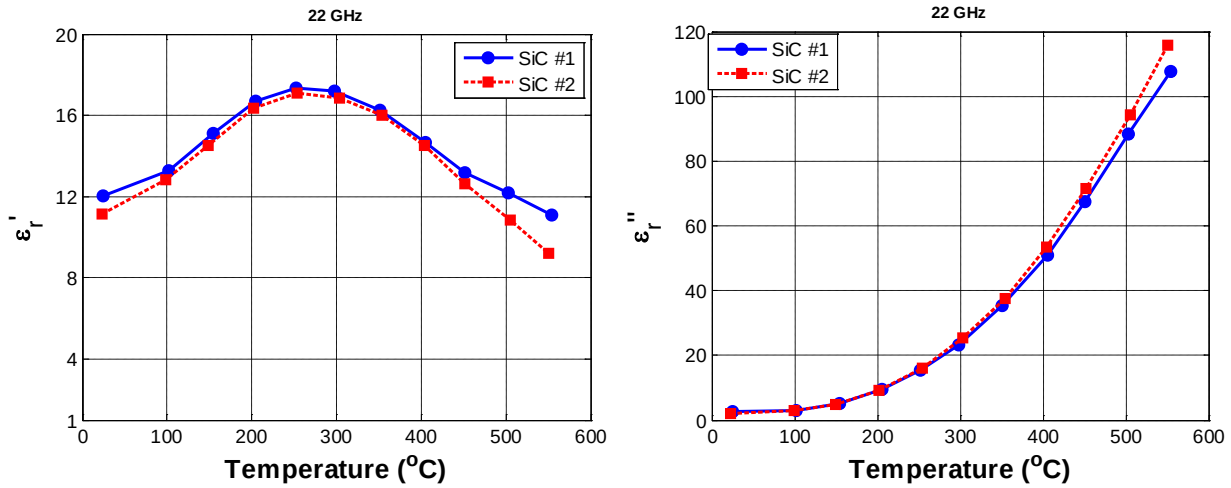

(a) (b)

Figure 10. Comparison between estimated permittivity of the SiC samples (a) Real part of permittivity (ε_r', dielectric constant) and (b) Imaginary part of permittivity (ε_r'', loss property of material).

The scattering parameters were measured up to approximately 800 °C. Data above 550 °C showed periodic dips on the *S*-parameter curves which are not shown in this report. One plausible explanation for the dips is the possibility of a small gap between the sample and the waveguide flanges at a high temperature due to the different thermal expansion coefficients between the stainless steel fixture (waveguide flange and bolts jointing the flanges) and the silicon carbide.

The estimated conductivity for both test samples #1 and #2 from the measured data at 22 GHz are shown in Figure 11 along with the curve-fit data. It appears that the conductivity varies with temperature in a quadratic manner.

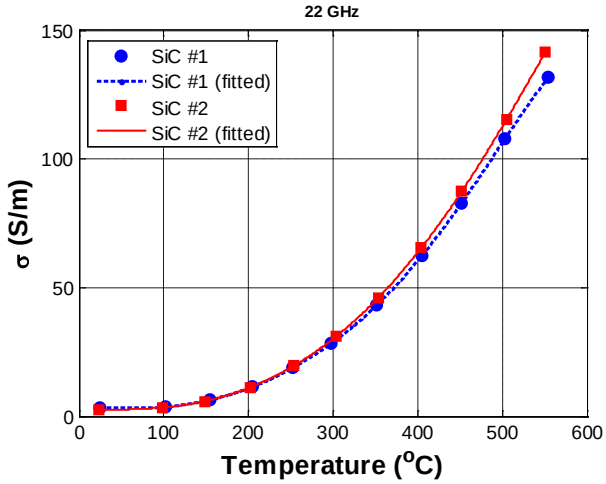

Figure 11. Measured conductivity @ 22 GHz

The percent change of conductivity over temperature variation may be defined as

$$Conductivity\,Change\ (\%)\ \ for\,Temperature\ \ Range\ T_2 - T_1$$
$$= \frac{[\sigma(T_2) - \sigma(T_1)]/\sigma(T_1)}{T_2 - T_1} x100 \qquad (11)$$

where $\sigma(T_i)$ is the conductivity at temperature T_i. Using this definition of the percentage change of conductivity, the percent change in conductivity per °C for SiC sample #1 over the temperature range from 25° C to 554° C was determined to be 7.5% per °C. Similarly, the percent change in conductivity per °C for SiC sample #2 over the temperature range from 23° C to 551° C was determined to be 10.4% per °C. This strong dependence of conductivity on temperature suggests that silicon carbide samples tested would be well suited for fabrication of the GMRF metamaterial temperature sensor.

2.2 Metamaterial Sensor Design

To aid in testing at the beginning of the program, and to experimentally determine the number of grating periods needed, samples were numerically designed to emulate the response of

a sensor. The structure chosen was a Jerusalem cross because it has a long history and has been well characterized in the literature.

Figure 12 shows the simulated reflectance from an infinite array of slot elements in a copper sheet, as would be the case if fabricated using standard printed circuit board techniques. With a grating period of 0.697 cm, the structure produces a strong null around 10 GHz where the device is resonant. Smaller slots would produce a narrower resonance due to weaker coupling so that width of the resonance could be controlled.

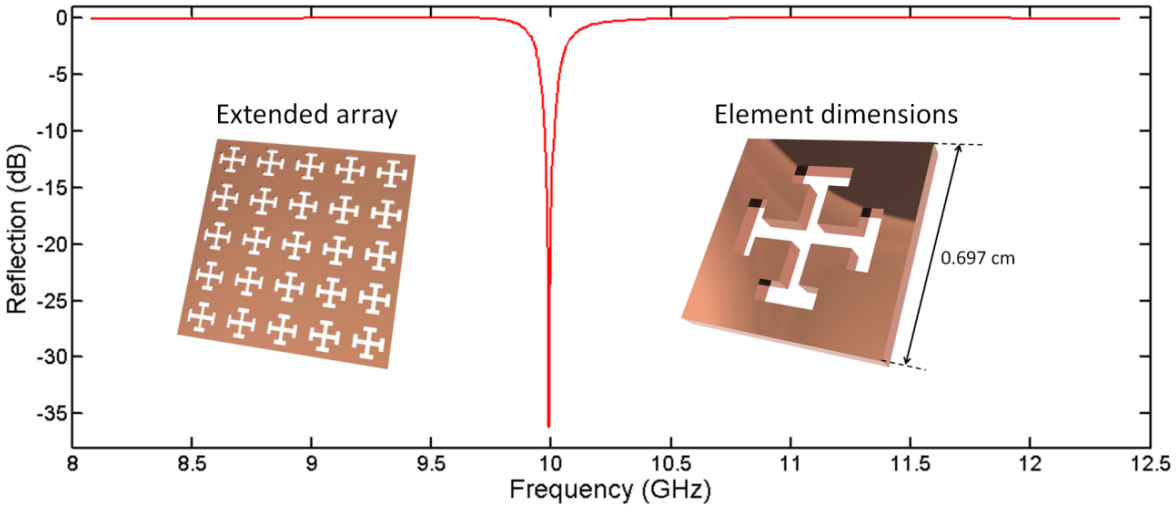

Figure 12. Simulated reflectance from a slot array

2.2.1 *Estimation of Number of Grating Periods*

There are several factors that combine to determine the size and frequency of operation of the sensor. First, any frequency bands with high attenuation from hot gases or particulates in the gasifier or boiler that should be avoided. Testing in the Babcock & Wilcox Small Boiler Simulator described in Section 4.1, however, showed that attenuation of the electromagnetic waves is not too severe at any frequency due to the low concentration of conductive particles in the operational atmosphere. Given a chosen frequency *f*, the free space wavelength λ_0 is calculated as

$$\lambda_0 = \frac{c_0}{f} \tag{12}$$

where c_0 is the speed of light in air. High frequencies correspond to shorter wavelengths so that the size of the sensor can be reduced simply by operating at a higher frequency. However, higher frequencies involve more expensive components and are more vulnerable to channel effects so there is motivation to operate at as low of a frequency as possible.

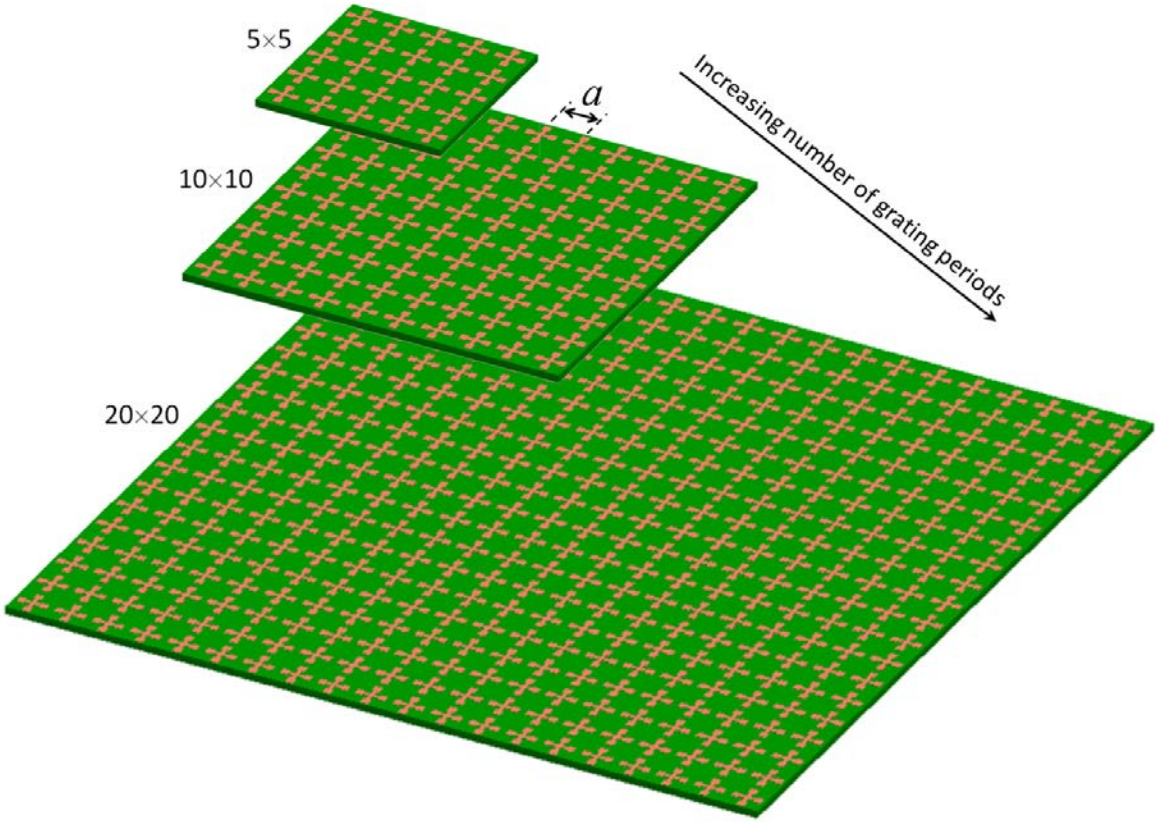

Figure 13. Sensor test samples with increasing number of grating periods

Second, the period of the grating inside the sensor is approximately half of the free space wavelength or smaller. For the structure depicted in Figure 12, the element spacing is just under a quarter of the wavelength. The specific answer to this item depends on whether the structure is resonant or non-resonant. There are benefits and drawbacks of both.

Third, the total physical size of the sensor is the grating period multiplied by the total number of periods. The more periods the sensor incorporates the stronger the electromagnetic response, but the larger the sensor. This is illustrated in Figure 13. To fit a sufficient number of grating periods within the sensor, the operational wavelength must be made smaller until that critical number of periods can fit within the space of two to three inches. In other words, small sensors can be designed, but they must operate at higher frequencies.

Another degree of freedom in the design of the sensor is the elements themselves. Designs can be chosen to produce as strong of an electromagnetic response as possible in as small of a form factor as possible. Slow wave structures couple external waves into slowly propagating surface waves within the sensor. This effectively reduces the wavelength in the array so the element size and spacing can be made much smaller than $\lambda_0/2$. Slow wave structures can be produced by operating the array near a resonance condition.

The elements should also be designed to produce as narrow of a resonance as possible. Elements can be the resonant type or they can be non-resonant. Narrow resonances arise when

the coupling between external waves and surface waves is weak. This configuration also means that larger grating arrays may be needed to allow for sufficient coupling to occur.

It is not feasible, or necessary, to perform rigorous electromagnetic simulations of the finite structures shown in Figure 13. A single simulation would take weeks to compute even on modern supercomputing platforms. Instead, simulations of infinitely periodic devices were performed in this research so only one period of the device had to be stored in memory and designs could be produced quickly.

2.2.2 BASELINE SENSOR DESIGN

In the approach pursued in this program, a metamaterial employing guided mode resonance (GMR) was investigated. In the GMR approach, a microwave diffraction grating is attached to the slab waveguide. For a narrow range of frequencies, incident microwaves will be diffracted by the grating and coupled into guided electromagnetic modes in the slab waveguide. Since the waveguide is a reciprocal device, the guided modes are leaked into radiating modes. These radiating modes combine with the incident microwaves to form the electromagnetic response of the metamaterial guided mode resonance filter (GMRF). The GMRF metamaterial can be designed to either pass a narrower range of frequencies and reflect the rest, forming a bandpass filter, or reflect a narrow range and pass the rest, forming a band stop filter. If the slab waveguide is made from a dielectric material that has conductivity that changes with temperature, then the width and sharpness of the filter spectral response (the Q or quality factor) will change with temperature, providing a mechanism for measuring temperature

The baseline metamaterial sensor design first adopted for simulation during this project is illustrated in Figure 14. It shows a metamaterial slot array located between two sheets of ceramic that have temperature dependent conductivity. This stack is intended to be hermetically sealed inside a single crystal sapphire package. To avoid delamination of metal films, bonding of dissimilar materials, or build-up of internal stresses from mismatched CTE, the layers could be encapsulated in a single crystal sapphire package, but not bonded in any way. The fit would be snug, but still allow for mismatched thermal expansion. As long as the ceramic remains in close proximity to the slot array, the electromagnetic performance will not be affected by slight misalignments caused by temperature fluctuations or mechanical vibration. The small spaces shown in Figure 14 between the materials inside the package convey that these are not bonded in any way.

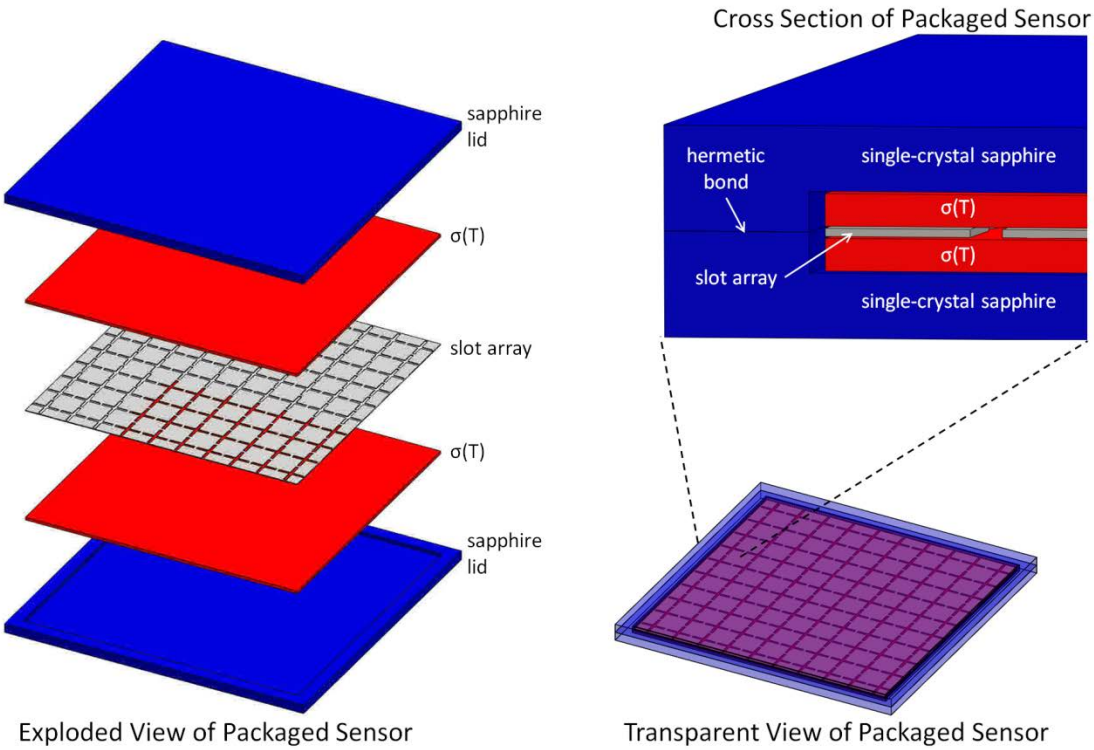

Figure 14. Baseline sensor design

The materials being investigated for the sensor and package were evaluated based on their electrical and mechanical properties at high temperature. It was desirable to have an all-dielectric package that is hermetically sealed and resists the corrosive environment. Single crystal sapphire was the primary candidate for the sensor encapsulation

The metallic slot array should be of sufficiently low resistance and also have a high melting point so that geometry is maintained at temperature. The active ceramic layers also need to have geometric stability at temperature as well as a resistance that is a strong function of temperature. A selection of candidate materials and their relevant properties are shown in Table 2.

Table 2. A selection of candidate materials for construction of the proposed sensor design

MATERIAL	RESISTIVITY (Ω·m)	MELTING POINT (°C)	CTE ($\times 10^{-6}$ /°C)
Sapphire	high	2053	8
Hexalloy SE SiC	low		4
Platinum	10.5×10^{-8}	1770	9
Tungsten	5.65×10^{-8}	3400	4
Tantalum	12.4×10^{-8}	2980	6
Chromium	13×10^{-8}	1860	6

2.3 Testing of Metamaterial GMRF Sensor Prototypes

Testing was performed at the Virginia Tech Antenna Group laboratories to characterize the electromagnetic response of two prototype sensors based on a guided mode resonance filter (GMRF) design. The GMRF design employed two 1mm thick stainless steel plates on both sides of a 1mm thick silicon carbide slab. Both steel plates contained a square array of 0.58 mm diameter through holes, with a pitch of 4.7mm. Numerical modeling of the GMRF response predicted that the design would have a resonance at 20 GHz and a FWHM of 50 MHz. One of the GMRF sensors had a surface area of 2"×2", and the other had an area of 4"×4". In addition, a solid metallic plate, a dipole array, and a solid slab of silicon-carbide were also included in the testing to compare with the response of the sensors.

2.3.1 MEASUREMENT SET-UP

A bi-static radar using two identical horn antennas (gain: 16 dBi @ 16 GHz and 18 dBi @ 24 GHz) was set up in a typical laboratory environment with a HP 8510C vector network analyzer as shown in Figure 15. One of horn antennas transmits a band-limited signal (16 GHz – 24 GHz with 10 MHz step) toward a target, while the other antenna receives signals scattered from the target[ii]. The target was located on a styrofoam pole in order to be at the straight line-of-sight angle (boresight) from the antenna. Each single-frequency data was averaged 256 times, but there was no averaging between frequency points.

Due to the high radiation-directivity of the antennas, the multi-path effects of objects surrounding the measurement setup were not significant. However, big metallic objects were moved to other place or covered by absorbing materials as a precautionary measure.

2.3.2 MEASUREMENT RESULTS

Pictures of the various targets are shown in Figure 16 and Figure 17. Both 2"×2" and 4"×4" GMRF sensors were the primary target for this experiments. Other targets including a solid metallic plate, a dipole array, and a solid silicon-carbide plate were used to compare with the response of the GMRF sensors. Particularly, the dipole-array target was considered to demonstrate an alternative sensor concept, as well as to identify the validity of the measurement setup. Simulated scattered far-field response of the dipole array versus frequency, using a commercial moment-method code (FEKO suite v5.5), is depicted in Figure 18. The bandwidth of a dipole depends on the radius, size, and loss of wires used in constructing the dipole, but typically 10% fractional bandwidth is assumed. Because the fractional bandwidth of interest is about 40%, the dipole array response looks broad as shown in Figure 18. If we make the length of dipole element shorter and add an additional inductive structure in the dipole, the curvature

[ii] The response basically corresponds to s_{21} or s_{12} ($s_{21} = s_{12}$ for passive network) of the collected scattering parameters through the vector network analyzer.

shape of the dipole-array response would be narrower, resulting in a higher Q structure than the original dipole element.

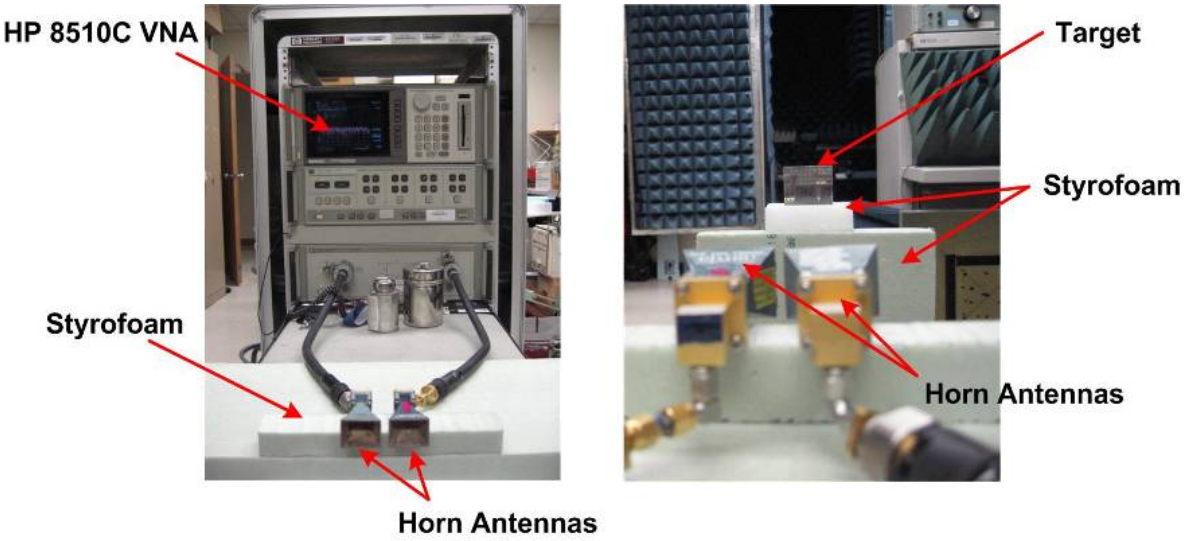

(a) (b)

Figure 15. Pictures of measurement setup – (a) Bi-static radar setup and (b) Target and antennas in a typical laboratory environment.

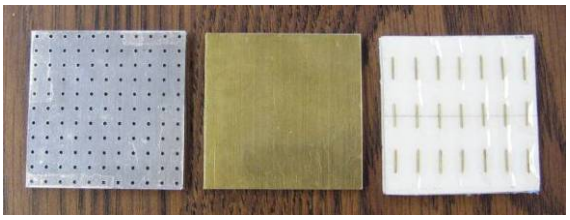

(a) (b) (c)

Figure 16. Picture of 2" × 2" targets – (a) Sensor using silicon-carbide substrate, (b) Solid brass plate, and (c) Dipole array.

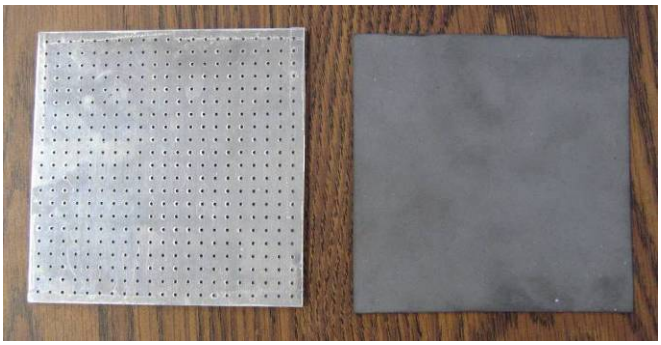

(a) (b)

Figure 17. Pictures of 4" × 4" targets – (a) Sensor using silicon-carbide substrate and (b) Solid silicon carbide.

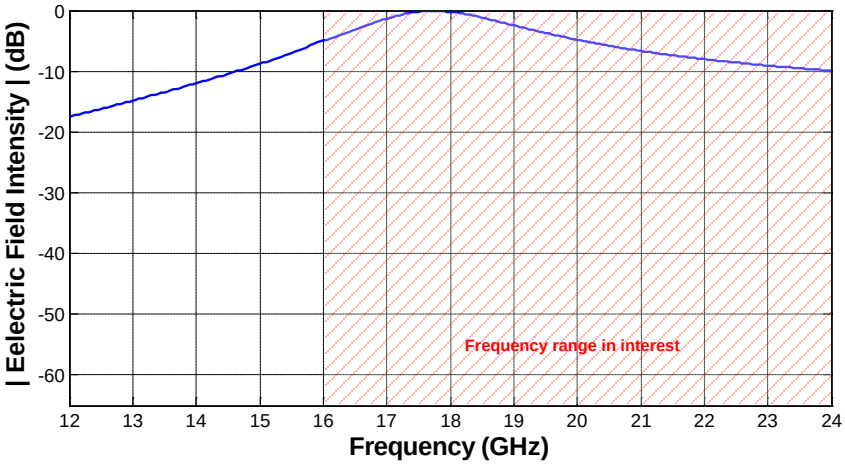

Figure 18. Simulated scattered, far-field electric-field intensity of dipole array for plane-wave incidence.

For the case where the detecting radar and the targets are separated by 0.45 m, the measured responses of the targets are shown in Figure 19, compared to the response that is obtained when the target is not present (laboratory-environment response). In the plots shown, the laboratory-environment response was subtracted from each target response.

One can observe that there is no significant signature in the response of the 2"×2" GMRF sensor. In addition, the response of the 2"×2" sensor is very similar to the response of the solid metallic plate of the same size. However, the response of the dipole array shows a peak and an amplitude decrease after the peak, as we observed in the simulation result. The 4"×4" GMRF sensor response is a similar to the response of the 2"×2" sensor. The 4"×4" silicon-carbide plate also shows a similar response to the response of the 4"×4" sensor, but overall level of the silicon-carbide plate case is lower than the 4"×4" sensor response due to the loss of the silicon carbide.

The equivalent time-domain response of the 2"×2" sensor is shown in Figure 20. The round-trip time corresponding to the 0.45 m separation between the radar and the target is 3 ns. After the main response of the sensor, we cannot observe any strong multi-path response, indicating that no spurious reflections from the laboratory environment influenced the results.

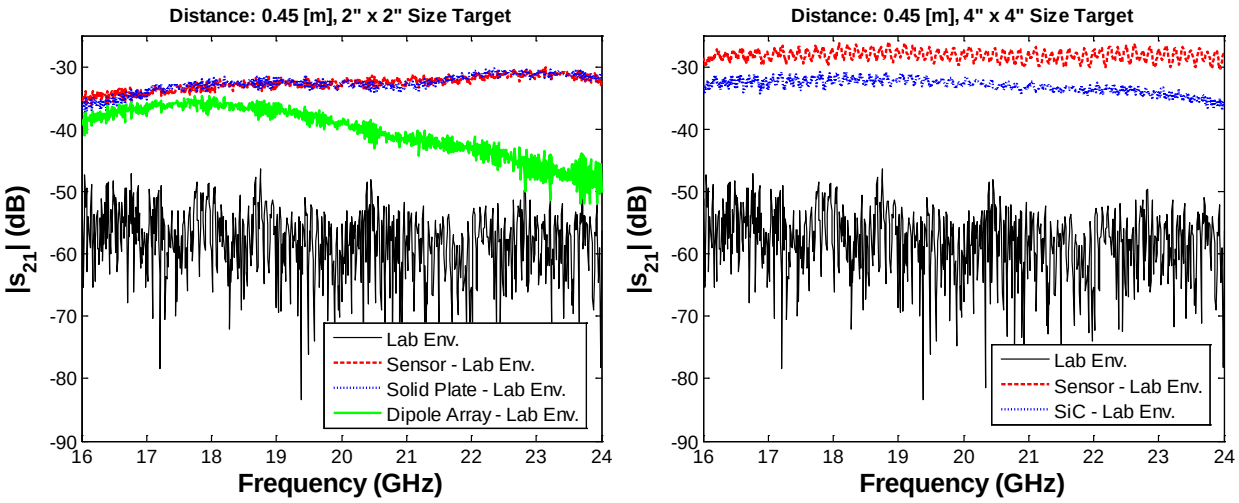

(a) (b)

Figure 19. Measured response from 0.45 m distance – (a) 2" × 2" targets and (b) 4" × 4" targets.

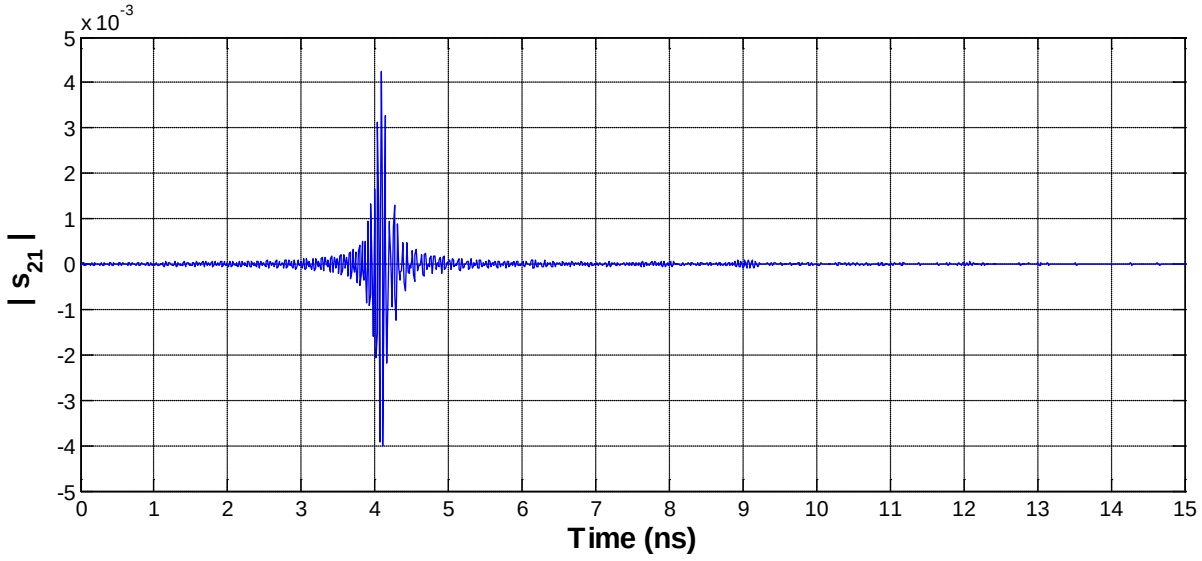

Figure 20. Time-domain response of 2" × 2" sensor.

With the same measurement setup, tests are carried out for the cases of 1.06 and 1.67 m separation between the radar and targets. The measured results are depicted in Figure 21and Figure 22 respectively. Other than the overall level shift, these responses are similar to the previous 0.45 m distance case.

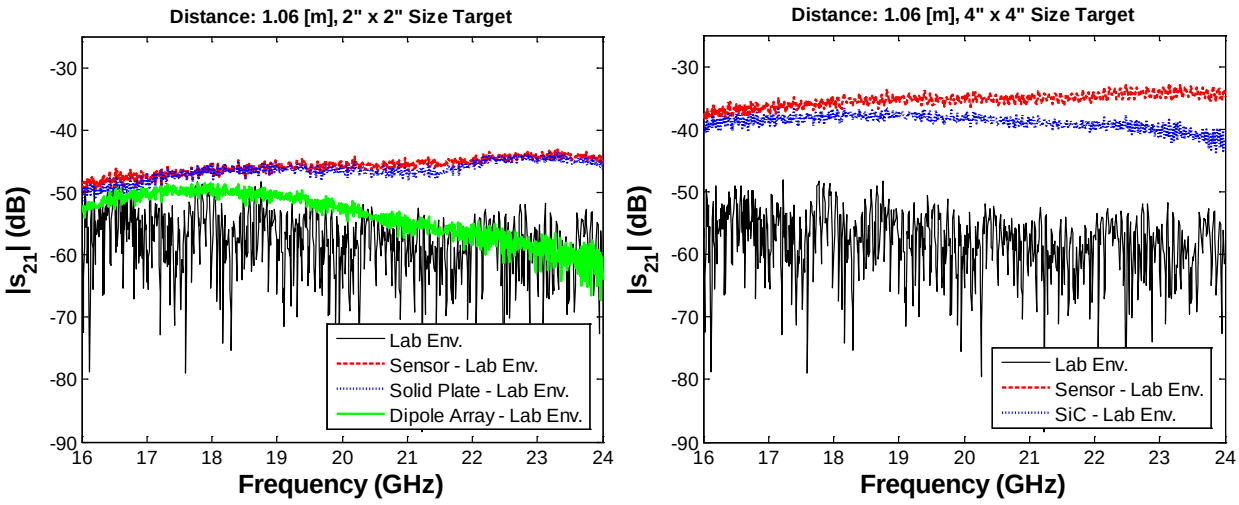

(a) (b)

Figure 21. Measured response from 1.06 m distance – (a) 2" × 2" targets and (b) 4" × 4" targets.

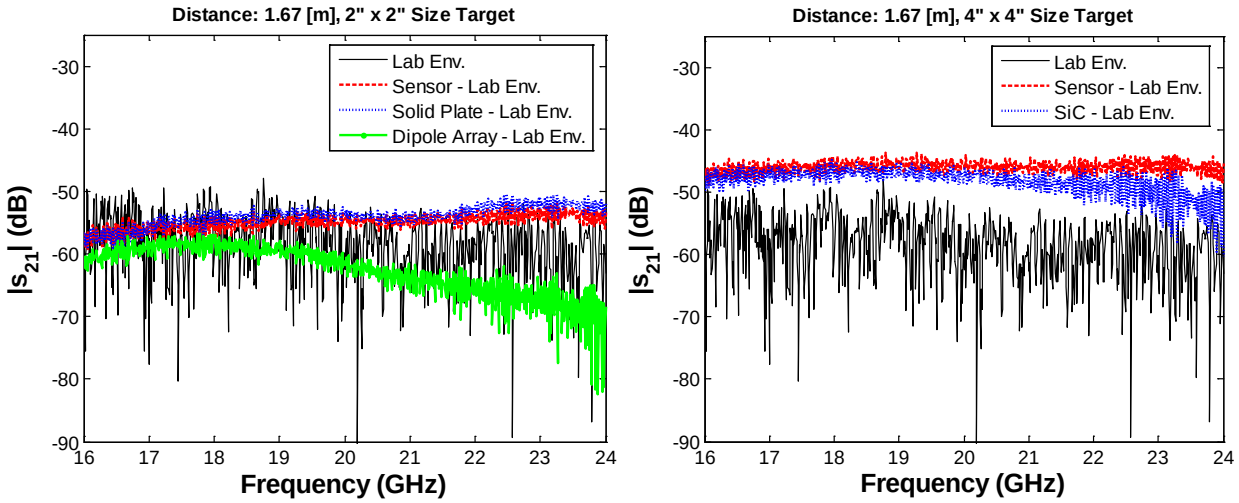

(a) (b)

Figure 22. Measured response from 1.67 m distance – (a) 2" × 2" targets and (b) 4" × 4" targets.

The experiment was repeated with the same conditions except that the diameter of the holes on the 2"×2" GMRF sensor were made approximately 4 times larger in diameter than those in the previous 2”x2” prototype. In addition, solid silicon-carbide and FR4 plates were included in the measurement, as shown in Figure 23. Note that the solid silicon-carbide plate was damaged during a previous experiment to characterize the dielectric properties of the material. The broken parts were glued with cyanoacrylate glue, but there were still some cracked parts. Measurement for the 4"×4" targets was not carried out at this time.

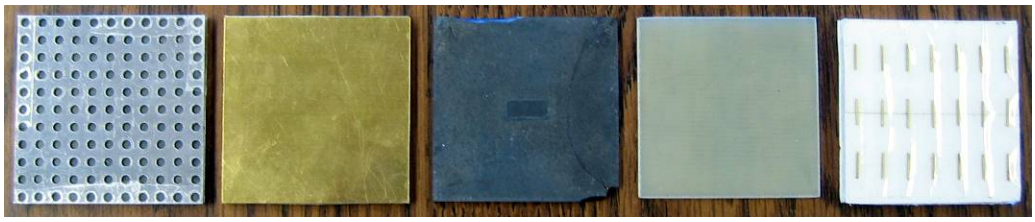

(a) (b) (c) (d) (e)

Figure 23. Picture of 2" × 2" targets – (a) Sensor using silicon-carbide substrate, (b) Solid brass plate, (c) Solid silicon-carbide plate, (d) FR4 plate, and (e) Dipole array. Note that the hole size of the sensor is approximately two times larger than the previous experiment.

As depicted in Figure 24, the measurement responses of the sensor, metal plate, and dipole array from the detecting radar at 0.455 m distance were similar to those obtained in the previous measurement of the GMRF sensor with the smaller holes. Again, no significant “signature” of the sensor was found, despite the larger holes on the metal plate of the sensor. However, a broadband dip was observed for the solid silicon-carbide plate around 17 GHz, which can be seen as a “signature.” The dip is likely created due to the resonance of the overall silicon-carbide plate including the thickness, i.e. a null around the observation angle. Due to the loss property, the overall amplitude of the solid silicon-carbide plate is lower than that of the solid metal plate or sensor, but slightly higher than that of the FR4 plate. The measured results at 1.065 and 1.675 m distance show basically the same result with the 0.455 m case. These results are depicted in Figure 25 and Figure 26 respectively.

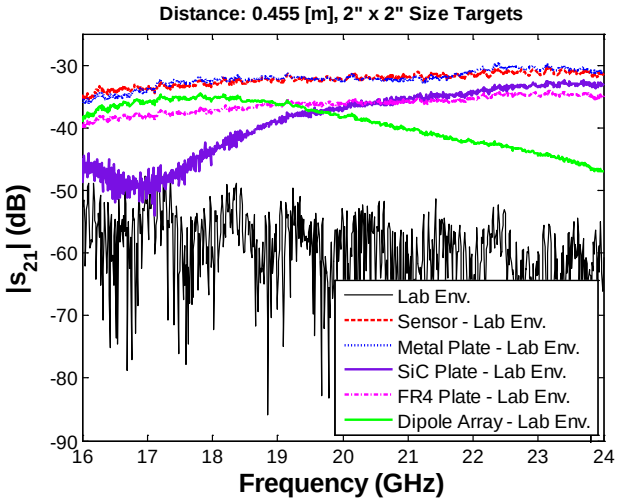

Figure 24. Measured response from 0.455 m distance for 2" × 2" targets.

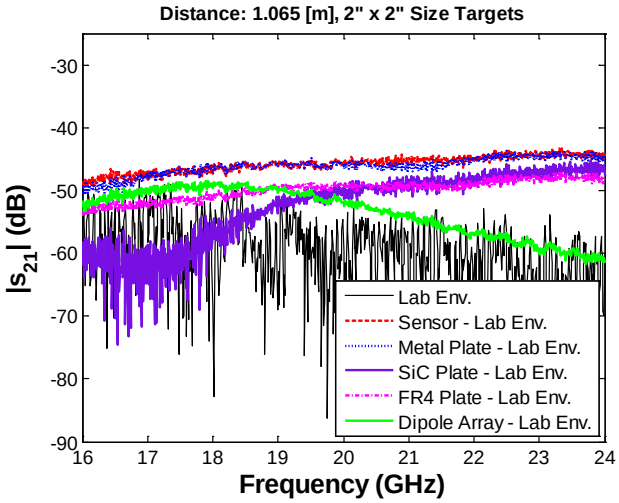

Figure 25. Measured response from 1.065 m distance for 2" × 2" targets.

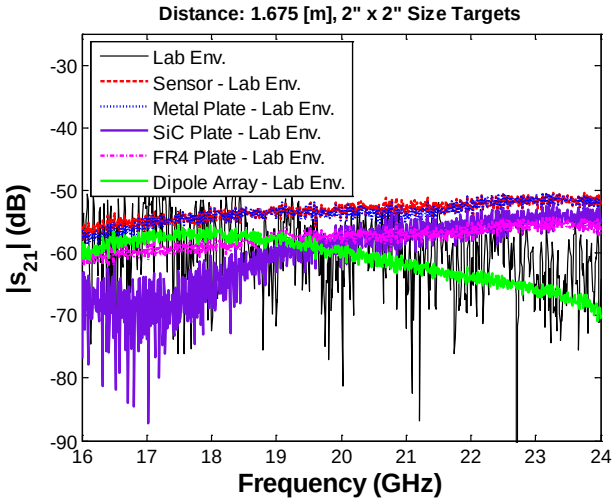

Figure 26. Measured response from 1.675 m distance for 2" × 2" targets.

2.3.3 Experiment to Evaluate Use of Copper Tape to Minimize Edge Effects

An experiment was conducted to evaluate whether conductive tape could be used to provide boundary conditions at the edge of the GMRF sensors to minimize edge effects. As shown in Figure 27, four targets were considered. Unlike the tests described in the previous section (Section 2.3.2), the edges of targets were covered with copper tape; the tape that was used has a conductive adhesive, so that electrical continuity is maintained between the tape and the metal plates, providing a "short" condition around the periphery of the sensor (Figure 28).

The measured target responses measured at three different distances are depicted respectively from Figure 29 through Figure 31. Again, there were no identifiable signatures of the sensors covered with copper tapes on edges, compared to the solid metal targets.

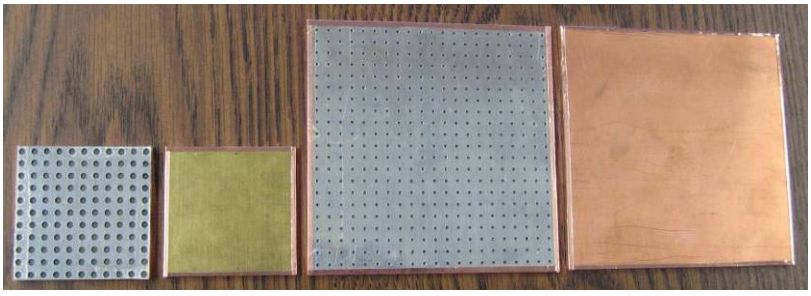

(a) (b) (c) (d)

Figure 27. Picture of 2" × 2" and 4" × 4" targets with copper tapes on edges – (a) 2" × 2" sensor using silicon-carbide substrate, (b) 2" × 2" solid brass plate , (c) 4" × 4" sensor using silicon-carbide substrate, (d) 4" × 4" solid copper plate. Note that holes on the 2" × 2" sensor is approximately four times larger than that of the 4" × 4" sensor.

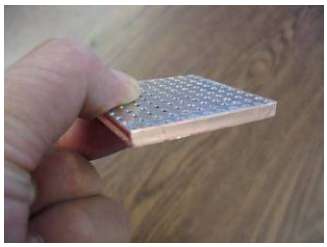

Figure 28. Picture of 2" × 2" sensor with copper tapes on edges (perspective view).

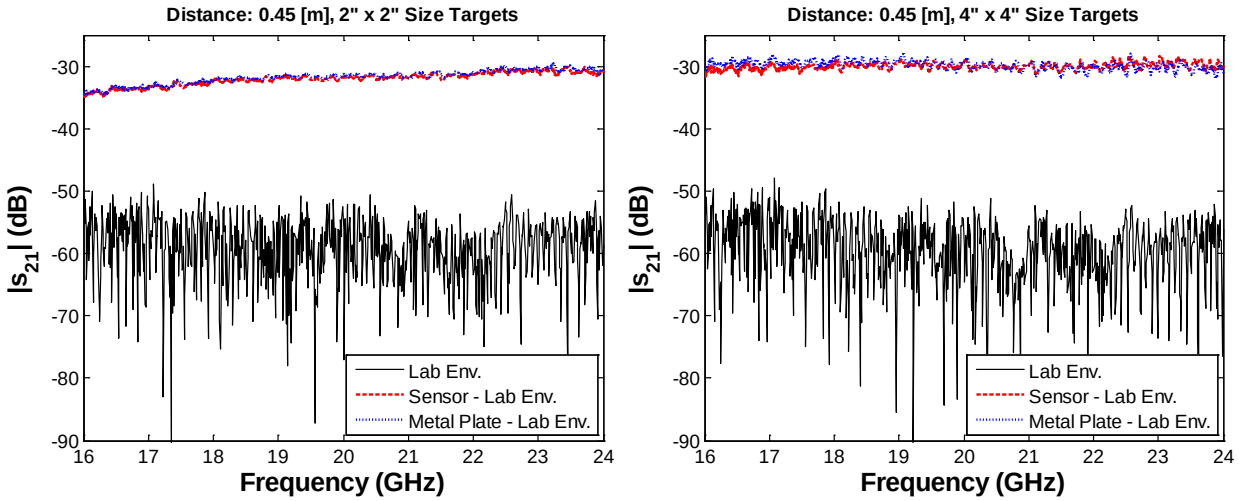

(a) (b)

Figure 29. Measured response from 0.45 m distance – (a) 2" × 2" targets and (b) 4" × 4" targets.

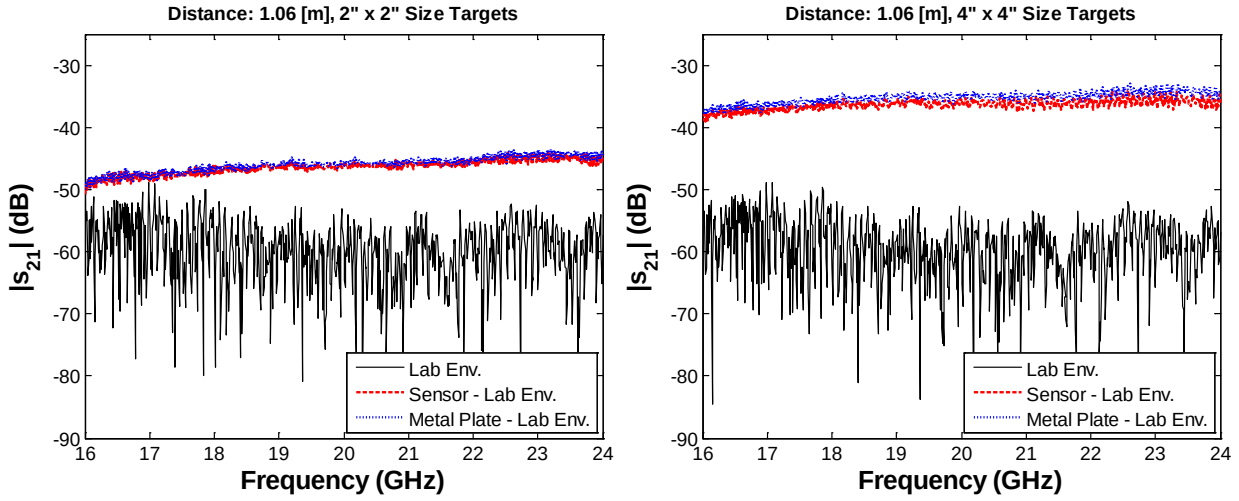

(a) (b)

Figure 30. Measured response from 1.06 m distance – (a) 2" × 2" targets and (b) 4" × 4" targets.

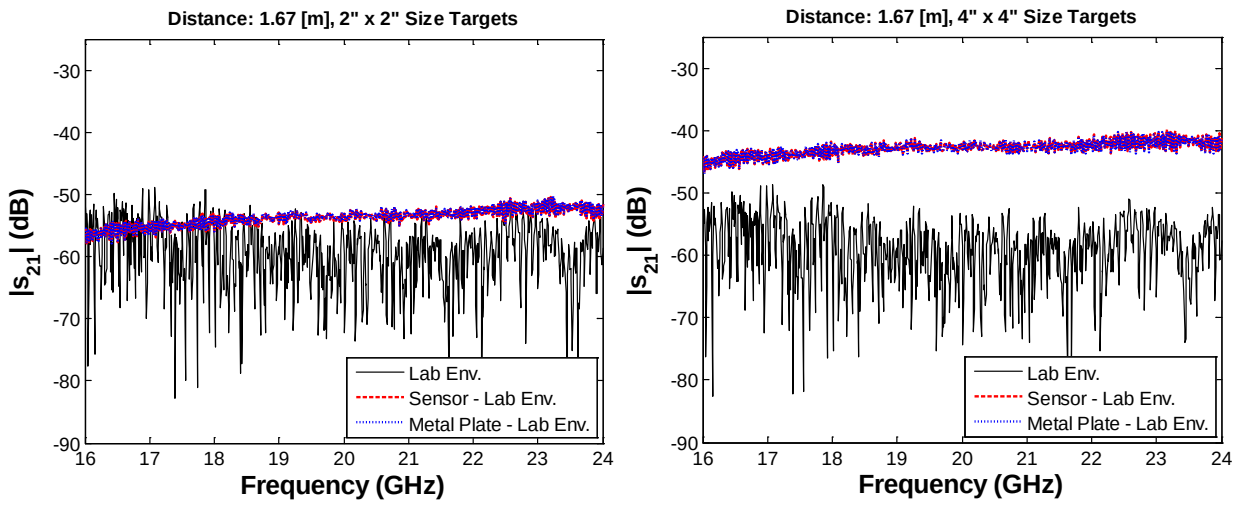

(a) (b)

Figure 31. Measured response from 1.67 m distance – (a) 2" × 2" targets and (b) 4" × 4" targets.

2.3.4 *Test of GMRF Sensor with Air Dielectric Core*

The results of Section 2.3.2 indicated that the sensor response may be hidden in the data due to the high dielectric constant and high electromagnetic loss of the silicon-carbide substrate. In order to eliminate potential effects of the silicon-carbide substrate, the responses of sensors with an air substrate were measured. Styrofoam supports at the corners were used to support the metallic structure of the sensors, as shown in Figure 32. The dielectric constant of the styrofoam is close to that of air. The gap distance between the metallic plates was 3 mm. Three targets, a 2"×2" sensor, a 2"×2" sensor with 4 times larger holes, and a 4"×4" sensor, were considered. A picture of these sensors is shown in Figure 33.

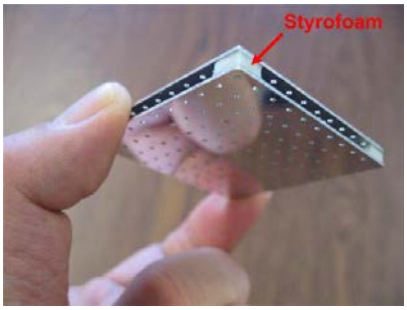

Figure 32. Picture of 2" × 2" sensor with styrofoam supports at each corner.

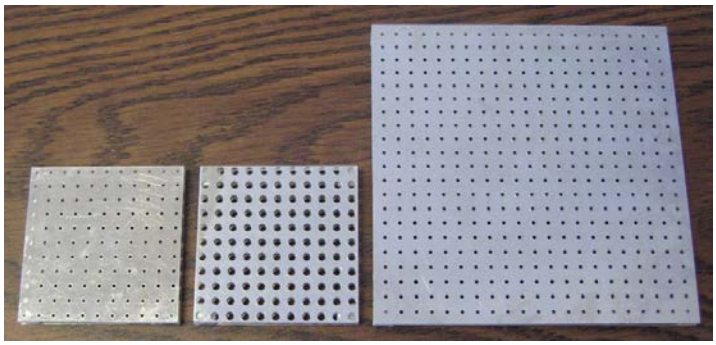

(a) (b) (c)

Figure 33. The 2" × 2" and 4" × 4" targets with an air substrate – (a) 2" × 2" sensor, (b) 2" × 2" with four times larger holes, (c) 4" × 4" sensor.

Measured results, at three different separation distances between the target and the radar, are presented in Figure 34 through Figure 36. The detected signals from the 2"×2" sensors are similar to each other, though one of 2"×2" sensors has holes that are 4 times larger than the holes in the other sensors. It is not easily discerned in the figure, but there may be a small signature (approximately 1.5-dB dip) around 18.5 GHz for the 2"×2" sensors. For the 4"×4" sensor, no noticeable signature was found. We could not exclude the possibility that the potential small signature of the 2"×2" sensors might be a contribution from the edge effects instead of the holes.

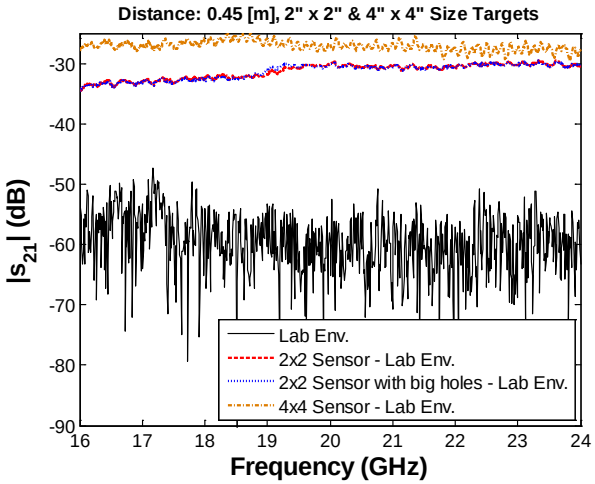

Figure 34. Measured response from 0.45 m distance for 2" × 2" and 4" × 4" targets.

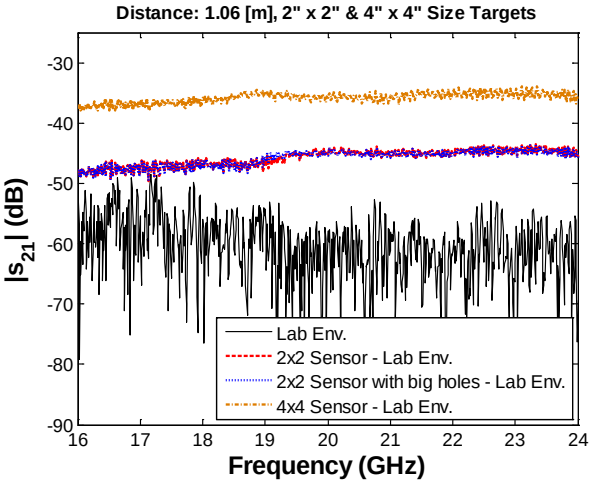

Figure 35. Measured response from 1.06 m distance for 2" × 2" and 4" × 4" targets.

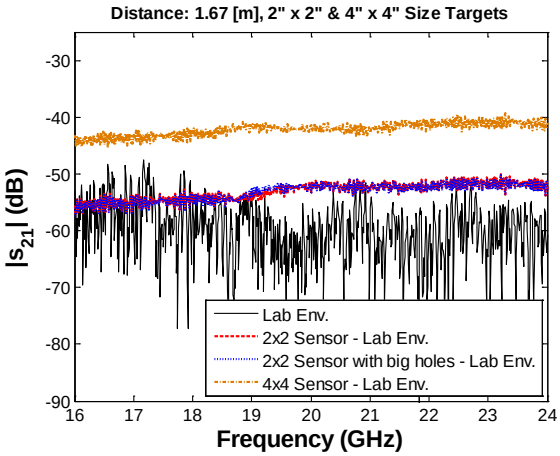

Figure 36. Measured response from 1.67 m distance for 2" × 2" and 4" × 4" targets.

2.4 Alternative Metamaterial Sensor Designs

Several alternative metamaterial sensor designs distinct from the GMRF design were evaluated, either by numerical simulation or by experimental measurements, including sensors based on a dipole array, a split-ring resonator array, a spherical resonator, and a loop antenna array.

2.4.1 *Split-Ring Resonator High-Q Sensor Structure*

One sensor design considered was a planar array of split ring resonators. As illustrated in Figure 37, each element of the array consists of two concentric rings, each with a split in the ring. The splits for the two concentric rings are arranged to be 180 degrees in opposition.

The split-ring resonator (SRR) in Figure 37 has a small form factor, compared the full-size dipole case. Thus, we one can expect a sharp-peak response, i.e. high-*Q*. In the model considered in the figure, the split rings were assumed to be made of copper, and the substrate material was air ($\varepsilon_r = 1$).

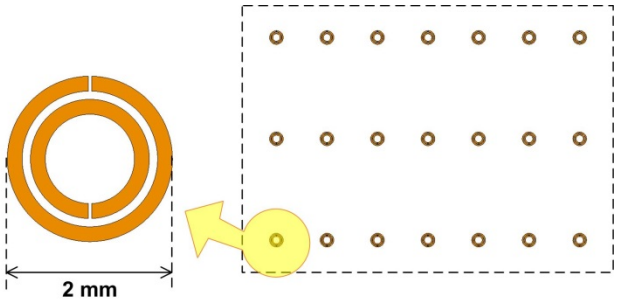

(a) (b)

Figure 37. Structure of a high-*Q* resonator and its array – (a) SRR and (b) Array of SRRs.

The response of an SRR array was modeled using FEKO software, which employs the Method of Moments integral formulation of Maxwell's equations, in addition to finite element models. The response, shown in Figure 38, is compared with the simulated results for an array of dipoles, which is seen to have a response with lower Q. The response of a sensor based on a slot-type structure, as discussed earlier, may be dominated by diffractions from outer edges of the metallic plate; this behavior would not be seen in simulations that assume an infinite array. Thus, sensors based on dipole, bent-dipole, and loop structures might be considered as an alternative approach, as demonstrated in Figure 38.

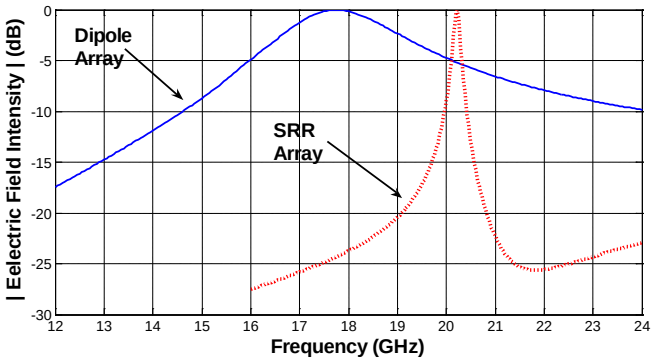

Figure 38. Simulated scattered, far-field electric-field intensity of dipole array and split-ring resonator (SRR) array for plane-wave incidence.

2.4.2 *SPHERICAL SENSOR*

The core of the spherical sensor is made out of metallic material. The outer part of the metallic core is surrounded by a thin silicon carbide layer as depicted in Figure 39. Typically, a spherical shape is not a high-*Q* structure. However, if the size of the spherical sensor becomes electrically large, a higher-order spherical mode can be excited at a single frequency (approximately 20 GHz for the dimensions shown in Figure 39). So, the spherical sensor can have a sharp response.

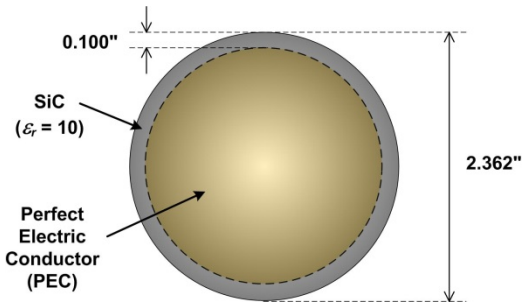

Figure 39. Geometry of spherical sensor.

As loss tangent of the silicon carbide increases, the frequency location and amplitude of the frequency dip associated with resonance decreases as seen in Figure 40. The decreasing rate can be controlled by changing the SiC layer thickness of the spherical sensor. Since the spherical sensor has an isotropic shape, one can expect the same response from any angle.

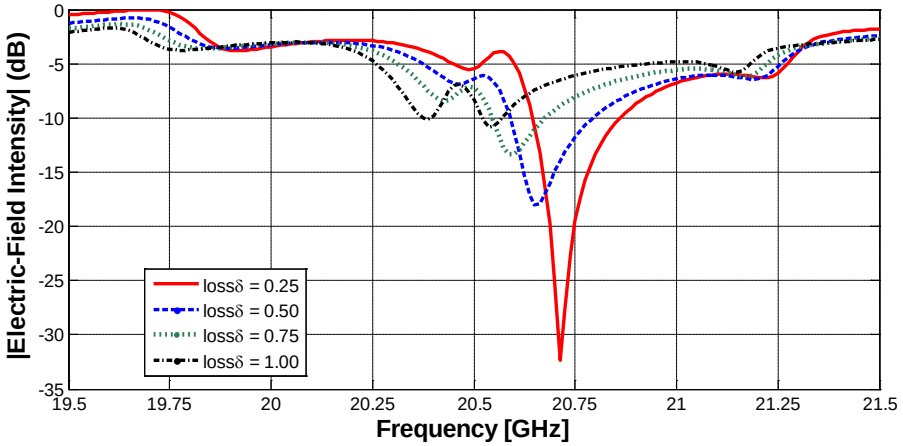

Figure 40. Simulated scattered, far-field electric-field intensity of the spherical sensor with loss property variation of silicon carbide (SiC) for plane-wave incidence.

2.4.3 FRED SENSOR ON AIR SUBSTRATE

As shown in Figure 41, the element of the FRED (Finite Resonant Element array of the loopeD type) sensor is basically a resonant loop structure (magnetic dipole). The loop element has three rectangular-shape arms. Each arm is parallel to other arms in adjacent elements. Thus, the center-to-center distance between elements is same. The field distribution of loop antennas is dual to that of electric dipole antennas. As a result, we can expect that the scattered electric fields will have a null in the normal direction to the plane of the sensor at a resonant frequency. Recall that the previously described dipole array (Figure 38) had a peak response at the same direction.

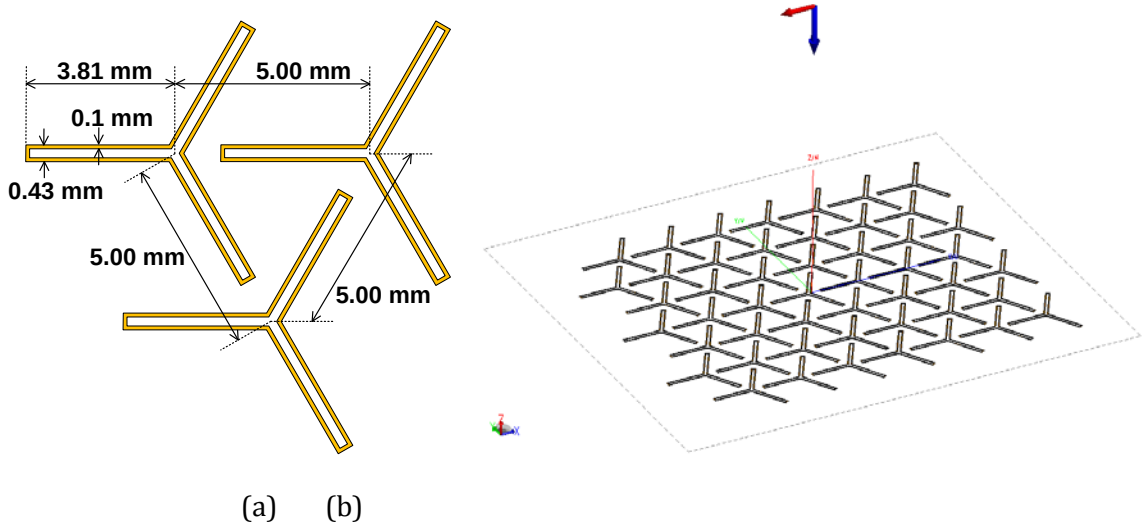

(a) (b)

Figure 41. Geometry of 7 × 7 FRED sensor – (a) Dimension and spacing between elements and (b) Simulation setup with an incident of linearly-polarized incoming plane waves modeled in the commercial method-of-moment code[iii] (The red arrow indicates the direction of the linear polarization and the blue arrow shows the direction of the plain wave incidence).

The strip lines in the loop element were assumed to have a thickness of 0.1 mm. The conductivity of a typical copper (5.6e7 S/m) was used in the simulation. An infinite-size[iv] planar air-dielectric material (ε_r = 1) with 0.025" thickness was located below the FRED sensor. For the various loss properties of the air-dielectric materials ($tan\delta$ = 0.00, 0.25, 0.50, 0.75, and 1.00), simulations were carried out and the result is presented in Figure 42.

The basic performance of the FRED array (7 × 7) was investigated using FEKO. Instead of a finite-size SiC substrate, an infinite air-dielectric (ε_r = 1) substrate with 0.025" thickness was used in the study due to the required large-size memory in computer simulations. As expected, the scattered electric field strength versus frequency shows a dip around 20 GHz. The depth and

[iii] FEKO Suite v5.5, available at http://www.feko.info

[iv] A sensor model using a 3-D finite-size substrate required more than 16 GB memory. Thus, the Green's function for multiple planar layers was used for the simulations in order to consider loss effects on the substrate. The size of the substrate was infinite in a *xy*-plane, but finite in a *z*-axis (thickness).

frequency of the dip decreases as the loss of the air-dielectric material increases, as summarized in Table 3. It is observed that the 3-dB dip (notch) bandwidth of the FRED sensor with a substrate loss is much broader than the case of the previous spherical sensor design. Thus, the substrate loss range showing a sharp curvature of the dip for the FRED may be limited for radar detection in practice. If a realistic substrate with a higher dielectric constant ($\varepsilon_r > 2$) is considered, the curvature of the dip may be smoother due to the multiple reflections inside the substrate than the air-dielectric case ($\varepsilon_r = 1$). The previous dipole antenna could also have a similar smooth-curvature dip issue.

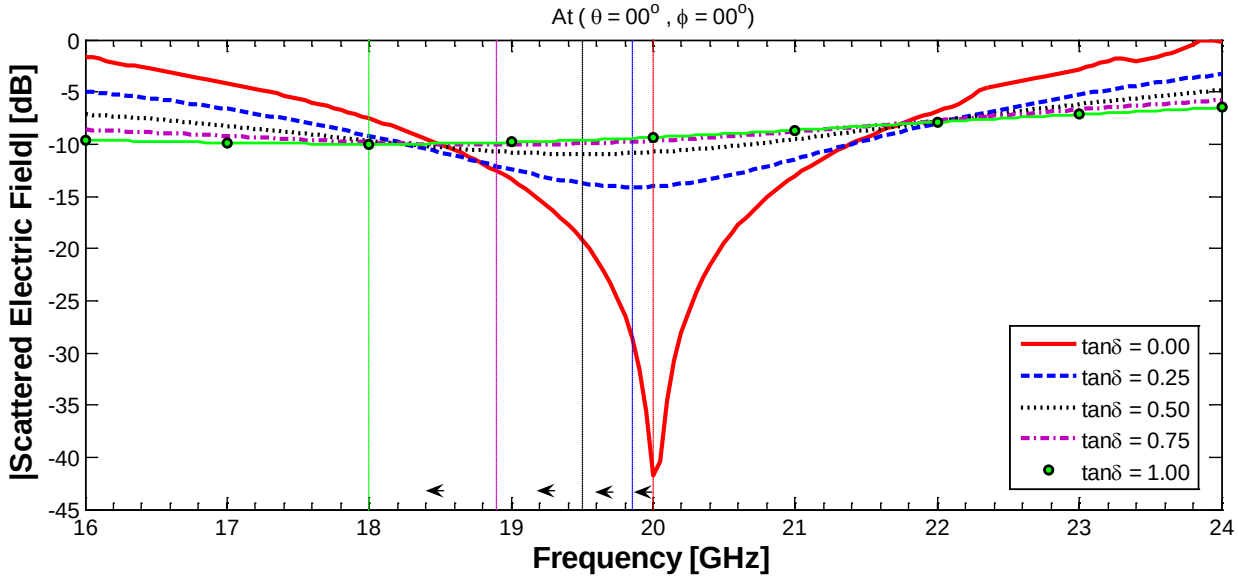

Figure 42. Simulated scattered, far-field electric field of the FRED sensor with loss property variation of air-dielectric substrate for a linearly-polarized plane-wave incidence. The vertical lines indicate the frequency location of the minimum scattered field.

Table 3. Location and depth of scattered E-field dip at $\theta = 0°$ and $\phi = 0°$.

Loss Tangent ($tan\delta$)	Frequency Location of Dip	Minimum $\lvert E_{scattered} \rvert$
0.00	20.00 GHz	-41.74 dB
0.25	19.85 GHz	-28.65 dB
0.50	19.50 GHz	-19.17 dB
0.75	18.90 GHz	-12.60 dB
1.00	18.00 GHz	-7.55 dB

In order to investigate the angular sensitivity of the FRED sensor, simulations with cases of various incident angles were carried out using FEKO. As illustrated in Figure 43, responses for both bounce-back (back scattering) and specular reflection were considered for a linearly-polarized wave with an oblique incidence ($\theta > 0°$). The simulated results for several incident angles are presented in Figure 44. The dip locations of specular reflections do not change

significantly. In the worst case (19.80 GHz θ = 80°), the frequency location of the dip is only off by 1% relative to the reference case (20.00 GHz @ θ = 0°). In contrast, the dip locations of bounce-back reflections show more deviations particularly at high θ angles (θ > 40°). The incident angle versus frequency location of dip for the variation of incident-wave angle is summarized in Table 4. Note that the angular sensitivity will also vary with a ϕ variation because the FRED sensor does not have a spherical symmetry in shape. However, it is expected that the ϕ-direction sensitivity of the FRED sensor is lower than that of the previous dipole sensor due to the identical arms of single element on the FRED sensor.

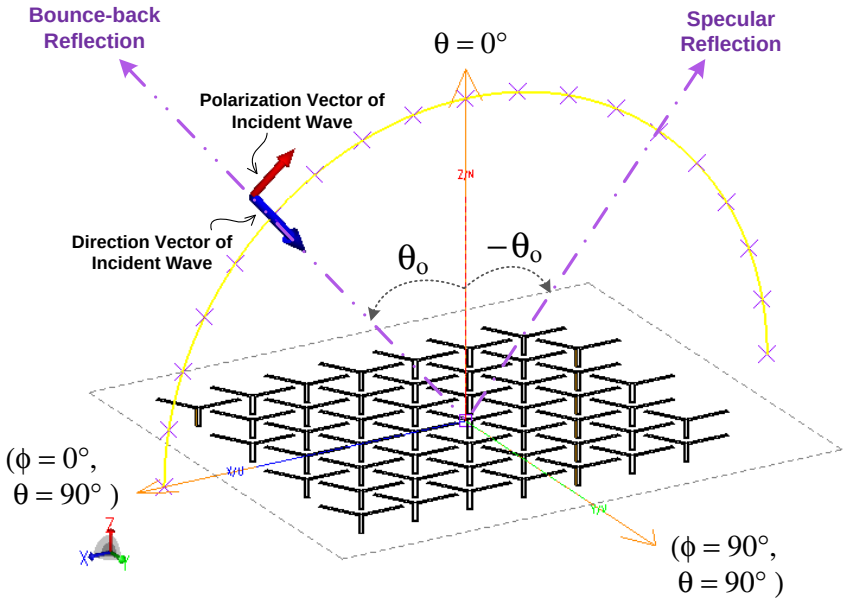

Figure 43. Illustration of simulations setup to investigate an angular sensitivity of FRED sensor.

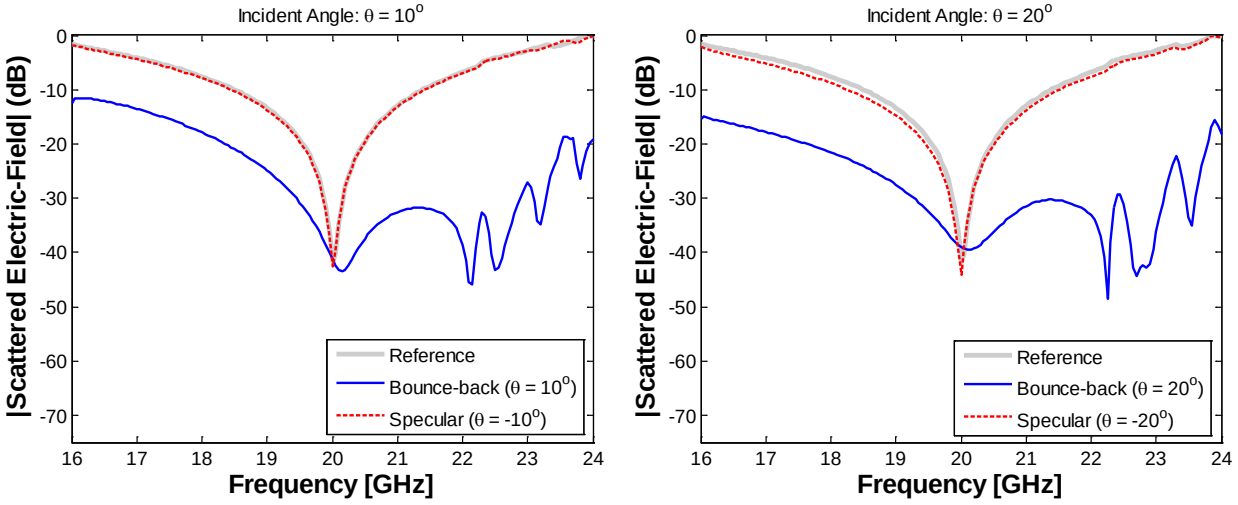

(a) θ = 10° (b) θ = 20°

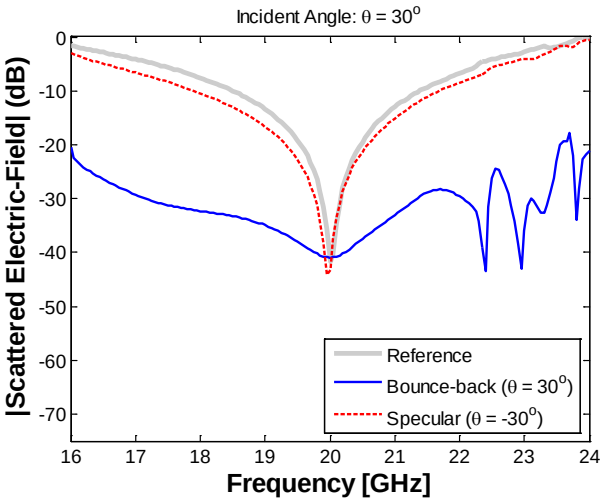

(c) $\theta = 30°$

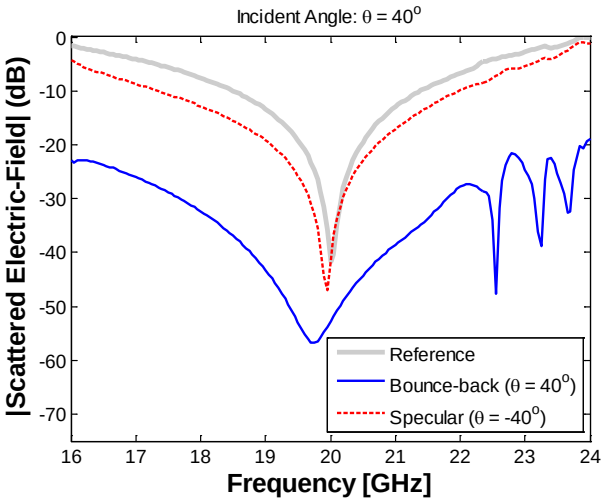

(d) $\theta = 40°$

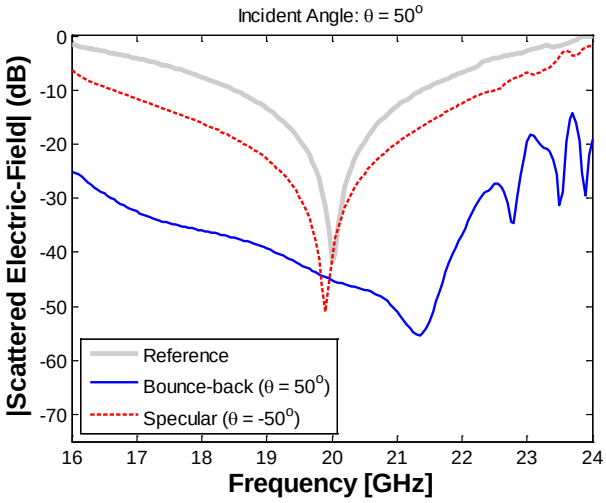

(e) $\theta = 50°$

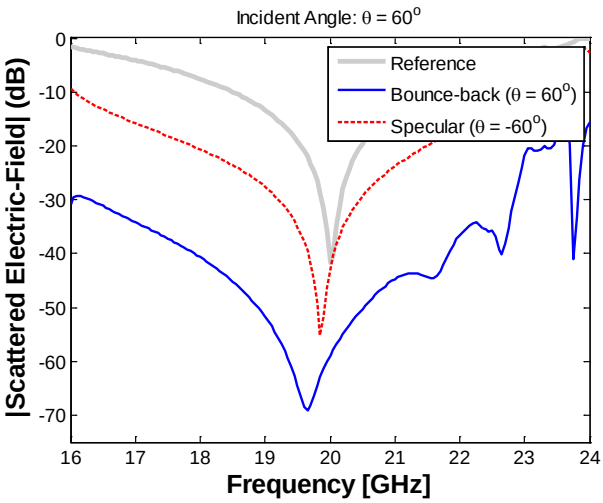

(f) $\theta = 60°$

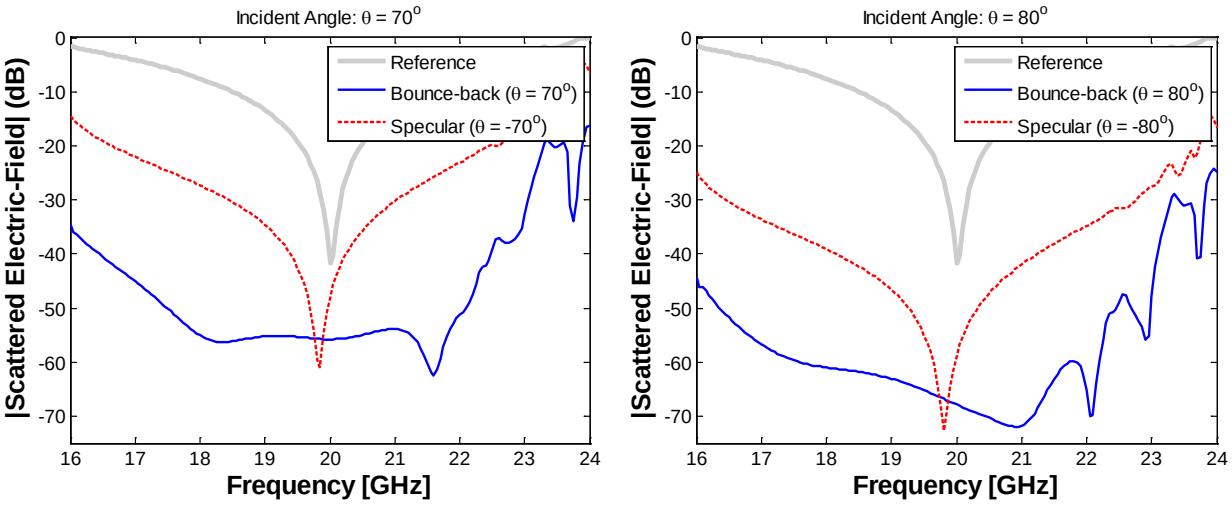

(g) $\theta = 70°$ (h) $\theta = 80°$

Figure 44. Simulated scattered, far-field electric field of the FRED sensor with variation of wave incident angle. The reference curve is for the case of $\theta = 0°$ incidence; the loss tangent was assumed to be zero.

Table 4. Wave incident angle versus frequency location of both bounce-back and specular reflections.

Incident Angle ($\phi = 0°$)	**Frequency Location of Dip**	
	Bounce-back Reflection	**Specular Reflection**
$\theta = 10°$	20.15 GHz	20.00 GHz
$\theta = 20°$	20.10 GHz	20.00 GHz
$\theta = 30°$	20.00 GHz	19.95 GHz
$\theta = 40°$	19.75 GHz	19.95 GHz
$\theta = 50°$	21.35 GHz	19.90 GHz
$\theta = 60°$	19.65 GHz	19.85 GHz
$\theta = 70°$	21.60 GHz	19.85 GHz
$\theta = 80°$	20.90 GHz	19.80 GHz

The FRED sensor does not show significant angular-sensitivity in terms of a dip location, though an applicable angle-range may be limited in practice because of the level of reflected signal at high θ angles.

As mentioned above, for cases of high dielectric constant and/or lossy substrates, the dip in the frequency-selective response of the FRED sensor will be diminished. Therefore it is necessary to consider designs with low dielectric constants and low loss. Although the SiC

substrate identified for use in sensor design has a rather high loss, the effective loss can be tuned by adjusting the substrate thickness. In the following simulations the FRED sensor element on a finite-size silicon carbide (SiC) substrate is investigated.

2.4.4 FRED SENSOR ELEMENT ON A FINITE-SIZE SIC SUBSTRATE

We can predict the frequency behavior of the FRED array on a finite-size SiC substrate by considering a single FRED element (see Figure 45). The FRED array will have higher scattering response than that of the single FRED element. At the same time, the angular variation of the scattered field amplitude will be higher than that of the FRED element. However, frequency variation behavior of the scattered electric-field amplitude for both array and element cases will be similar at boresight. In order to confirm the frequency behavior aspect, a simulation was carried out. As depicted in Figure 46, the overall frequency variation behavior between the FRED array and a single element are similar. However, due to the array effect, the amplitude of the FRED array (7×7) is approximately 30 dB higher than that of FRED element.

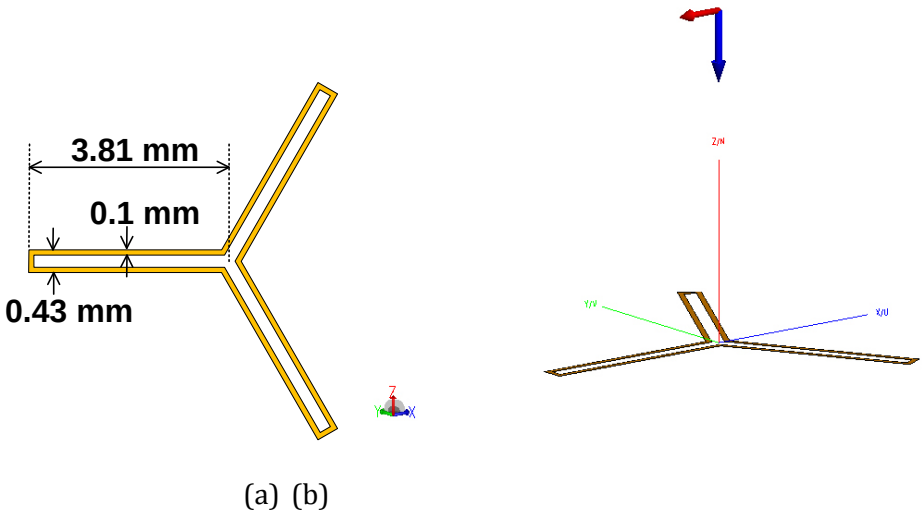

(a) (b)

Figure 45. FRED sensor element – (a) Dimension and (b) Simulation setup with an incident of linearly-polarized incoming plane waves modeled in the commercial method-of-moment code (The red arrow indicates the direction of the polarization and the blue arrow shows the direction of the plain wave incidence).

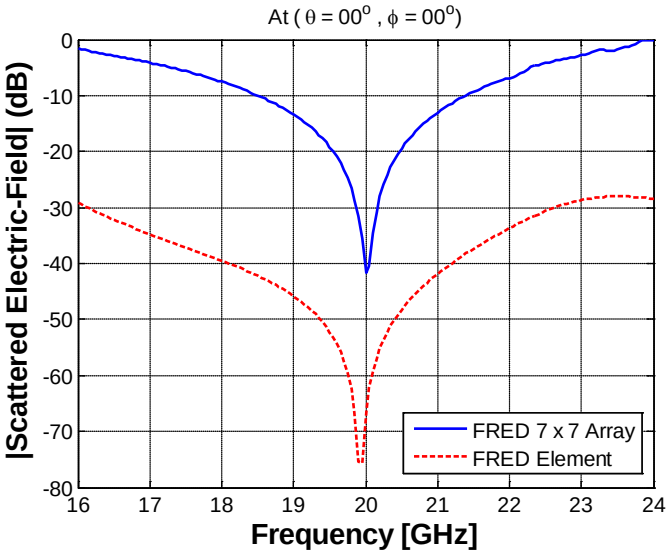

Figure 46. Frequency versus scattered electric-field amplitude comparison for both FRED array and element. Both curves are normalized by the peak of the FRED array response.

As shown in Figure 47, a single FRED element on a finite-size (11.43 mm × 11.43 mm × *t*) SiC substrate with ε_r = 10 and *loss*δ = 0.25 was considered. The substrate length is about three times of the length of one of arms in the FRED element. The strip lines in the element were assumed to be a copper (5.6e7 S/m) with thickness of 0.1 mm.

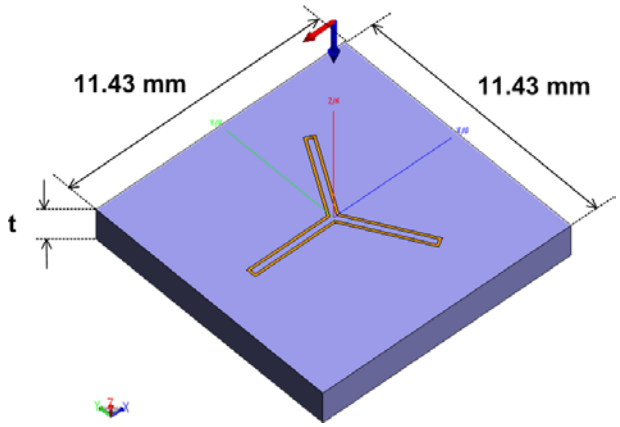

Figure 47. Simulation model of FRED sensor element on a finite-size SiC (ε_r = 10).

Simulation results for the cases varying the thickness of the SiC substrate (*t* = 0.1, 0.5, and 1.0 mm) are presented in Figure 48. For the cases of t = 0.5 and 1.0 mm, it appears that the response of the silicon-carbide dominates the response of the FRED element, which is similar to what was observed from the simulations and measurements of previous sensor designs using SiC

substrates. It is also observed that the response of the thickest case (t = 1.0 mm) is higher than that of the t = 0.5 mm case. This is due to the fact that the effective dielectric constant[v] for the t = 1.0 mm case is higher than that of the t = 0.5 mm case. Therefore we see more reflection at the air-to-SiC boundary for the t = 1.0 mm case.

When the thickness of the SiC becomes thin (t = 0.1 mm), we can see from the simulation result that the FRED element response is dominant over the response of the SiC substrate. Compared to the lossless case ($loss\delta$ = 0.00) and keeping the same dielectric constant of the SiC (ε_r = 10) in Figure 48, the t = 0.1 m case shows a lower-Q response. This encouraging result indicates that the FRED array on a 0.1 mm-thick SiC exhibits the desired behavior that Q changes with loss, which is the envisioned transduction mechanism for the passive wireless sensor.

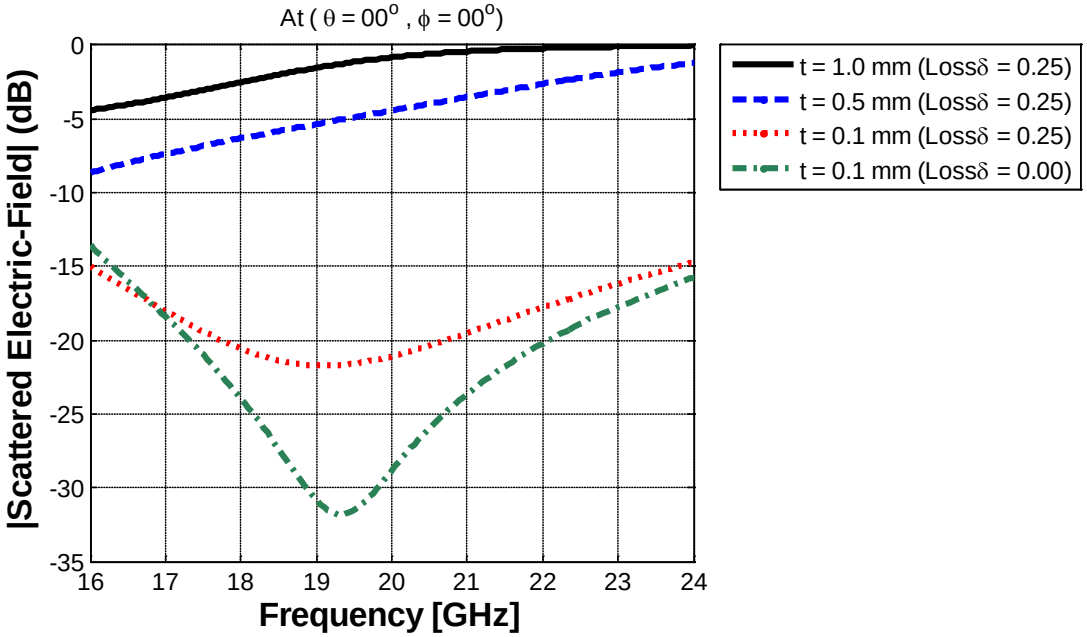

Figure 48. Frequency versus scattered electric-field amplitude of FRED element with varying thickness of a silicon-carbide substrate. Note that each curve was normalized by the peak value of the t = 1.0 mm case.

For this case of the FRED element on a finite thickness SiC substrate, the simulation shows that the response of the single FRED element on a finite-size SiC substrate with 0.1 mm thickness is not dominated by the response of the SiC substrate. However, the mechanical reliability of extremely thin silicon carbide plates is questionable in practice and would need to be supported or backed by the sensor packaging materials. A multi-layered or engineered

[v] For multi-layered materials, each layer may be composed of a different material than the other layers. An effective dielectric constant is a single number for the case replacing a multi-layered dielectric structure with an equivalent homogeneous material. In this case, the SiC layer and the air layer (semi-infinite thickness) below the SiC can be considered as a multi-layered structure. Thus, the effective dielectric constant of silicon-carbide is lower than the intrinsic dielectric constant of SiC due to the dielectric constant of air (ε_r = 1).

substrate mixing both SiC and a low-dielectric-constant material might provide an opportunity to increase the thickness of the substrate and achieve a low effective dielectric constant of the composite material while keeping the loss property of the SiC. Alternatively, we could utilize many small holes in the SiC or a porous variety of SiC in order to lower the effective dielectric constant of the SiC substrate, i.e. mixing the SiC and the air.

2.5 Conclusions from Research on Metamaterial Sensor Approaches

From the experimental results of testing of the guided mode resonance filter (GMRF) metamaterials sensor along the boresight with a bi-static radar approach, we could not identify any significant signature corresponding to an electromagnetic resonance, even for the cases of large holes on the metallic plate of the sensor, with and without copper tape. In addition, it was observed that the response of the sensors is similar to that of the solid plates. However, for the case of 2"×2" sensors with an air substrate, a small signature (1.5-dB dip) was observed. It was not clear that it represents anything related to the holes, but even if it did the strength of the signature is not adequate to be used for a sensor. During testing of radio wave propagation in Babcock & Wilcox's Small Boiler Simulator (SBS), as described in Section 4.1, a ±5 dB amplitude-variation in the channel environment was observed. Therefore, the observed signatures of the 2"×2" sensors would not significant in comparison with the background variations due to changes in the SBS environment.

In contrast to the tests of the GMRF metamaterial sensors, a noticeable signature was observed in the responses of the simple dipole array and the solid silicon-carbide plate at various distances. Particularly, the response of the simple dipole array was similar to the numerical simulation result, which confirmed the validity of the measurement setup.

After investigation of the metamaterial-based sensor, the following problematic issues were identified through extensive measurements and simulations:

1. *The sensor response was weak and indistinguishable from background clutter*. High dielectric loss in realistic sensor materials such as silicon carbide prevented efficient energy coupling to the sensor and/or reduced the level of the reflected waves. Dielectric loss was not included in the original simulations of GMRF metamaterial response. The temperature information encoded in the sensor's Q response could not be detected due to other environmental factors, including edge effects and surface reflections. It was nearly impossible to detect the sensor signal or estimate the temperature information.

2. *A working metamaterial sensor would have to be very large to have a sufficient number of periods to generate a usable response.* Edge effects, including diffractions and creeping waves for a finite-size sensor, dominated the desired sensor response. In addition, high reflection at the boundary between air and the sensor substrate with a high dielectric constant dominated the desired sensor response.

3. *The sensor was angle sensitive.* Numerical simulations show that the sensor response changes with any deviation from exact normal (90 degree) angle of incidence. The metamaterial-based sensor was composed of periodic, electrically-small elements, i.e., an array. Due to the inherent directive nature of the array, angular sensitivity issues could not be overcome.

For these reasons, further research on the use of GMRF-based metamaterials for the design of a passive wireless temperature sensor was discontinued, and research began on a mechanically modulated antenna temperature sensor, as described below in Section 3.

3 MECHANICALLY MODULATED ANTENNA SENSOR DEVELOPMENT

Due to the limitations of the metamaterials sensor approach described above in Section 2.5, a new passive wireless sensor concept was investigated and evaluated. The sensor is based on radio frequency (RF) Doppler radar interrogation of a mechanically modulated antenna structure and is referred to as MMA (Mechanically Modulated Antenna). The MMA structure incorporates a mechanical resonator arranged in such a way that oscillations of the resonant beam alter the capacitive loading of the antenna and therefore the antenna's resonant frequency. Doppler radar is used to wirelessly detect the beam oscillation frequency, which is proportional to temperature. Remote excitation of the mechanical resonator is achieved using free-space acoustic waves.

3.1 Mechanically Modulated Antenna (MMA) Design

A solid rendering of the design of the prototype mechanically modulated antenna (MMA) is shown in Figure 49. A copper-clad circuit board optimized for use at microwave frequencies is used as the ground plane for the antenna. A slot is cut out of the copper cladding to form the antenna element; the slot is folded to reduce the overall size of the sensor. Two conductive metal posts are attached to the ground plane, one along the outer periphery of the folded slot, and another to the "peninsula" in the interior of the U-shaped slot. To the post along the outer periphery of the slot, a thin copper cantilever beam is attached. In operation, this cantilever beam is induced to vibrate by incident acoustic waves. As the beam vibrates, the impedance of the antenna changes at the same frequency as the resonant frequency of the beam vibration, due to the change in capacitance as the distance between the inner post and the vibrating beam changes during vibration.

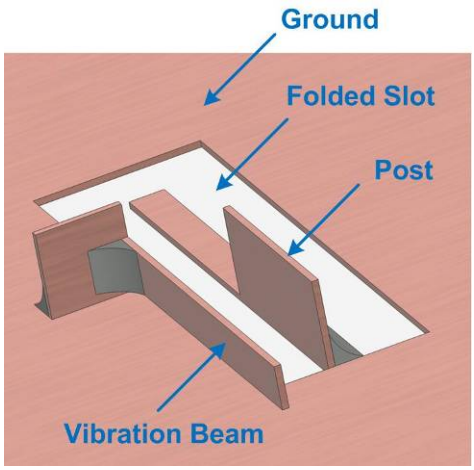

Figure 49. Geometry of the designed sensor with vibration beam.

A schematic of the MMA sensor system interrogated by a Doppler radar system is depicted in Figure 50. A microwave power source generates radio waves used to interrogate the sensor. Simultaneously, a low-frequency acoustic power source (with a frequency chosen to match the beam's resonant frequency) excites the resonant cantilever beam and the resulting beam deflections modulate the impedance of the antenna. As a result, the reflected signal from the sensor has a modulated form which is centered at a different frequency than other background reflections around the sensor. At the receiver, the modulated reflected signal is mixed (heterodyned) with the original high-frequency RF signal, and using a simple diode detector and low-pass filter, the beam vibration frequency (ω_n) can be detected.

The beam vibration frequency (ω_n) changes with temperature due to temperature dependent changes in beam stiffness, so that we can therefore measure temperature by monitoring the detected vibration frequency.

Potential advantages of the MMA passive wireless sensor approach over the GMRF metamaterial approach include:

1. The sensor is not composed of multiple elements, i.e. it is not an array. Thus, the sensor has a very wide operational angle (± 70 degrees). The inherent angular sensitivity issue evident with the original metamaterial sensor is resolved.

2. Because the detection system extracts a modulation frequency from the reflected sensor signal, the influence of environmental clutter (backscatter) is not a problem. In addition, since the mechanical modulation frequency (approximately 2 kHz) is very low compared to the RF frequency (11 GHz), scattering and reflections due to the RF source will not affect the beam vibration frequency embedded in the modulated signal.

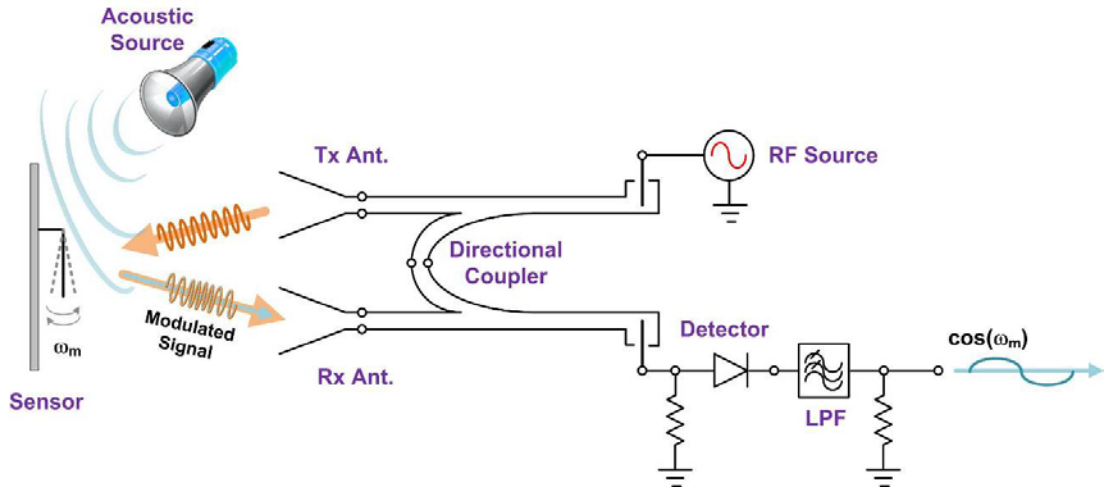

Figure 50. Illustration of new sensor system based on a hybrid approach.

3.2 Interrogator Design for Mechanically Modulated Antenna

The vibrating cantilever beam on the MMA varies the impedance of the antenna at a frequency equal to the cantilever beams resonant frequency, and this harmonically varying impedance imparts a phase modulation to incident microwaves as they re-radiate, which can be detected by a Doppler radar.

The Doppler radar system design used for this project transmits high-frequency RF power source (approximately 11 GHz for the prototype shown) interrogate the sensor. Simultaneously, an acoustic power source (at a frequency matching the beam's resonant frequency) excites the resonant cantilever beam and the resulting beam deflections modulate the impedance of the antenna. As a result, the reflected signal from the sensor has a modulated form which at a different frequency than other background reflections. At the receiver, the modulated reflected signal is detected and mixed (heterodyned) with the original high-frequency RF signal using a simple diode detector and low-pass filter. The output of the detector has a frequency equal to the cantilever beam's frequency. The beam vibration frequency (ω_n) changes with temperature due to temperature dependent changes in beam stiffness, so that we can therefore measure temperature by monitoring the detected vibration frequency.

3.2.1 Modeling and Simulation of Mechanically Modulated Slot Antenna Interaction with Doppler Radar Interrogator

To investigate possible limitations of the Doppler radar interrogator, the researchers at the Virginia Tech Antenna Group (VTAG) modeled the interaction between the radar and the mechanically modulated antenna sensor using the principle of reciprocity of a communications link.

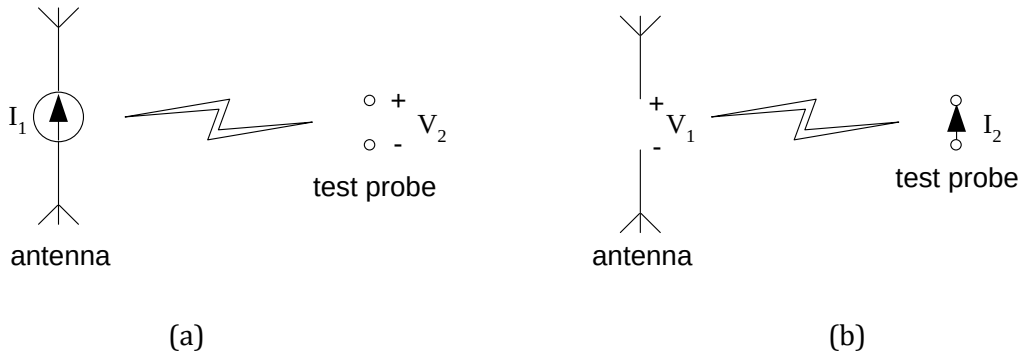

Figure 51. Relationship between antenna and test probe : (a) antenna transmission, (b) antenna reception

Given a current I_1 on an antenna with a current density J_1, the electric field E_2 at an arbitrary point in space may be determined by measuring the voltage V_2 developed across a test probe antenna at that point. Then, if I_2 is the current of an infinitesimal dipole, with current density J_2, located at the same position as the measured radiated voltage, V_2, in Figure 51, then the electric field E_1 developed across the antenna, which generates an open circuit voltage V_{oc}, is given by the reciprocity theorem as

$$\int_V \mathbf{J}_1 \cdot \mathbf{E}_2 \, dv = \int_V \mathbf{J}_2 \cdot \mathbf{E}_1 \, dv \,. \tag{13}$$

The analysis applies this principle to the Doppler radar-MMA sensor interaction as illustrated schematically in Figure 52, where the subscript *r* refers to the reader (or radar), and the subscript *s* refers to the sensor. $Z_{st} = Z_{ts}$ is the free space impedance between the sensor and reader, and Z_{stub} refers to the impedance presented to the MMA sensor by the vibrating beam (stub). I_r is the current generating the radiated radio wave in the reader, and I_s is the current generated in the sensor antenna by the received radio wave.

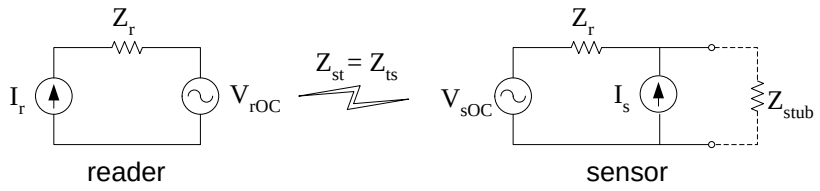

Figure 52. Schematic illustration of interaction between Doppler radar (reader, left) and MMA sensor (right)

The reciprocity analysis considers three cases:

- I_r creating the open circuit voltage V_{sOC} at the sensor terminals (no stub)
- I_s creating the open circuit voltage V_{rOC} at the reader terminals (no stub)
- The effective current I_s created by the loading of the stub (vibrating beam) with incidence from the reader. For this analysis, the reader will be considered for the current and open circuit voltage separately.

The coupling from the reader to the sensor is defined within the open circuit voltage and is described above in terms of the effective length of the antennas or structures. Basic reciprocity says that

$$I_r V_{rOC} = I_s V_{sOC.} \tag{14}$$

In a testing mode, we assume that $I_r = I_s$ giving $V_{rOC} = V_{sOC}$, which implies that $Z_{ts} = Z_{st}$, where

$$Z_{rs} = \frac{V_{roc}}{I_s} \text{ and } Z_{sr} = \frac{V_{soc}}{I_r}. \tag{15}$$

To consider the reader/sensor interaction, we start with a transmitter current of I_r, yielding an open-circuit voltage at the sensor based on effective length. The current for the reverse problem then becomes

$$I_s = -\frac{I_r Z_{st}}{Z_s + Z_{stub}} \tag{16}$$

to give a reader open circuit voltage of

$$V_{roc} = -\frac{I_r Z_{st}^2}{Z_s + Z_{stub}} \tag{17}$$

If a folded dipole with a stub is considered, the effective length of the antenna can be calculated to be

$$\vec{h}(\theta,\phi) = -\frac{\vec{E}(\vec{r})}{j\omega\mu\left(e^{-jkr}/4\pi r\right)I} = -\frac{4\cos\left(\frac{\pi}{2}\cos\theta\right)}{k\sin\theta}\hat{\theta} = -\frac{2\lambda\cos\left(\frac{\pi}{2}\cos\theta\right)}{\pi\sin\theta}\hat{\theta} \tag{18}$$

and its input impedance to be $Z_{in} = 292.5\Omega$.

For the case where the sensor and the reader are both at a peak gain, with respect to each other, each using a folder dipole antenna, the mutual impedance then becomes

$$V_{SOC} = -j\omega\mu\frac{e^{-jkr}}{4\pi r}I_r h_r(90°)h_s(90°) \tag{19}$$

where

$$h_r(90°) = h_s(90°) = h = -\frac{2\lambda\cos\left(\frac{\pi}{2}\cos 90°\right)}{\pi\sin 90°} = -\frac{2\lambda}{\pi} \tag{20}$$

is the effective length of the reader antenna and the sensor antenna, respectively. This gives the open circuit voltage on the sensor

$$V_{SOC} = -j\frac{2\pi}{\lambda}\eta\frac{e^{-j\beta r}}{4\pi r}I_r\frac{4\lambda^2}{\pi^2} = -j\frac{e^{-j\beta r}}{4\pi r}I_r 960\lambda \tag{21}$$

or

$$Z_{st} = -je^{-jkr}76.4\left(\frac{\lambda}{r}\right). \tag{22}$$

The two-way link then becomes

$$V_{ROC} = \frac{I_r\left(e^{-jkr}76.4\left(\frac{\lambda}{r}\right)\right)^2}{292.5\left(1+\frac{Z_{stub}}{292.5}\right)} = I_r\frac{19.95\left(\frac{\lambda}{r}\right)^2}{\left(1+\frac{Z_{stub}}{292.5}\right)} \tag{23}$$

For the recent testing of the MMA sensor with a Doppler radar system, a frequency of 10 GHz has been used, with the Doppler horn antenna separated from the MMA sensor by a distance of 1m. The input power was 100 mW, giving

$$I_r = \sqrt{\frac{2*0.01}{292.5}} = 26.1\ mA \ . \tag{24}$$

Then

$$V_{rOC} = \frac{0.0261*19.95\left(\frac{0.03}{1}\right)^2}{\left(1+\frac{Z_{stub}}{292.5}\right)} = \frac{0.470\ mV}{\left(1+\frac{Z_{stub}}{292.5}\right)} \tag{25}$$

This indicates that $V_{rOC} \leq 0.470$ mV, which is just at the limit of a typical oscilloscope input. . An increase to 10W will increase V_{rOC} peaks to 4.7 mV for this 1 m distance at 10 GHz.

To estimate the noise present in the signal, we assume that a bandwidth of 50 kHz is used, in order to track the approximately15 kHz acoustic sidebands. Assuming an antenna temperature of 100 K in a lossless system, the noise voltage is given by

$$V_n = \sqrt{4kTBR} = \sqrt{4*1.38*10^{-23}*100*5*10^4*292.5} = 0.284\,\mu\text{V} \tag{26}$$

This noise voltage is approximately 65 dB lower than the voltage signal due to the antenna, which indicates that a low noise amplifier (LNA) could be used to boost the signal voltage, and retain a strong signal-to-noise ratio. When a digital processing oscilloscope (DPO) is used to observe the signal, as has been the case in the experimental work to date, the noise level will be much higher, due to the broad bandwidth of the oscilloscope. For a DPO at maximum sensitivity and restricted to a 200 MHz bandwidth, RMS noise levels on the order of 100 µV are commonly observed. An LNA with a gain of 30 dB should result in an additional factor of 31.6x over the predicted 0.47 mV signal, or 14.9 mV, which should be adequate for monitoring with a DPO.

An analysis of the Doppler radar system interrogator was used to determine the sensitivity of the radar system to the distance separating the interrogator from the MMA sensor. MATLAB was used to model the Doppler radar system, in which a peak detector is used to mix the modulated signal from the MMA with the local oscillator (LO) signal, which is tapped off from the RF source by a directional coupler. The voltage amplitude of the modulated signal was assumed to be 10% of the voltage amplitude of the LO signal. The frequency of the RF source

was modeled to be 10 GHz, and the modulation imposed by the vibrating beam was assumed to be 100 MHz.

Figure 53 shows the detected signal measured following the low pass filter (LPF) when the phase difference between the modulated signal and the LO signal is 0°. When the phase between the modulated signal and the LO is adjusted to be 90°, the detected signal illustrated in Figure 54 results. Comparison of the two results shows that, when a peak detector is used, the output is sensitive to the phase difference between the local oscillator signal and the modulated signal.

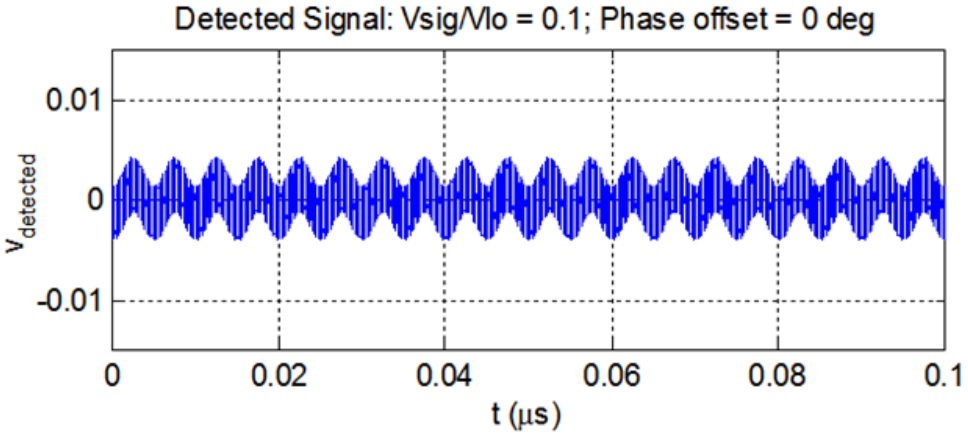

Figure 53. Simulated Doppler radar output for 0° phase difference between modulated signal and local oscillator signal.

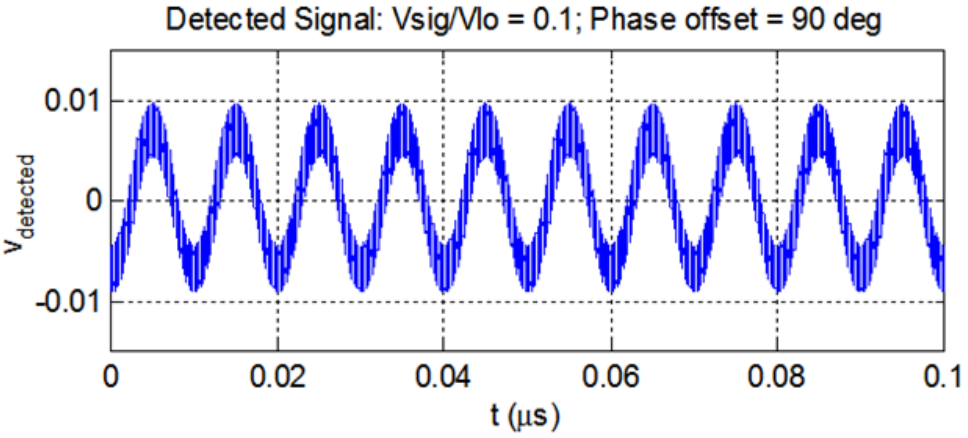

Figure 54. Simulated Doppler radar output for 90° phase difference between modulated signal and local oscillator signal.

For the Doppler system at 10 GHz, the wavelength is approximately 3 cm. A 90° phase shift between the modulated signal and the local oscillator signal can be caused by changing the

separation between the radar and the MMA sensor by an eighth of a wavelength, or 3.75 mm. This will make the sensor system sensitive to the positioning of the radar antennas relative to the sensor.

In order to eliminate the sensitivity of the output to the position of the radar antennas, the researchers at the Virginia Tech Antenna Group proposed using I/Q demodulation of the modulated signal. In the I/Q, I refers to "in-phase" and Q refers to "quadrature." One possible implementation is shown in Figure 55. The output of the microwave RF source is directed to the transmit antenna, but some part of the output is tapped off by a directional coupler to serve as the LO signal. This LO signal is again split by a coupler into two LO signal paths. A phase shifter is used to introduce a 90° phase shift into one of the LO paths. The modulated signal reflected from the MMA is captured by the received antenna and amplified by a low noise amplifier (LNA). This amplified modulated signal is split by a coupler and the modulated signal is then mixed with the two LO signals. The mixers typically employ a nonlinear element such as a high-speed diode. After low pass filtering, the output of one mixer is a signal that it proportional to the component of the modulated signal in-phase with the local oscillator signal. The output of the other mixer (after low-pass filtering) is proportional to the quadrature component of the modulated signal (90 degrees out of phase). By taking the ratio of the I (in-phase) and Q (quadrature) signals, the phase of the modulation (beam vibration) can be determined.

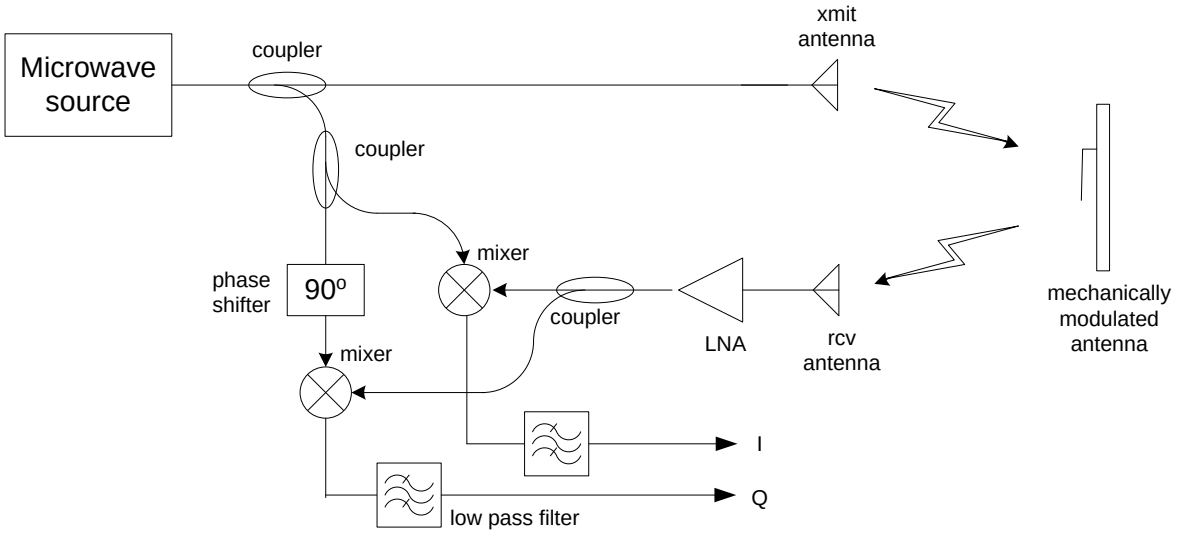

Figure 55. Schematic of I/Q Doppler radar interrogation system

3.2.2 FINAL INTERROGATOR DESIGN

In Section 3.2.1, analysis of the Doppler radar interrogation system concluded that a low noise amplifier (LNA) could be used to boost the signal voltage and achieve a strong signal-to-noise ratio. The analysis predicted that an LNA with a gain of 30 dB should result in an additional factor of 31.6x over the predicted 0.47 mV signal, or 14.9 mV, which should be adequate for monitoring with a digital processing oscilloscope (DPO), which typical exhibits

RMS noise levels on the order of 100 µV with the DPO set to maximum sensitivity and restricted to a 200 MHz bandwidth.

The baseline noise of the DPO was measured to be about 2 mVp-p with the input set to the 1 mV/div scale. This is typical for a sampling ADC front end typically used on a DPO which is usually a fast (4 G samples per second) 8 bit device. With this noise level, the received signal was not visible within the noise, so a wideband low noise RF amplifier was placed between the receiver horn antenna and the directional coupler. This RF amplifier provided 23 dB of gain. By triggering the scope on the acoustic source and using averaging of 16X, a relatively clean signal of about 1 mVp-p was observed when the acoustic source was matched to the resonant frequency of the sensor beam.

With the improved signal strength, it was then determined that the baseband (audio frequency) signal from the detector should be amplified before being applied to the scope. Furthermore, there was a low frequency modulation of the detector due to reflections from objects in the room due to slight movements, which was an additional noise source. Because of these conditions, a high-pass filter function (200 Hz) was added to the amplifier to reduce this noise source due to sensitivity to movements in the test environment.

These changes resulted in a significant improvement in the signal level to about 60 mVpp without the need of averaging, but it was observed that there was a medium audio frequency noise content. An adjustable, low pass filter was added to the signal path and this noise source was reduced as well.

As a result of the described design modifications, the revised Doppler radar interrogator was finalized as illustrated schematically in Figure 56.

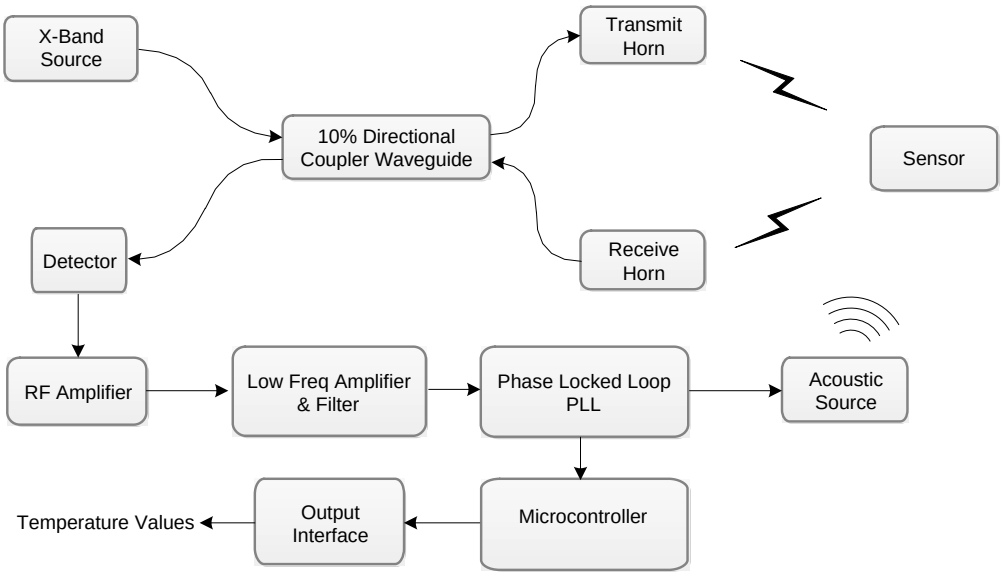

Figure 56. Revised Doppler radar interrogator design.

In addition to the low noise radio frequency amplifier, the baseband (low-frequency) amplifier and filter is also shown. The function of this section is to amplify the demodulated baseband sensor signal output by the detector, and to limit the signal bandwidth in order to improve signal-to-noise ratio. The components of this section are a high impedance, high pass gain stage with a 200 Hz low end cutoff followed by and adjustable, 8^{th} order low pass filter with the low pass adjustable from 440 Hz to 3300 Hz followed by a gain stage with a fixed 10 kHz low pass filter.

In addition, the revised interrogator also included a phase locked loop (PLL), which is used to determine the natural frequency of the sensor's resonator as the temperature of the sensor changes. The PLL automatically adjusts the frequency of the acoustic source to maximize the signal output by the low-frequency amplifier and filter section. The signal will be maximized when the amplitude of the sensor resonator is maximized, which occurs when it is acoustically driven at its natural resonance. Using a servo loop, the PLL will track the natural frequency of the sensor resonator as it changes due to varying temperature. The PLL outputs the resonator frequency to the microcontroller for conversion to an engineering value of temperature.

3.2.3 Acoustic Excitation of Vibrating Beam on MMA

Initial testing of the first MMA prototype employed a 100 W horn speaker driven by an audio power amp in order to excite the vibrating arm on the MMA to resonance. A sound pressure level (SPL) on the order of 115 dBA in the vicinity of the sensor was achieved by positioning the speaker approximately 1 m from the sensor. For practical applications in power plants, however, the speaker might be as much as 10 m from the sensor. In that case, the SPL at the speaker will be significantly less due to the expanding wavefront of the sound wave as it propagates away from the speaker. Focusing of the acoustic waves into a tightly collimated beam would require acoustic lenses (or a phased array) with a wide aperture in order to minimize diffraction due to the long acoustic wavelength. Use of a wide aperture acoustic source would be difficult in many power plants. Alternately, a shorter wavelength (higher frequency) could be used to reduce diffraction, but then the frequency will not match the resonant frequency of the sensor's resonant beam.

A solution to this problem was found in the use of nonlinear ultrasonic waves. The concept is illustrated in Figure 57. Two speakers are directed so that their outputs overlap in some spatial region (illustrated as a gray wedge shape in the figure). One speaker is driven at a frequency f_1 in the ultrasound regime (greater than 25 kHz), and the second speaker is also driven at the ultrasound frequency f_1 but is also amplitude modulated with some audio frequency signal Δf. If the sound pressure levels of the outputs of the two speakers are sufficiently high (generally above 100 dB), then the air acts as a nonlinear medium and heterodynes the two speaker outputs, producing new frequencies at both the sum and the difference of the two speaker frequencies. Since the difference frequency is $(f_1 + \Delta f) - f_1$, an audible signal in the audio frequency range is produced in the region where the two speaker outputs overlap. Since ultrasound wavelengths are much shorter than audio wavelengths, diffraction effects are reduced and the ultrasound beams can be more tightly collimated, permitting the region where the audio frequencies are produced to be controlled and restricted.

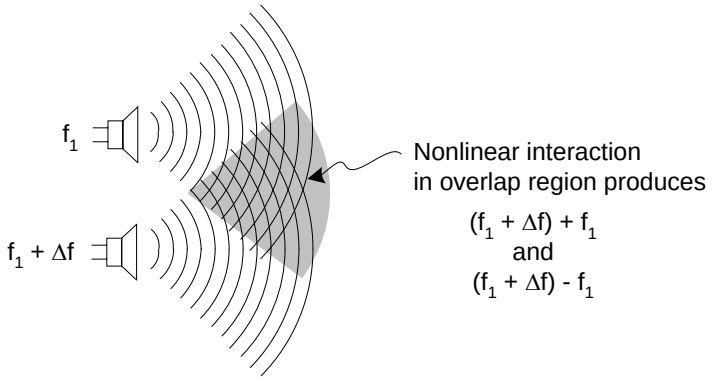

Figure 57. Generation of audio frequency sound from nonlinear interaction of two ultrasound beams.

A commercial Hypersonic Sound H450 directional speaker system manufactured by American Technology Corporation was obtained to evaluate its use for acoustically exciting the sensor. This two-speaker system uses PVDF piezo speakers driven at a carrier frequency between 40 kHz and 50 kHz, and is rated to achieve a maximum SPL exceeding 80 dB one meter from the speakers. At a distance of 10 m, an SPL of greater than 65 dB is specified. Testing of the speaker system confirmed that an SPL of approximately 80 dBA could be achieved in close proximity to the speakers.

Figure 58. HyperSonic Sound H450 directional ultrasonic speaker evaluated for acoustic excitation.

3.3 Design of First MMA Prototype

A folded slot sensor having a beam structure was designed for proof of concept experiments, according to the design shown in Figure 49. The overall footprint of the actual sensor is approximately 5 mm × 2 mm, though the sensor was built on a 50 mm × 50 mm circuit board (Rogers 4003C) for convenience. The beam structure surface faces the surface of the post to provide a parallel plate type capacitive loading. Because the root of the beam is connected at a place far from the post, there will be an inductive loading as well. When the beam vibrates back

and forth these parasitic loadings change the effective impedance of the antenna structure. The dynamic change of the sensor impedance generates modulation of the RF signal.

In order to test the sensitivity of the sensor impedance change due to beam displacement, electromagnetic simulations were carried out using FEKO electromagnetics modeling software. Three cases are shown in Figure 59: (a) center-located beam, (b) +558 μm beam displacement, and (c) -558 μm beam displacement. The simulated return loss results in Figure 60 show that the sensor antenna experiences a huge detuning due to the beam displacement, which indirectly indicates the sensor impedance changed significantly. For the case of ± 10 μm beam displacement, the model predicts several tens of MHz detuning.

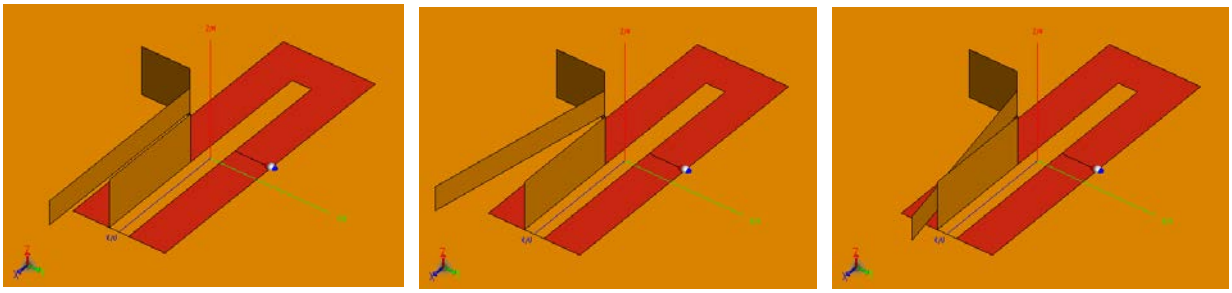

(a) (b) (c)

Figure 59. Sensor simulation models – (a) Beam is located at the center, (b) +558 μm beam displacement, and (c) -558 μm beam displacement.

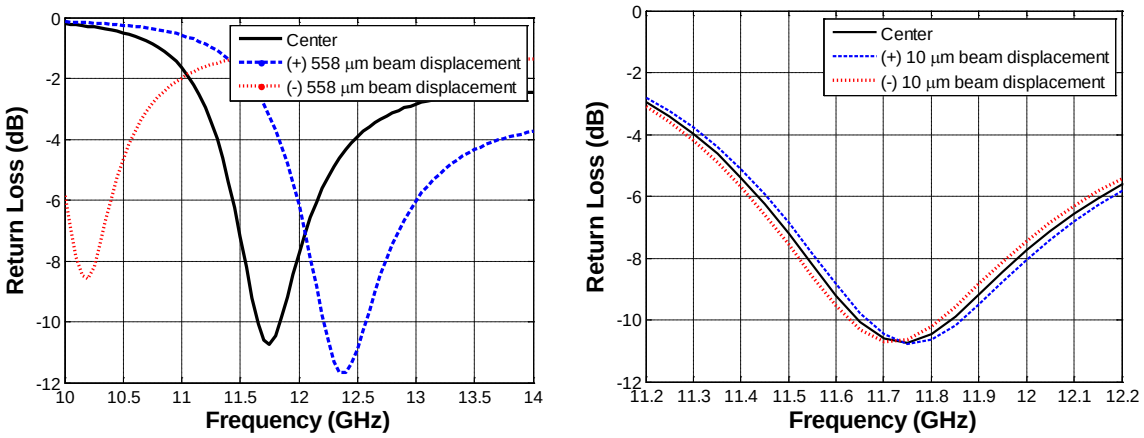

(a) (b)

Figure 60. Simulated detuning effect due to the beam displacement – (a) Case of ± 558 μm beam displacement and (b) Case of ± 10 μm beam displacement.

3.4 First Prototype MMA Fabrication and Room Temperature Testing

A prototype was constructed according to the general design of Figure 49. A picture of the fabricated sensor is shown in Figure 61a. In order to monitor the sensor input impedance during experiments, a semi-rigid coaxial cable was attached, but cable was not intended to be part of a final device. Initially, an optical fiber was attached to the sensor ground plane, and a high-powered diode laser was used to excite resonance in the beam by shining the laser output (through the optical fiber) onto the vibration beam. The laser output was intensity modulated, and the modulation frequency was swept until vibrations of the beam were detected by an optical interferometer. The deflections occur due to localized heating of the beam on the surface of the beam facing the laser.

Figure 61b shows the overall experiment setup. With a slow frequency sweep, multiple resonances were observed in the measured return-loss plot of Figure 62a indicating the dynamic change of the beam displacement. With averaging of 64 sweeps, a 20-MHz detuning was identified as shown in Figure 62b as determined by connecting a vector network analyzer to the coaxial cable attached to the antenna. This experiment confirmed that the fabricated sensor can modulate the interrogating radio wave signal effectively with beam vibration. It was determined that approximately +/- 10 μm of beam tip displacement were needed to produce enough change in antenna impedance to resolve the modulation.

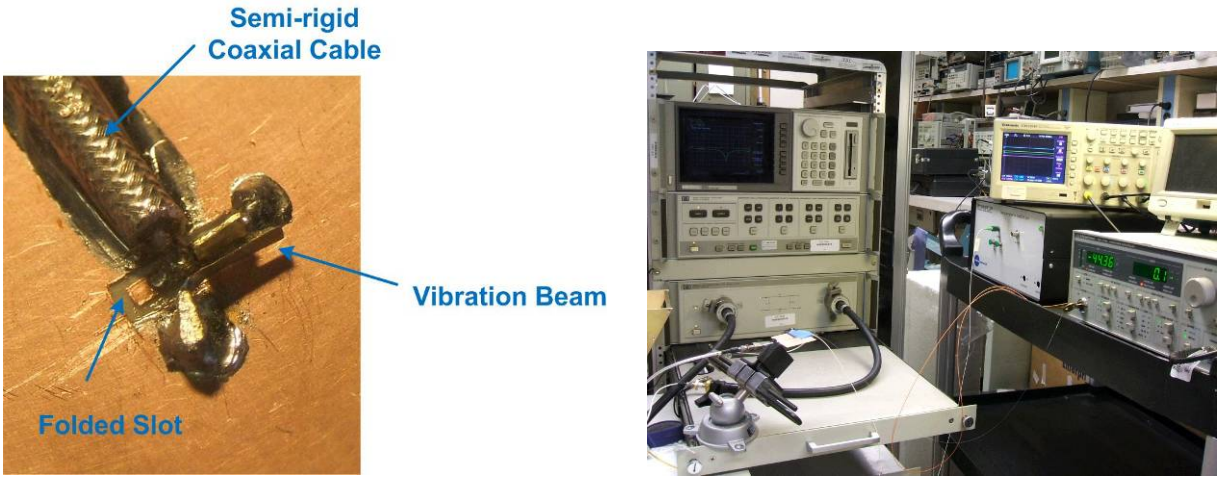

Figure 61. (a) Fabricated sensor and (b) Measurement setup for antenna test with a beam vibration through a direct laser beam excitation.

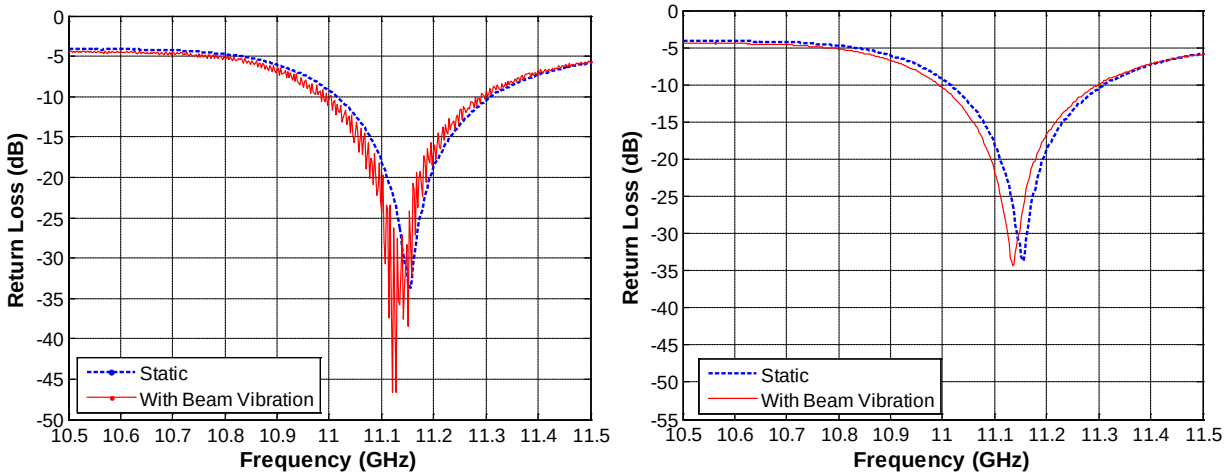

Figure 62. Measured return loss comparison between static and beam vibration cases – (a) without averaging and (c) With averaging (64 averaging at each frequency).

After demonstrating that the antenna modulation using the vector network analyzer connected to the coaxial cable, an experiment was performed to evaluate remote RF Doppler radar detection of the modulation, as shown in Figure 63. The sensor coax feed was terminated with an open-circuit standard load to prevent any potential direct coupling through the sensor terminal. The source RF power output at 11 GHz was approximately 2 dBm, which is relatively low compared to typical radiation power of cell phones (30 dBm). The beam was excited again with the high-powered laser source at a resonant frequency of approximately 1.8 kHz. For both boresight (radio wave at normal incidence) and 70° off normal incidence, the modulation frequency could be detected (approximately 1.786 kHz, corresponding to a period of 560 μs), as depicted in Figure 64.

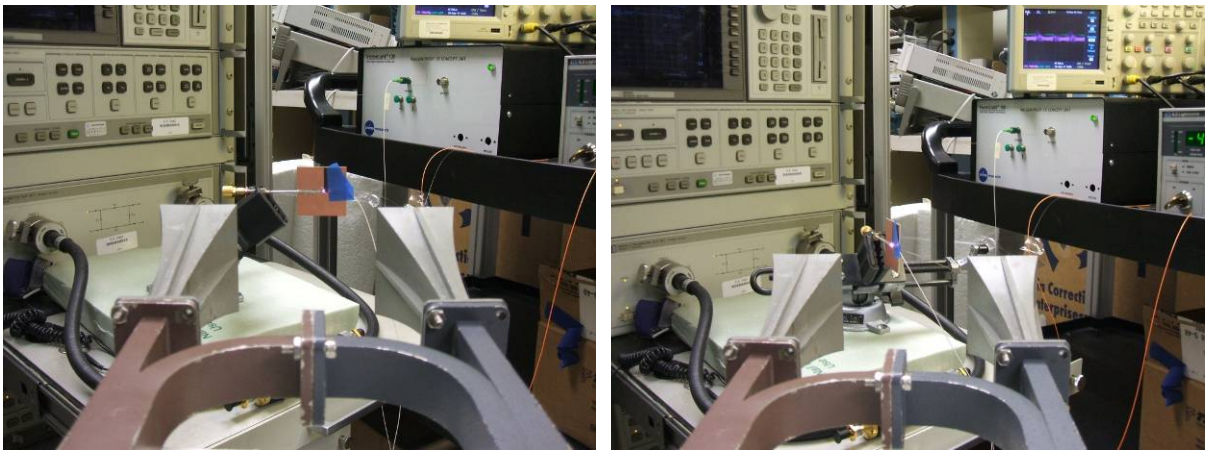

Figure 63. Doppler radar detection setup for the off-angle test with direct laser beam excitation – (a) Boresight and (b) approximately 70 degree off.

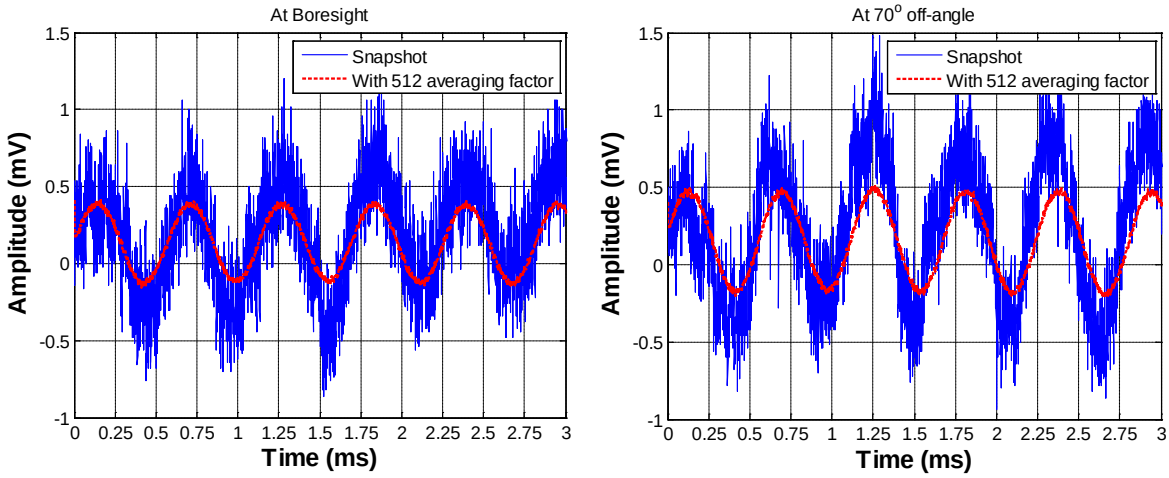

(a) At boresight (b) 70°-off angle

Figure 64. Measured, detected beam vibration frequency through the Doppler-radar approach.

Next, an experiment was designed to demonstrate both remote acoustic excitation and remote RF Doppler interrogation. The excitation laser was replaced with a remote acoustic source as shown in Figure 65 and Figure 66. A horn loudspeaker was driven by an audio amplifier at a frequency of approximately 1.8 kHz; the measured sound pressure level (SPL) was approximately 115 dBA.

Two cases were evaluated: one case with the sensor in free space and a second case with the sensor attached to a poster board. For both cases, the RF Doppler antennas were approximately 30 cm from the sensor and the acoustic source was 1 meter away from the sensor. RF power output from the Doppler radar horn antenna was about 2 dBm. Even without any optimization of the acoustic coupling or antenna sensitivity, the modulation frequency could be clearly detected, as shown in Figure 67.

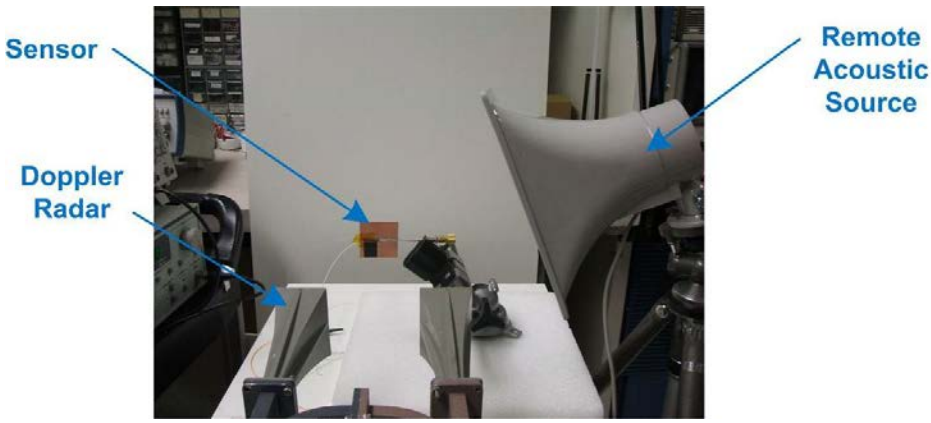

Figure 65. Measurement setup for remote radio frequency and acoustic excitations for the sensor in free space.

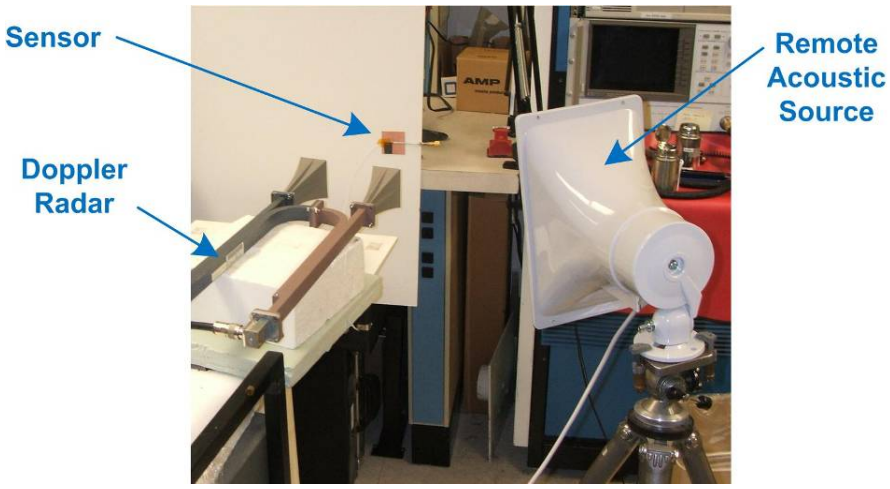

Figure 66. Measurement setup for remote radio frequency and acoustic excitations for the sensor mounted on a cardboard wall.

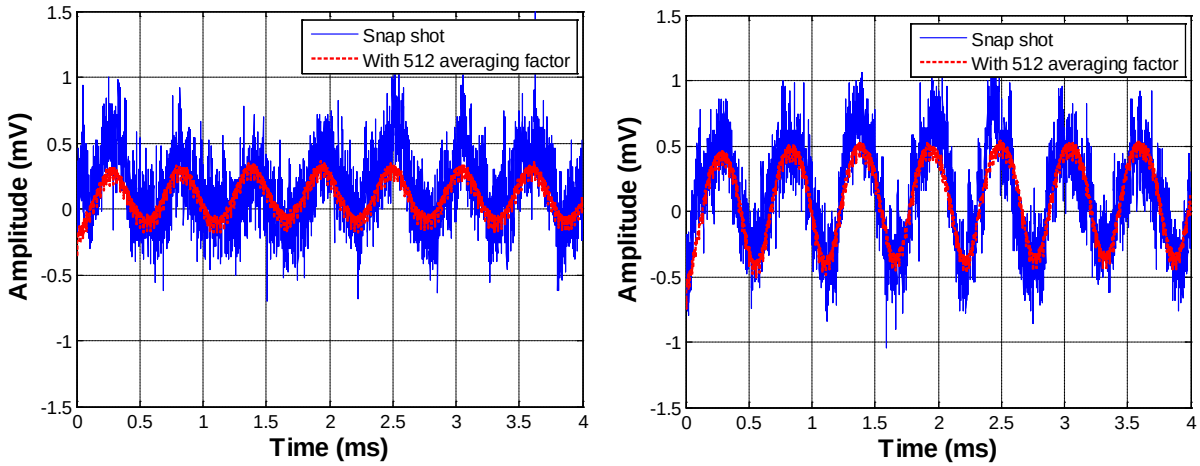

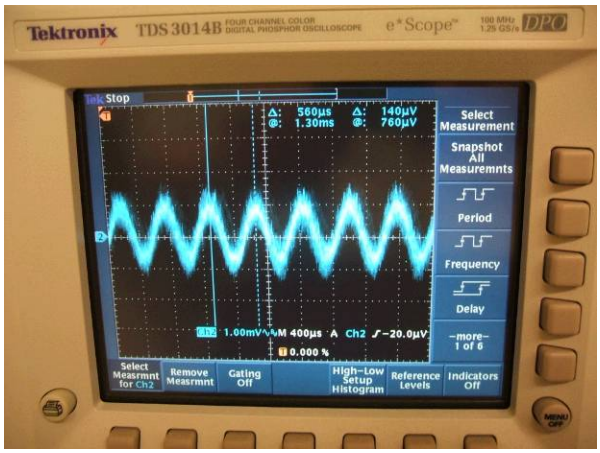

(c)

Figure 67. Measured/detected signals from the Doppler radar – (a) Sensor in free space, (b) Sensor on poster board, and (c) Picture of a detected signal during the measurement.

3.5 Computational Electromagnetics Model of MMA Sensor

To better understand the MMA sensor operation, an electromagnetic simulation of the sensor structure was performed to evaluate the relative amplitude and phase variations due to the flexing of the beam. Using FEKO, the sensor was simulated as being interrogated from above by a microwave frequency plane wave, and the reception was measured at both the small probe in the slot (by use of a shorting wire for tuning) and at a receiving antenna in the far backscattered direction from the sensor. The probe provides information on the resonant properties of the sensor, while the receiving antenna was used to simulate the effect of the reading by the remote antenna in the system. These results are given in Table 5. The beam deflection (swing) exceeds the expected vibration limits by more than ten times the expected maximum amplitude of 10 μm. The properties of the probes versus deflection are shown in Figure 68.

Table 5. Current coupling and far-field reflection data for the sensor versus beam deflection

Swing (mm)	Load Current (dB/deg)	E_θ *(0,45)* in Far Field (mag/phase)
-0.5	-92.17∠1.78°dB	114.50∠91.2°mV
-0.4	-90.90∠-0.52°dB	114.50∠91.07°mV
-0.3	-88.97∠-5.09°dB	114.38∠90.82°mV
-0.2	-86.56∠-12.53°dB	114.10∠90.46°mV
-0.1	-83.35∠-27.69°dB	112.94∠89.79°mV
0	-80.30∠-68.10°dB	108.94∠90.16°mV
0.1	-82.57∠-113.15°dB	109.48∠92.47°mV
0.2	-86.35∠-133.49°dB	111.58∠92.79°mV
0.3	-89.46∠142.69°dB	112.48∠92.66°mV
0.4	-91.55∠147.50°dB	113.0∠92.57°mV
0.5	-93.39∠150.31°dB	113.15∠92.44°mV

The configuration of the sensor structure used in the simulation was similar to the physical structure created for testing of the first prototype (Figure 49), but the emphasis here was to gain an understanding of the scattering process that would be detected, as well as potential problems. A probe wire was part of the original design to provide low impedance sampling of the resonance nature of the sensor. The system was interrogated by a plane wave (1V/m) incident from the top (z-direction) and data collected for both the current probe and a far field probe located 5 far-field distances above the sensor structure (not shown in the diagram).

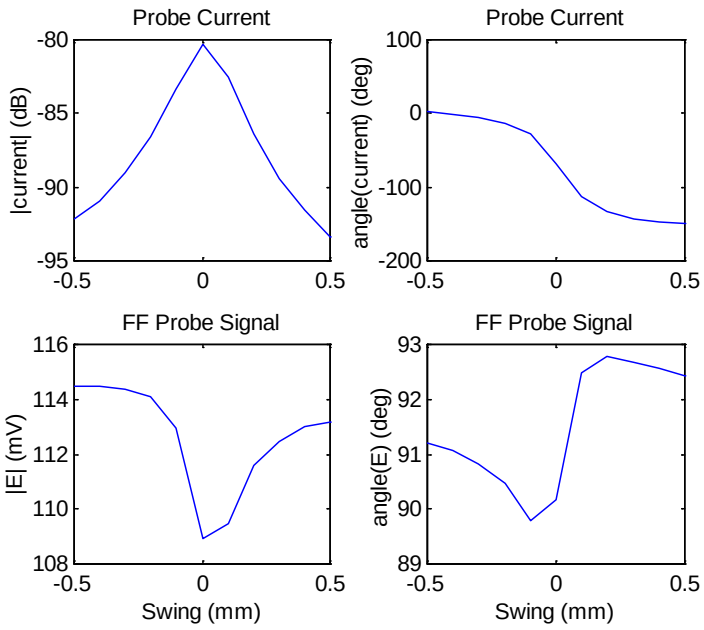

Figure 68. Current and Radiation Probes versus deflection of the beam. The Current probe clearly shows the expected resonance of the sensor with a peak in received signal. The far-field probe provides a measurable of response of the sensor.

The current probe is shown in red and blue in Figure 69 in the mesh diagram used to define the finite elements used for the FEKO simulation. From the simulated probe current output (Figure 68), it appears that the signal goes through a 10-15 dB shift and a 180° phase shift over the range of beam vibration amplitude simulated. The sensor is electromagnetically resonant at the center probe position (0) and the RF frequency was adjusted to this value for the computation. The phase must be considered relative in this simulation since there is no phase reference used. In practice, the phase reference is obtained by mixing with the radiated field with the interrogator that has not been modeled in this simulation.

The far field antenna provides information of the form we would expect to measure in the field. The simulated output of the farfield antenna consists of only the scattered field and not the exciting plane wave. The output shows that there is a significant change of the signal as the signal passes through resonance, though not to the same degree as with the current probe. Part of the reason for the apparent small difference is that the simulated response includes backscatter from the ground plane surrounding the sensor. There will be a DC term that includes the bulk reflection of the ground plane. However, only the resonance variation is of importance for reception with the Doppler-type mixing process. The variation of the received signal over the full simulated range of tip vibration amplitudes is about 3% of the signal level with a phase variation of about 4 degrees. The simulation suggests that 1 mm or so of deflection is necessary to obtain the full range of data, and that a tip vibration amplitude of 0.1 mm results in approximately 2% change in the detected field.

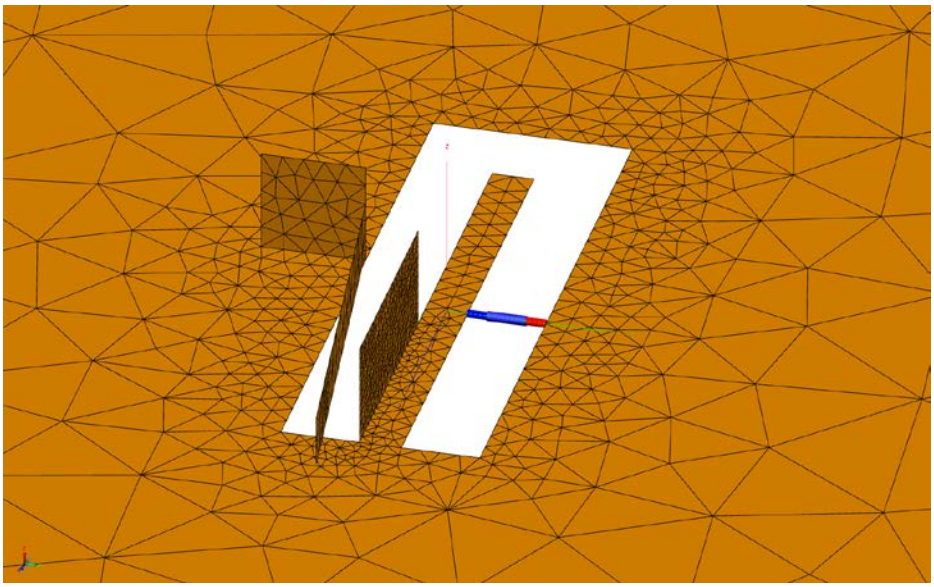

Figure 69. Mesh used for FEKO analysis of the MMA sensor structure. The resonant beam is shown bent to illustrate the vibrations whose frequency is proportional to the temperature of the beam.

A strong resonance of the antenna structure with good efficiency and reasonably narrow bandwidth is important to maximize the antenna sensitivity for the measurement. A high gain is not desired since that would lower the probability of detection over a wide angular field of view. However, high efficiency and narrow bandwidth increase the sensitivity of the system.

Additional considerations must be given to the polarization of the antenna systems and to avoiding phase shifts that could cause a signal null at the receiver mixer. A circularly polarized interrogator radiation field could be used to minimize polarization fading.

Care must be taken to ensure the ground plane is not resonant at the same frequency as the antenna under consideration, to remove any stray resonance that may dampen the viewed resonance of the sensor portion of the structure.

If sensor sensitivity needs to be increased further, the gain may be increased, but with a corresponding reduction in the view angle. Lower wavelengths lead to a larger structure, but improve the potential received power due to the λ^4 term in the 2-way power budget equation.

3.5.1 Effect of Varying Mechanically Modulated Antenna Ground Plane and Slot Size

Additional modeling of mechanically modulated slot antennas was performed to determine the role of the antenna ground plane and slot size in the antenna performance. First, the mechanically modulated slot antenna was modeled using FEKO method of moments software, and the far field magnitude (electric field strength) and phase were calculated.

Figure 70 shows the result over the range from 1 to 12 GHz. Plane wave excitation at boresight (incidence normal to the plane of the antenna) was modeled, and the far field values shown simulate measurement at boresight. The effect of the vibrating resonant arm, with its capacitive loading of the antenna, was included in the simulation.

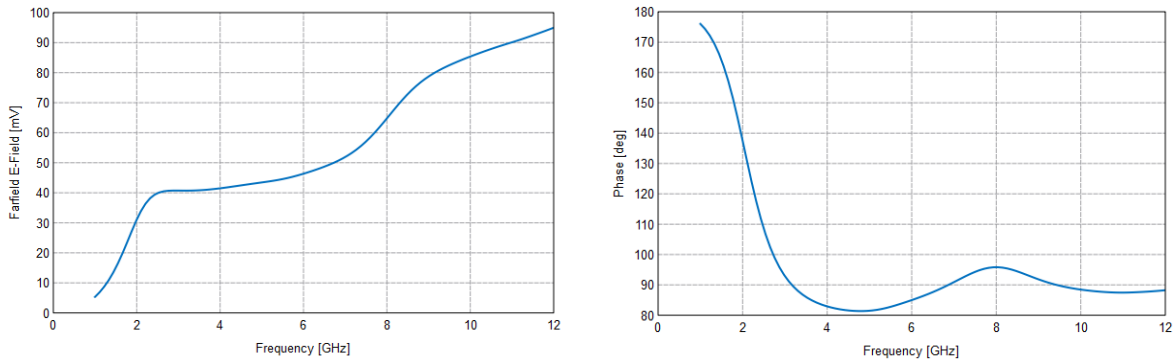

(a) (b)

Figure 70. Simulated far-field response at boresight of the mechanically modulated folded slot antenna, with plane wave excitation at boresight: (a) electric field strength, and (b) phase.

In the Figure 70 plots of the simulated response for the MMA slot antenna, no strong resonances associated with the slot can be seen, which had been found experimentally to resonate at approximately 11.1 GHz. The E-field strength, which gradually increases as frequency increases in the plot, is thought to result from reduced diffraction of incident waves as the frequency increases (and the wavelength decreases). At 2 GHz, the wavelength is 15 cm, and significant amounts of the incident wave will diffract and scatter from the edges of the antenna ground plane, which has dimensions of 5 cm x 5 cm. At a frequency of 6 GHz, the wavelength is 5 cm, so that the ground plane is exactly one wavelength long on each side. For frequencies above 6 GHz, the incident waves are shorter than the ground plane dimensions, and the waves are increasingly reflected as specular reflections. For specular reflections, the angle of reflection equals the angle of incidence, and more power is reflected back along the boresight instead of scattered from the edges of the ground plane.

Further models of folded slot antennas of different sizes with differing ground plane dimensions were also simulated using FEKO. Figure 71through Figure 73 show the simulated farfield response of a folded slot antenna with slot dimensions 68% larger than the first prototype MMA slot antenna simulated in Figure 70.

In Figure 71 an antenna with a square ground plane 6.35 mm long on each side was simulated. The blue curve represents the result for simulation of a ground plane with no slot or vibrating arm, the green curve represents the ground plane with a folded slot but no vibrating arm, and the red curve represents the ground plane with both the folded slot and the vibrating capacitive arm. The plots show the trend for the reflected E-field to increase in magnitude as frequency is increased. Also, the appearance of a resonance at approximately 7 GHz is noted as the slot is added. The frequency of the resonance decreases as the vibrating capacitive arm is added.

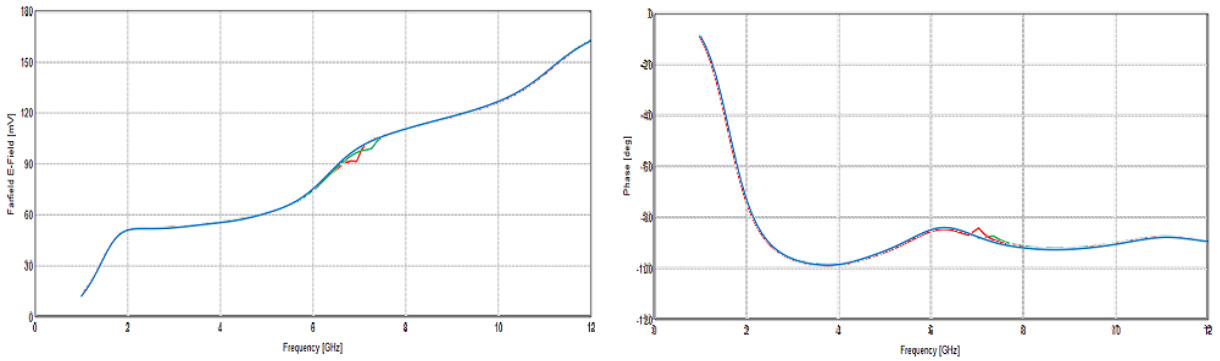

(a) (b)

Figure 71 Simulated far-field response at boresight of mechanically modulated folded slot antenna with slot scaled 68% larger than first prototype MMA antenna and with 6.35cm x 6.35cm ground plane, with plane wave excitation at boresight: (a) electric field strength, and (b) phase. The blue curve is for the ground plane alone, the green curve is for the ground plane with a slot and no vibrating arm, and the red is for the ground plane with a slot and a vibrating capacitive arm.

In Figure 72, the simulation is repeated with the same slot size (68% larger than the MMA antenna slot), but with a smaller 5 cm x 5 cm ground plane. It can be observed that the resonant frequency remains the same as seen in Figure 71, but the decrease in E-field strength is greater (Figure 72a). This larger dip in the E-field strength at resonance likely results from coupling of the RF power to the antenna slot at resonance. At frequencies away from resonance, the ground plane acts like a mirror, and the radio waves incident at boresight (0° elevation and 0° azimuth) are reflected back to the farfield along boresight. At resonance, though, the RF power is coupled to currents in the antenna, which are recoupled to outgoing radiating waves. The power in the radiating waves is distributed over a much wider angular spread than the specular reflections; therefore, the power of the radiated waves at resonance along boresight is lower than the specular reflections at frequencies off resonance.

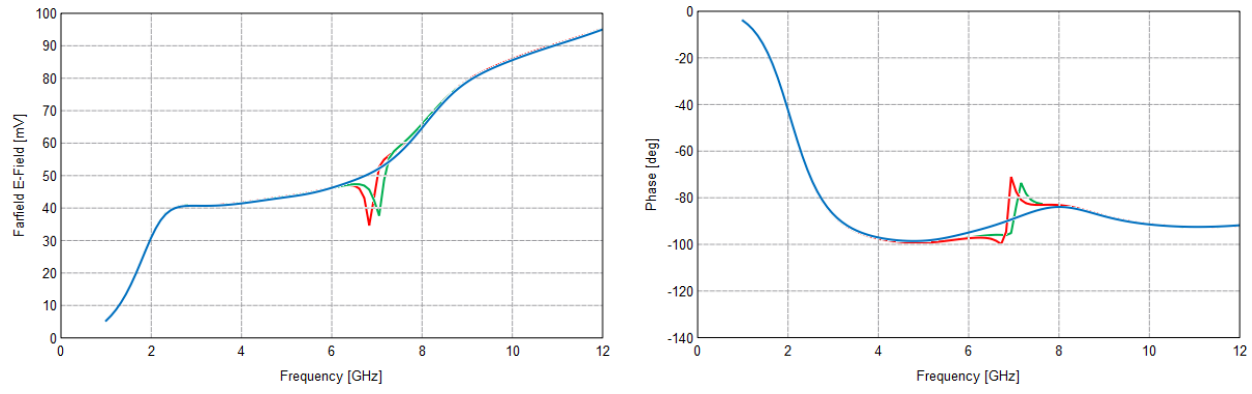

(a) (b)

Figure 72. Simulated far-field response at boresight of mechanically modulated folded slot antenna with slot scaled 68% larger than first prototype MMA antenna and with 5cm x 5cm ground plane, with plane wave excitation at boresight: (a) electric field strength, and (b) phase.

A phase response typical of resonance, in which the phase swing negative and then positive relative to the baseline, is also observed around 7 GHz, in Figure 72(b).

Similarly, Figure 73 shows plots of the simulated response of a slot antenna 68% larger than the MMA antenna, but with ground plane dimensions reduced to 4 cm x 4 cm. In Figure 73(a), only the curve for the antenna with slot and vibrating arm is plotted. Again, it can be observed that the slot resonance remains at 7 GHz. The phase plot in Figure 73(b) shows a strong phase response at resonance. So, for Figure 71 through Figure 73, the trend is that the phase response increases as the ground plane is made smaller.

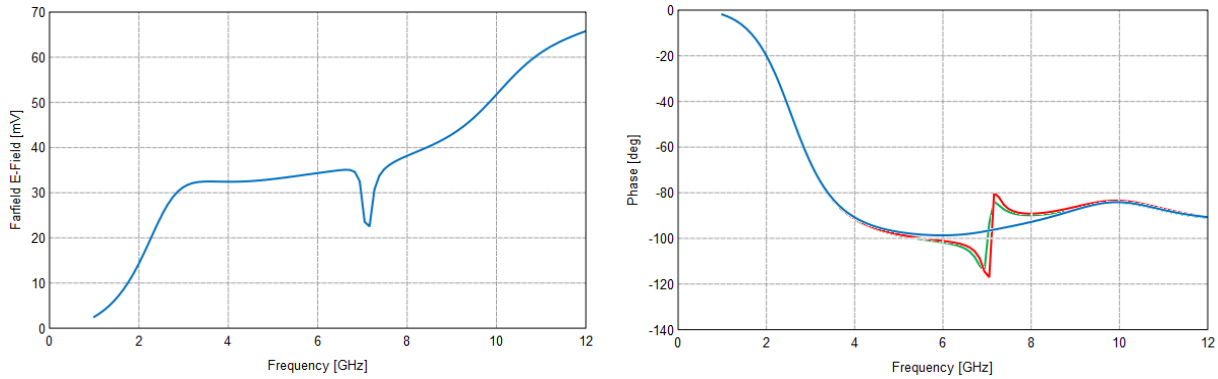

(a) (b)

Figure 73. Simulated far-field response at boresight of mechanically modulated folded slot antenna with slot scaled 68% larger than first prototype MMA antenna and with 4 cm x 4 cm ground plane, with plane wave excitation at boresight: (a) electric field strength, and (b) phase.

Figure 74 and Figure 75 are plots of a similar analysis, in which the size of the slot is fixed, but the ground plane is reduced in size. For both figures, the size of the slot was scaled to 20% larger than the slot in the original MMA antenna. Figure 74 shows the results obtained for the simulation where the ground plane was assumed to be 5 cm x 5cm. A small resonance can be observed at approximately 9.5 GHz.

When the size of the ground plane is reduced to 4 cm x 4 cm, both the magnitude of the dip in the E-field strength and the size of the phase response are seen to increase in Figure 75 while the resonant frequency remains at 9.5 GHz.

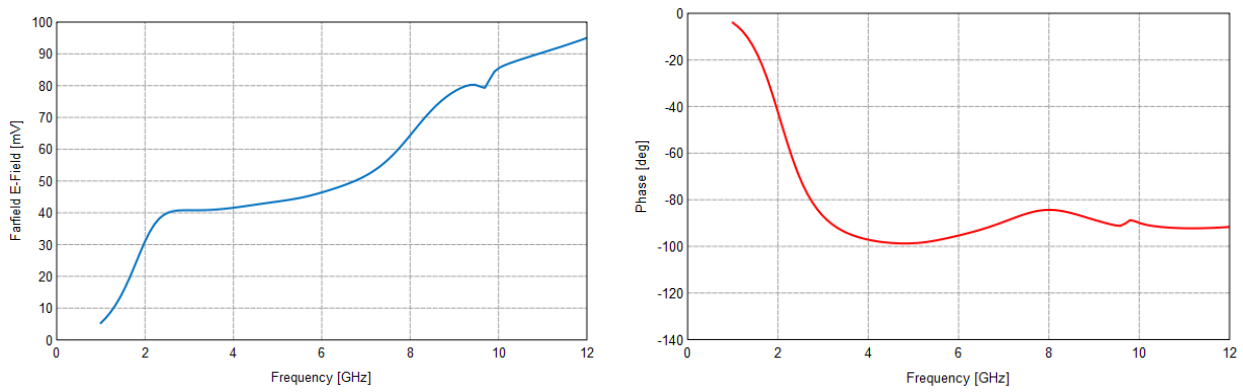

(a) (b)

Figure 74. Simulated far-field response at boresight of mechanically modulated folded slot antenna with slot scaled 20% larger than first prototype MMA antenna and with 5cm x 5cm ground plane, with plane wave excitation at boresight: (a) electric field strength, and (b) phase.

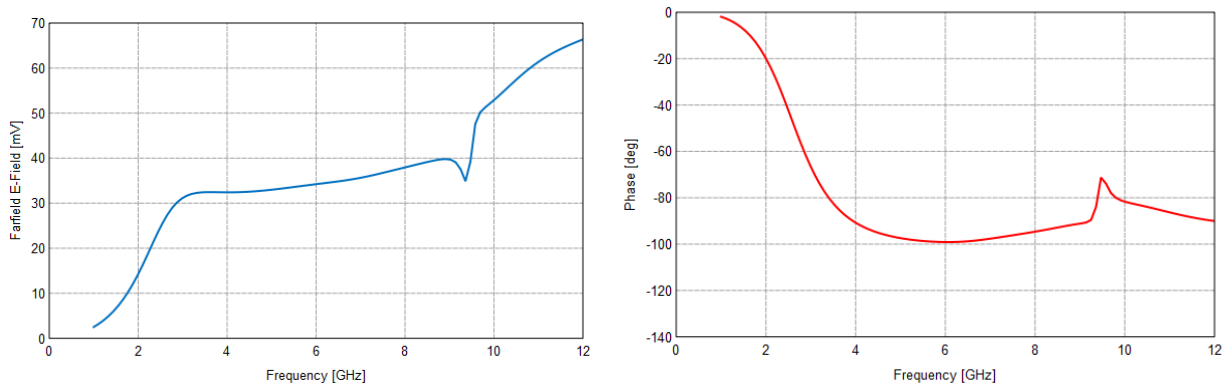

(a) (b)

Figure 75. Simulated far-field response at boresight of mechanically modulated folded slot antenna with slot scaled 20% larger than the first prototype MMA antenna and with 4 cm x 4cm ground plane, with plane wave excitation at boresight: (a) electric field strength, and (b) phase.

A simulation was also run to investigate the effect of a rectangular ground plane. Figure 76 shows the result for a folded slot antenna with a slot 20% larger than the original MMA antenna and with a 7 cm x 3.5 cm ground plane. The resonance is still located at about 9.5 GHz, but the resonance is slightly weaker than that seen in Figure 75. This suggests that the long side of the ground plane dominates the influence of the ground plane dimensions on the resonance.

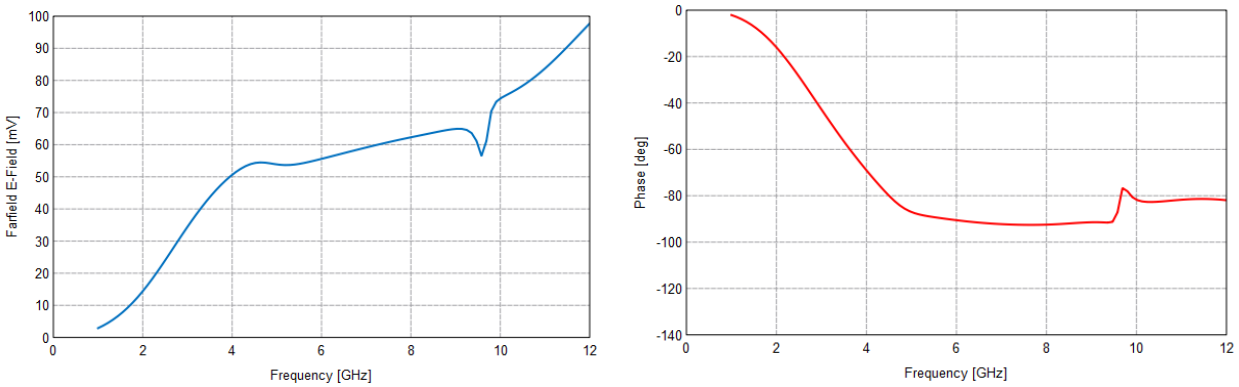

(a) (b)

Figure 76. Simulated far-field response at boresight of mechanically modulated folded slot antenna with slot scaled 20% larger than first prototype MMA antenna and with 7cm x 3.5cm ground plane, with plane wave excitation at boresight: (a) electric field strength, and (b) phase.

Another set of simulations was run and the results were plotted on the same graph to make the changes due to varying antenna parameters clearer. In these simulations, the slot size was scaled to be 32% larger than the size of the slot used for the MMA antenna. Figure 77(a) shows the simulated farfield E-field strength at boresight for several ground plane sizes. The color key for the various curves is displayed in Table 6.

Table 6. Color key for Figure 77.

Color	Ground Plane
orange	6 cm x 4 cm
light blue	6 cm x 2.5 cm
red	7 cm x 1.75 cm
dark blue	5 cm x 1.75 cm
green	4 cm x 1.75 cm
dark cyan	2 cm x 2 cm

The plot clearly shows the trend to higher E-field strength as the ground plane size is increased, which as explained earlier, is due to the specular reflections off the ground plane at frequencies off resonance. However, if the magnitude of the dip in E-field strength at resonance is normalized by dividing the magnitude by the value of the baseline just outside resonance, then the "normalized dip" in the E-field strength at resonance is larger for smaller ground planes (Table 6).

As Figure 77(b) illustrates, the phase response also increases as the ground plane dimensions decrease. If the phase response is defined as the difference between the minimum and maximum phase at frequencies near resonance, then the phase responses for the various ground plane sizes are tabulated in Table 7. Clearly, the phase response is increased for smaller ground planes. This suggests that a smaller ground plane is preferred for the mechanically modulated antenna in order to improve phase response.

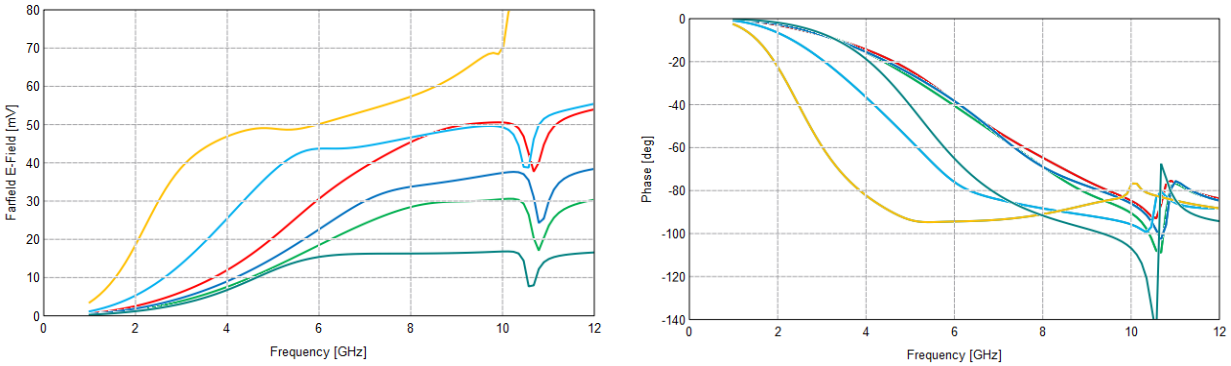

(a) (b)

Figure 77. Simulated far-field response at boresight of mechanically modulated folded slot antenna with slot scaled 20% larger than first prototype MMA antenna, for differing ground plane sizes:

green:	4 cm x 1.75 cm
dark blue:	5 cm x 1.75 cm
red:	7 cm x 1.75 cm
light blue:	6 cm x 2.5 cm
orange:	6 cm x 4 cm
dark cyan:	2 cm x 2 cm

Table 7. Normalized dip in E-field strength, calculated by dividing magnitude of decrease of E-field strength at resonance to baseline E-field strength off resonance, and phase response, calculated by the difference in maximum and minimum phase at resonance.

Color	Ground Plane	Normalized dip in E-field strength	Phase response (degrees)
orange	6 cm x 4 cm	0.03	6
light blue	6 cm x 2.5 cm	0.20	17
red	7 cm x 1.75 cm	0.24	15
dark blue	5 cm x 1.75 cm	0.32	26
green	4 cm x 1.75 cm	0.40	31
dark cyan	2 cm x 2 cm	0.56	67

3.5.2 CALCULATION OF REFLECTED FIELD OFF BORESIGHT

The numerical simulations described in Section 3.5.1 determined the electric field intensity and phase of the reflected field along boresight (perpendicular to the antenna ground plane). Additional simulations were performed to investigate the scattered field off boresight. To accomplish this, slot antennas were simulated with incident waves modeled as being oriented at boresight (incident wave direction normal to the ground plane). The resulting distribution of current in the slot antenna was determined, and the electric field strength and phase response for scattered waves 30° off boresight were calculated. By calculating the response at an angle different from boresight, the influence of specular reflections from the incident waves was eliminated.

In these simulations, the dimensions of the antenna slot were assumed to be fixed, and the ground plane size was varied. Three ground plane sizes were evaluated: 2 cm x 2 cm, 3 cm x 3 cm, and 4 cm by 4 cm. Figure 78 shows the distribution of currents induced in the ground planes by the incident radio waves. The surface current plots do not suggest much of an interaction with the ground plane, though the distribution seems to change as the size changes.

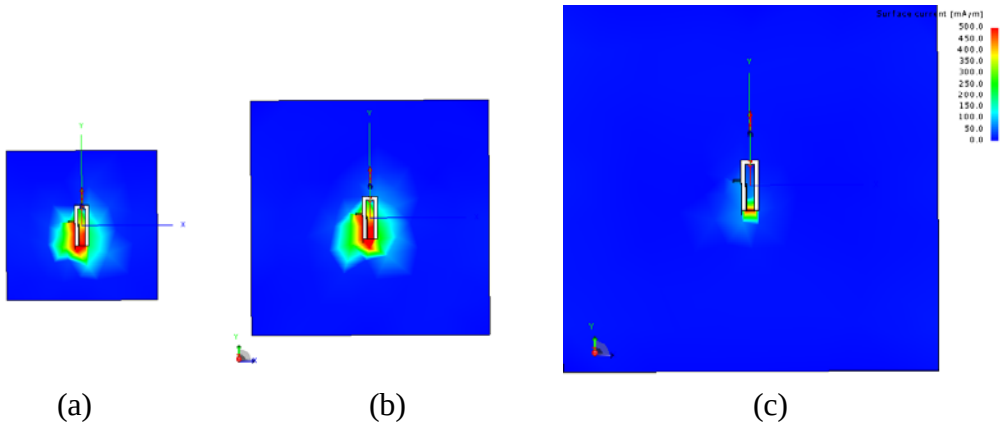

Figure 78. Simulations of electric current distributions in folded slot antenna, for three ground plane sizes (not to scale): (a) 2 x 2 cm, (b) 3 x 3 cm, (c) 4 cm x 4 cm

Figure 79 is a plot of the far field electric field intensity for the three folded slot antennas with ground planes of different sizes. In this simulation, the incident wave was modeled to be oriented at boresight (normal incidence with respect to ground plane), and the farfield was calculated at a point one meter away and 30° off of boresight. The results illustrated support the conclusions obtained in Section 3.5.1that larger ground planes result in a higher scattered E field strength, even off boresight.

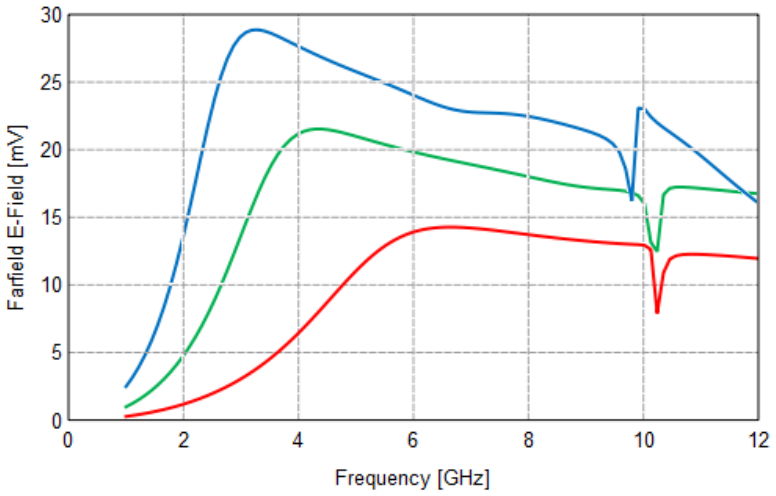

Figure 79. Total electric field of magnitude for three folded slot antennas with differing ground plane sizes: 4 cm x 4 cm (blue trace), 3 cm x 3 cm (green), and 2 cm x 2 cm (red).

The resonance due to the slot can be seen around 10 GHz. The plot illustrates that the frequency of the slot resonance shifts to lower frequencies as the ground plane size is increased. In addition, the overall field strength increases with the size of the ground plane. The cause of this was determined to be the ground plane alone by modeling the response of different sized ground planes without slots (Figure 80).

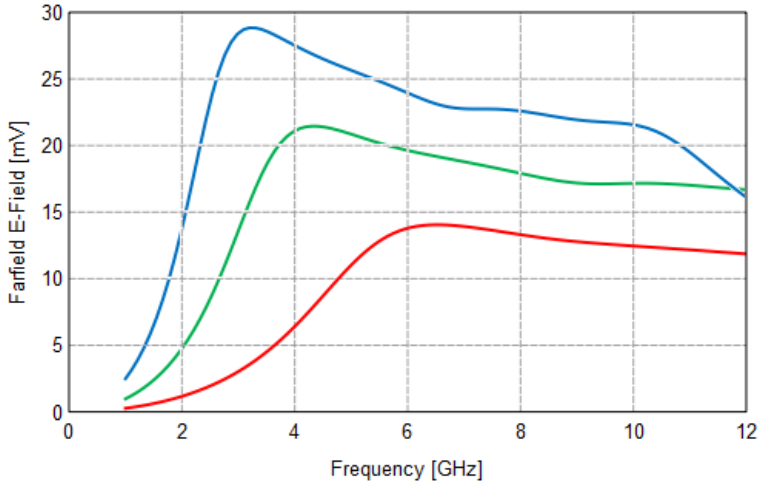

Figure 80. Total electric field of magnitude for three ground planes with differing sizes: 4 cm x 4 cm (blue trace), 3 cm x 3 cm (green), and 2 cm x 2 cm (red).

Figure 80 shows a broad peak for each ground plane, which varies from 3.2 GHz for the 4 cm by 4 cm ground plane, to 6.3 GHz for the 2 cm x 2 cm plane. These peaks appear to be due to the resonance of the ground plane alone. A simple calculation for a 4 cm x 4 cm square indicates that it will support a half wave resonance at 3.75 GHz, which is close to that shown in

Figure 80. Also, the strong resonance around 10 GHz in Figure 79 is absent in Figure 80 when the slot is removed, showing that the 10 GHz resonance results from the slot.

The slope of the electric field plot in Figure 79 and Figure 80 as it varies with frequency is seen to be negative in the frequency range between the ground plane resonance and the slot resonance. This slope is due to the fact that the electric field intensity is sampled at a 30° offset from boresight. At low frequencies, the ground plane acts as an antenna with a very broad pattern. As frequency increases, the pattern becomes more like a pencil beam (at boresight). This effect can be seen clearly by considering Figure 81, where FEKO software has been used to render a 3-D surface illustrating the antenna pattern resulting from scattering of microwaves at three frequencies from a 5 cm x 5 cm copper ground plane. At lower frequencies, the pattern is seen to be broad, and more directed and specular at higher frequencies.

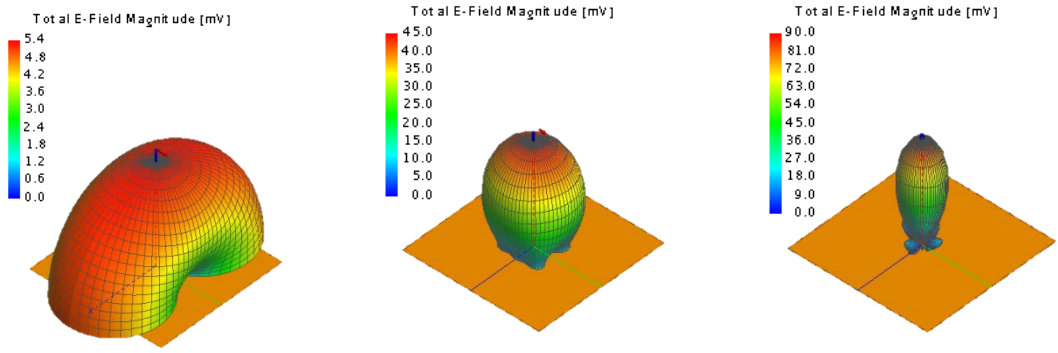

(a) (b) (c)

Figure 81. Electric field intensity 3D plots for scattering from 5 cm x 5 cm ground planes for three frequencies: (a) 1.0 GHz, (b) 5.07 GHz, and (c) 10.02 GHz.

Figure 82 plots the simulated phase response for the three slot antennas with differing ground plane sizes. The simulation generated this plot assumed boresight incidence of the radio wave, and the phase was sampled at a point 30° off boresight. The phase excursions typical of resonances are clearly seen around 10 GHz. The phase response increases as the ground plane size is decreased, which is consistent with results described in Section 3.5.1.

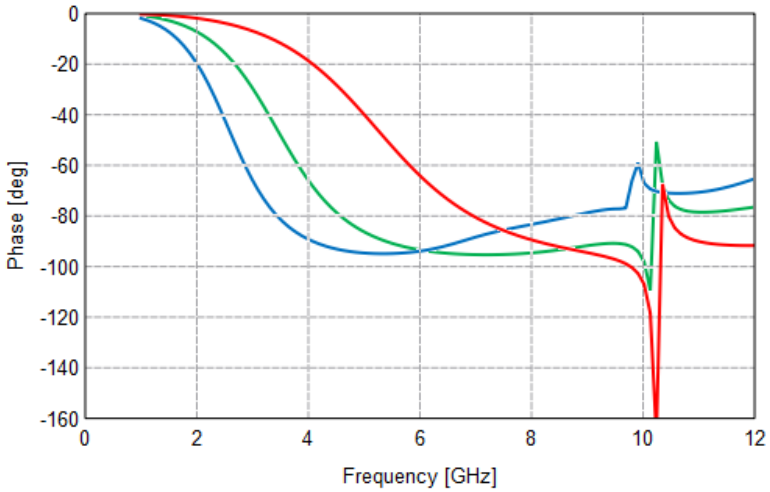

Figure 82. Plot of phase variation for three folded slot antennas with differing ground plane sizes: 4 cm x 4 cm (blue trace), 3 cm x 3 cm (green), and 2 cm x 2 cm (red).

3.5.3 Effect of Ground Plane Motion on Antenna Phase Response

The effect of out-of-plane motion of the antenna ground plane on the phase response of the mechanically modulated antenna was investigated. The response of the antenna to this motion, shown as z- displacement in Figure 83, was modeled using FEKO method-of moments software. In the figure, the reference planes are indicated at the origin, and the ground plane and U-slot with capacitance sensor are centered at (0X, 0Y, 0Z). The plane wave excitation is directed in the (0,0,-Z) direction, coming from 'above' the sensor. The ground plane is assumed to be 3 cm x 3 cm.

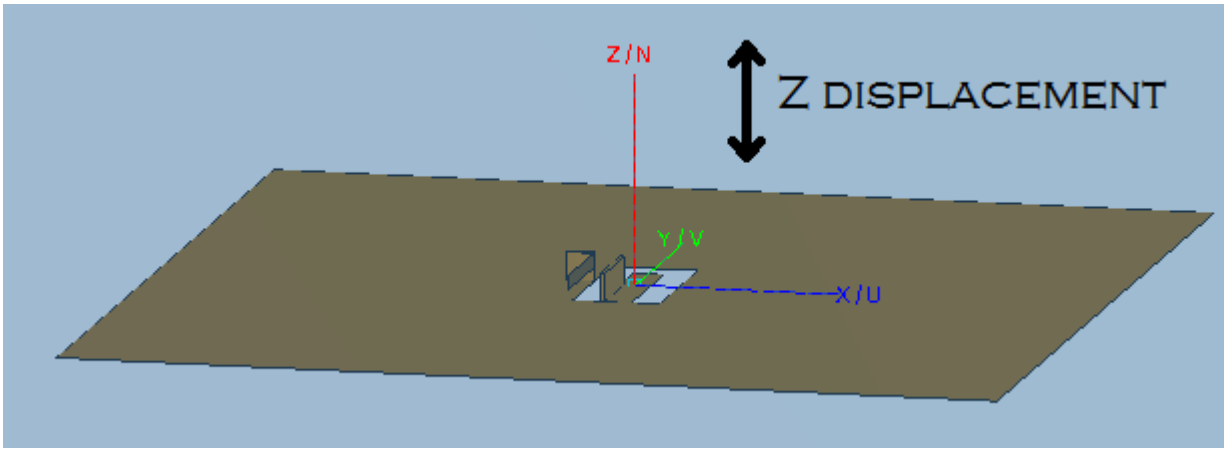

Figure 83. 3-dimensional image of the U-slot with capacitive arms and X, Y, Z reference unit vectors

The phase response of the simulated antenna in its rest position is shown in Figure 84.

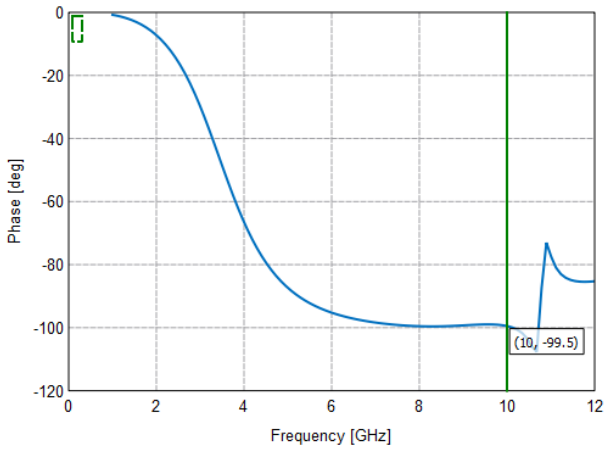

Figure 84. Phase response vs. frequency, antenna at rest position (0x, 0y, 0z).

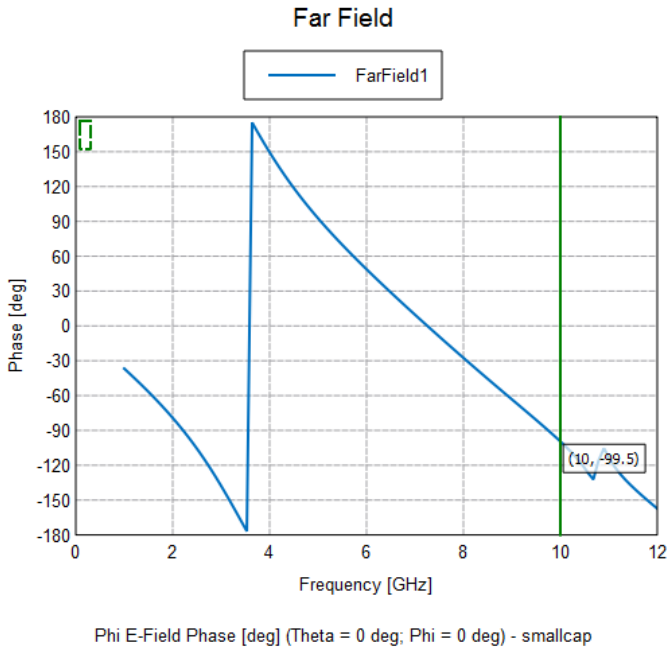

Figure 85. Phase response vs. Frequency, 3x3 cm ground plane with capacitance, (0 X, 0 Y, +lambda Z), 10 GHz frequency

The wavelength of a 10 GHz electromagnetic wave is 3e8/10e9 = 0.03m. In Figure 3, the phase is -99.5° at 10 GHz, equal to the phase measured at 10GHz in Figure 2. The single vertical blue line in the phase response denotes a change from +180° to -180°. With one wavelength distance displacement, the phase response has 360° change. Various displacements and excitation angles were tested to demonstrate the possible change of phase that would occur during combustion chamber use, shown in Table 8.

Table 8. Values of Displacement and Angle vs. Phase

Displacement (Z direction)	Angle of Incidence	-10°	-5°	0°	+5°	+10°
+0.001m		-106.0°	-107.0°	-107.0°	-107.0°	-106.0°
+0.0001m		-95.4°	-96.0°	-96.2°	-95.9°	-95.2°
+0.00001m		-94.3°	-94.9°	-95.1°	-94.8°	-94.1°
0.0m		-94.2°	-94.8°	-95.0°	-94.7°	-94.0°
-0.00001m		-93.9°	-94.6°	-94.8°	-94.5°	-93.7°
-0.0001m		-91.8°	-92.4°	-92.6°	-92.3°	-91.6°
-0.001m		-70.4°	-70.9°	-71°	-70.7°	-70.1°

The results in Table 8 show up to 36 degrees in phase change, but involving extreme movement of the sensor. If the sensor were twisted 10° along the Y-axis shown in Figure 83 and displaced +/- 1mm in the Z direction, 36 degrees of phase change could occur. However, with only +/- 100um of displacement in the Z direction, a maximum of 1.4° of phase change would occur. The phase change due to displacement is directly proportional to the wavelength of the RF involved in the sensing system, so a small displacement results in minimal effect on the resultant signal.

3.6 Computational Electromagnetics Model of Mechanically Modulated Dipole Antenna

During initial laboratory testing of the first prototype MMA sensor, the difference between amplitude and phase from the reflection of the sensor was not significant enough to determine if phase or amplitude modulation would be more efficient. Therefore, a decision was made to investigate a mechanically modulated dipole antenna that would allow for a larger difference between amplitude and phase of the received signal in order to determine the dominant effect in the signal modulation. In addition, it was decided to minimize the use of a reflecting plate (ground plane) in the new design, in order to reduce the strength of the reflection from the reflecting plate. During experimental measurements of the prototype MMA sensor, the reflected signal from the ground plane was several orders of magnitude stronger than the modulated signal from the resonating arm, though the modulated signal was still resolvable with a Doppler measurement.

Towards this end, a dipole antenna with acoustically resonant arms attached to it was analyzed using FEKO. A dipole would allow the reflected signal to be modulated by the vibrating arms, with the arms tuning the antenna due to the resonant motion. The dipole would also allow the sensor to have an almost omni-directional pattern allowing for the receive system to be located at angles that are not at bore sight (direction of the antenna beam) with the antenna. The structure for the conceptual sensor is shown in Figure 86.

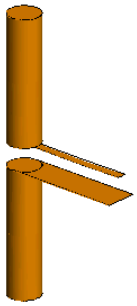

Figure 86. Dipole sensor structure.

The sensor is a dipole with a tuning stub that works together to produce half-wave length dipole characteristics. In the antenna that was simulated, the dipole has a height of 1.102 cm and the stub tuner (vibrating beam) is 0.468 cm in length. The bottom stub element is a fixed (non-vibrating) piece of metal and the smaller arm connected on top is the resonating arm that will vibrate due to acoustic excitation. The stub separation is 0.937 mm, providing a gap to allow the resonant arm to swing. The length and separation of the stub elements were adjustable parameters in the simulation. One of the requirements for the sensor was that it should operate in the range of 10 – 20 GHz, a specification met by this design. Using FEKO electromagnetic simulation software to simulate the antenna properties, the sensor's resonant frequency was found to be near 15 GHz. The antenna far field patterns predicted by the software are seen in Figure 87 through Figure 89. The sensor beam pattern is almost omni-directional but has some spots that are weaker than others.

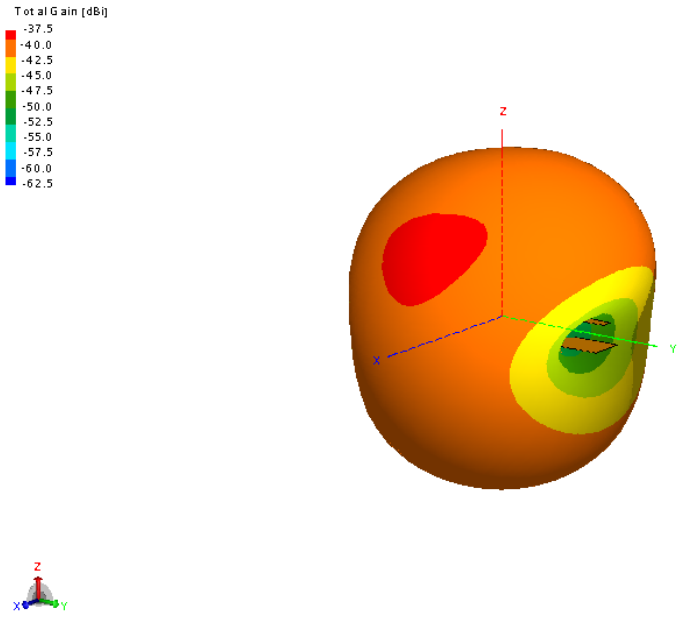

Figure 87. 3D far field pattern for the sensor viewed at the same direction as figure 1. The colors on the pattern are an indication of intensity with red being the highest and green being the lowest level.

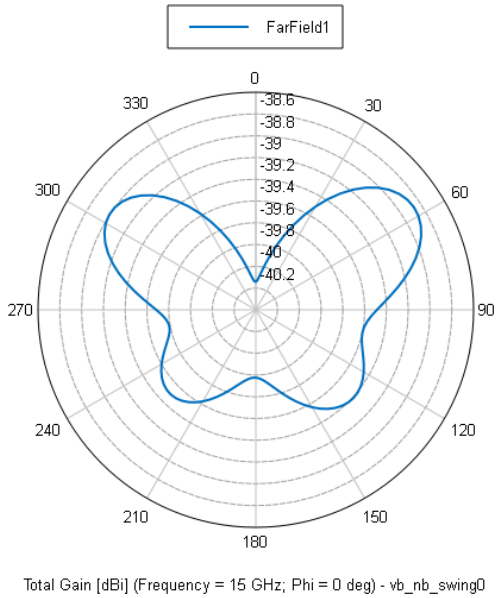

Figure 88. Polar plot of the same pattern as in Figure 68. This is viewed looking at the antenna length wise and arms in the direction of the viewer.

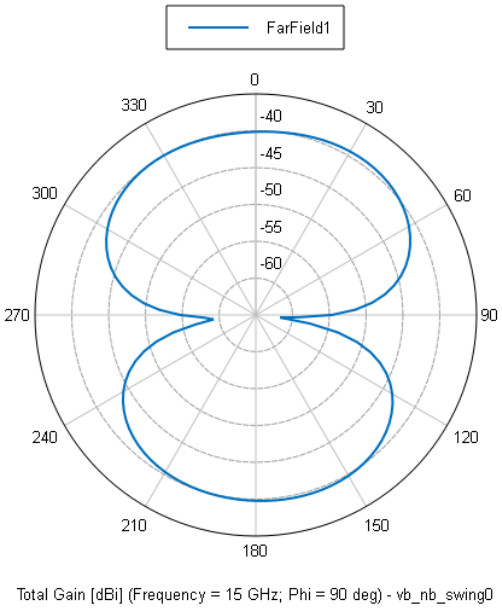

Figure 89. Polar plot of the same pattern as Figure 68. This is viewed looking from above the sensor with the arms at 90 degrees.

For this simulation, the excitation antenna was located looking broadside to the dipole with the arms completely extended to one side of the antenna. Instead of a plane wave for excitation, a horn antenna was used with a 15 dBi gain with an output of 2 W. In this simulation, a probe wire was not used on the sensor to measure antenna currents, since it would change the antenna characteristics. Therefore, all data came from the simulated receive antenna, which is the

same 15 dBi horn that is used for excitation. The outcomes from the simulations are shown in Table 9 and Figure 90, Figure 91, and Figure 92.

Table 9. Table of coupling and phase factors for the receive antenna. The overall change in the receive phase and amplitude can be seen in the last row.

swing (mm)	Magnitude (W)	Magnitude (dBW)	Phase (deg)
-0.5	1.76E-08	-77.55	21.97
-0.4	1.83E-08	-77.38	19.59
-0.3	1.89E-08	-77.25	17.40
-0.2	1.93E-08	-77.13	15.41
-0.1	1.98E-08	-77.04	13.58
0	1.99E-08	-77.02	12.61
0.1	1.99E-08	-77.00	11.57
0.2	2.02E-08	-76.94	10.15
0.3	2.04E-08	-76.90	8.94
0.4	2.07E-08	-76.85	7.66
0.5	2.09E-08	-76.80	6.42
	overall change:	0.75	15.55

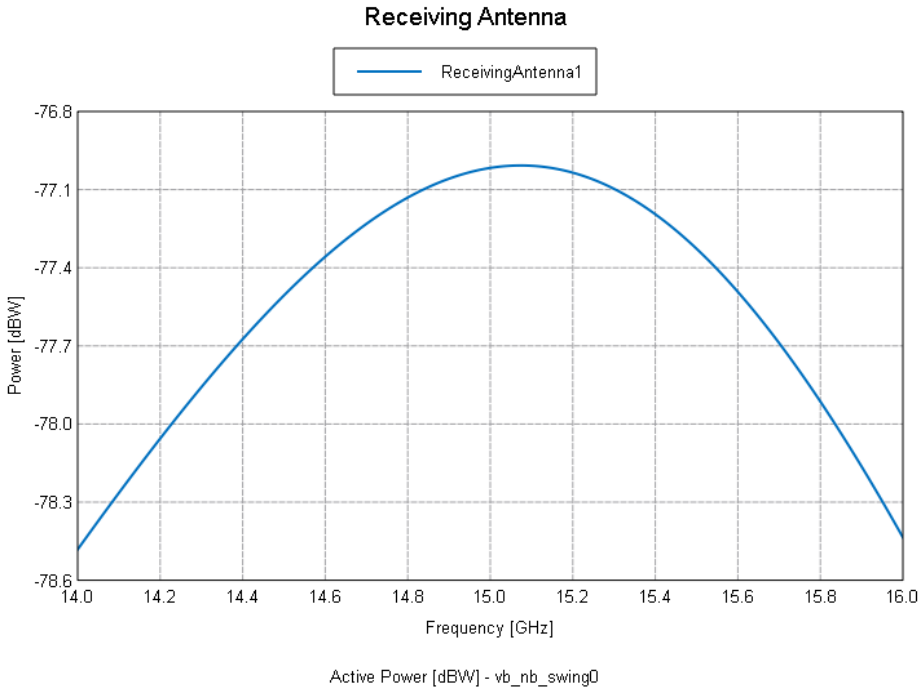

Figure 90. Frequency sweep from 14 to 16 GHz when the tuning stud is vibrating.

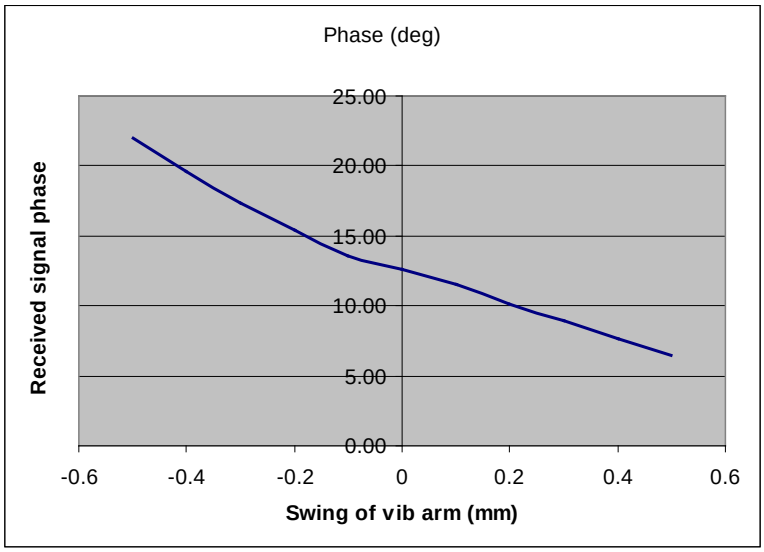

Figure 91. Graph of the phase change as the resonant arm vibrates.

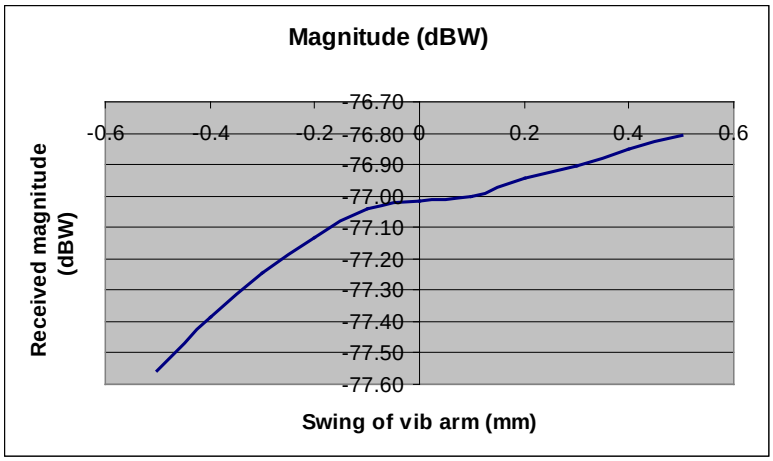

Figure 92. Graph of the amplitude change as the resonant arm vibrates.

The results from the simulation show that the sensor is predominately phase modulated and that the response is somewhat linear. The results also indicated that the simulated receive signal would exhibit low signal strength. This low receive signal is due to the small radar cross section of the sensor. However, if one were to add a reflecting plate behind the sensor, a pattern effect is created of two dipoles and there would also be a detuning of the dipole, shifting the resonant frequency.

3.6.1 *Study of Effect of Vibrating Arm*

An analysis of the effect of rotating the vibrating arms of the mechanically modulated dipole antenna was performed. In this analysis, the vibrating tuning arms were twisted 90°, as shown in Figure 93 and Figure 94. The analysis, performed using FEKO software, assumed that the vibrating arm is excited by a 15 dBi horn outputting 0.1 W at 15.15GHz. The predicted far field pattern is shown in Figure 95.

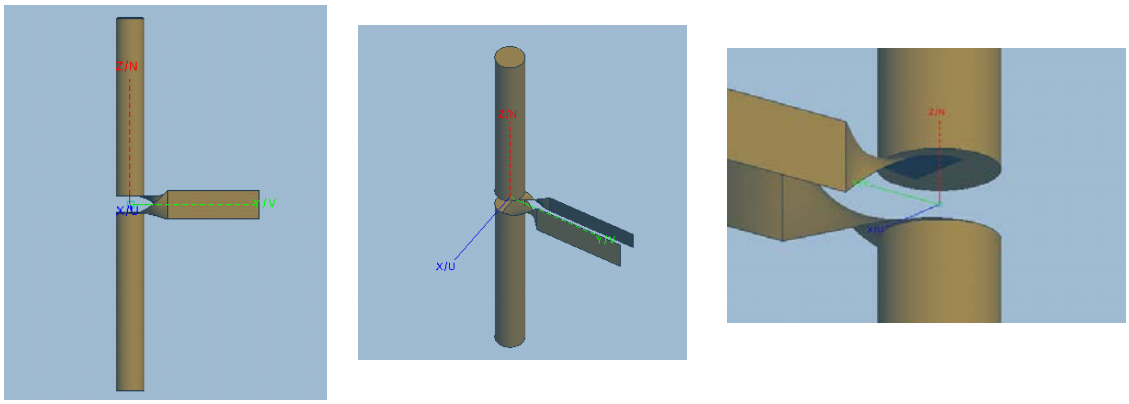

Figure 93. 3D sensor simulation model, 90° rotated capacitive tuning arms.

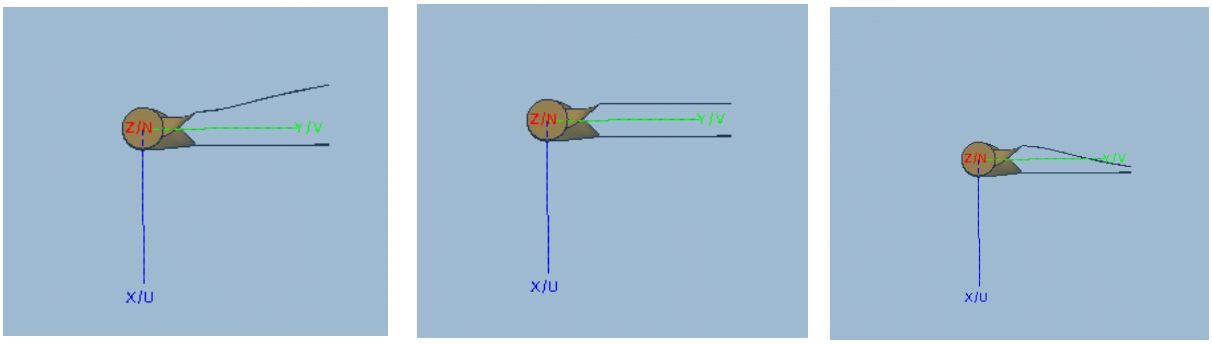

(a) (b) (c)

Figure 94. 3D sensor simulation model of the acoustically modulated flex arm.
(a) +0.5mm swing position (b) zero displacement (c) -0.5mm swing position

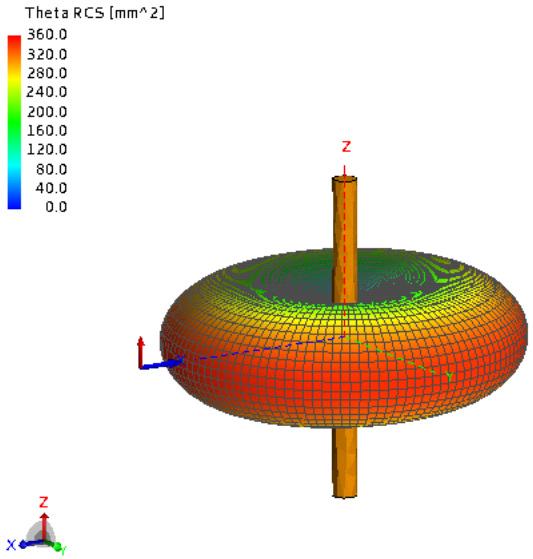

Figure 95. 3D far field pattern of February sensor concept.

This pattern is more azimuthally uniform than the far field pattern predicted in the simulation described in Section 3.6 for the dipole with vibrating arms that are not twisted. This will allow for more freedom in receiver placement. Figure 96 and Figure 97 show the frequency dependent radar cross-section (RCS) for the dipole antenna with the twisted arms and the straight arms, respectively. The RCS is plotted for three cases of vibrating arm tip displacement (-500 µm, 0 µm, and +500 µm) for both antennas. The frequency at which the RCS peaks is the frequency at which the antenna resonates electrically for the given tip displacement.

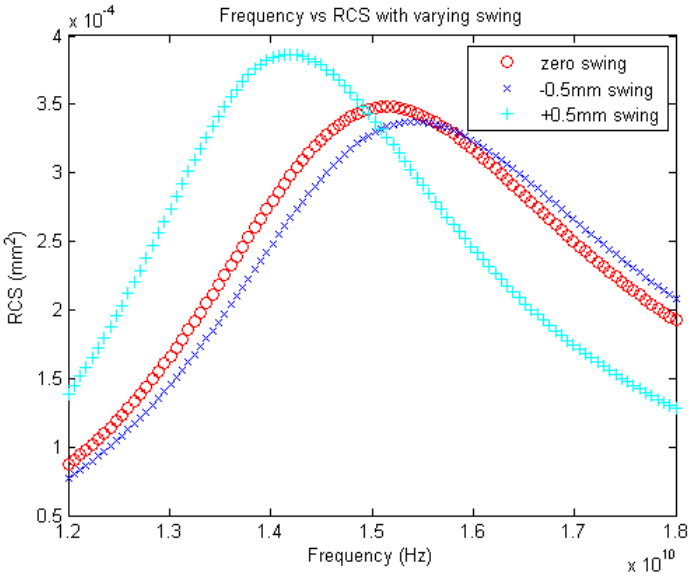

Figure 96. Plot of radar cross-section (RCS) for varying frequencies for dipole with twisted vibrating arms. The three traces represent the displacement of the tip of the vibrating arm.

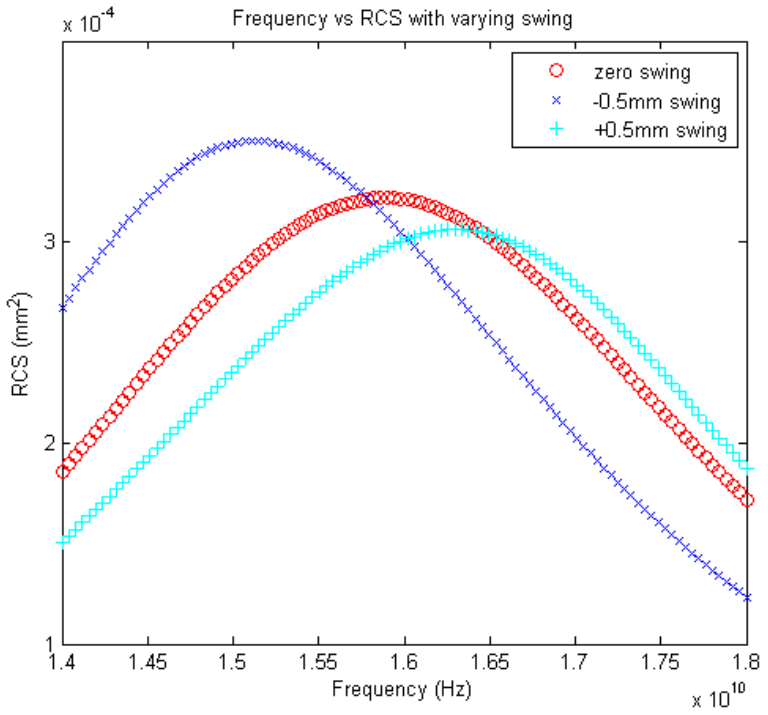

Figure 97. Plot of radar cross-section (RCS) for varying frequencies for dipole with straight (not twisted) vibrating arms. The three traces represent the displacement of the tip of the vibrating arm.

The antennas' electrical resonant frequency varies by more than 1 GHz in both dipole antenna designs. Table 10, Table 11, Figure 98, and Figure 99 show the phase and magnitude response of the received signals for both sensor concepts.

Table 10. Predicted received signals strength and phase for dipole with twisted arms.

swing (mm)	Magnitude (W)	Magnitude (dBW)	Phase (deg)
-0.5	1.41E-11	-108.51	152.70
-0.4	1.60E-11	-107.96	151.60
-0.3	1.77E-11	-107.52	150.10
-0.2	1.94E-11	-107.12	149.70
-0.1	2.10E-11	-106.78	148.70
0	2.26E-11	-106.46	147.70
0.1	2.44E-11	-106.13	146.80
0.2	2.58E-11	-105.88	145.90
0.3	2.74E-11	-105.62	144.90
0.4	2.85E-11	-105.45	144.10
0.5	3.07E-11	-105.13	143.00
	Overall change	3.38	9.70

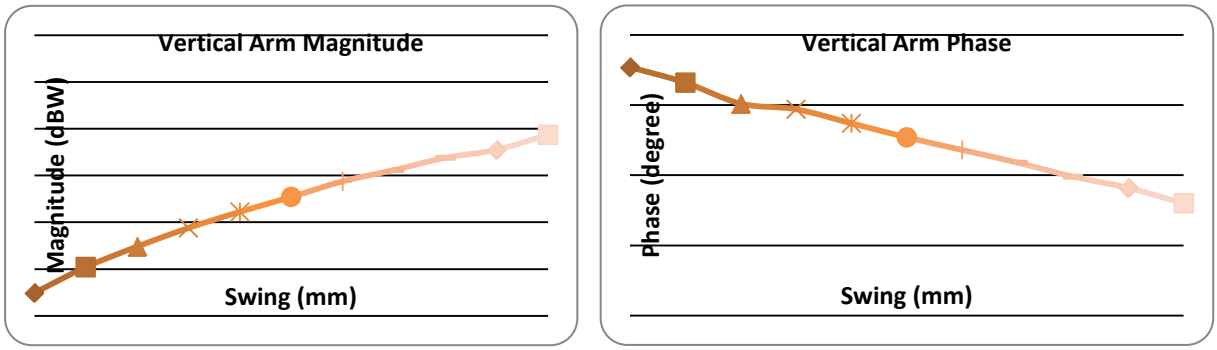

Figure 98. Response of the twisted arm dipole antenna for varying arm tip displacement.

Table 11. Response of the straight (untwisted) arm dipole antenna for varying arm tip displacement.

swing (mm)	Magnitude (W)	Magnitude (dBW)	Phase (deg)
-0.5	2.43E-10	-96.14	133.40
-0.4	2.50E-10	-96.02	131.10
-0.3	2.56E-10	-95.92	128.90
-0.2	2.61E-10	-95.83	127.00
-0.1	2.64E-10	-95.78	125.4
0	2.65E-10	-95.77	124.30
0.1	2.64E-10	-95.78	123.6
0.2	2.66E-10	-95.75	122.2
0.3	2.68E-10	-95.72	121.00
0.4	2.69E-10	-95.70	119.80
0.5	2.71E-10	-95.67	118.80
	overall change	0.47	14.60

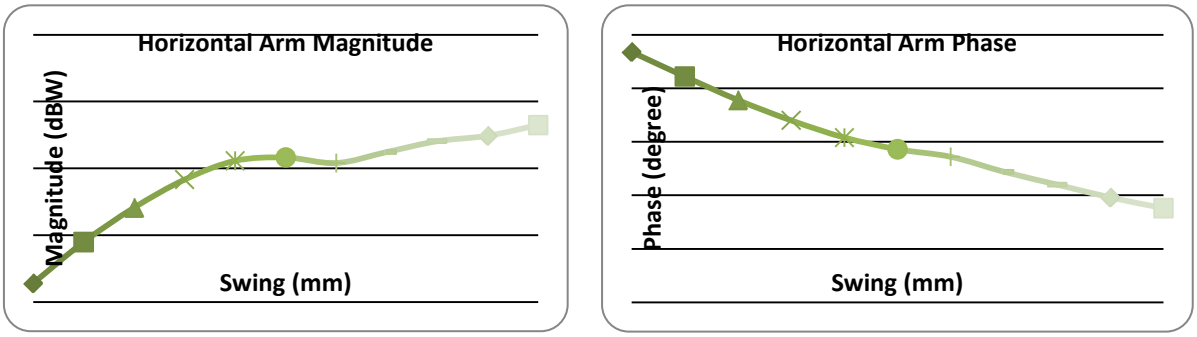

Figure 99. Response of the straight (untwisted) arm dipole antenna for varying arm tip displacement.

These results show the phase response for both twisted and straight dipole antennas are fairly linear. However, while the change in magnitude of the dipole antenna with straight arms was relatively unchanged (0.47 dBW) from one extreme of the beam tip displacement to the other extreme (±500 µm), the antenna with twisted arms demonstrates a change in magnitude of 3.38 dBW.

3.6.2 Study of The Effect of Directors on Antenna Performance

A study was conducted to investigate the effect on performance of the mechanically modulated dipole of adding one or more directors to the antenna. A director is a parasitic element (no electrical connection to signal) used as a lens to focus incoming radio waves onto the dipole antenna. Directors are most commonly used in Yagi-Uda antennas, which are dipole antennas with a reflector and one or more directors added.

The theory behind adding a director is relatively simple. The director mutually couples with the excited dipole and constructively adds in phase with the dipole in the direction the director is displaced in relation to the dipole. A single dipole is shown in 3D and a plot of the gain is shown in the polar coordinate system in Figure 100. It can be seen that the gain of the dipole in dB in the 0° Phi (+x direction of the 3D plot) is 2.13 dBi.

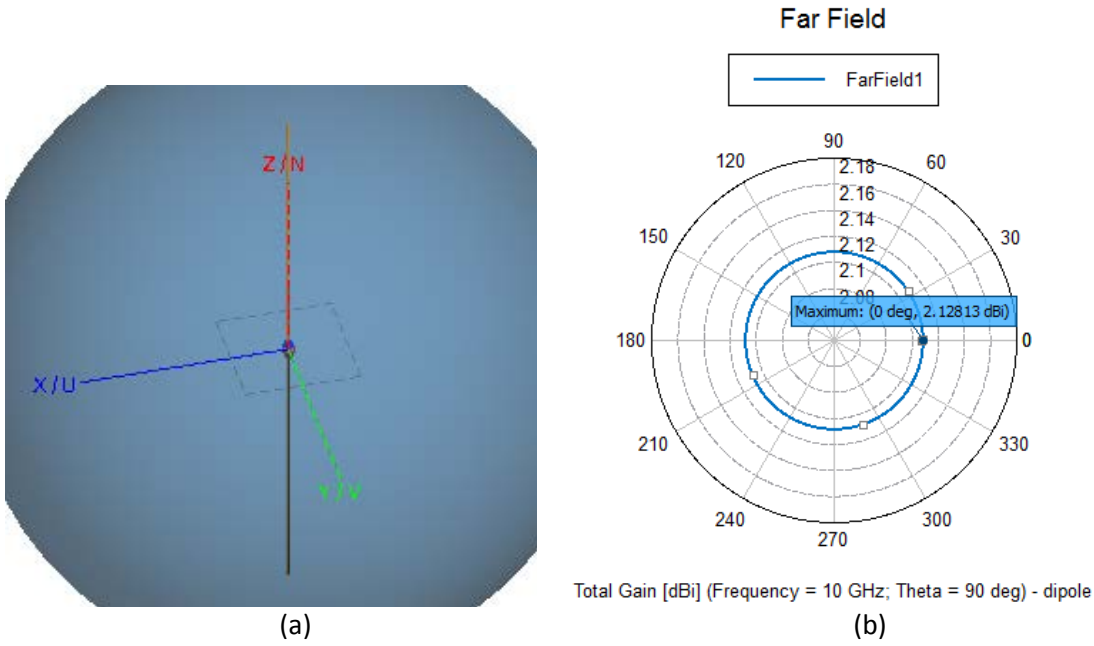

Figure 100. (a) Single dipole excited in the middle in 3D (b) gain of the dipole in a polar graph [X-Y plane]

A single director will change add directivity in the direction the director is displaced in relation to the dipole, shown in Figure 101. The gain in the 0° phi (+x direction) is 3.77 dBi.

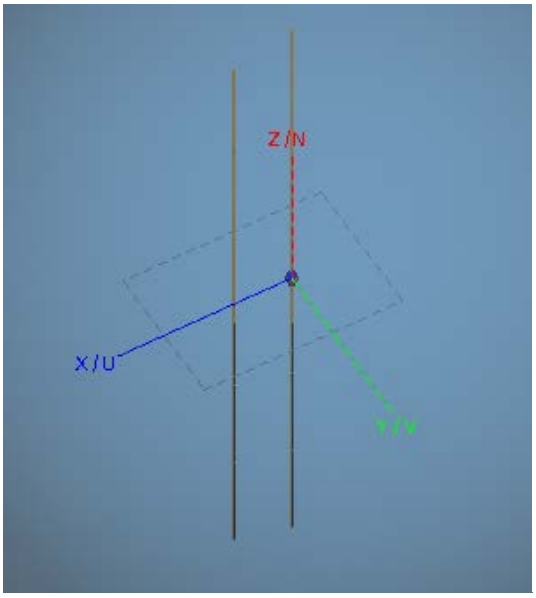

(a)

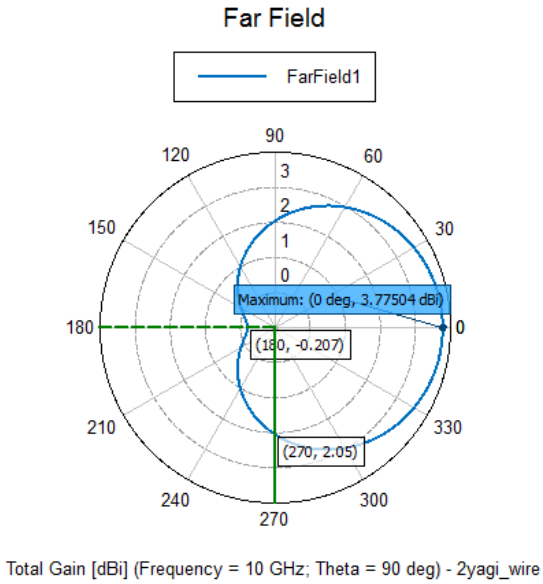

(b)

Figure 101. (a) Dipole with a single director in 3D (b) Gain of the dipole/director in a polar graph [X-Y plane]

It is also worth noting that the gain in the 180° phi direction (-x direction) is -0.207 dBi, and the gain in the 270° phi direction (-y direction) is 2.05 dBi.

The addition of a second director was also examined, placing the two directors in a specific way (one at a +x, -y, 0 position and one at a +x, +y, 0 position in Cartesian coordinate system). This can be seen in Figure 102.

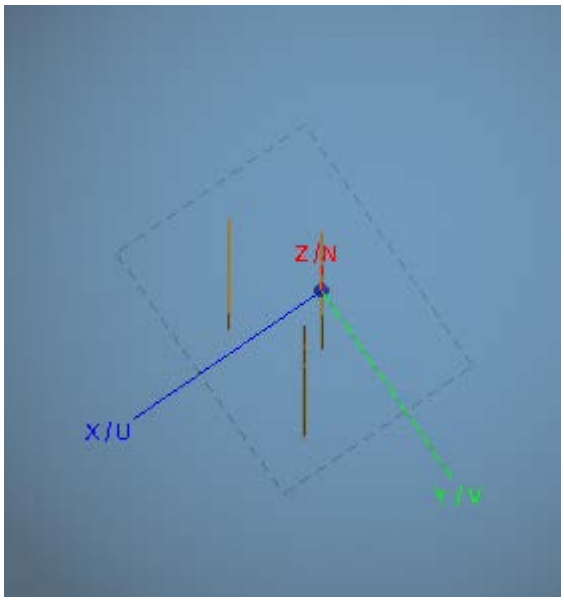

(a)

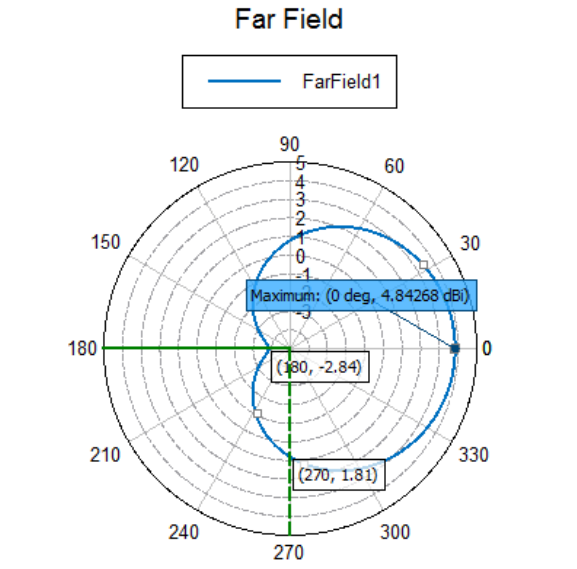

(b)

Figure 102. (a) Dipole with two directors in 3D (b) Gain of the dipole/directors in a polar graph [X-Y plane]

In Figure 102, the 0° phi gain is 4.84 dBi, the 180° phi gain is -2.84 dBi, and the 270° phi gain is 1.81 dBi. This design with two directors appears attractive because it directs the most energy back toward the Doppler radar interrogator. It also has only a 0.2 dBi difference in the 270° direction and a ~2.5dBi difference in the 180° direction, which is beneficial because the directivity in the entire +x direction (from 90° to 0° to -90°) is somewhat maximized. This would allow for different positions of the Doppler radar interrogator and allow for unintentional rotations of the dipole caused by vibration.

The performance of the dipole antenna with one, two, and no directors was simulated using FEKO software. The meshing used to analyze the antenna with a single director is illustrated in Figure 103.

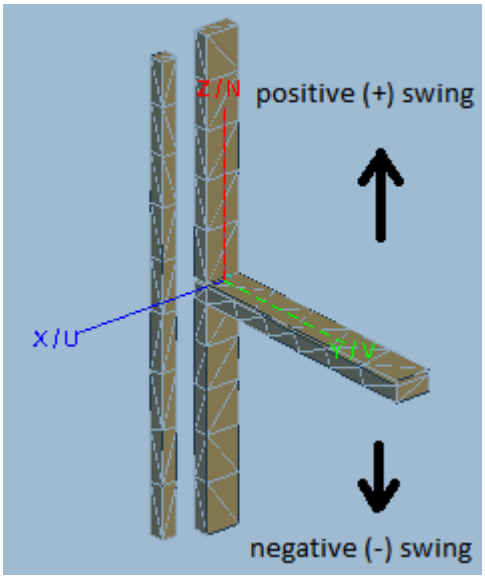

Figure 103. Graphic of meshing used to analyze the dipole with a single director and tuning stub in the positive Y-direction. In the analysis, the TX/RX Doppler radar was placed in the positive X direction.

For comparison, simulations were run with no director. The results, tabulated in Table 12 and plotted in Figure 104 yield a 3.0° phase change and 0.09 dB of magnitude change over 100 microns of “swing” from the vibrating stub. The phase change is very nearly linear.

Table 12. Tabulated performance of dipole with no director for varying vibrating arm tip displacement.

No Director

swing (mm)	Magnitude (W)	Magnitude (dBW)	Phase (deg)
-0.05	2.30E-08	-76.38	93.60
-0.04	2.30E-08	-76.38	93.30
-0.03	2.31E-08	-76.36	93.00
-0.02	2.32E-08	-76.35	92.70
-0.01	2.33E-08	-76.33	92.4
0	2.33E-08	-76.33	92.20
0.01	2.34E-08	-76.31	91.8
0.02	2.34E-08	-76.31	91.5
0.03	2.35E-08	-76.29	91.20
0.04	2.35E-08	-76.29	90.9
0.05	2.35E-08	-76.29	90.60
	overall change	**0.09**	**3.00**

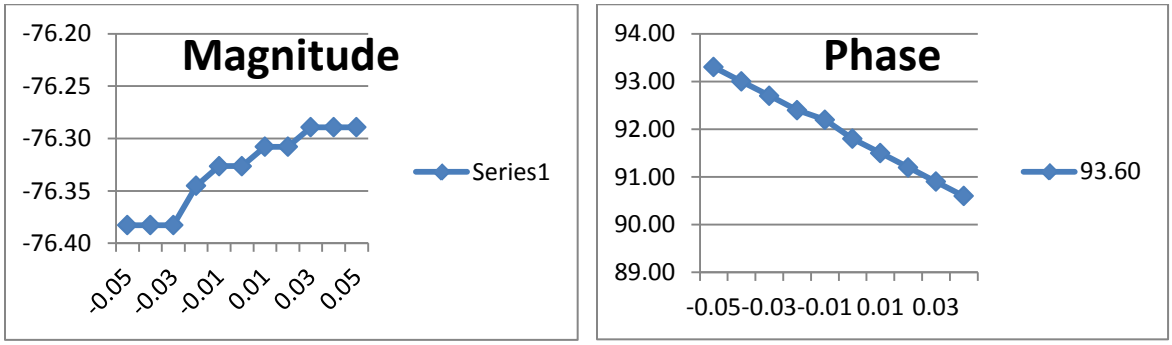

Figure 104. Magnitude and phase of dipole with no director for varying vibrating arm tip displacement.

The analysis was then repeated for a dipole with a single director in front of the dipole as illustrated in Figure 103. As the results in Table 13 and Figure 105 show, the phase change is 7.8° and the change in the magnitude of the returned power is 0.46 dB over a 100 micron "swing" of the vibrating stub. However, the phase change is slightly non-linear.

Table 13. Tabulated performance of dipole with one director for varying vibrating arm tip displacement.

Single Director in front of dipole

swing (mm)	Magnitude (W)	Magnitude (dBW)	Phase (deg)
-0.05	2.01E-08	-76.97	67.60
-0.04	1.95E-08	-77.10	67.90
-0.03	1.87E-08	-77.28	68.00
-0.02	1.70E-08	-77.70	67.50
-0.01	1.67E-08	-77.77	65.9
0	1.64E-08	-77.85	63.70
0.01	1.66E-08	-77.80	62.1
0.02	1.71E-08	-77.67	61
0.03	1.75E-08	-77.57	60.40
0.04	1.78E-08	-77.50	60
0.05	1.81E-08	-77.42	59.80
	overall change	**0.46**	**7.80**

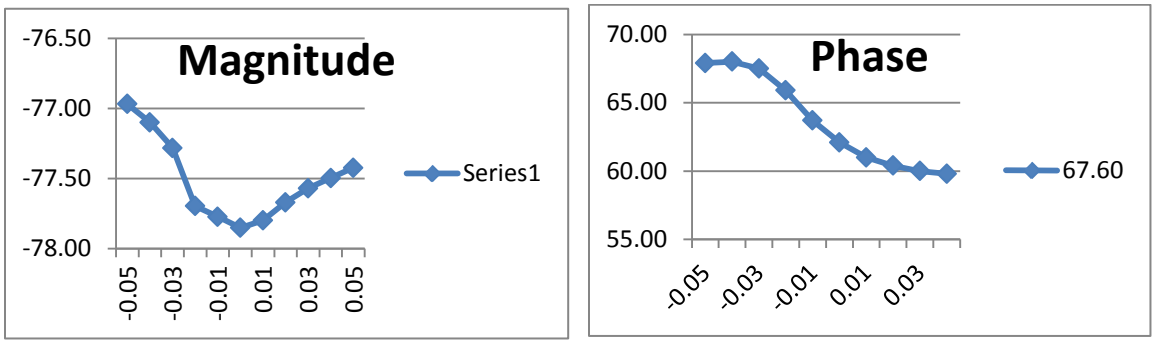

Figure 105. Magnitude and phase of dipole with one director for varying vibrating arm tip displacement.

The analysis was then repeated for a dipole with two directors placed at +45 and -45 degrees from the front of the dipole as illustrated in Figure 106. As the results in Table 14 and Figure 107 illustrate, the phase change of the dipole with two directors is 6.2° and the magnitude change is 0.75 dBm over 100 microns of swing, and the phase change is, again, slightly non-linear.

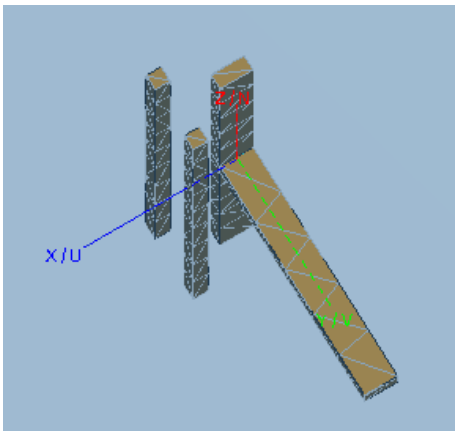

Figure 106. Dipole with two directors. TX/RX Doppler radar is in the positive X direction.

Table 14. Tabulated performance of dipole with two directors for varying vibrating arm tip displacement.

Two Directors

swing (mm)	Magnitude (W)	Magnitude (dBW)	Phase (deg)
-0.05	2.02E-08	-76.95	66.50
-0.04	1.99E-08	-77.01	66.60
-0.03	1.95E-08	-77.10	66.8
-0.02	1.90E-08	-77.21	66.80
-0.01	1.83E-08	-77.38	66.7
0	1.75E-08	-77.57	66.00
0.01	1.69E-08	-77.72	65.1
0.02	1.66E-08	-77.80	63.7
0.03	1.65E-08	-77.83	62.30
0.04	1.67E-08	-77.77	61.1
0.05	1.70E-08	-77.70	60.30
	overall change	**0.75**	**6.20**

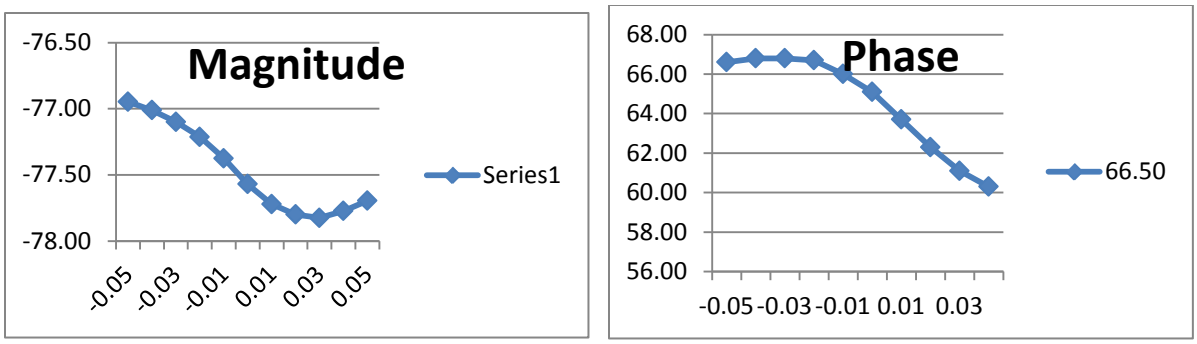

Figure 107. Magnitude and phase of dipole with one director for varying vibrating arm tip displacement.

The results of the simulations shown above for the dipole antennas with one and two directors indicate that the power gain was not as significant as the theory suggested it would be. However, the total phase difference between +50 microns and -50 microns for the vibrating arm more than doubled from the 'no director' dipole to the single and double director dipoles. This increase in phase change came with an added non-linearity for tip displacements greater than about ±20 µm. This suggests that for mechanically modulated dipole antennas with resonant beams designed for tip displacements less than 20 µm, that the use of directors would increase the sensitivity of the sensor.

3.6.3 Fabrication and Testing of Mechanically Modulated Dipole Antenna

In order to test the predictions of the performance of the mechanically modulated dipole antenna, a simple dipole was fabricated with perpendicular tuning arms, as shown in Figure 108 below. A 1.7 mm diameter copper rod was cut into two segments, one 7.2 mm long and the other 6.5 mm long. To one end of the first segment, a flat copper plate 4.6 mm x 2.1 mm x 0.45 mm was soldered. This plate was chosen to be relatively stiff so that any vibration during mechanical excitation would be minimal. Then, to one end of the second segment, a flat beryllium copper (BeCu) strip 4.6 mm x 1.6 mm x 0.15 mm was soldered. This more flexible plate was intended to function as the vibrating resonant beam. These two segments were mounted on a small block of closed cell foam using an RTV adhesive. The foam was selected due to its low dielectric constant, which would provide only minimal loading of the antenna response. The two segments were positioned so that they were collinear, with the flat tuning plates separated by 0.5 mm.

Figure 108. Experimental prototype of mechanically modulated dipole antenna

The performance of the prototype mechanically modulated dipole antenna was compared experimentally with the performance for the mechanically modulated slot antenna prototype shown in Figure 61. Due to the low levels of the received signal from the dipole antenna, it was necessary to use a lock-in amplifier to achieve sufficient signal-to-noise ratio (SNR) during the measurement. A lock-in amplifier is an electronic instrument that combines a high-gain amplifier with a narrowband filter, using a phase locked loop to ensure that the narrow bandpass of the filter is centered on the signal frequency. By using a very narrow filter, out-of-band noise is rejected and the signal-to-noise ratio is improved. The use of the lock-in amplifier in the experimental setup is illustrated in Figure 109. A mechanical shaker table was used to excite the resonant beam to vibrate.

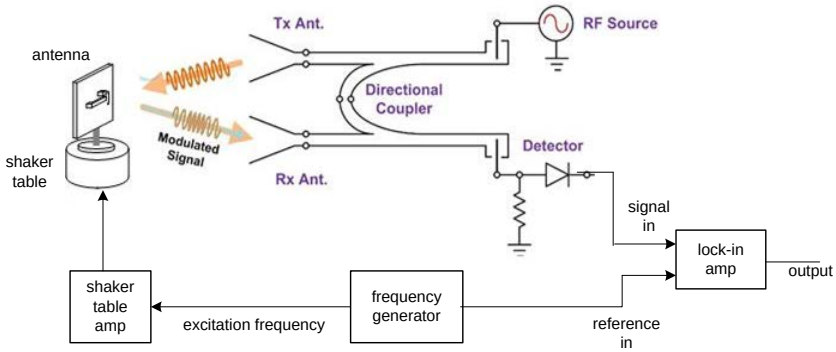

Figure 109. Experimental set-up used to compare outputs of slot antenna and dipole antenna.

Figure 110 (a) shows the results obtained when the slot antenna was tested. The plot shows the output power of the RF source in dBm on the x-axis, and the output of the lock-in amplifier (which is proportional to the signal detected by the Doppler radar) in dBµV on the wire-axis. A time constant of 10 seconds was used for the lock-in filter, and acceleration of 24 g was used for the shaker table. The plot shows that the noise floor for this test was approximately -13 dBµV.

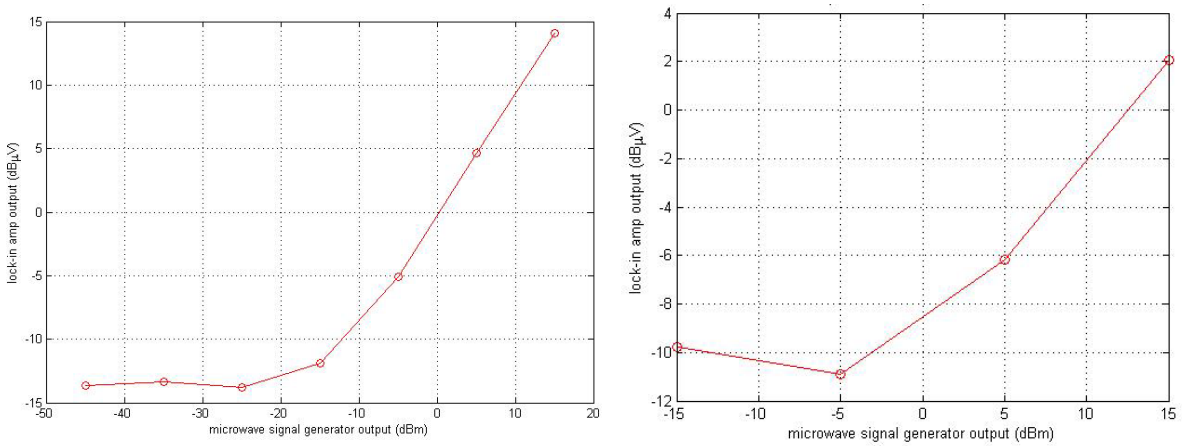

(a) (b)

Figure 110. Comparison of detected signal strength for mechanically modulated dipole antenna (a) and mechanically modulated slot antenna.

This result can be compared with that obtained for the dipole as shown in Figure 110 (b), where the signal from the dipole is about 12 dB lower than that of the slot antenna. This is likely due to the smaller surface area of the dipole antenna compared to the slot antenna with a 5 cm x 5 cm backplane, and suggests that the slot antenna would be preferred for its stronger signal.

3.7 Mechanical Testing of Mechanically Modulated Antenna

In order to characterize the mechanical motion imparted to the vibrating arm of the mechanically modulated slot antenna by acoustic excitation, a fiber interferometer was attached to the antenna to monitor the amplitude of the vibrating beam tip displacement. The end of a single mode optical fiber was attached to the ground plane of the antenna, so that the gap between the fiber endface and the side of the vibrating beam formed a Fabry Perot cavity. During testing, the beam was excited to vibration in two ways: first the antenna was mounted on the shaker of a vibration test set, on which the frequency and acceleration of vibration could be varied (Figure 111). In later tests, the antenna was mounted a few inches in front of a horn loudspeaker, which was driven by a signal generator through an audio amplifier.

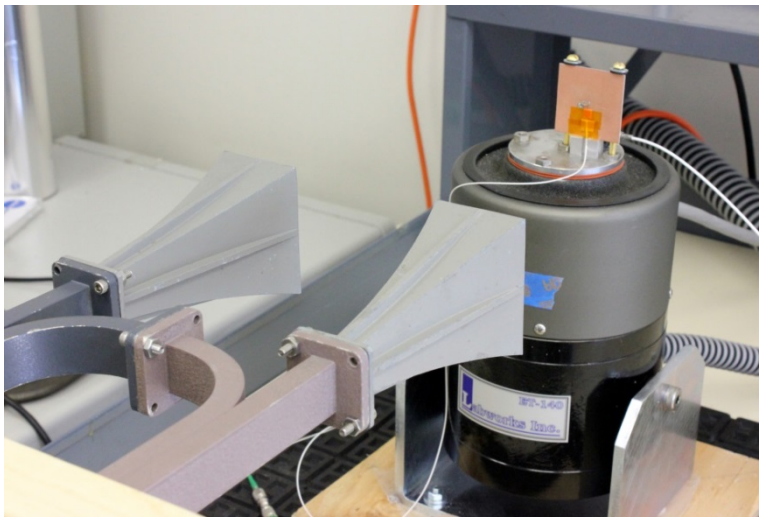

Figure 111. Mechanically modulated slot antenna mounted on vibration shaker table for excitation of mechanical resonant beam. Transmit and receive microwave horn antennas used for RF interrogation of slot antenna are also shown.

A 1550 nm laser diode was used as the optical source for the interferometer, and an optical receiver (transimpedance preamp followed by a voltage amplifier) was used to convert the optical signal to an electrical signal.

During initial tests of the first MMA prototype as described in Section 3.4, the beam tip displacements under acoustic excitation had also been measured using a fiber Fabry Perot interferometer. Figure 112 shows a plot that was obtained at that time when the mechanically modulated antenna, suspended in air, was excited by acoustic waves of approximately 115 dBA intensity. In the plot, which is a display of the digital oscilloscope connected to the output of the Doppler radar's mixer, the y-axis represents the voltage sampled by the digital oscilloscope. The x-axis represents time; the numbers refer to sample number for the voltage samples.

In the plot, a sinusoidal fringes corresponding to alternating constructive and destructive interference can be observed, overlaid with a slowly varying envelope shaping the maximum level of the fringes. Two red arrows are used to indicate "turn-arounds," points in the fringes that correspond to a change in direction of motion of the oscillating resonant beam. The fringes between the arrows represent constructive and destructive interference as the beam tip moves away from the fiber end. This direction can be inferred from the fact that the envelope of the fringes is decreasing between the two arrows. Since the light emitted from the fiber end is diverging, the optical power captured by the fiber after reflection off the beam depends on the separation between fiber and beam. When the beam tip is close to the fiber, more light is returned, and when the beam tip is farther away, less light is returned. In the plot, 44 fringes can be counted between turn-arounds. Each sinusoidal period corresponds to a tip displacement of one half of the optical wavelength, or 775 nm, so for the experiment recorded in Figure 112, the peak-to-peak vibration amplitude of the beam tip was 34 μm. On the same day that this result was obtained, vibration amplitudes of 46 μm were also obtained by mounting the antenna on a foam board, which improved the collection of acoustic power.

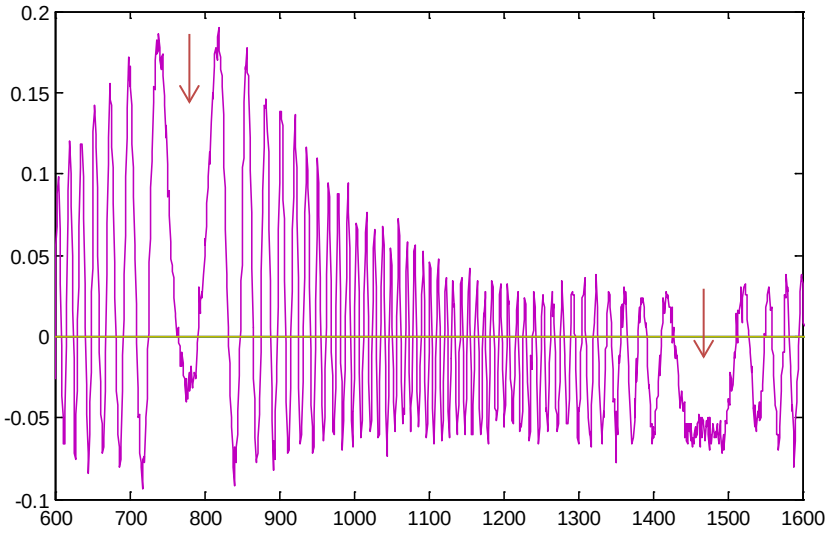

Figure 112. Interference fringes resulting from acoustic excitation of resonant beam during Budget Period 1 testing.

Further mechanical testing of resonant beam motion of the first prototype was conducted. Figure 113 (a) through (f) show the interference fringes resulting from successively higher levels of excitation of the MMA antenna using the shaker table. The x-axis represents the sample number for the digital oscilloscope used for data acquisition, and the y-axis represents the voltage of the interference signal. The estimated displacements are tabulated in Table 15; displacements for 16 g and 32 g excitation could not be estimated due to the difficulty in resolving the fringes.

As described above, a sinusoidal envelope can usually be observed in the fringes for large displacements. This results from the diverging optical beam emitted by the interrogating optical fiber. The complex envelope shapes seen here appeared to be evidence of the presence of higher order vibrational modes in the vibrating beam, such as torsional modes. It can be observed that, despite higher amplitudes achieved in earlier testing shown in Figure 112, no complex envelope was observed in that earlier testing. In contrast, interference fringes from the more recent testing shown in Figure 113 exhibit much more complex envelopes, which may result from complex motions of the beam due to the presence of higher order vibration modes.

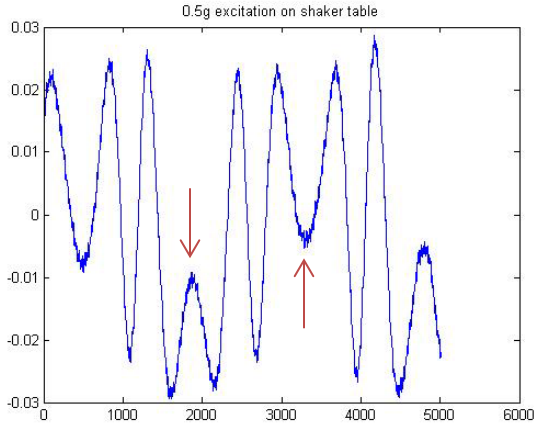

(a) Shaker, 0.5 g

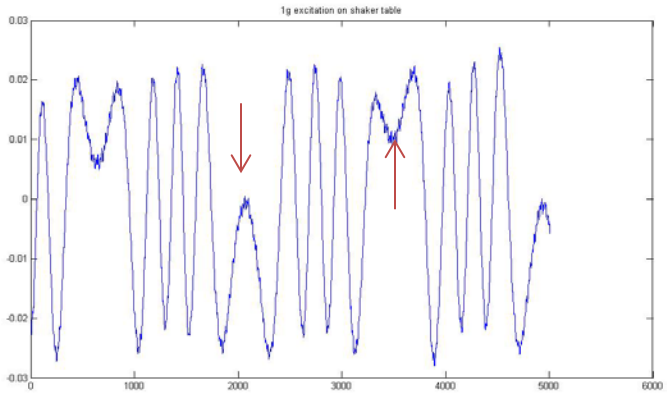

(b) Shaker, 1 g

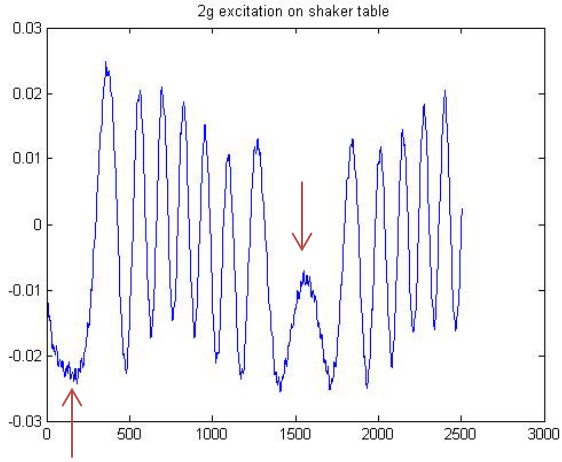

(c) Shaker, 2 g

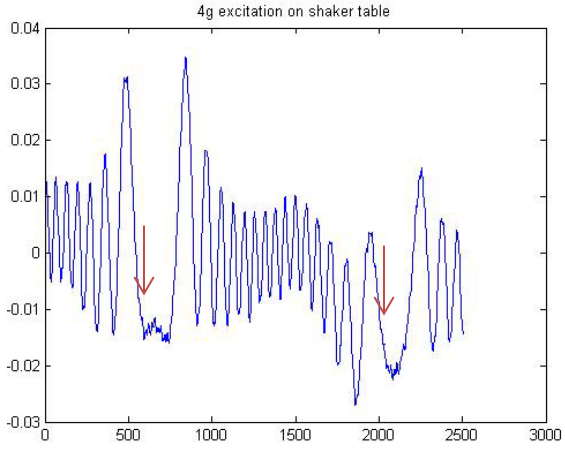

(d) Shaker, 4 g

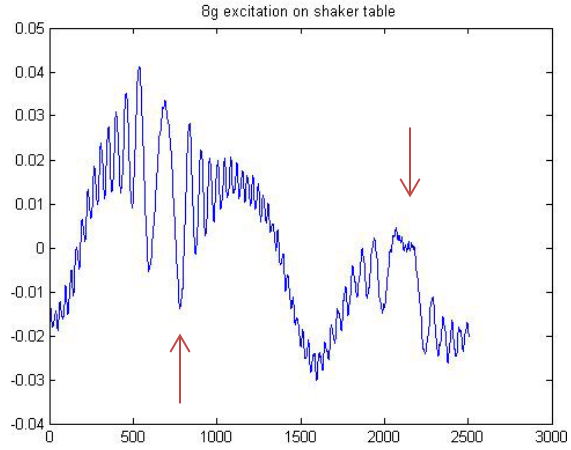

(e) Shaker, 8 g

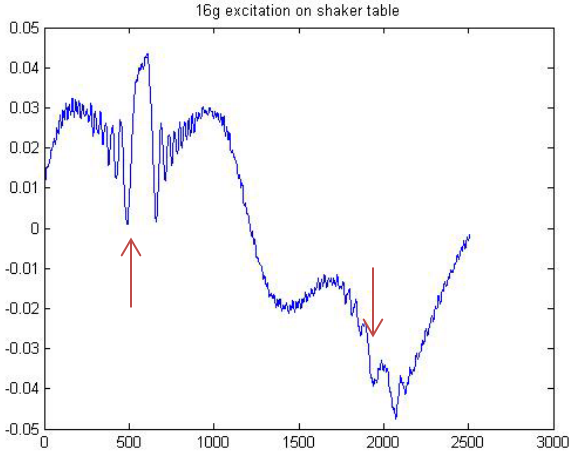

(f) Shaker, 16 g

Figure 113. Interference fringes resulting from vibration of resonant beam during vibration of antenna.

Table 15. Estimate of tip displacements for varying levels of excitation

Excitation (g)	Fringes	Displacement (μm)
0.5	1.4	1.1
1	3.8	2.9
2	7.2	5.6
4	15.0	11.6
8	30.5	23.6
16	*	*
32	*	*

The vibration test was repeated with a second prototype MMA sensor constructed using the same physical dimensions as the first prototype, but without the coaxial cable. By sweeping the frequency of the shaker table excitation while monitoring the fiber interferometer, it was determined that the peak resonance for this particular sensor occurred at 2118 Hz. Next, while maintaining the shaker table excitation at 2118 Hz, the stroboscope frequency was slowly varied in 1 Hz steps from 100 Hz to 4500 Hz as the beam was visually monitored through a microscope. At several discrete frequencies, motion of the beam was evident. At some frequencies, the motion clearly corresponded to torsional (twisting) vibration, and at others the motion was a bending vibration. For motion detected at very low frequencies, the vibration amplitude was not large enough to clearly distinguish the vibration mode.

The observed vibrations are summarized in Table 16. In the table, the measured frequencies corresponding to observed vibrations are summarized in the first column. It was observed that many of the frequencies corresponded to harmonics of the frequency for peak resonance (2118 Hz). To show this clearly, the harmonics were calculated and matched with the observed frequencies. The second column displays the frequencies predicted for the harmonics named in the third column. These results support the hypothesis that complex mode shapes associated with the observed harmonics are responsible for the complex fringes observed in the interference fringes.

Table 16. Frequencies for which vibrations were observed stroboscopically while exciting beam vibration at 2118 Hz.

measured	predicted	harmonic	notes
4234	4236	2f	torsional mode, 120-140 um amplitude
2825	2824	4f/3	torsional mode, 30 um amplitude
2118		f	bending mode, high amplitude, same as drive freq.
1412	1412	f/1.5	torsional tip mode, 80 um amplitude
1059	1059	f/2	bending mode, 120-150 um amplitude
706	706	f/3	bending mode, 80-100 um amplitude, may have had some torsional motion
529	530	f/4	bending mode, 60 um amplitude, may have had some torsional motion
none	424	f/5	
353	353	f/6	bending mode, 60 um amplitude
303	303	f/7	torsional mode, 30-40 um amplitude
265	265	f/8	bending mode, small amplitude
none	235	f/9	
none	212	f/10	
192	193	f/11	possibly torsional, 20 um amplitude
176	177	f/12	bending mode, 20 um amplitude
164	163	f/13	possibly torsional, small amplitude
152	151	f/14	small amplitude
none	141	f/15	
none	132	f/16	
124	125	f/17	small amplitude
118	118	f/18	small amplitude

3.8 Final Design of Mechanically Modulated Antenna

The vibration testing described in Section 3.7 revealed the presence of several vibrational modes in the motion of the resonant beam, corresponding to both harmonics and subharmonics of the shaker table frequency. The presence of torsional vibration modes degrades the radio frequency modulated response of the MMA.

In order to minimize the occurrence of torsional modes, the mechanical design of the MMA was refined by widening the resonant beam to reduce the amplitude of the torsional modes. As illustrated in Figure 114, the resonant beam was moved to the end of the ground plane, to facilitate fabrication so that it could be formed by cutting two slots in the ground plane. By making the resonant beam coplanar with the ground plane, this also improved coupling of incident acoustic waves to vibratory motion of the beam. In the final application of the sensor, the acoustic waves will be incident normal to the plane of the MMA, so placing the beam

coplanar with the ground plane will improve acoustic coupling, as opposed to the previous design, where the resonant beam vibration was normal to the direction of the propagation of the acoustic waves.

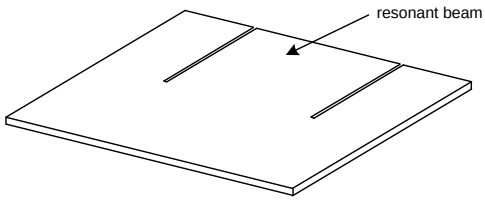

Figure 114. Revised MMA sensor with enlarged resonant beam.

4 TESTING

4.1 Tests to Assess Radio Wave Attenuation in Coal-Fired Powerplant Exhaust

The Small Boiler Simulator (SBS), a 6 MBtu facility at the Babcock and Wilcox Research Center in Barberton, Ohio, was used to characterize the RF environment inside a coal-fired boiler. Figure 115 shows a schematic of the SBS illustrating the location of an aspirated viewport where initial tests were performed to investigate the RF environment inside the boiler.

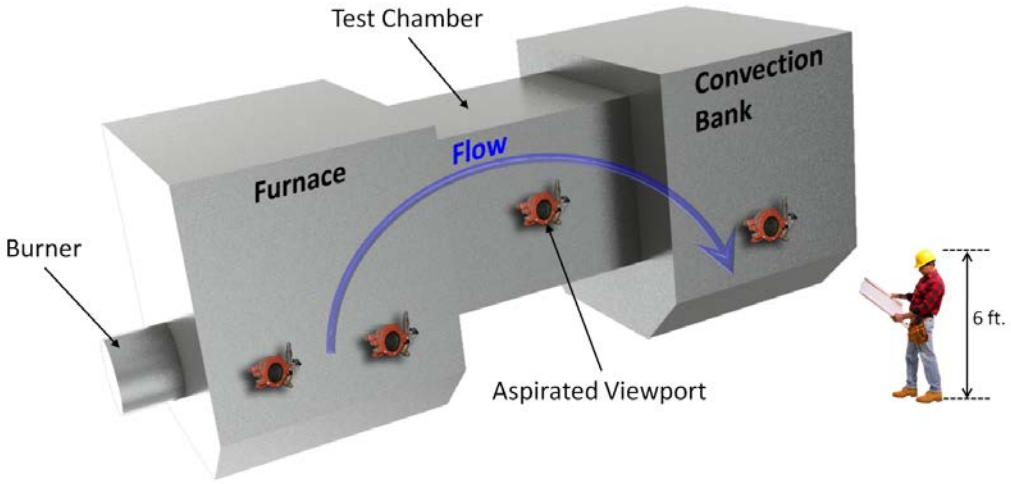

Figure 115. Schematic showing layout of B&W's Small Boiler Simulator and indicating the location of an aspirated viewport where preliminary testing of radio wave propagation will take place.

Photographs of one side of the SBS are provided in Figure 116. Testing was performed three levels up from the ground floor. That region is difficult to discern from these photographs, but is located on the reverse side and up three floors from where these photographs were taken.

Figure 116. B&W Boiler simulator

Figure 117 shows the platform where the testing was performed in the pass between the furnace and the convection bank. The chamber is on the left side of this photograph. RF test equipment, including a high frequency RF network analyzer, was placed on this platform and cables were installed around the outside of the chamber.

Figure 117. Platform where testing was performed

Physical access to the chamber was through the aspirated viewport shown in Figure 118.

Figure 118. Access to chamber through viewports

Physical access to the chamber was only through viewports installed in the chamber wall. The viewport shown in Figure 119 was provided by B&W for development of test antennas. The pipe which penetrates the chamber wall is roughly 3" inner diameter.

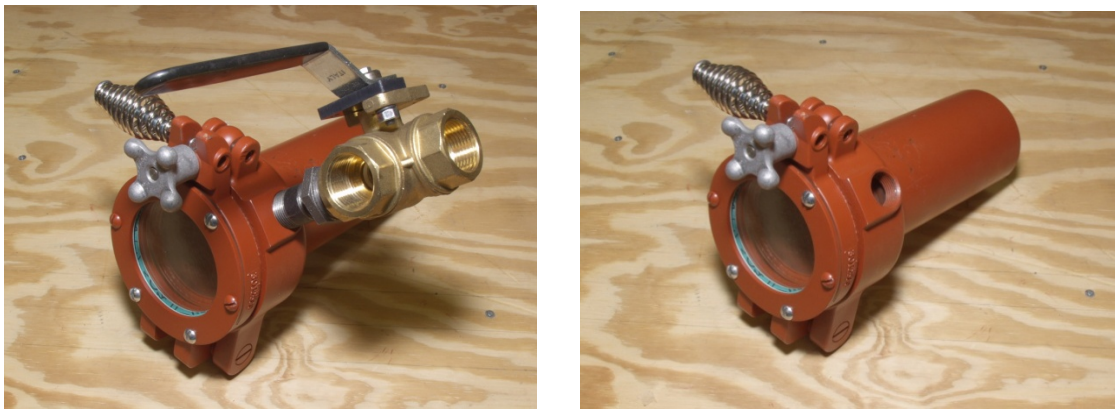

Figure 119. (Left) Viewport with external hardware for aspiration of port. (Right) Viewport with penetrating pipe visible.

4.1.1 Antenna Design

Vivaldi (exponentially tapered slot) and TEM-horn antennas were considered for the probe antenna to characterize the radio frequency (RF) environment inside the SBS. The probe antenna is intended to cover the frequency range from around 2.5 GHz (cutoff frequency of the 2.5" diameter tubing) to above 40 GHz (limit of the HP 8510 Vector Network Analyzer that will be used in the tests at the SBS). As a result of this work, the TEM-horn was identified as the antenna of choice due to its greater polarization purity, superior gain performance, and easier and

more robust construction. The robust construction was particularly important because it will be required to function at high temperature and in the presence of aspirated air in the viewport.

Both antenna designs would operate in travelling wave mode to achieve broadband performance. For this reason, return loss above 10 GHz will still be low. Gain will increase with frequency, but will converge to a maximum value due to loss at the higher frequencies.

4.1.1.1 VIVALDI ANTENNA

The basic geometry of the Vivaldi antenna is provided in Figure 120. This was chosen initially due to its simple design, potential for broadband operation, and ability to control polarization. Simulations of this antenna were quite computationally intensive due to the electrical size and non-symmetric shape. The antenna geometry was optimized using a genetic algorithm (GA) to simultaneously reduce reflections at low frequencies (< 5 GHz) and pattern distortion at high frequencies due to the surrounding metallic tubing.

The exponential curvature of this antenna can be defined using the following set of equations where *b* is the tapering rate:

$$f\left(z\right) = -ae^{-bz} + c \tag{27}$$

$$a = \frac{\mathrm{Tap}_L}{e^{b\cdot \mathrm{MS}_W/2} - e^{-b(\mathrm{Ant}_W/2 - \mathrm{Ant}_{W_C})}} \tag{28}$$

$$c = \mathrm{Bal}_L + ae^{b\cdot \mathrm{MS}_W/2} \tag{29}$$

In order to insert this antenna into a cylindrical viewport, the slot was incorporated into a copper tube. The geometry for this assembly was imported into the FEKO antenna modeling tool. This geometry is shown in Figure 121.

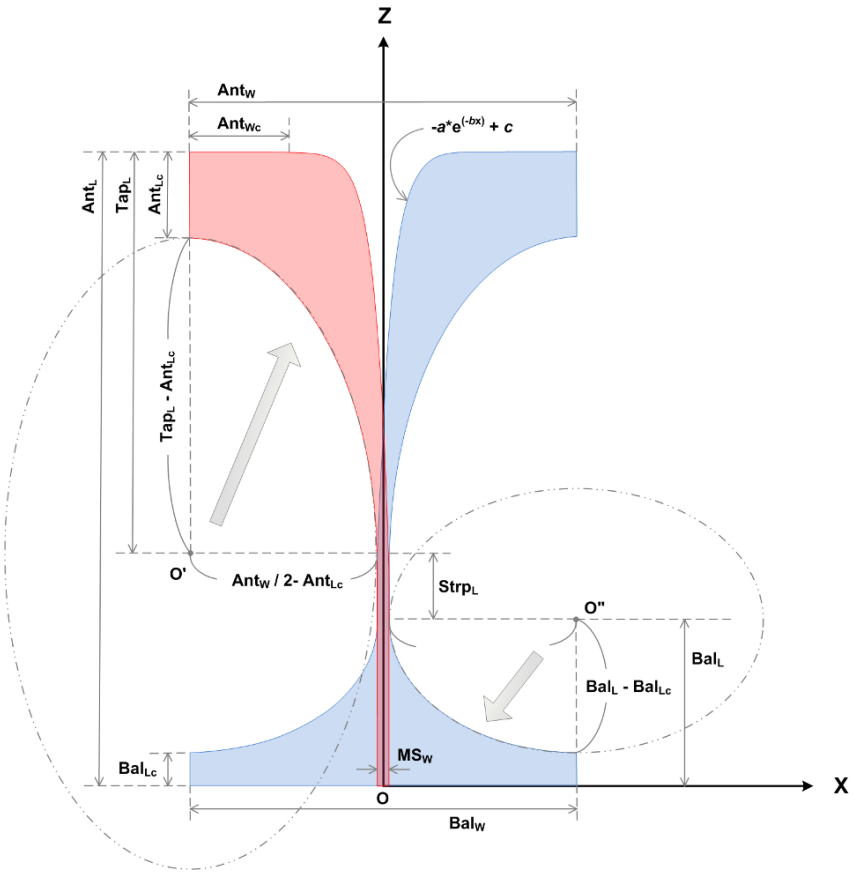

Figure 120. Geometry and design parameters for the Vivaldi antenna

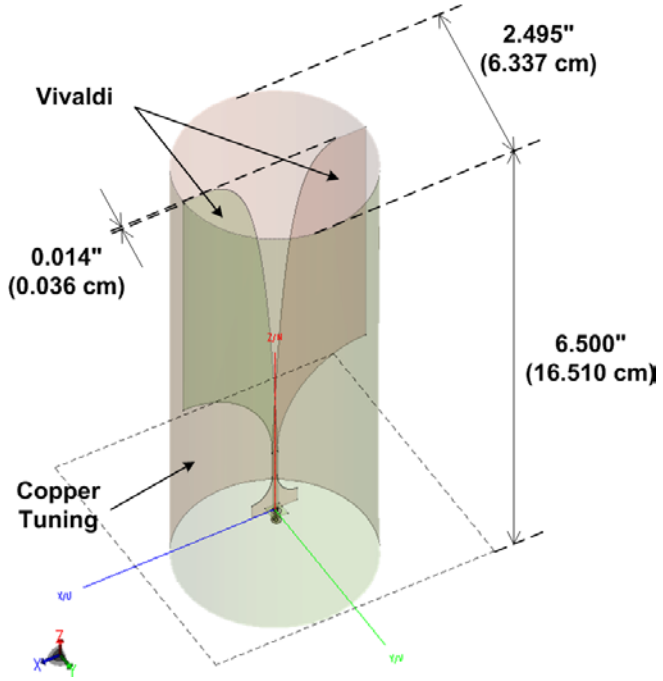

Figure 121. Simulation geometry of Vivaldi placed in a copper tube

Simulations were performed to predict the behavior and performance of the antenna inside the copper tube. Input impedance as a function of frequency is provided in Figure 122. It approximately maintains 75 © input impedance over a very wide band of frequencies. Both its voltage-standing-wave-ratio (VSWR) and boresight directivity are provided in Figure 123. To be more illustrative, the three-dimensional pattern of the antenna for selected frequencies is provided in Figure 124.

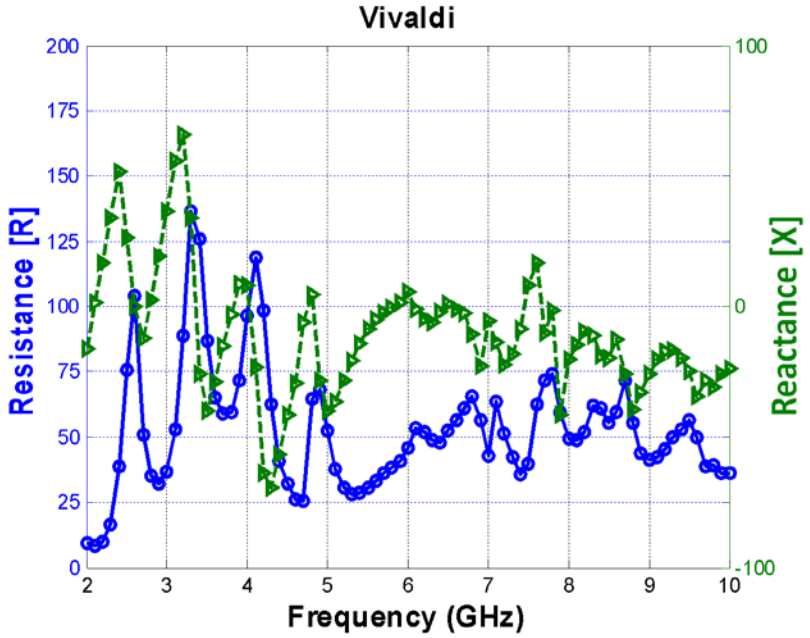

Figure 122. Simulated input impedance vs. frequency

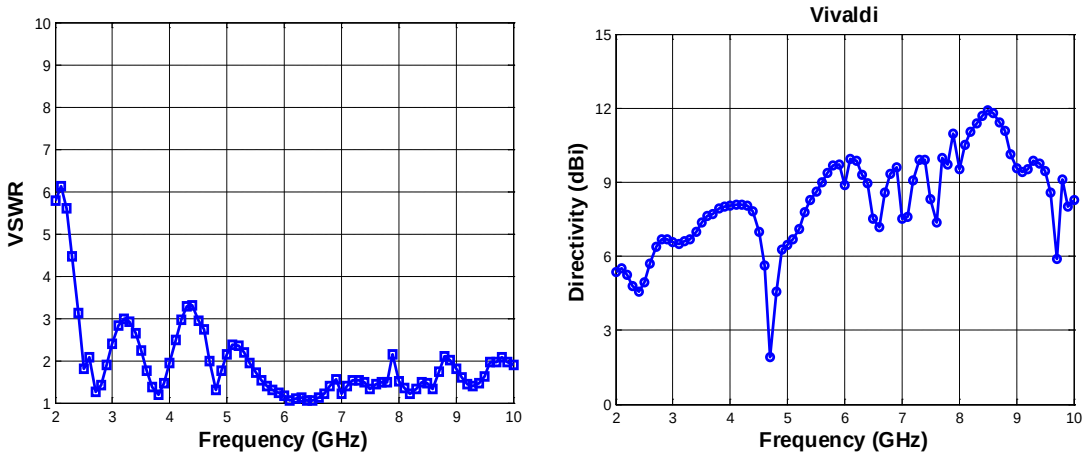

Figure 123. (Left) Simulated VSWR. (Right) Simulated directivity at boresight.

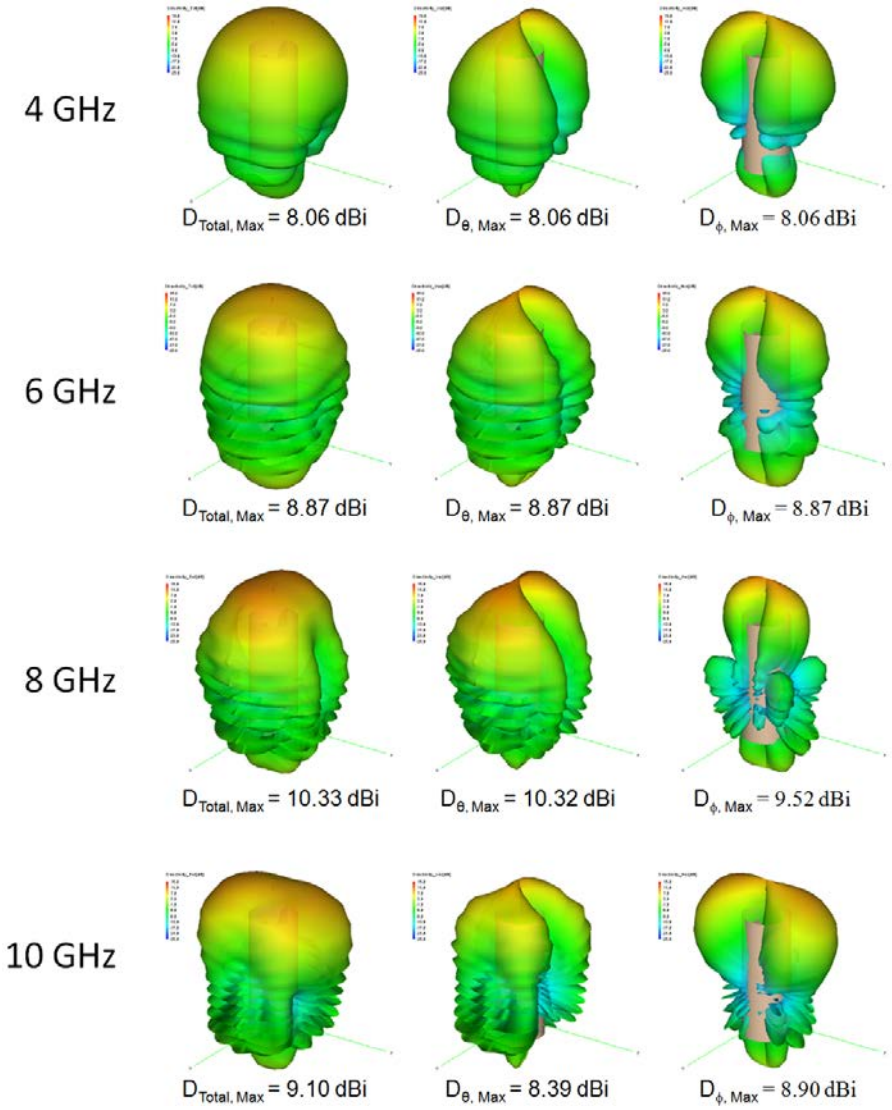

Figure 124. Simulated directivity at selected frequencies.

4.1.1.2 TEM HORN

The basic geometry of the TEM horn is shown in Figure 125. It is essentially composed of two parallel plates where the width of each is tapered from the feed outward. The separation between the plates is also tapered away from the feed portion.

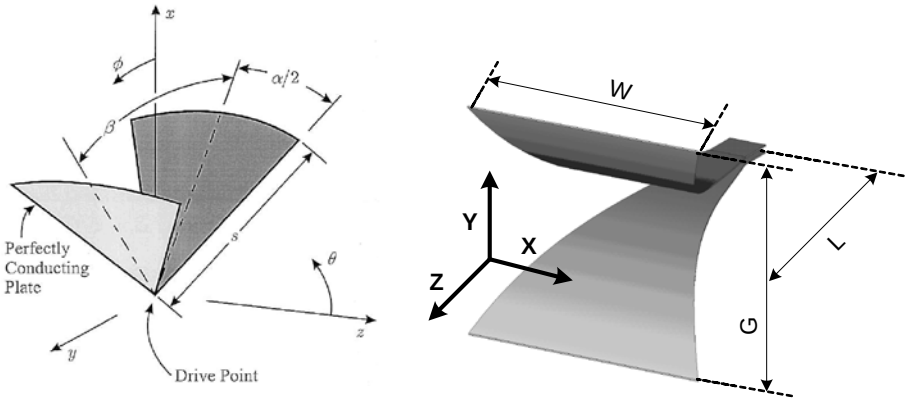

Figure 125. TEM horn antenna. (Left) linear taper. (Right) Exponential taper.

Assuming perfect transverse electromagnetic (TEM) fields, the characteristic impedance of the cross-section of the flared plates is described by

$$Z(z) = \eta_0 \frac{G(z)}{W(z)} = z_0 \, e^{\frac{z}{L}\ln\left(\frac{120\pi}{z_0}\right)}, \tag{30}$$

$$G(z) = ae^{bz} + c, \tag{31}$$

$$b = \frac{1}{L}\ln\left(\frac{W_L - c}{a}\right), \tag{32}$$

$$c = G_0 - a, \tag{33}$$

where the free space impedance is $\eta_0 = 120\pi$, and z_0 is the reference impedance of 50 ©. $G(z)$ and $W(z)$ are the gap and width functions at a given location z. L is the total length of the antenna. Figure 126 shows the TEM horn designed into a copper tube.

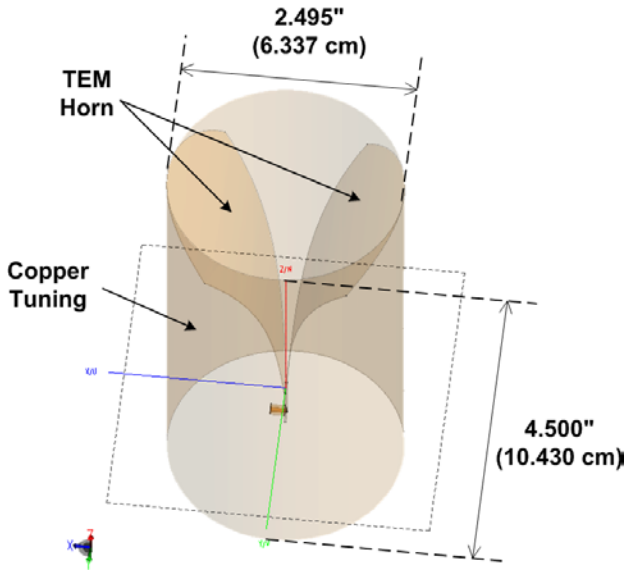

Figure 126. Model and dimensions of the designed TEM horn in a copper tube.

The model illustrated Figure 126 was simulated in FEKO to arrive at the input impedance response provided in Figure 127. The real component is just below 50 ©, but is better behaved than the Vivaldi antenna. The reactive component is near zero over almost the entire simulated spectrum. Finally, three-dimensional patterns were simulated for selected frequencies. These are shown in Figure 128.

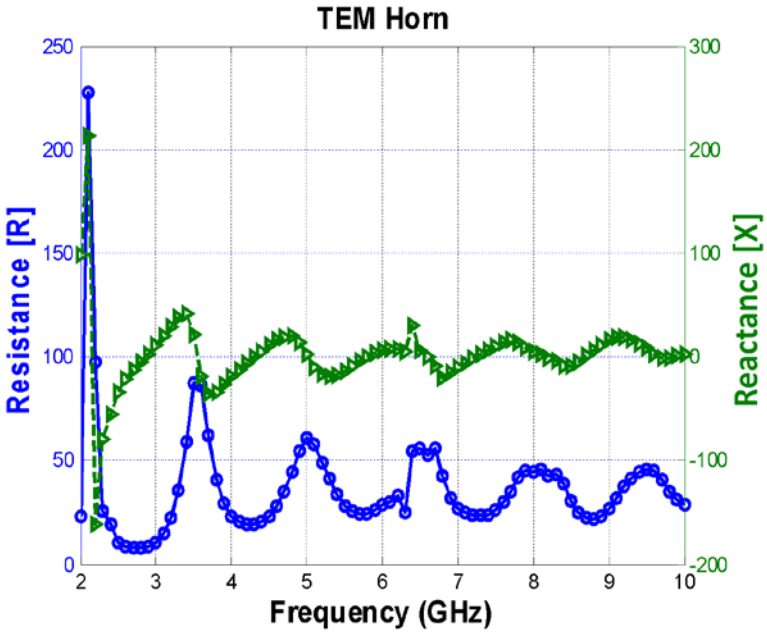

Figure 127. Simulated input impedance

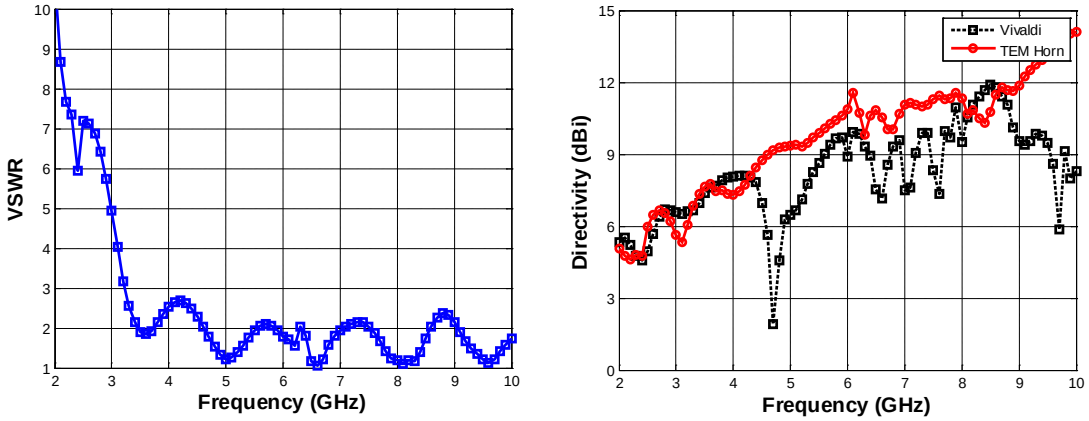

Figure 128. (Left) Simulated VSWR. (Right) Simulated directivity at boresight.

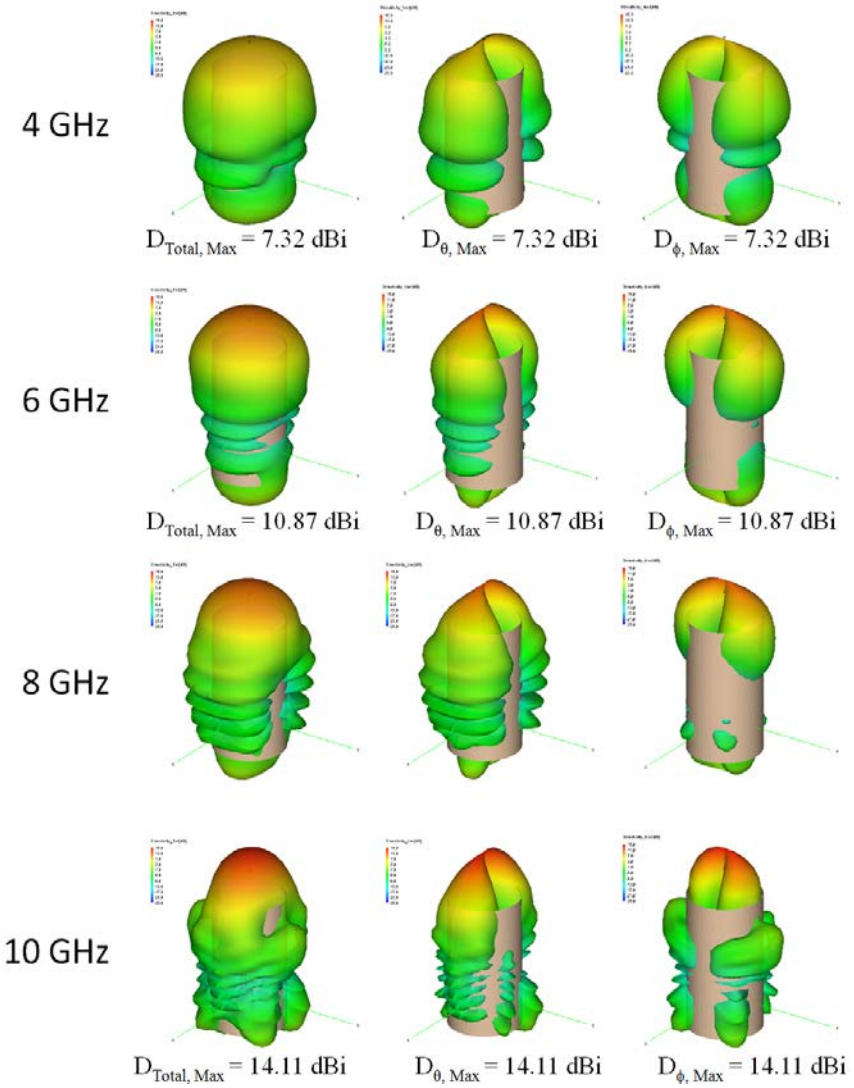

Figure 129. Simulated directivity of TEM horn antenna at selected frequencies.

Return loss is comparable to the Vivaldi design, but the gain performance is superior to the Vivaldi design, as well as its polarization purity at higher frequencies.

4.1.1.3 INFLUENCE OF VIEWPORT

While both of the antennas considered above were designed inside a copper tube, in the real environment they will also be inserted into a viewport. The geometry of this configuration is illustrated in Figure 130. The influence of the viewport on the behavior of the TEM horn was investigated through simulation. Influence on input resistance is summarized in Figure 131. Influence on the reactance and directivity is summarized in Figure 132. The three-dimensional patterns are provided in Figure 133

.

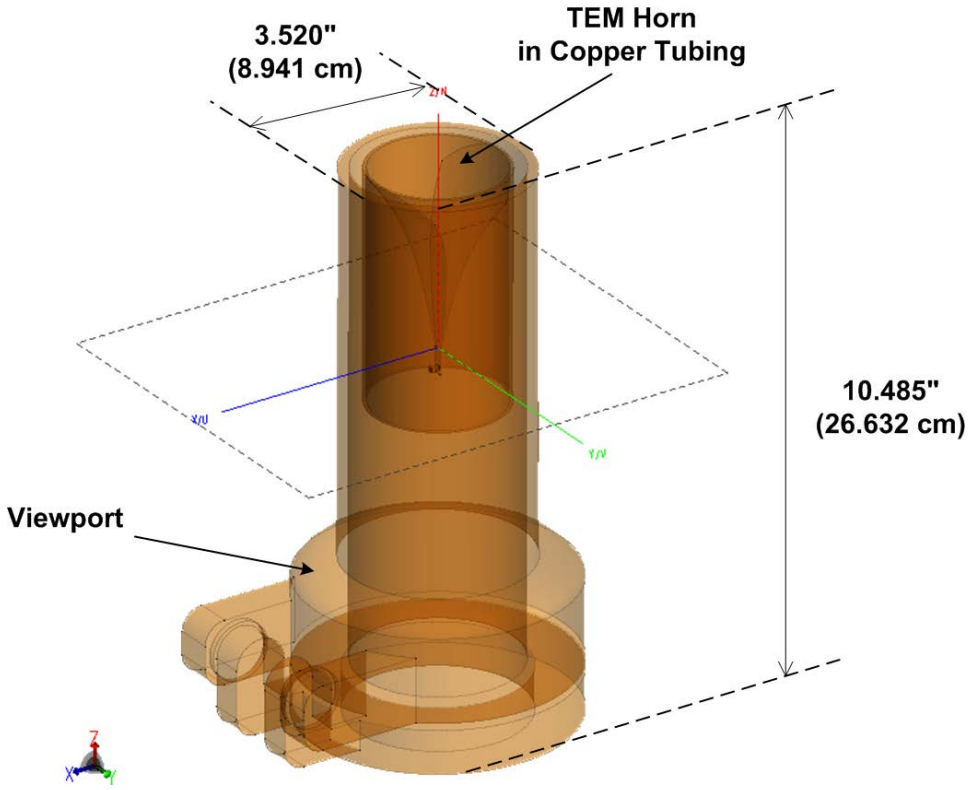

Figure 130. Geometry of TEM horn inside viewport

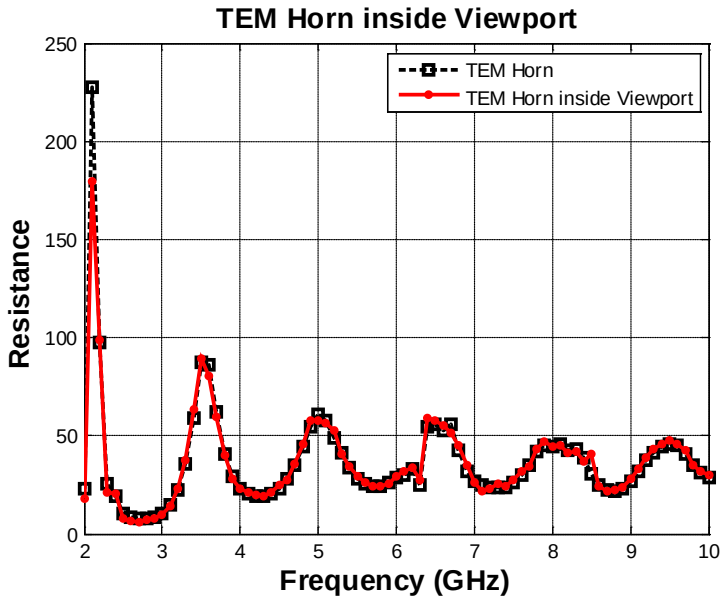

Figure 131. Influence on input resistance.

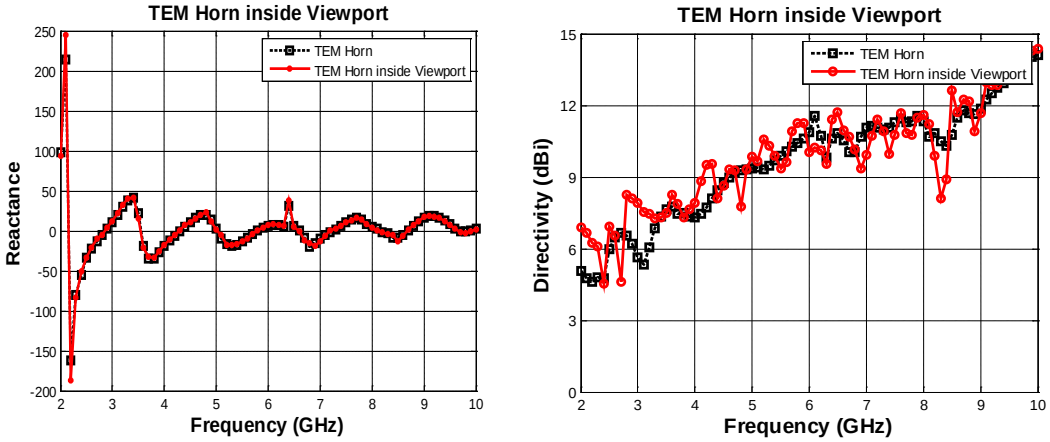

Figure 132. (Left) Influence on reactance. (Right) Influence on directivity.

4.1.1.4 PROBE CONSTRUCTION AND INITIAL TESTING

The probe antenna is intended to cover the frequency range from around 2.5 GHz (cut-off frequency of the 2.5" diameter copper tubing) to above 40 GHz. Both the Vivaldi (exponentially-tapered slot antenna) and the TEM horn were considered initially as candidates of the probe antenna, but the TEM horn was chosen due to the expected high temperature around a viewport and relatively simple construction, compared to the Vivaldi that has a supporting dielectric material in between two radiating elements. The basic TEM horn antenna design with 10:1 impedance bandwidth is straightforward, but this project required more than 15:1 bandwidth. So, the required fine mechanical construction of the feed region was challenging. Mechanical connections between the TEM horn antenna and the surrounding copper tubing were

experimentally evaluated in order to provide a better temperature tolerance and support the tapered shape of the TEM horn antenna. These connections, however, created multiple resonances inside the desired bandwidth, which prevented the TEM horn from being a traveling-wave antenna. Another challenging aspect was the wideband balun converting a balanced mode to an unbalanced mode. The classic TEM horn antenna has a balanced structure, so the current-amplitude distribution on each radiating element is identical. However, when a coaxial cable (unbalanced structure) is connected to the TEM horn directly without a balun, a current can flow on the cable which distorts the radiation pattern. In severe cases, the connected cable can function unintentionally as the primary radiator.

Through careful design evolution, the double-ridged TEM horn design shown in Figure 134 was obtained. The integrated balun and the coaxial line are located on the plane of symmetry to minimize the inclusion effect of the balun and cable. As shown in Figure 135, the designed antenna provides reasonable performance. It exhibits a relatively symmetric radiation pattern due to the balun and it provides short-pulse radiation due to the wideband performance.

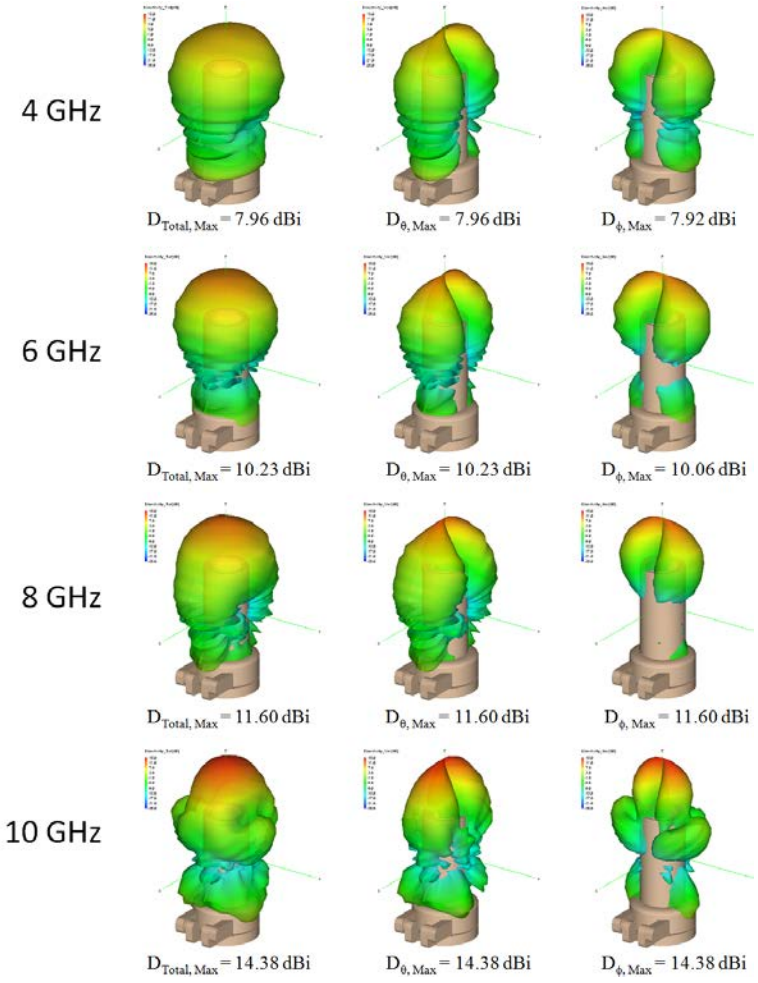

Figure 133. Influence of viewport on pattern

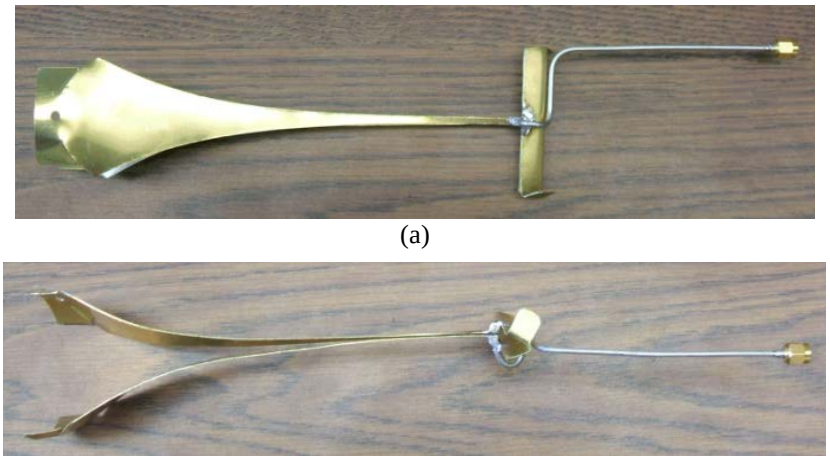

(a)

(b)

Figure 134. Photographs of fabricated test probe antenna. (a) View from top. (b) View from side.

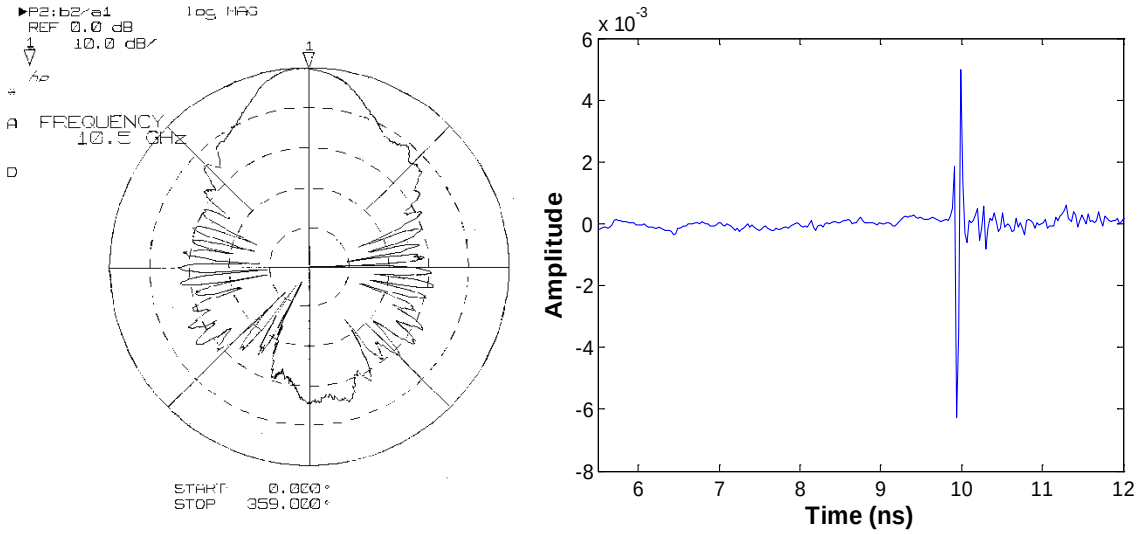

(a) (b)

Figure 135. Measured antenna characteristics. (a) Radiation pattern at 10.5 GHz. (b) Radiated pulse.

For a proof-of-measurement concept, two identical probe antennas (designed TEM horns) were used in parallel for monostatic radar detection. The laboratory setup is depicted in Figure 136. A sphere representing a radar cross section (RCS) standard and 9-element dipole array representing a temperature sensor were located at different distances from the probe antennas. The measured time-domain response in Figure 137 shows the clear response of each object separated in time.

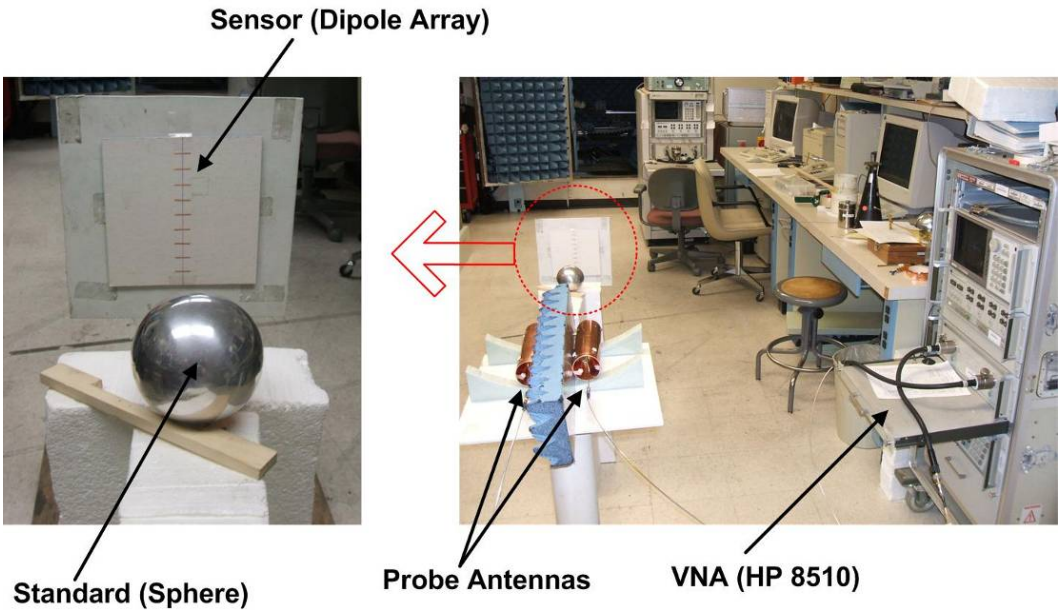

Figure 136. Picture of measurement setup in a lab environment.

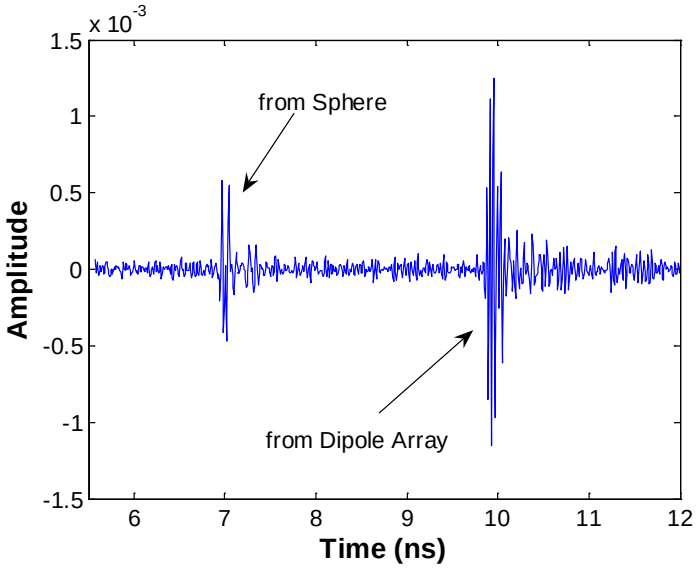

Figure 137. Time domain response from both sphere and dipole array.

4.1.2 Test of Attenuation during Natural Gas Firing

On June 10, 2010, Russell May from Prime Research and Bill Davis and Taeyoung Yang from Virginia Tech Antenna Group (VTAG) performed tests at the B&W SBS and obtained s-parameter data while the SBS was quiescent and while it was fired with natural gas.

4.1.2.1 EXPERIMENTAL SET-UP

The set-up used for the tests at the B&W SBS is shown schematically in Figure 138. The antennas used were of a design that was a variation of the TEM horn antennas described in the previous section (Figure 134). The newer antennas that were installed in the SBS included a zig-zag taper that was optimized by the use of a genetic algorithm. Both antennas were installed in the viewports on the test chamber (Figure 139). Antenna A was fed through a 30-dB RF amplifier while the antenna B was connected directly to the HP 8510C vector network analyzer (VNA). It can be seen in Figure 139 that the ends of the antennas protrude out of the back of the viewports. This was unintentional, as the antennas were designed so that the back end of the antennas would be flush with the viewport flange after installation of the antennas. However, during installation of the antennas, it was discovered that welds that extended into the inner bores of the viewports prevented the antennas from being fully inserted.

After installation of the antennas, the equipment (antennas, coaxial cables, amplifier, and VNA) was calibrated. Reflection-and-isolation calibration was chosen as the main transmission calibration technique due to the short characterization time of the technique.

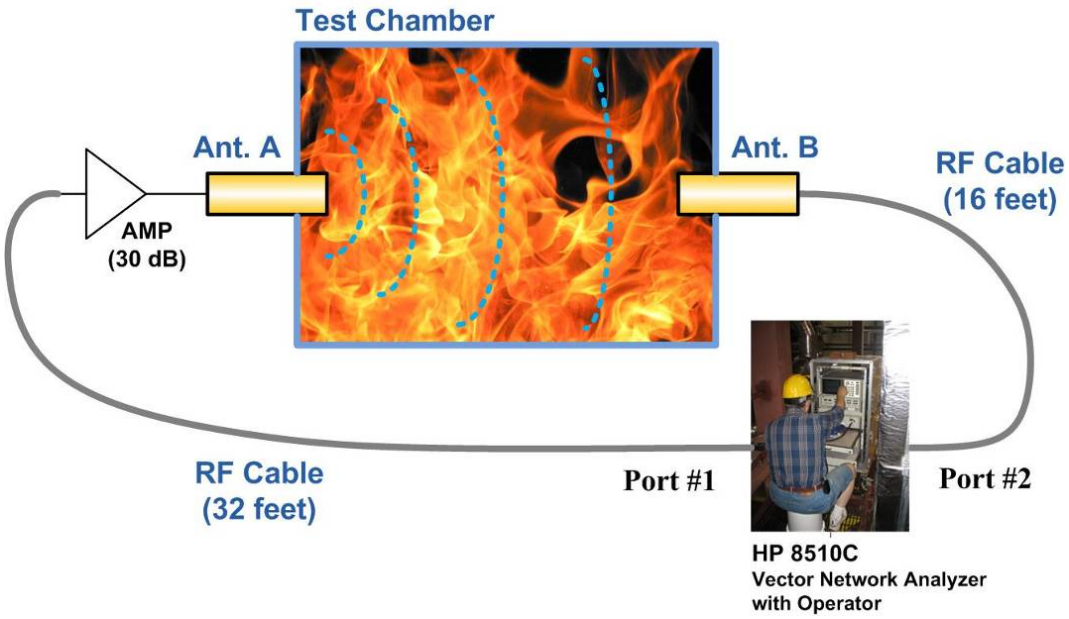

Figure 138. Illustration of the measurement set-up at the B&W SBS.

(a) (b)

Figure 139. Photographs of (a) Antenna A and (b) Antenna B installed in viewports in the SBS.

4.1.2.2 TEST RESULTS DURING NATURAL GAS FIRING

Figure 141 is a plot of the results obtained for the s_{21} parameter. The s_{21} parameter compares the power received at Antenna B to the power launched from Antenna A. Therefore, this parameter provides a useful measurement of the losses incurred by the radio wave during propagation across the SBS convection pass. The plot in Figure 141(a) shows the s_{21} parameter before firing (quiescent state, blue trace), and the s_{21} parameter during firing with natural gas (red trace). Therefore, the attenuation introduced by factors within the SBS, such as absorption due to hot gases, is found by subtracting the red trace from the blue trace.

During testing on June 10, 2010, the HP 8510C reported an internal error indicating that the intermediate frequency (IF) stage of the VNA failed a self-test. The RF coaxial cables were removed and cables with lower losses were substituted, but this failed to eliminate the error message. For this reason, full confidence cannot be placed on the data obtained during the tests on this day. Further troubleshooting of the VNA at the Virginia Tech Antenna Group laboratories following the test disclosed that overheating of the instrument had led to the error message. This will be corrected for the July tests by adding an additional cooling fan.

At the conclusion of testing on June 10, 2010, the antennas were removed from the viewports and examined. It was discovered that solder bonding the semi-rigid coax antenna feed to the balun in the antenna had failed due to overheating. Figure 140 illustrates the location of the solder bond. In addition, it was observed that the polyethylene dielectric in the antenna feed had melted.

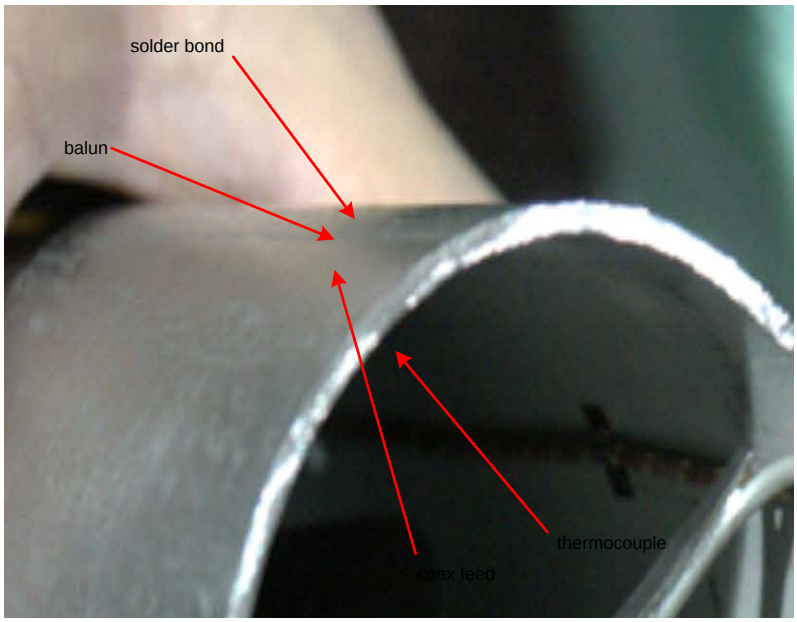

Figure 140. Photo of back end of antenna (before test), showing location of balun, coax feed, and solder bond between balun and coax feed.

Two factors were believed to be responsible for the overheating. First, weld lines in the inner bores of the viewports made it impossible to insert the antenna fully into the viewports. The outer diameter of the antenna tube was chosen to fit with close tolerances into the sample viewport that had been provided to Prime Research by B&W. However, upon arriving at the SBS facility to install the antennas, it was discovered that the viewports on the SBS had been extended in length by welding an additional steel tube to the back end of the tube. The weld line between the viewport tube and the extension tube protruded into the inner bore of the viewport, so that the antenna could not be inserted beyond this weld line.

The antennas had been designed so that they would not obstruct the aspiration ports in the viewport. In normal operation, cooling air is introduced into the viewports through aspiration ports. However, the antenna tube covered the aspiration ports due to the protruding position of the antenna.

Secondly, the SBS is typically operated so that a slight negative pressure is maintained inside the convection pass relative to the outside atmosphere. Under that condition, air is drawn from the outside, through the open viewport, cooling the antenna. However, during the tests on June 10, 2010 hot gases were observed to exit through the viewports, indicating that the SBS interior was at a positive pressure relative to the outside. In that operating condition, the hot gases were heating the antennas.

In Figure 141(a), the sharp drop in the amplitude of s_{21} at around 20 GHz and the additional 10 dB attenuation above 18 GHz might be the result of the broken antenna feed. To obtain the data plotted in the graph, the vector network analyzer scans the range of frequencies, starting at 50 MHz and then linearly ramping the frequency up to 40 GHz. Therefore, the abrupt

increase in attenuation for frequencies greater than approximately 18 GHz may have resulted from a failure of the antenna feed as the VNA scan was passing 18 GHz. The measurement was repeated with the 30 dB amplifier removed from the coax cable that fed Antenna A. The results, shown in Figure 142, showed a nominal 10 dB attenuation over the entire measured spectrum above the cut-off frequency (approximately 2.3 GHz), which supports the conjecture that the attenuation might be due to the damaged antenna feed.

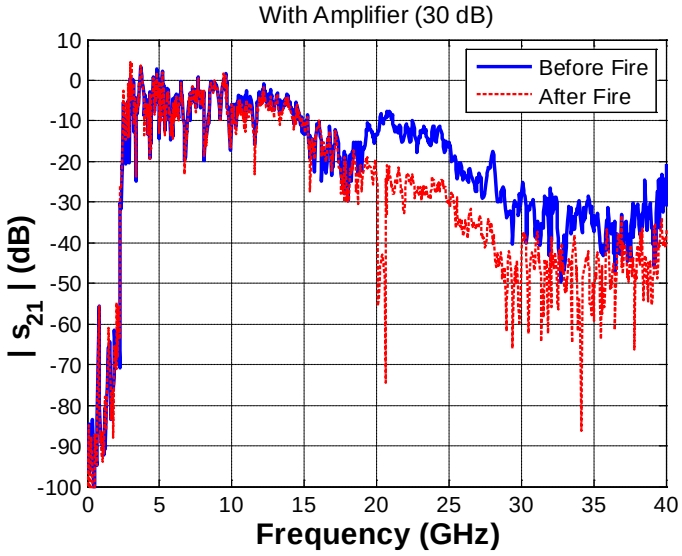

(a) Amplitude

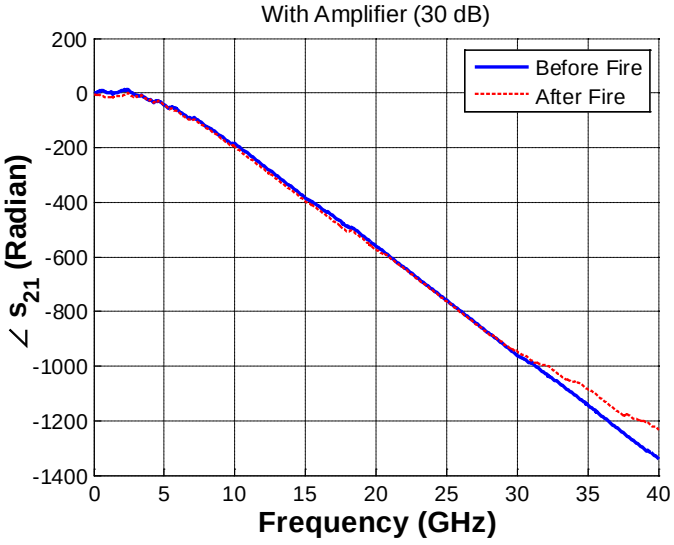

(b) Phase

Figure 141. (a) Amplitude and (b) Phase response comparison of s_{21} for the without and with-fire cases (30 dB amplifier was used).

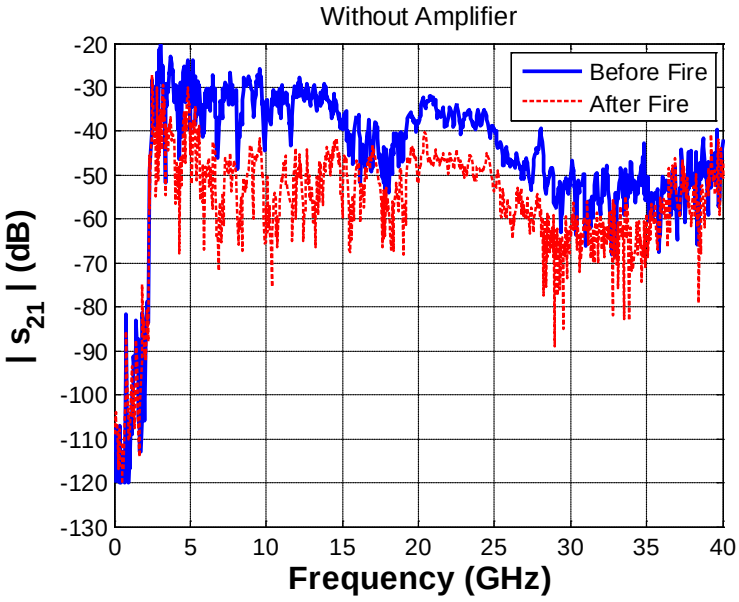

(a) Amplitude

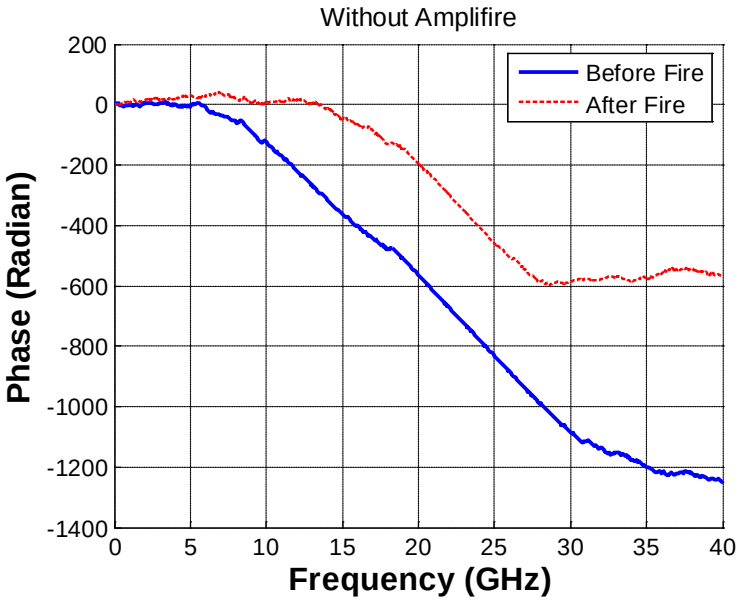

(b) Phase

Figure 142. (a) Amplitude and (b) Phase response comparison of s21 for the without and with-fire cases (No amplifier was used).

4.1.3 TEST OF ATTENUATION DURING BIOMASS FIRING

4.1.3.1 EXPERIMENTAL SET-UP

Prior to additional tests at the SBS facility, changes were be made to the TEM horn antennas to address the problems introduced by the heating of the antennas observed during the natural gas firing tests. First, small holes were drilled into the sides of the steel tubes of the antennas to permit flow of cooling air from the aspiration ports into the interiors of the antennas (Figure 143). The locations of the small drilled holes were positioned so that they would align with the aspiration ports of the viewports when the antennas were installed.

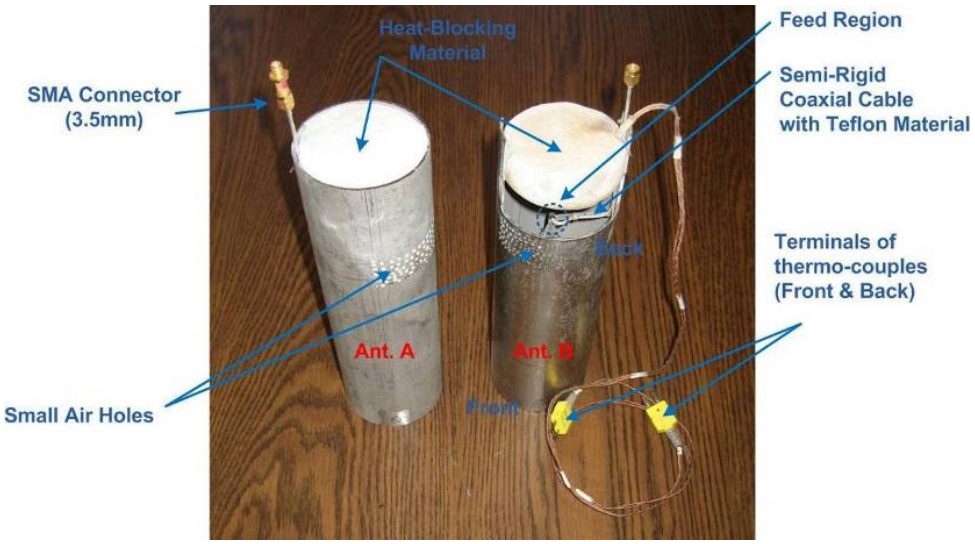

Figure 143. Picture of the prepared antennas.

Since the viewport windows could not be closed when the antennas were installed (due to the coax cables), an alumina-based fiberboard insulation was installed in the back end of the antennas to limit the flow of hot gases through the antennas and out of the viewports. The insulating material was first tested to determine that its dielectric properties (dielectric constant and loss tangent) would not significantly change the antenna properties. A 50Ω, 7 mm coaxial air line was prepared to load the test materials, as illustrated in Figure 144. The material under test (MUT) was partially filled inside the air line. After measuring two-port s-parameters, the air-filled part of the coaxial line was "de-embedded." In this context, "de-embedding" means that the contribution of the remaining air-filled section to the s-parameters was removed from the measurement by deconvolution.

Next, the permeability and permittivity of the MUT was estimated from reflection and transmission coefficients by using single and two-transmission line approaches.[1] The results of both approaches agreed well. Since the MUTs do not contain magnetic materials, only dielectric constant and loss tangent estimated from the single transmission line approach are depicted in Figure 145.

Figure 144. Picture of 7 mm coaxial air line loaded with a material under test (MUT).

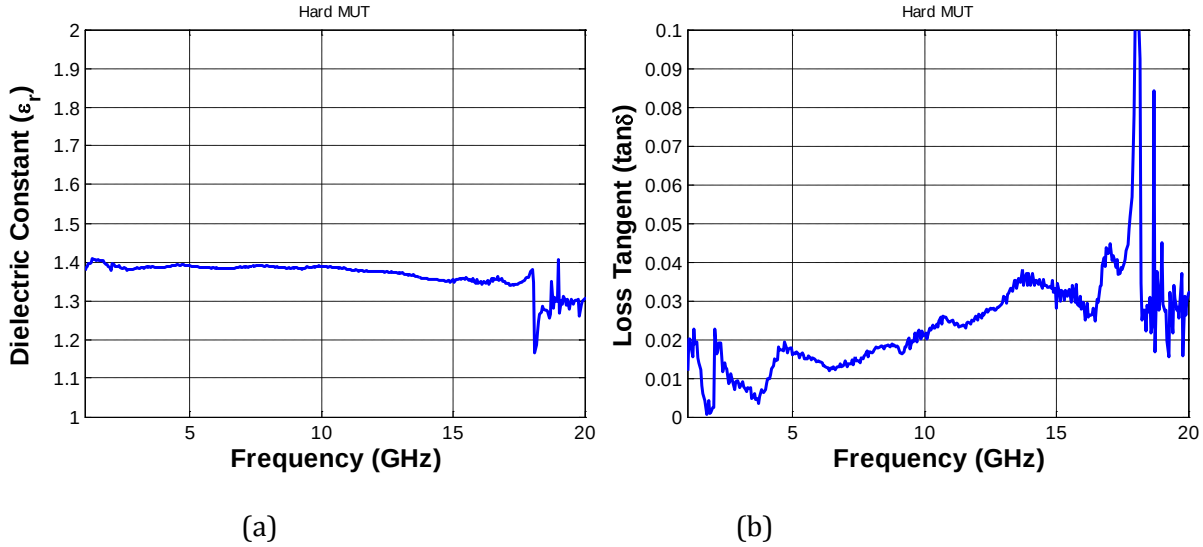

(a) (b)

Figure 145. Measured material property of the alumina-based heat-blocking material – (a) dielectric constant and (b) loss tangent.

Because the electrical length of the test material is short at low frequencies (< 500 MHz) and because the operational frequency of 7 mm calibration kit (especially the open standard), the frequency range of the estimated material property was limited to 20 GHz. In addition, there is a glitch around 18 GHz due to a resonance or a multi-mode effect of 3.5 mm adapters. However, basically we obtained material properties for 10:1 bandwidth.

The test material was found to have a low dielectric constant of approximately 1.4. The loss tangent did not exceed 0.04, which is also relatively low compared to other composite bulk materials. Thus, no significant change in antenna performance was expected

when the material is inserted inside the stainless steel tube. The blocking materials could be located either front or back side of the antenna.

Another issue addressed in the modification of the TEM horn antennas was the susceptibility of the dielectric in the semi-rigid coax cable to melting. As shown in Figure 146, the bent semi-rigid coaxial cable used in the natural gas firing tests was soldered on an extended metallic strip which served as a balun for low operating frequencies as well as a support for the coax cable at the back end of the antenna. The outer conductor of the coax was soldered to one of antenna arms while the center conductor of the coax was soldered to the other arm of the antenna. The two arms of the antenna were separated by a small air gap and supported by the center dielectric material of the coax.

Figure 146 (b) shows a close-up of one antenna following the test under natural gas firing conditions. It can clearly be seen that the solder joint between the coax cable and the balun (metallic strip) failed during the test, and that the polyethylene dielectric in the coax melted. As a result, there might be an increased return loss from the antenna over the operational frequency range, which may have contributed to the 10 dB loss observed in the natural gas firing test.

The dielectric material existing in between the outer and inner conductor of the coax is a polyethylene. The melting point of polyethylene varies with the density of the material, but the typical melting point of the polyethylene is 105 - 130 °C (221 - 266 °F).[2] During the natural gas firing test, the temperature of the back side of the antenna was monitored with a thermocouple and was observed to vary between 100 and 150°C. Thus, it is not surprising why the feed region was damaged.

The soldered part can be protected from the heat damage by wrapping a thin tinned wire around the coax and the extended strip of the antenna. Then, high temperature 50:50 solder can be applied to make sure a solid connection is achieved between the structures.

In order to address the melting issue of the center dielectric material of the coax, we chose to use a semi-rigid coaxial cable filled with Teflon for further testing. It is known that the melting point of the Teflon is about 342 °C. The chemical properties of the Teflon does not change until it reaches the melting point.[3] With these solutions, it is expected that the antenna feed region will be fine up to 300 °C.

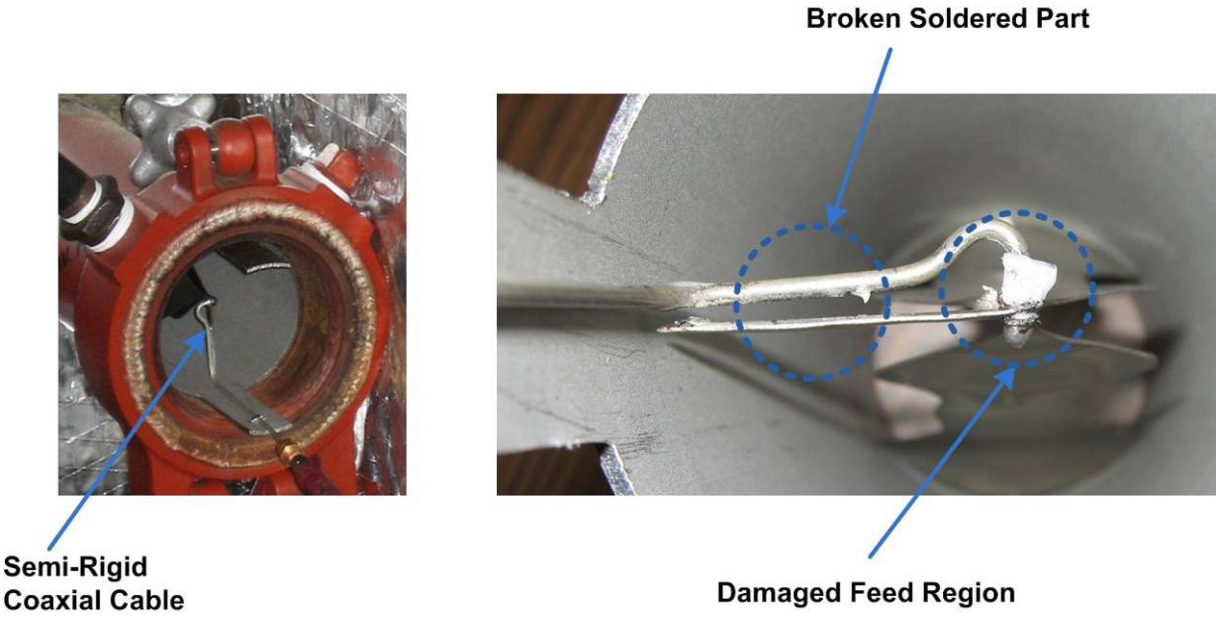

(a) (b)

Figure 146. Pictures of antenna feed region (a) before and (b) after firing.

In order to determine if the semi-rigid coaxial cable filled with the Teflon could handle the temperatures expected in the SBS, a test was carried out. As shown in Figure 147(a), a thermocouple was attached right beside a coax cable with Teflon dielectric, in order to monitor the temperature. One can also notice that the outer conductor of the coax is aligned with the center Teflon. The end part of the coax was then heated by using a butane lighter. We tried to maintain the monitored temperatures at 100, 200, 300, and 400 °C. Each targeted temperature was maintained for about 10 minutes. Up to 300 °C, no shape change was observed. However, as the temperature increased above 350 °C, the center Teflon starts expanding. After finishing the experiment, a picture was taken and shown in Figure 147(b) where the extended center Teflon can be observed. The heat damage happened when the temperature increased from 350 to 400 °C and maintained at 400 °C for about 10 minutes. Therefore, this test confirmed that the semi-rigid coaxial cable with the Teflon dielectric can be used up to 300 °C.

4.1.3.2 TEST RESULTS DURING BIOMASS FIRING

On July 21, 2010, John Coggin from Prime Research and Bill Davis and Taeyoung Yang from the Virginia Tech Antenna Group (VTAG) obtained s-parameter scattering data while the SBS was unfired, then while it was fired with natural gas, and finally when it was fired with biomass (“Ag pellets”).

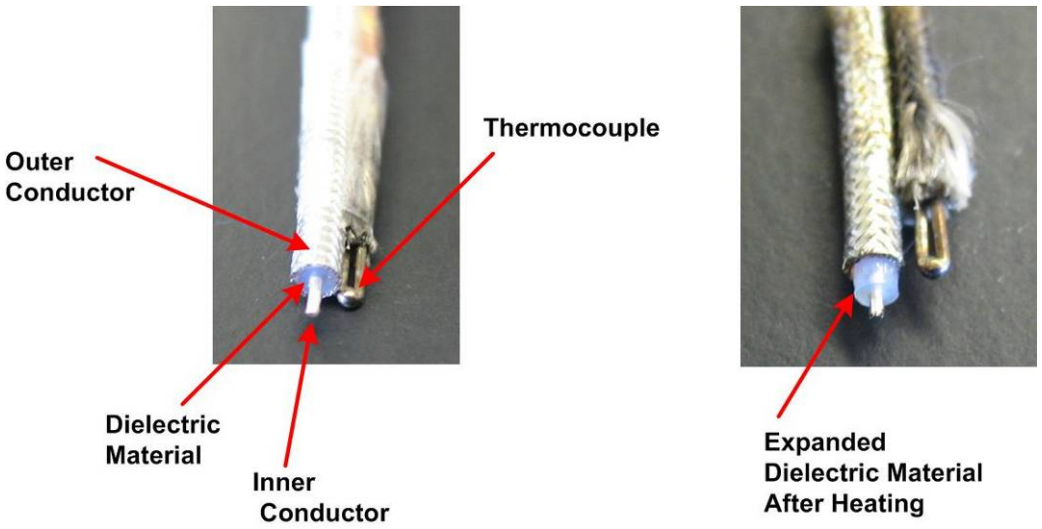

(a) Before heating (b) After heating

Figure 147. Pictures of the burning test results for the semi-rigid coaxial cable filled with the Teflon.

During the setup, a concern about high oxygen levels inside the test chamber was raised by the B&W SBS crew for their biomass combustion test measurements. Thus, additional blocking materials were added at the back side of the viewport; as shown in Figure 148(b) and Figure 149(b). The addition material was a refractory wool similar to Kaowool. A picture of the biomass samples used for firing is shown in Figure 150.

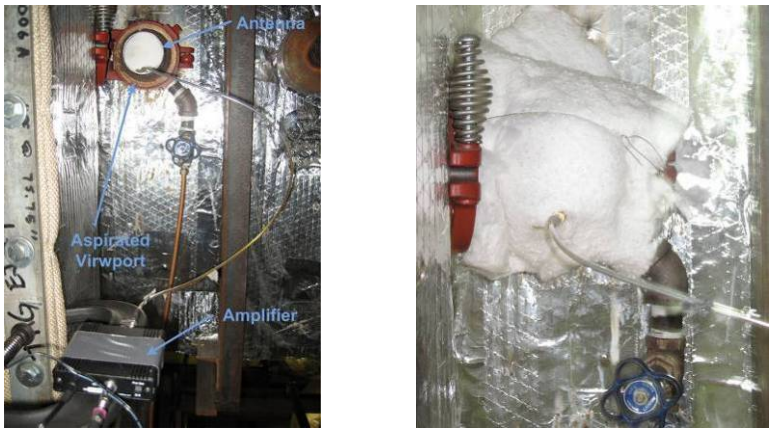

(a) (b)

Figure 148. Pictures of installation of antenna *A*, amplifier, and additional heat-blocking material (Port #1) – (a) Before and (b) after adding additional refractory wool heat-blocking material.

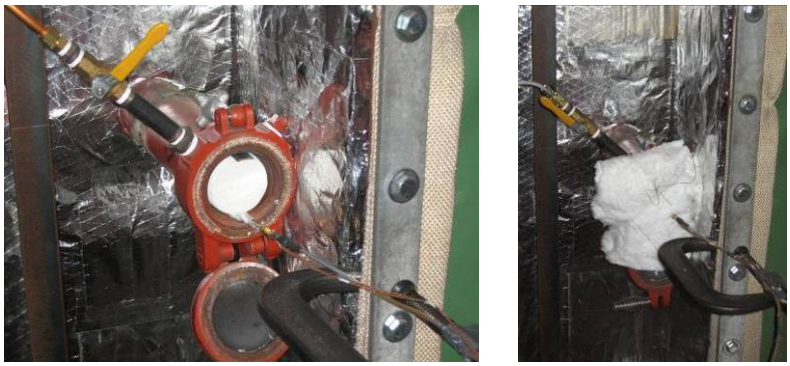

(a) (b)

Figure 149. Pictures of installation of antenna *B* and additional heat-blocking material (Port #2) – (a) Before and (b) after adding additional refractory wool heat-blocking material.

Figure 150. Picture of biomass used for firing test.

The system, including antennas, amplifier, and channel, was calibrated by using a response-and-isolation approach. An averaging factor of 1024 was used for the calibration in order to obtain an improved dynamic range by suppressing random noise. Later, it was observed that there was no noticeable difference between 128 and 1024 averaging samples on the measured data. After that, a 128 averaging factor was applied to the subsequent measurements, though the calibration was made with a 1024 factor.

Measurement and experiment events were noted with a time stamp. The temperature of Antenna A at both front and back was monitored periodically during the measurements. The notes recorded during the testing are summarized in Table 17.

The measured data for the s_{21} scattering parameter (link response between antennas) before and after biomass firing is shown in Figure 134. Both calibrated (blue) and un-calibrated (red) are depicted. Based on the un-calibrated data, the measured data below 2.4 GHz (cut-off frequency) and above 37.5 GHz seem to be noise. The dip around 17.5 GHz might be caused by excitation of high order electromagnetic modes in the circular guide region (viewport), meaning

that the dip could be relocated by changing the size of the viewport or choosing other antenna designs. As the comparison plots in Figure 151shows, most of amplitude fluctuations occur with a ±5 dB variation, which is not severe. Thus, one may consider windows in the range from 2.5 – 30 GHz to sense the spot temperature inside the test chamber if a sensor can provide greater response than the ±5 dB amplitude variation. Particularly, frequency windows of 10 – 15 GHz and 20 – 25 GHz have relatively linear phase responses. These two windows would be good candidates for selections of a frequency window.

Table 17. Summary of main events, corresponding time and monitored temperature

Time	**Event**	**Monitored Temperature**	
		Front	Back
05:00	Measurement started	41.0 °C	37.5 °C
-	Calibration and collecting initial data	-	-
06:20	Measured link response with 128 averaging factor before gas firing	-	-
07:00	Natural gas burner turned on to start process	41.1 °C	46.1 °C
07:00	Nitrogen aspiration connected to antenna viewports and started		
08:45	Biomass firing started (Natural gas + Biomass)	-	-
08:51	-	130.0 °C	130.0 °C
08:55	-	137.0 °C	110.0 °C
09:00	-	106.0 °C	73.0 °C
-	Hot air came out of the back side of the antenna B. Added addition blocking materials	-	-
09:20	Gas turned off, biomass firing only	64.0 °C	43.0 °C
09:30	Measured link response with 128 averaging factor (Pure biomass)	-	-
09:32	Biomass firing turned off (latent heat only)	56.0 °C	41.0 °C
09:58	Measured link response with 128 averaging factor (Latent heat – 1)	54.0 °C	37.5 °C
10:50	Measured link response with 128 averaging factor (Latent heat – 2)	53.7 °C	37.1 °C
11:00	Measurement ended	-	-

The cause for the phase variation shown in Figure 152b is unclear. However, the phase variation with the minus sign indicates that there was signal-transfer delay. If the delay was caused by multi-path reception, it would be a non-linear curve. However, the plot appears to be linear up to 25 GHz. This suggests that the delay was due to the lossy material such as fly ash and other particulates in the SBS.

The condition of the antenna-feed after completion of the biomass firing test is shown in Figure 153. Apparently, some solder melted and was dispersed during the test. However, the wrapped wires still held the semi-rigid coaxial cable on the antenna feed structure. The Teflon dielectric of the semi-rigid coaxial cable did not appear to have melted or extended beyond the exterior sheath of the cable.

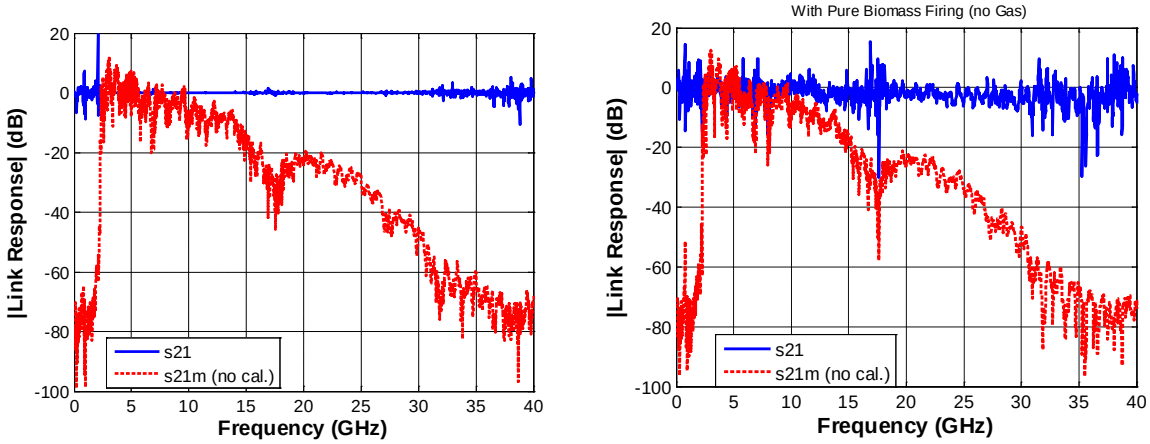

(a) (b)

Figure 151. Link response (a) before and (b) during the biomass firing.

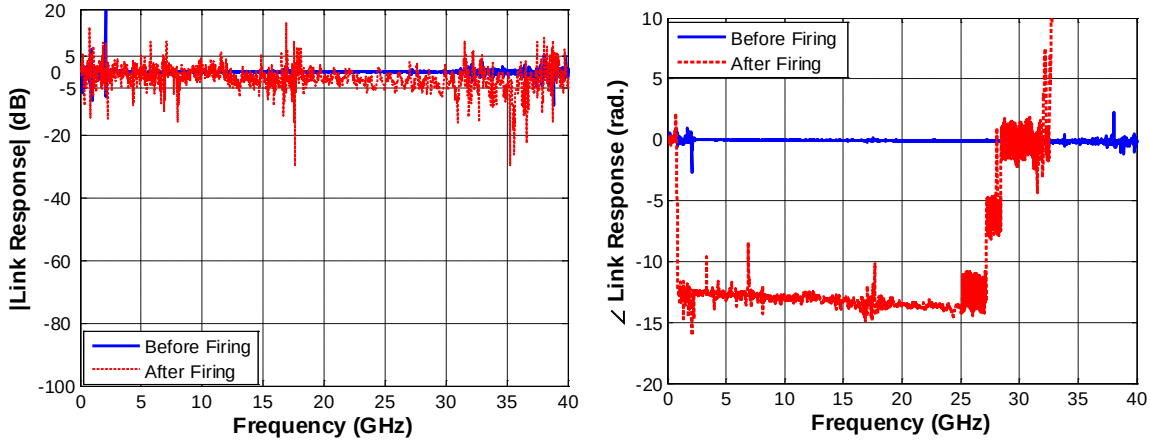

(a) Amplitude (b) Phase

Figure 152. Link response comparison between before and after firing (difference in amplitude (a) and phase (b) for measurements made before and during biomass firing).

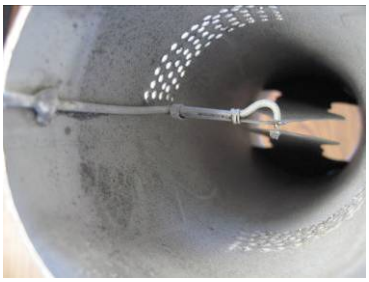

Figure 153. Close-up photo of antenna feed following biomass firing test.

For the biomass firing in the SBS plant, it was observed that any of the frequencies tested may be used for propagation of radio waves inside the SBS convection pass, other than below the cut-off frequency (2.4 GHz, limited by viewport size) or above 35 GHz (limited by antenna gain + amplifier gain + VNA power). In that frequency range, the measured link response fluctuated with a ±5 dB variation except a few peaks. Frequency regions of 10 – 15 GHz and 20 – 25 GHz had a relatively-linear phase response. These two bands can be considered as good candidates for a frequency window, though any frequency other than very low or high frequencies could be selected.

These results illustrate that two wide frequency ranges are suitable for radio frequency interrogation of passive metamaterial temperature sensor patches in an environment resembling the convection pass of a boiler system under conditions of biomass firing. In particular, the attenuation of the radio waves in these two bands (10 – 15 GHz and 20 – 25 GHz) was measured to be less than 5 dB/m; the separation of the two antennas in the SBS was measured to be less than 10 feet (3.0 m). Since the total loss of the radio waves across the SBS convection pass was less than 5 dB in the two frequency bands, attenuation of < 2 dB/m was measured.

4.1.4 Test of Attenuation During Pulverized Coal Firing

On November 14, 2011, Russell May (PPLC) and Bill Davis (Virginia Tech Antenna Group) visited Babcock & Wilcox's SBS facility in Barberton Ohio to perform attenuation testing. Two TEM horn antennas were installed in viewports that had been previously installed in opposing exterior walls of the convection pass, as depicted in Figure 138. The viewports, and therefore the installed antennas, were aligned coaxially and were separated by about 3 meters across the convection pass. The antennas were connected to an HP 8510C vector network analyzer (VNA) using RF coaxial cable. Due to the losses in the cable at high frequencies, a 30 dB microwave amplifier was used to boost the signal at the far end of the 32 foot cable.

Calibration of the equipment (VNA, coaxial cables, amplifier, and antennas) required some modified approaches due to the system configuration. Two calibrations were used: a through calibration and a reflection calibration at the receive port. These modifications were

necessary to accommodate the 30 dB amplifier in the system. Even so, additional measurements for comparison were required to account for the presence of the antennas in the system. In order to minimize loss effects in the coaxial cables, the amplifier was inserted at the input port of the chamber as shown in Figure 138, and the VNA was situated next to the output viewport in the convection pass, minimizing the cable length for the reflection measurement.

During the testing on November 14, 2011, temperatures in the vicinity of the VNA next to the convection pass (at the top of the SBS plant) exceeded 90° F. The VNA displayed an error message that indicated that the instrument phase lock was lost, which may have reduced the precision of the measurement as well as require additional time for the frequency sweep. Despite this error condition, calibration was completed using the reflection-and-isolation technique. However, the calibration procedure does not account for the effect of antennas; the reflection-and-isolation technique uses calibrated terminations on the end of the coaxial cables to simulate open and matched impedance conditions. In this way, the VNA and coaxial cables are calibrated without the antennas. Following this calibration, the terminations are replaced with the antennas. For this reason, the useful data obtained in the following tests is found by comparing the microwave scattering during coal firing with the microwave scattering when clean air was blown through the SBS during cool-down.

Testing proceeded in three steps: first, the antennas were set up outside and below the convection pass, but with the same coaxial alignment and 3 meter separation. In that way, proper operation of the VNA, antennas, amplifier, and cables could be verified through RF wave propagation in free space (outside the convection pass) before the antennas were installed in the viewports.

Next, the antennas were installed in the viewports. Measurements were then made to obtain scattering parameters, with an emphasis over the frequency range from 5 GHz to 20 GHz, while the SBS was fired with pulverized coal. The temperature of antenna A (the transmitting antenna) was monitored periodically using a thermocouple; the maximum temperature recorded during the testing was 234 °F (112 °C). Finally, scattering parameters for propagation through the convection pass were obtained during cool-down of the SBS; at that time, the coal combustion had been extinguished, and fans were used to run air through the SBS.

Figure 154 compares the magnitude of the scattering parameter s_{21} (the transmission) for the three cases. The s_{21} parameter represents the link response between antennas, or the loss (magnitude and phase) of radio wave propagation between the transmitting antenna (Antenna A) and the receiving antenna (Antenna B). Similarly, Figure 155 shows the phase of the scattering parameter s_{21} for the three cases. The data shown in Figure 154 and Figure 155 are the raw data obtained from the calibration without the antennas, requiring the additional comparison to data with the antennas to back out the propagation performance, as noted above. Thus, the comparison of the data with the antennas is the important measurement observation. An additional observation may be made in the data of Figure 154. Below about 2.5 GHz, the signal strength drops off dramatically. This is due to the low frequency cutoff of the antennas. In Figure 154b and c, the drop off is more pronounced due to the effect of the circular waveguide mode cutoff of the viewports. This frequency limitation is not a major issue since that lower frequency

is not of specific interest in the current design, but may help the reader understand the information presented as being reasonable.

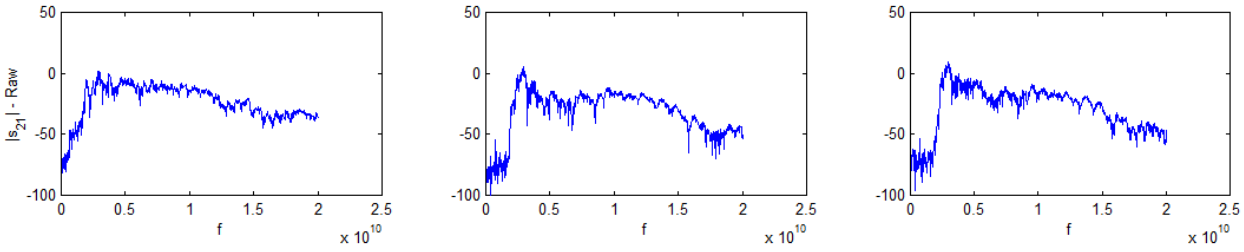

(a) (b) (c)

Figure 154. Spectral plots of the magnitude of the scattering parameter s_{21} (link response) for the cases (a) propagation in air outside the SBS, (b) propagation through the SBS convection pass during coal firing, and (c) propagation through the SBS convection pass during cool-down (air only in the SBS).

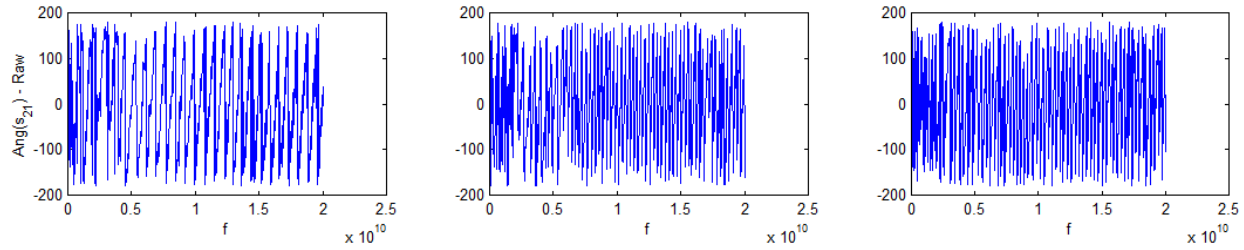

(a) (b) (c)

Figure 155. Spectral plots of the phase of the scattering parameter s_{21} (link response) expressed in degrees for the cases (a) propagation in air outside the SBS, (b) propagation through the SBS convection pass during coal firing, and (c) propagation through the SBS convection pass during cool-down (air only in the SBS).

In order to determine the contribution to the RF attenuation made by the coal combustion exhaust, the raw data for s_{21} obtained during coal firing was divided by the s_{21} data obtained during cool-down (air). The result is plotted in Figure 156. In this figure, data plotted between 10 GHz and 15 GHz is clustered around 0 dB loss, which implies no apparent loss. Above 15 GHz, wide variations in the result are seen. Note that values greater than 0 dB are likely due to noise, as positive values imply gain (amplification) of the signal due to the coal combustion, which is physically unlikely. Those wide variations are likely due to noise in the measurement, which was exacerbated because of low signal strength due to the losses in the coaxial cables at frequencies above 15 GHz. Similarly, data below 10 GHz show excessive noise. In this frequency band, the noise is likely due to multimode effects in the TEM horn antennas, due to the metallic cylindrical walls of the viewports surrounding the antennas and potential chamber resonances. Fortunately, the 10 to 15 GHz band with low loss is identical to the band identified as acceptable for radio frequency propagation in previous testing with natural gas and biomass firing. A couple of minor

attenuation points of about 3 to 5 dB are seen between 13 to 14 GHz. These are not considered significant, and are not expected to present a serious obstacle to sensor operation. Based on the results shown, operation of the sensor at 10 to 13 GHz would be a reasonable decision.

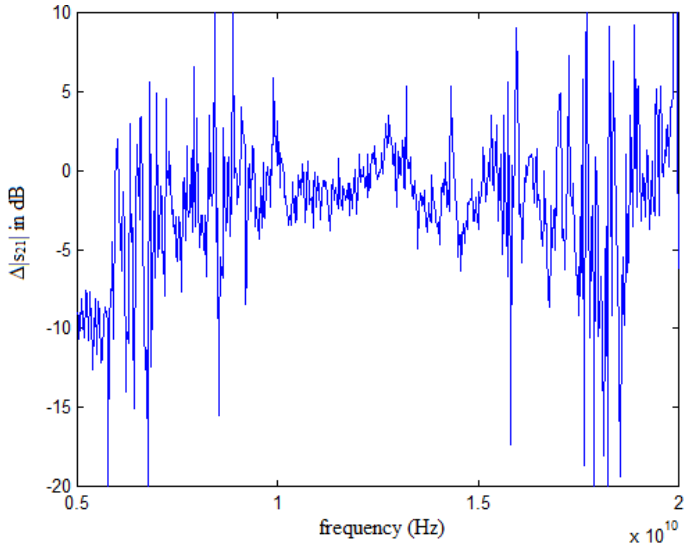

Figure 156. Change in magnitude of scattering parameter s_{21} between measurement when SBS was fired with coal and measurement when SBS was cooled with air. In this plot, negative values represent loss.

Figure 157a shows the difference in phase between the s_{21} data obtained during coal firing and that obtained during cool-down. In the range between 10 and 15 GHz where noise level was relatively low, the phase change very slowly and linearly with frequency. The linear variation phase suggests that lossy material such as fly ash or other particulates in the SBS were responsible for the phase change.

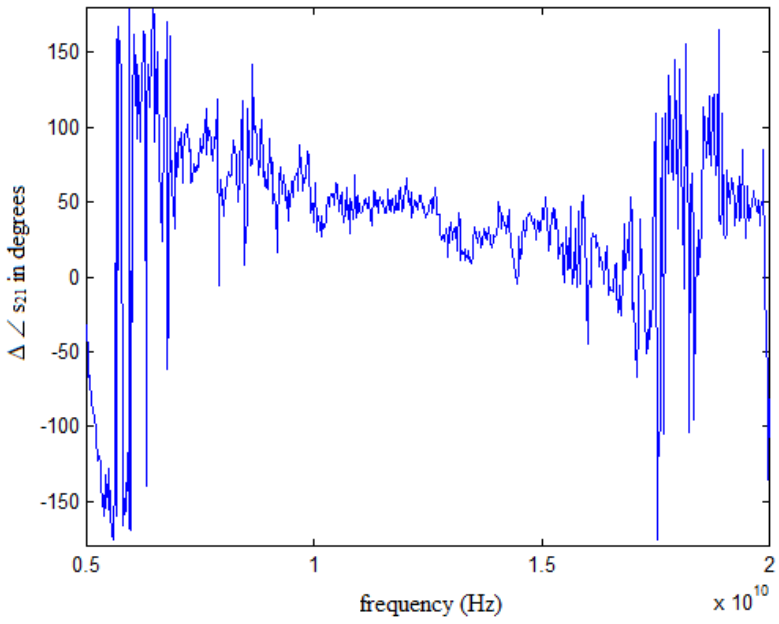

Figure 157. Change in phase angle of s_{21}, expressed in degrees, between measurement when SBS was fired with coal and measurement when SBS was cooled with air.

The RF attenuation measurements obtained on the SBS during coal firing indicate that the frequency range from 10 to 13 GHz (or conservatively, 10 to 12 GHz). As Figure 156 illustrates, the signal loss due to exhaust gases and fly ash from coal firing was less than 5 dB. When the 3 meter separation between antennas is considered, an attenuation of less than 2 dB/m is estimated for the band from 10 to 13 GHz. This result is similar to the attenuation values obtained on the SBS during firing with natural gas and biomass as fuels.

4.2 Temperature Tests of First MMA Prototype

The temperature sensitivity of the first prototype of the MMA sensor design (shown in Figure 61a) was characterized. An analysis was first performed using Mathematica to predict the change in vibrating beam resonant frequency with changing temperature. The model accounted for changes in elastic modulus, density, and dimensions of the beam, all of which depend on temperature and affect the natural frequency of the beam. The model predicted a temperature sensitivity of -0.2 Hz/°C, as shown in the plot in Figure 158.

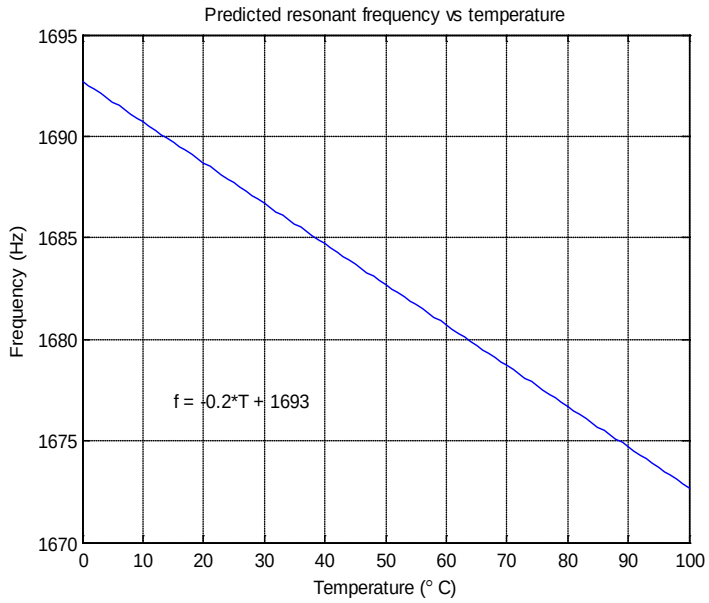

Figure 158. Predicted change in resonant frequency of the MMA antenna vibrating beam with changing temperature.

To test the prediction, a Type-K thermocouple was mounted onto the antenna in close proximity to the resonant beam. The antenna was mounted on a vibration test set shaker table (as seen in Figure 111) in order to excite the mechanical beam to resonance. The Doppler radar was set up with the transmit and receive horn antennas facing the MMA antenna and separated from the antenna by approximately two feet. An industrial heat gun was mounted so that hot air was blown onto the MMA antenna. As the temperature of the antenna increased, the frequency of the shaker table vibration was varied to find the maximum signal output by the Doppler radar interrogator.

Figure 159 plots the shaker table frequency which yielded the peak radar output for each temperature recorded. Due to the difficulty in maintaining a constant temperature in the experimental setup, some scatter and the data is observed. A linear regression was performed to determine the temperature sensitivity. As the figure shows, the temperature sensitivity given by the slope of the linear fit was found to be - 0.30 Hz/°C. Considering that the exact alloy of the copper used to fabricate the resonant beam in the first prototype MMA antenna is not known, the experimental data is in reasonable agreement with the prediction of the finite element model.

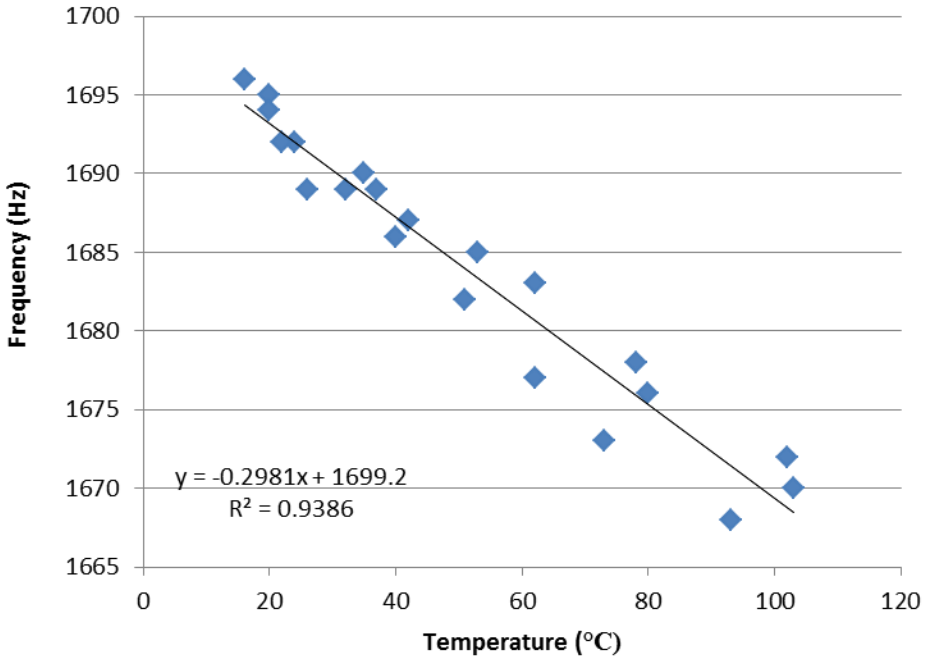

Figure 159. Vibration frequency yielding peak radar output for varying temperature.

4.3 Temperature Tests of Second MMA Prototype

A second prototype MMA sensor was fabricated, with dimensions chosen to duplicate the first MMA prototype as closely as possible, with the exception that a coaxial cable (current probe) was not added (see Figure 160). A 2" x 2" square of Rogers 4003C RF circuit board was used to form the ground plane. As this commercially available circuit board is clad on both sides with copper, copper cladding was removed from one side of the board. Next, a utility knife was used to cut a U-shaped slot in the remaining copper cladding. Two copper posts were then soldered on both sides of the slot, and a rectangular piece of beryllium copper (BeCu) was soldered to one of the posts the form the resonant beam. After measuring the dimensions of the beam and using well known values for the Young's modulus of BeCu, calculations were used to estimate that the natural frequency of the fundamental vibrational mode of the beam would be approximately 2 kHz.

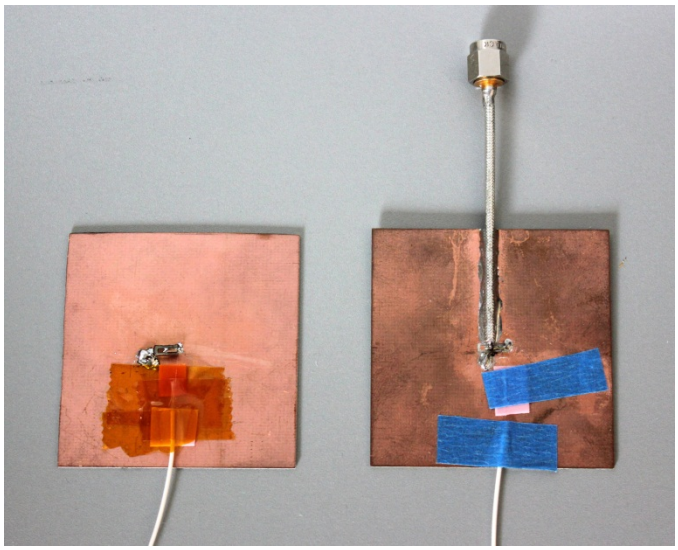

Figure 160. Comparison of new mechanically modulated slot antenna (left) and first prototype mechanically modulated slot antenna. The coax cable on the first prototype antenna was used as a current probe during preliminary testing. Optical fibers are mounted on each antenna for interferometric monitoring of resonant beam vibration amplitudes.

In order to experimentally determine the resonant frequencies of the beam, a single mode optical fiber was attached to the antenna to form a Fabry Perot cavity between the fiber end and the side of the beam. As with the testing of the first prototype antenna, the fiber was attached to a 1550 nm laser diode and an optical receiver through a single mode coupler. The output of the receiver was monitored using an oscilloscope. The antenna was in turn mounted on the shaker table of the vibration test set. The test set controller was programmed to vibrate the antenna sinusoidally with an acceleration of 8 g over a frequency range from 200 to 2500 Hz. The first resonance of the second prototype was found to be 2.1 kHz, in close agreement with the value predicted through calculation.

Knowing the frequencies of the mechanical resonances of the beam, it was then possible to determine the frequency of the electrical RF resonance. While the antenna was still mounted on the shaker table, the Doppler radar was set up to irradiate the antenna with microwaves. The frequency of the RF source output was slowly scanned over a range from 4 GHz to 15 GHz while the output of the Doppler radar's detector was monitored using a digital processing oscilloscope. When the RF source frequency matched that of the antenna's fundamental resonant frequency, a sinusoidal signal with a frequency equal to that of the resonant beam (the baseband frequency) could be observed on the oscilloscope. In addition, the oscilloscope was set to display a Fast Fourier Transform of the detector's output to facilitate measuring the magnitude of the baseband signal.

Using this process, the RF resonant frequency of the second prototype MMA was determined to be 9.5 GHz. While efforts were made during construction of the antenna to duplicate the materials and dimensions of the first MMA prototype, the resonant frequency of the new antenna was less than that of the first antenna. The difference is most likely attributed to the

presence of the coaxial cable (current probe) on the first antenna, which added capacitance to the antenna.

To prepare the antenna for testing, the antenna was mounted to a small laboratory vibration shaker table, with the ground plane mounted vertically. A Type K thermocouple was taped to the surface of the ground plane to monitor the temperature. A single mode optical fiber was also taped to the ground plane with the end face of the fiber in close proximity to the tip of the vibrating beam. The space between the end face of the fiber and the surface of the vibrating beam forms a Fabry-Perot resonant cavity, and the cavity length was measured by connecting the output of the optical fiber to a fiber optic Fabry-Perot interrogator. A small aluminum block containing a resistive cartridge heater was mounted on the back of the antenna using thermally conductive paste. The heater cartridge in turn was connected to an Omega controller, with the thermocouple used as feedback. During the test, the temperature was increased from room temperature and 10° increments until a temperature of 120° C was attained. At each temperature tested, the shaker table was actuated with an acceleration of 24 g, and the frequency of vibration was varied from 1500 to 2500 Hz while the fiber interferometer was used to monitor the amplitude of vibration of the vibrating beam. When the peak amplitude of vibration was detected, the frequency corresponding to this peak was recorded, along with the temperature.

The results of this testing are illustrated in Figure 161. In this graph, the blue data points represent data obtained as the temperature of the antenna was increased. After a temperature of 120° C was reached, the heater was turned off and the antenna was allowed to cool. As the temperature decreased, the resonant frequency of the beam was determined at 20° C increments. The results show at most a small hysteresis. The sensitivity of the antenna as a temperature sensor was estimated by using a linear regression set to determine the slope of the traces, which yielded an estimate of -0.36 Hz/°C.

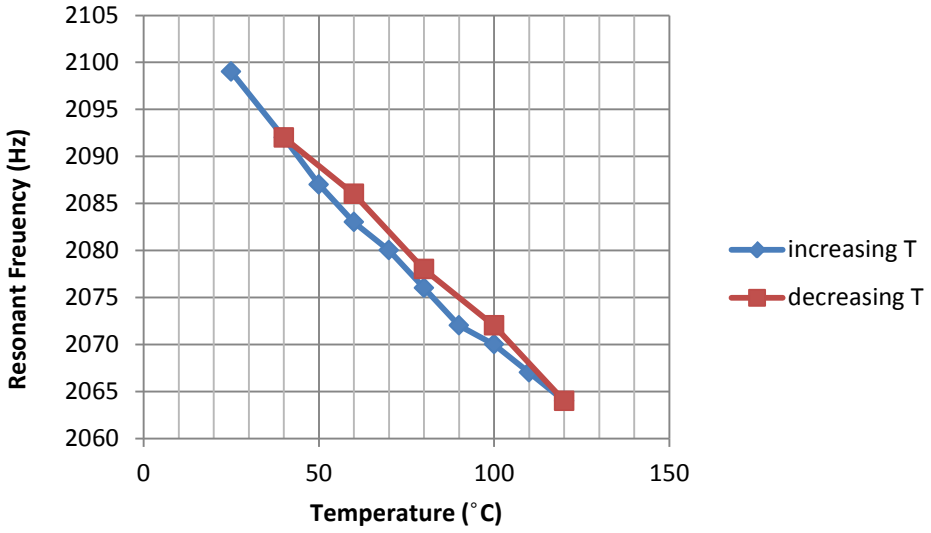

Figure 161. Result of testing frequency response of new mechanically modulated slot antenna.

The temperature test was conducted a second time to derive an estimate of repeatability. The results of that test are plotted as the red trace (Trial 2) in Figure 162, where the results of the

first test are plotted as the blue trace (Trial 1). A linear regression fit was calculated for the red trace, giving an estimate of -0.48 Hz/°C for the sensitivity as determined in the second test. The reason for the difference in sensitivity between the two tests of the same antenna was unknown.

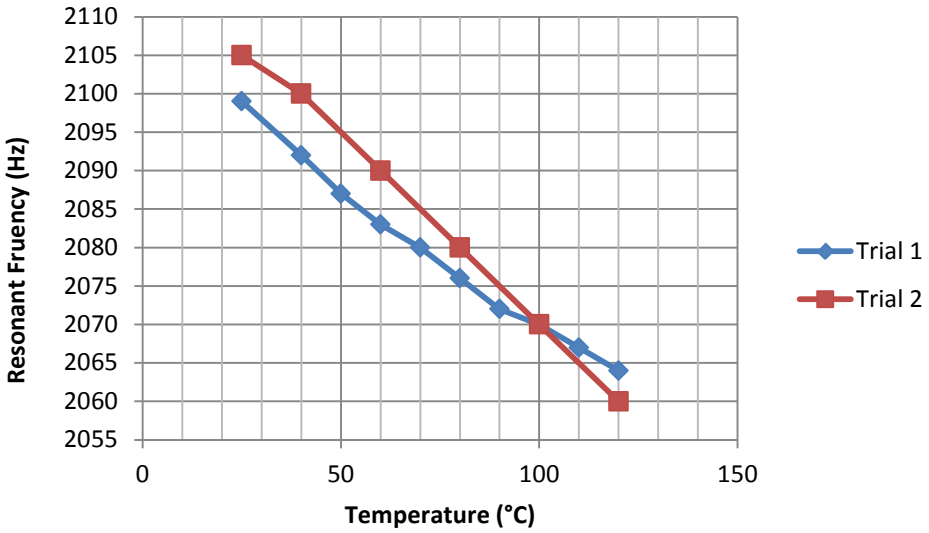

Figure 162. Comparison of two temperature tests of the new mechanically modulated slot antenna.

4.4 Temperature Tests of Final MMA Prototype Using Direct Bonded Copper

To test the final MMA design described in Section 3.8, a prototype was made according to the assembly drawing shown in Figure 163. For initial testing at room temperature, the base plate and resonator plate were fabricated from polycrystalline alumina plates, and were bonded together with a direct bonded copper (DBC) layer. DBC was used because it is a well-known process for bonding alumina parts, and because the copper layer would serve as a good microwave reflector, improving the relatively low X-band microwave reflection of the bare alumina. The thin top square of alumina was added due to fabrication restraints and would not be needed in a mass produced version of the MMA. The DBC oxidizes above 300 °C but can be used for short periods of time up to 1000 °C although the copper will be converted to copper oxide faster as the temperature is raised.

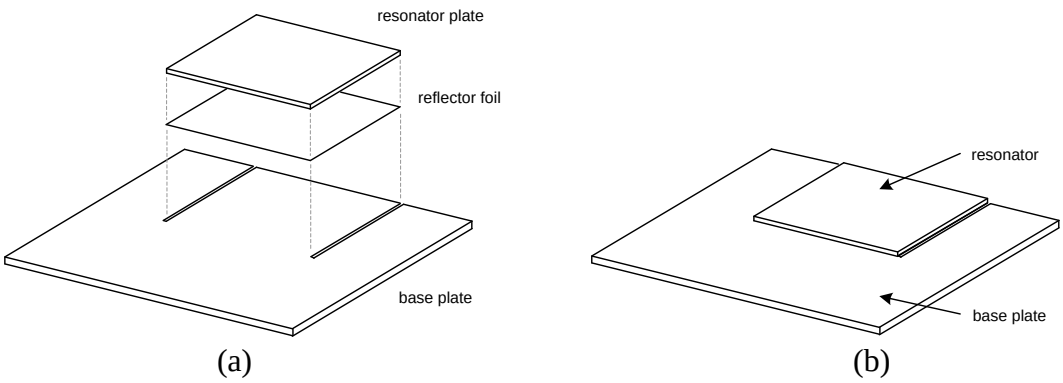

Figure 163. Assembly of prototype revised MMA sensor, showing (a) relationship of sensor components; (b) schematic of assembled sensor.

To bond the resonator plate to the base plate using direct bonded copper as shown in Figure 163. , a 2" x 2" x 1 mm polycrystalline alumina plate was selected as the base plate, and a 1" x 1" x 1 mm polycrystalline alumina plate was selected for the resonator plate. A 0.003 inch thick copper foil was used to bond the alumina parts. All of the parts were washed in hot water and rinsed with acetone. After air drying, the parts were stacked with a piece of ceramic (about one ounce) on top and rapidly brought to 1073 °C for one hour then cooled by turning off the oven. Argon was flowed into the furnace at a rate of approximately 0.5 cu. ft. per minute in order to inhibit oxidation of the copper.

The resonant frequency of the bonded assembly was relatively easy to find by imparting an impulse loading to the resonator plate of the sensor and examining the audio power spectrum as the vibrations decayed. Then a CW acoustic drive was applied with the ultrasonic speaker (Section 3.2.3) and the resonant response was detected with the interrogator. The resonant response had about a 1 Hz width, so the mechanical Q of the antenna was several hundred. Therefore, the ability to reject out of resonance vibrations was about 25 dB. This was a good match to the electrical performance of the rest of the system.

The sensor was then prepared for testing at elevated temperatures. Figure 164 shows the DBC sensor mounted to a plate of Zircar Type AL-25/1700 alumina insulation with alumina bolts. This mounting permitted the sensor to be placed in a high-temperature furnace for testing.

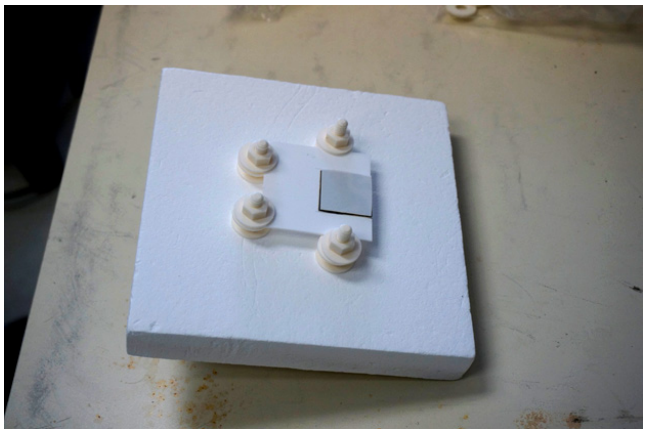

Figure 164. Prototype revised MMA with direct bonded copper (DBC) bonded alumina resonator plate. The MMA is mounted to a Zircar insulation plate for installation in a high-temperature furnace.

To test the DBC sensor at high temperatures, a Thermolyne 46100 furnace with molybdenum disilicide elements, capable of heating to 1700° C, was used. The Zircar refractory plate holding the DBC sensor was sized so that the refractory plate would fit in the entrance to the furnace, effectively sealing it so that the heat would be retained in the furnace cavity. Figure 165 shows the refractory plate in place in the furnace, with the sensor rotated so that it faced outside the furnace. Initial tests were performed in this orientation at room temperature to verify the proper operation of the sensor, and then the refractory plate was rotated so that the sensor was in the furnace for heating in subsequent tests.

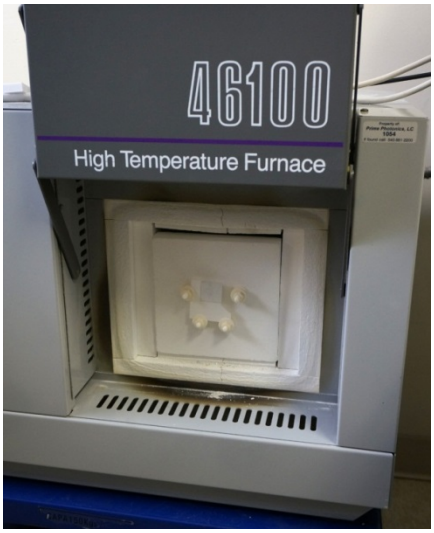

Figure 165. Zircar refractory panel in face of Thermolyne high temperature furnace. The DBC sensor can be seen held in position with alumina hardware. For high temperature tests, the Zircar panel was rotated so that the sensor was in the interior of the furnace cavity.

During the high temperature tests, the HSS 450 ultrasonic speaker system was positioned approximately 1 m from the furnace entrance. With the sensor on the inside of the furnace, the incident sound waves cause the surface of the Zircar plate to vibrate, and this vibration was transferred to the sensor through the alumina mounting bolts. Similarly, the transmit and receive microwave horn antennas of the Doppler radar interrogator were positioned approximately 1 m from the furnace entrance, with the antennas directed toward the furnace. During the tests, the interrogating microwaves passed through the Zircar plate, and were then reflected by the copper layer (or platinum layer in subsequent tests) of the sensor. Figure 166 shows the layout positioning of the horn antennas and microwave speakers relative to the furnace.

The interrogator used for the high temperature tests employed the components shown in Figure 56, with the exception that a lock-in amplifier was used in place of the phase locked loop and a digital processing oscilloscope (DPO) was used in place of the microcontroller. The use of the lock-in amplifier enabled a high measurement signal-to-noise ratio due to the programmable bandpass of the amplifier, and permitted measurement of the signal amplitude during testing.

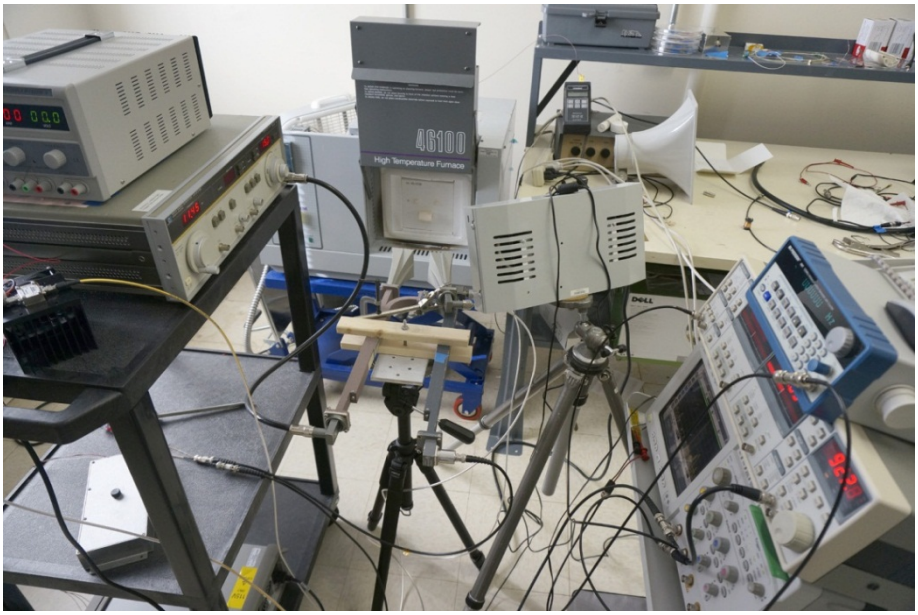

Figure 166. Laboratory set-up for high temperature tests of MMA sensors in Thermolyne high-temperature furnace.

Thermal testing verified that the resonant frequency of the antenna was correlated to the temperature. On the DBC bonded article, the response was about 0.5 Hz per 100 °C. Frequency resolution with manual tuning of the system was about 0.1 Hz; this could be improved substantially with a PLL controlled acoustic drive circuit. Figure 167 plots the measured resonant frequency of the DBC sensor as determined by the Doppler radar interrogation system.

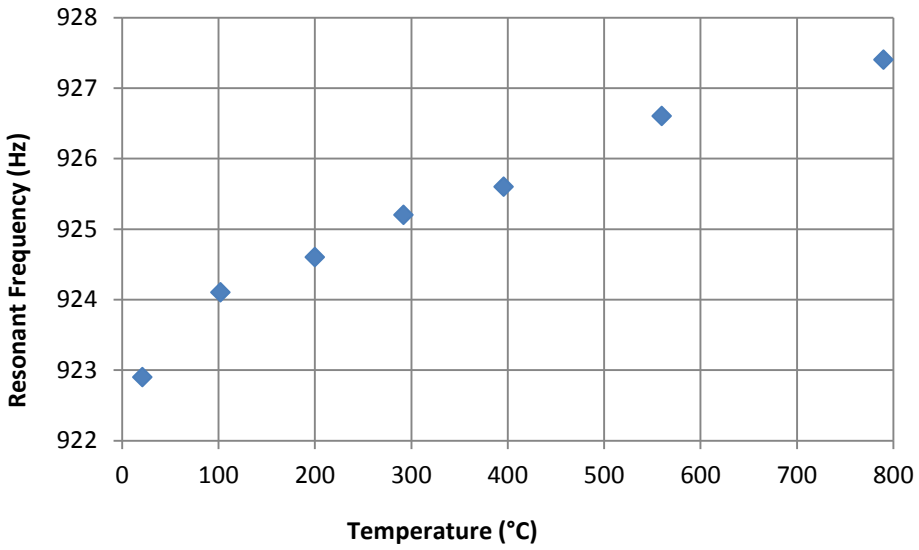

Figure 167. Resonant frequency of DBC sensor as measured by Doppler radar interrogator as sensor was heated in high temperature furnace.

The amplitude of the detected signal was also recorded during the temperature test and was observed to decrease as the temperature increased. As Figure 168 shows, the signal amplitude appears to asymptotically approach the 100 µV noise floor of the digital processing oscilloscope. For temperatures exceeding 790° C, the signal due to the sensor resonance could not be detected above the interrogation system noise.

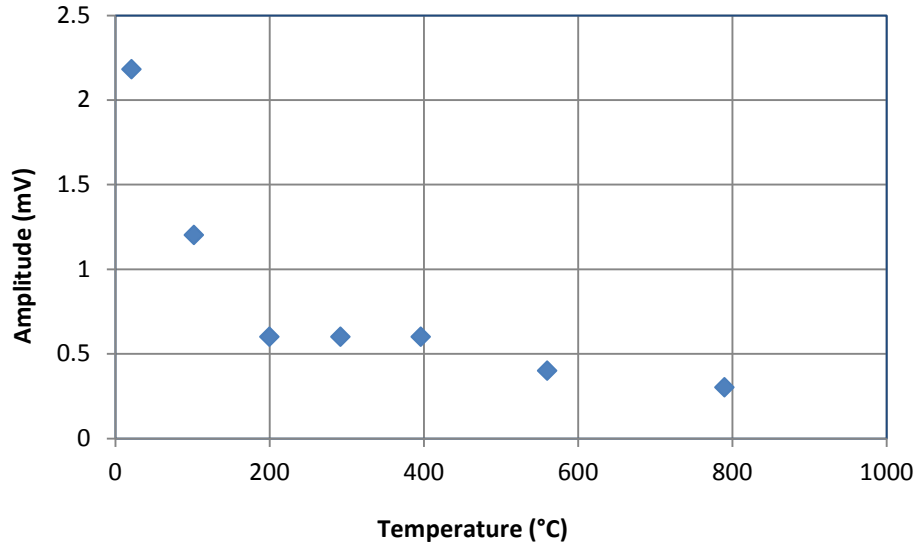

Figure 168. Amplitude of the detected signal from the DBC sensor as measured by Doppler radar interrogator as sensor was heated in high temperature furnace.

4.5 Temperature Tests of Final MMA Prototype Using Platinum Foil

Two prototype sensors were fabricated using platinum as the reflector foil for testing at higher temperatures. The sensor assembly used a 2" x 2" x 1 mm polycrystalline alumina plate for the base plate, a 1" x 1" x 0.25 mm polycrystalline alumina plate for the resonator plate, and a 1" x 1" x 0.10 mm platinum foil for the reflector. After stacking these components as shown in Figure 163, the assembly was sandwiched between two alumina plates and placed inside a high-temperature furnace. An alumina rod, with an alumina ball on the bottom to produce a point load, was used to transfer weight from a stack of steel weights to the assembly (Figure 169). The weights were chosen to result in an applied pressure of 0.8 MPa. The furnace was heated to 1200° C for three hours followed by nine hours hours at 1100° C to promote a diffusion bond between the alumina and the platinum. This procedure generally followed the process outlined by Allen and Borbidge.[12]

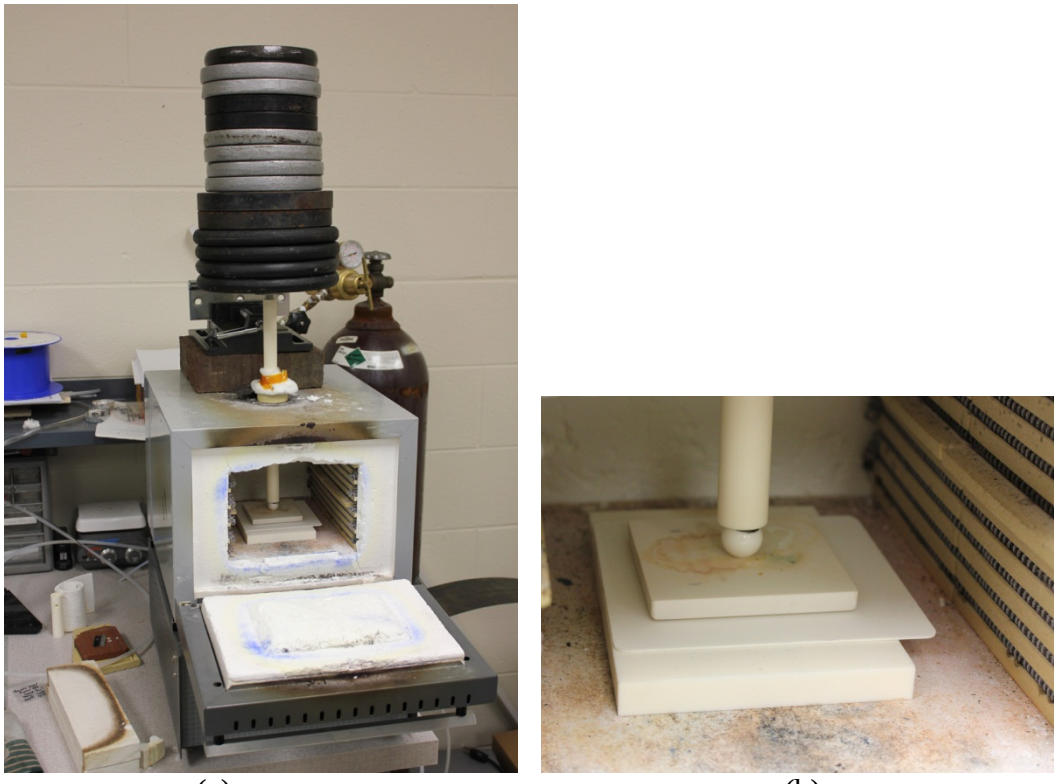

(a) (b)

Figure 169. (a) furnace used to heat Pt/alumina MMA to promote bonding between alumina plates and platinum foil. The weights used to apply pressure to the assembly are shown on top of the alumina rod; (b) an alumina sphere was used to achieve a point load on the top pressure plate.

The platinum/alumina sensor was then mounted on the Zircar alumina plate, which in turn was installed in the Thermolyne furnace for high temperature testing. Figure 170 shows the resonant frequency of the platinum/alumina sensor as measured by the Doppler interrogator as the temperature was raised to 272° C. As Figure 171 shows, the amplitude of the received signal

was seen to decrease as a temperature increase. Beyond 272° C, a discernible signal could not be detected above the noise floor of the interrogator.

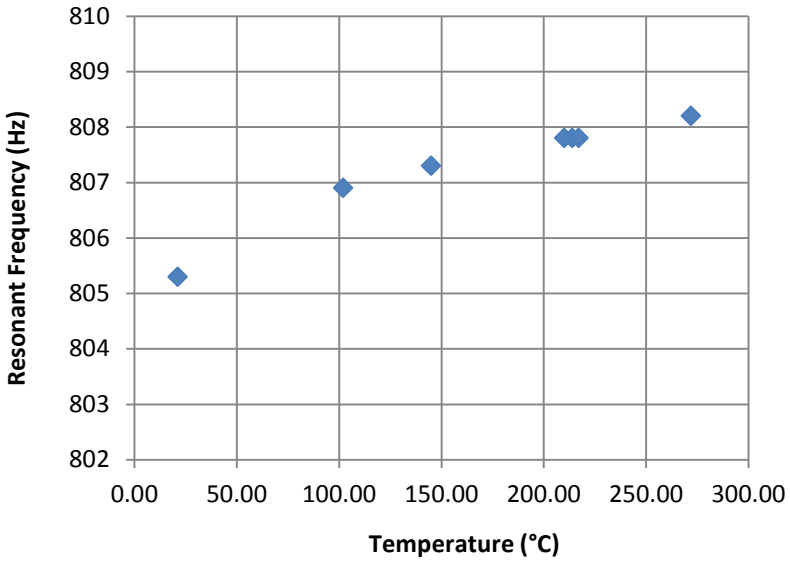

Figure 170. Resonant frequency of the Pt/alumina sensor as a function of temperature, measured by the Doppler radar interrogator.

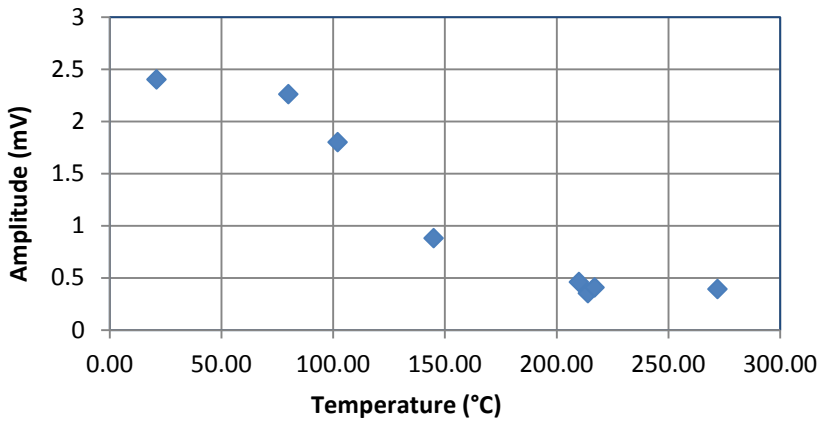

Figure 171. Signal amplitude of the Pt/alumina sensor as a function of temperature, measured by the Doppler radar interrogator.

Additional testing was performed to determine if the decrease in signal amplitude at higher temperatures was due to changes in the Zircar alumina insulation. Since the test set-up

required that both the microwaves and the acoustic waves pass through the insulation to reach the sensor in the interior of the furnace, it was hypothesized that the radio frequency or acoustic attenuation of the insulation might increase as temperature rises.

To test whether acoustic attenuation might be the cause, the ultrasonic speaker system was replaced with an apparatus used to directly excite the sensor resonator. As shown in Figure 172, a piezoelectric transducer was bonded to the end of a ¼ inch diameter, 18 inch long alumina rod using a cyanoacrylate adhesive. The rod was supported by a tripod, with the rod resting on ceramic wool insulation to minimize attenuation of acoustic waves in the rod. The free end of the rod was brought in contact with one of the alumina bolts used to mount the sensor to the Zircar plate, and a rubber band was used to maintain a small force on the rod to ensure contact. By driving the piezo transducer at the sensor's resonant frequency, acoustic waves could be launched through the alumina bolt to excite the sensor, bypassing the Zircar plate and eliminating any potential acoustic attenuation.

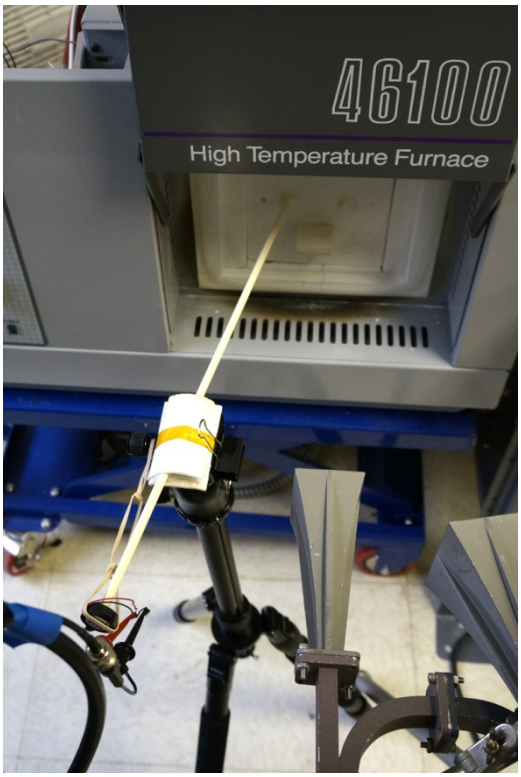

Figure 172. Alumina rod used to directly excite Pt/alumina sensor. A piezoelectric transducer attached to one end of rod was used to launch acoustic waves into rod. The other end of the rod was held in contact with the alumina bolts used to mount the sensor to the Zircar insulating plate.

As the sensor was heated from room temperature to 164° C, the resonant frequency of the sensor resonator was tracked and was found to be linear over that range (Figure 173). Above 164° C, an additional noise source was observed and the data was not considered reliable. As illustrated in Figure 174, the amplitude of the signal decrease as the temperature was increased

from 84° to 164° C. The signal amplitude at 21° C was anomalously low; the cause for that low reading is not known.

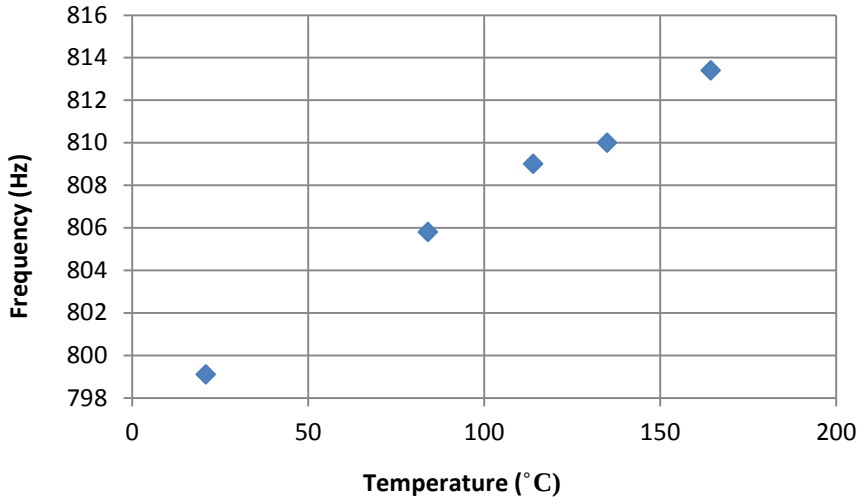

Figure 173. Resonant frequency of the Pt/alumina sensor as a function of temperature, with the sensor directly excited by alumina rod with piezo transducer.

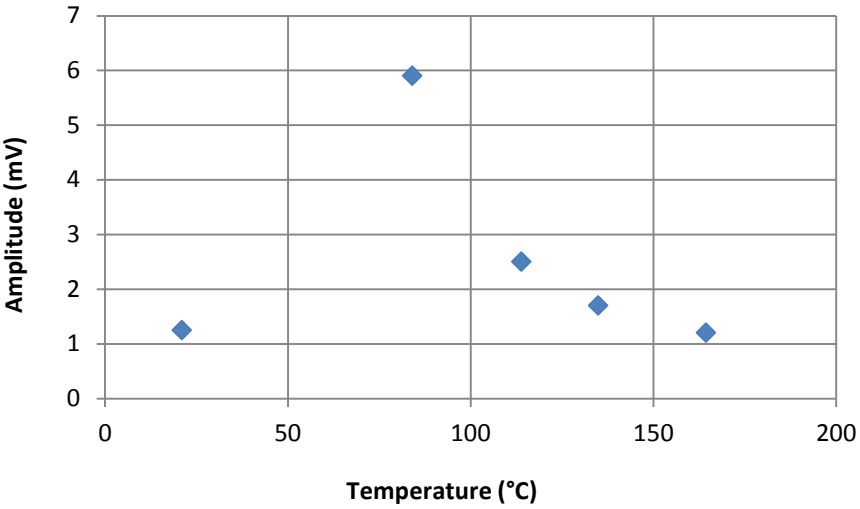

Figure 174. Signal amplitude of the Pt/alumina sensor as a function of temperature, with the sensor directly excited by alumina rod with piezo transducer.

An additional test was performed to examine the possibility of acoustic attenuation. A 6" x 6" x 1" plate of Zircar alumina refractory was placed on a hot plate, and insulation plates were placed around the Zircar to retain heat is shown in Figure 175(a). The insulation was positioned so that open apertures were provided in front of and behind the Zircar panel for transmission of

the acoustic waves. The HSS H450 ultrasounds speaker system was positioned directed towards one side of the Zircar plate. On the other side, a decibel meter was set up to measure the sound pressure level (SPL) through the Zircar plate. An 18" x 18" x 3" foam panel was used to block sound waves from reaching the decibel meter except through the Zircar plate. A through hole was cut in the foam panel and position next to the Zircar plate, and a decibel meter input was placed in the hole, as shown in Figure 175 (b).

(a) (b)

Figure 175. Test set-up to determine temperature sensitivity of acoustic attenuation of Zircar alumina

With the ultrasound source off, the SPL in the laboratory was recorded to be 39 dBA. When the source was turned on and excited at 1.0 kHz, the measured SPL was 70 dBA. The data recorded as the temperature of the Zircar panel (as measured by a thermocouple) was increased is given in Table 18. These results suggest that is unlikely that the decrease in MMA sensor signal strength with increasing temperature is due to changing acoustic attenuation of the Zircar panel.

Table 18. Sound pressure level (SPL) of 1 kHz acoustic waves transmitted through Zircar alumina panel as a function of temperature (T).

T(°C)	SPL (dBA)
22	70
200	70
250	70
265	70
270	70

The radio frequency attenuation of the Zircar panel in the microwave X-band as a function of temperature was also tested. Using a set-up similar to that described for the acoustic attenuation test, the Zircar panel was placed on a hot plate with insulation surrounding it. The insulation was positioned so that open apertures were provided in front of and behind the Zircar panel for transmission of the microwaves. The transmit horn antenna from the Doppler radar interrogator was placed in front of the Zircar panel, and the receive horn antenna was placed

behind the panel. The Doppler radar interrogator was used to measure the microwave power transmitted to the Zircar panel. The X-band source, with an output power of 15dBm, was fine-tuned around 11.40 GHz to give a maximum detector output of -98.9 to -99 mV with slight rapid fluctuations of the oscilloscope reading. The recorded data is shown in Table 19. These results suggest that is unlikely that the decrease in MMA sensor signal strength with increasing temperature is due to changing microwave attenuation of the Zircar panel.

Table 19. Output of Doppler radar interrogator as 11.40 GHz microwaves were transmitted through Zircar alumina panel as a function of temperature (T).

Temperature (°C)	Output (mV)
22.2	-99
100	-99
150	-99
200	-99
250	-99
275	-99

Figure 176. Experimental set-up used to measure temperature dependent microwave attenuation of Zircar alumina panel with temperature.

3 CONCLUSIONS

The objective of this program was the development of a passive wireless sensor for measurement of temperature in coal gasifiers and coal-fired boiler plants. The first technology investigated was a metamaterial sensor based on guided mode resonance filters (GMRFs). By attaching a dielectric slab waveguide to a diffraction grating, an electromagnetic filter is formed. If radio waves are directed at the filter, it will pass some frequencies while reflecting others. The sharpness (or Q) of the filter spectral response depend on the magnitude of dielectric loss of the slab waveguide. If the dielectric loss or conductivity of the waveguide changes with temperature, then a radio can be used to remotely determine the sharpness of the filter response and determine its temperature.

Laboratory testing determined that the electrical conductivity of silicon carbide varies quadratically with temperature and was suitable for fabrication of temperature sensors based on GMRF metamaterials. Prototype GMRFs were fabricated using a high-conductivity silicon carbide and tested in the laboratory. The desired spectral filter response was not obtained in the test results. Using the same test set-up, a two-dimensional dipole array was tested and the spectral filter response predicted for a dipole array was observed, ruling out experimental error in the test of the GMRF. After further analysis of the results, it was concluded that the GMRF spectral response was swamped by specular reflection of an interrogating radio waves off of the metallic diffraction grating.

Investigation then began into an alternative passive wireless sensor approach. The goal for the new approach was to design a temperature-sensitive antenna that would modulate the frequency of incident radio waves as they are re-radiated by the antenna, permitting easier discrimination of the sensor response from surrounding specular reflections of interrogating radio waves. Towards this end, a mechanically modulated antenna (MMA) was designed, fabricated, and tested. In this design, a folded slot is cut into a metal ground plane to form the antenna. A cantilever beam, fixed on one end and free on the other, is attached to the ground plane. Sound waves directed at the cantilever beam induced it to vibrate, and the sinusoidally varying separation between the cantilever beam tip and the ground plane changes the antenna impedance sinusoidally with time. The harmonically varying antenna impedance imparts a phase modulation on the incident interrogating radio waves. By using a Doppler radar system, the frequency of the cantilever beam's resonant vibration can be determined remotely. This frequency, in turn, can be used to determine the temperature of the cantilever beam, as its natural resonant frequency changes with temperature since elastic modulus of the resonant beam depends on temperature.

Finite element electromagnetics modeling software was used to design and simulate MMAs. Prototype MMA sensors were fabricated and tested at room temperature and at elevated temperatures. The Doppler radar system for interrogation of the MMA sensor was built and refined.

Testing of the prototype MMA sensors over a range of temperatures showed that the MMA cantilever beams resonant frequency varied linearly with temperature. However, the

amplitude of the modulated signal decreased with increasing temperature, and approached the noise floor of the Doppler radar interrogator, ultimately limiting the maximum temperature for which the signal could be obtained to 790° C. Additional testing to probe the cause for the reduction in signal strength at high temperature appeared to rule out experimental set-up as contributing to the signal attenuation, and suggested that sensor fabrication methods or limits in materials used were at least partly responsible for signal attenuation at high temperatures.

Tests were conducted at Babcock and Wilcox's Small Boiler Simulator in Barberton, OH to identify a suitable window in the microwave spectrum where little or no attenuation of radio waves occurs as the waves propagate through the exhaust of a coal-fired burner. A suitable window of less than 2 dB/m was found in the range from 10 to 13 GHz.

4 REFERENCES

[1] R. Marques, F. Martin, M. Sorolla, **Metamaterials with Negative Parameters: Theory, Design, and Microwave Applications**, Wiley, Hoboken, NJ, 2008.

[2] S. A. Ramakrishna, T. M. Grzegorczyk, **Physics and Applications of Negative Refractive Index Materials**, CRC Press, New York, NY, 2009.

[3] J. D. Joannopoulos, S. .G. Johnson, J. N. Winn, R. D. Meade, **Photonic Crystals: Molding the Flow of Light**, Princeton University Press, Princeton, NJ, 2008.

[4] J. M. Lourtioz, B. Berger, J. M. Gerard, H. Benisty, **Photonic Crystals: Towards Nanoscale Photonic Devices**, Springer-Verlag, New York, NY, 2005.

[5] W.D. Kingery, H.K. Bowen, D.R. Uhlmann, **Introduction to Ceramics**, John Wiley & Sons, 1976, p 923.

[6] Aiguo Kang, Longtu Lia, Xiangyun Denga and Xiaohui Wanga, "The study on high temperature conductivity of nanocrystalline BaTiO3 ceramics," *Materials Science and Engineering: B,* Volume 132, Issue 3, 15 August 2006, Pages 288-291

[7] Baeraky, T.A., "Microwave Measurements The Dielectric Properties of Silicon Carbide At High temperature" *J. Egyptian journal of Solids*, Vol. 25 (2), PP. 263, 2002.

[8] Ferber,M. K., Lin, H. T., and Keiser, J., "Oxidation Behavior of Non-Oxide Ceramics in a High-Pressure, High-Temperature Steam Environment," *Mechanical, Thermal and Environmental Testing and Performance of Ceramic Composites and Components*, M.G. Jenkins, E. Lara-Curzio, and S.T. Genezy, editors, ASTM STP 1392, 210-215 (2000).

[9] K. C. Gupta, "Microstrip Lines and Slotlines, Artech House, 2nd ed., 1996

[10] J. Baker-Jarvis, E. Vanzura, and W. Kissick, "Improved technique for determining complex permittivity with the transmission/reflection method," *IEEE Transaction on Microwave Theory Tech*, vol. 38, pp. 1096–1103, Aug. 1990.

[11] Gary L. Harris, *Properties of Silicon Carbide*, INSPEC, Institution of Electrical Engineers, 1995.

[12] R.V. Allen, W.E. Borbidge, "Solid state metal-ceramic bonding of platinum to aluminum," Jour of Materials Sci, 18 (1983) pp 2835-2843.